Annual Report

of

The Institute Of Physics

Academia Sinica

Volume 8 December 1978

The Institute of Physics, Academia Sinica
Nankang, Taipei, Taiwan, Republic of China

中央研究院物理研究所集刊

編輯委員會

The Annual Report is published annuall by the Institute of Physics, Academia Sinica, Nankang, Taiwan 115, Republic of China. The Annual Report is available on an exchange basis to other scientific, research, and educational institutions.

本集刊每年出版一次

非賣品

中央研究院

物理研究所集刊

第八卷

發行人：林爾康

編輯者：中央研究院物理研究所集刊編輯委員會

出版者：中央研究院物理研究所　臺北市南港區

印刷者：大地印刷廠

電話：九七一二二四四・九七一二二六六

中華民國六十七年十二月出版

中央研究院物理研究所集刊

第 八 卷

中央研究院物理研究所印行

CONTENT 目 錄

ARTICLES

ABSTRACTS

SPHERICALLY SYMMETRIC, STATIC FIELD OF AN EXTENDED STAR—A MODIFIED SCHWARZSCHILD PROBLEM

TA-YOU WU

Institute of Physics

Abstract

For an extended distribution of T^{ν}_{μ}, with $T^{\nu}_{\mu;\nu} = 0$, the field equations $G^{\nu}_{\mu} = -\kappa T^{\nu}_{\mu}$ for a spherically symmetric, static field

$$ds^2 = g_{11}(r)dr^2 - r^2d\theta^2 - r^2\sin^2\theta d\varphi^2 + g_{44}(r)dt^2$$

can be solved exactly without solving the nonlinear equation for $G_2^2 = G_3^3$, giving

$$-e^{\lambda} \equiv -g_{11}(r) = 1 - \frac{1}{r}\int \kappa T_4^4 r^2 dr - \frac{2m}{r},$$

$$-g_{11}(r)g_{44}(r) = \int \kappa (T_4^4 - T_1^1)\, e^{\lambda}\, r dr.$$

For the model

$$T_4^4(r) = \frac{B}{r^2} e^{-r/\rho}, \qquad \rho = \text{constant},$$

$g_{11}(r)$ has or does not have a singularity for $r > 0$ depending on whether $\rho < 2m$ or $\rho \geq 2m$.

I. THE SCHWARZSCHILD PROBLEM

For the spherically symmetric, static field of a massive point, the metric element is assumed to be

$$ds^2 = g_{11}dr^2 - r^2d\theta^2 - r^2\sin^2\theta\, d\varphi^2 + g_{44}dt^2 \tag{1}$$

where

$$g_{11}(r) = -e^{\lambda(r)}, \qquad g_{44}(r) = e^{\mu(r)} \tag{2}$$

are functions of r alone. With the $g_{\mu\nu}$ given by (1), one obtains the following nonvanishing three-index symbols

$$\left\{\begin{matrix}1\\11\end{matrix}\right\} = \frac{1}{2}\frac{d\lambda}{dr}, \qquad \left\{\begin{matrix}1\\22\end{matrix}\right\} = -r\, e^{-\lambda}, \qquad \left\{\begin{matrix}1\\33\end{matrix}\right\} = -r\sin^2\theta\, e^{-\lambda},$$

$$\left\{\begin{matrix}1\\44\end{matrix}\right\} = \frac{1}{2}e^{-\lambda+\mu}\frac{d\mu}{dr}, \quad \left\{\begin{matrix}2\\12\end{matrix}\right\} = \left\{\begin{matrix}2\\13\end{matrix}\right\} = \frac{1}{r}, \quad \left\{\begin{matrix}3\\23\end{matrix}\right\} = \cot\theta, \tag{3}$$

$$\left\{\begin{matrix}2\\33\end{matrix}\right\} = -\sin\theta\cos\theta, \quad \left\{\begin{matrix}4\\14\end{matrix}\right\} = \frac{1}{2}\frac{d\mu}{dr}, \quad R_{\mu\nu} = 0 \text{ for } \mu \neq \nu, \tag{4}$$

and the invarsant curvature R

$$\frac{1}{2}R = -e^{-\lambda}\left\{\frac{1}{2}\frac{d^2\mu}{dr^2} - \left(\frac{1}{4}\frac{d\mu}{dr} + \frac{1}{r}\right)\left(\frac{d\lambda}{dr} - \frac{d\mu}{dr}\right)\right\} + \frac{e^{-\lambda}}{r^2}(e^{\lambda} - 1). \tag{5}$$

The field equations

$$G_{\mu}^{\nu} = -T_{\mu}^{\nu} \tag{6}$$

where

$$\kappa = 8\pi G/c^4, \quad G = 6.67 \times 10^{-8} \text{ c.g.s.}, \tag{7}$$

are then

$$-e^{-\lambda}\left[-\frac{1}{r}\frac{d\mu}{dr}+\frac{e^{\lambda}-1}{r^2}\right] = -\kappa T_1^{\,1} \tag{8}$$

$$-e^{-\lambda}\left[\frac{1}{r}\frac{d\lambda}{dr}+\frac{e^{\lambda}-1}{r^2}\right] = -\kappa T_4^{\,4} \tag{9}$$

$$\frac{1}{2}e^{-\lambda}\left[\frac{d^2\mu}{dr^2}-\left(\frac{1}{2}\frac{d\mu}{dr}+\frac{1}{r}\right)\left(\frac{d\lambda}{dr}-\frac{\partial\mu}{\partial r}\right)\right] = -\kappa T_2^{\,2}. \tag{10}$$

On account of the spherical symmetry, the equation for $G_3^{\,3}$ is identical with (10).

We have the four identites

$$G_{\mu;\,\nu}^{\nu} = 0 \tag{11}$$

and the conservation equations

$$T_{\mu;\,\nu}^{\nu} = 0. \tag{12}$$

From (12), we have

$$\frac{\partial T_1^{\nu}}{\partial x^{\nu}}+\left(\frac{2}{r}+\frac{1}{2}\frac{d\mu}{dr}\right)T_1^{\,1}-\frac{1}{r}\left(T_2^{\,2}+T_3^{\,3}\right)-\frac{1}{2}\frac{d\mu}{dr}T_4^{\,4}=0$$

$$\frac{\partial T_2^{\nu}}{\partial x^{\nu}}+\cot\vartheta\left(T_2^{\,2}-T_3^{\,3}\right)=0 \tag{13}$$

$$\frac{\partial T_3^{\nu}}{\partial x^{\nu}}=\frac{\partial T_4^{\nu}}{\partial x^{\nu}}=0$$

These are the conditions for the non-vanishing

$$T_1^{\,1}(r), \quad T_2^{\,2}=T_3^{\,3}(r), \quad T_4^{\,4}(r).$$

If the space $r > 0$ is a "vacuum", i.e.,

$$T_1^{\,1}=T_4^{\,4}=T_2^{\,2}=T_3^{\,3}=0 \quad \text{for } r>0, \tag{14}$$

Schwarzschild solves the nonlinear equations (8), (9), (10) and obtains the well-known solution

$$-\frac{1}{g_{11}} = e^{-\lambda} = 1-\frac{2m}{r}, \quad g_{44} = e^{\mu} = 1-\frac{2m}{r}. \tag{15}$$

The constant of integration m can be shown to be the mass of the point source in units of length, namely, $m = MG/c^2$. $g_{11}(r)$ is singular on the spherical surface $r = 2m$ (which for a massive point of the mass of the Sun is 3 kms).

The properties of this singularity have been much studied. For example, it can be shown with the metric (1) that light from the sphere $r=2m$ takes an infinitely long time to reach any outer point, and that the invariant curvature R vanishes

$$R=0 \tag{16}$$

together with $R_{\mu\nu}$ for all μ, ν, although the tensor $R_{\lambda\mu\nu\sigma}$ does not vanish at all points.

II. SPHERICALLY SYMMETRIC, STATIC FIELD FOR AN EXTENDED STAR

If instead of a point mass M in vacuum for which a spherically symmetric static field exists, we consider a more physical model of a star (such as a neutron star or a black hole) with a finite distribution of $T_\mu^\nu(r)$ as in (13), there arises the question of consistency of the three equations (8), (9), (10), since there are three equations for two functions $\lambda(r)$ and $\mu(r)$. On substituting (8) and (9) into (10) and using (13), it can be seen that the equation (10) is identically satisfied for any T_μ^ν satisfying the equations (13). Schwarzschild's case (14) quarantees this consistency. For a finite distribution

$$T_1^{\,1}\neq 0, \quad T_2^{\,2}=T_3^{\,3}\neq 0, \quad T_4^{\,4}\neq 0, \quad r>0, \tag{17}$$

satisfying (13), one proceeds by solving (9), obtaining

$$e^{-\lambda}=1-\frac{\kappa}{r}\int T_4^{\,4}(r)\, r^2dr-\frac{2m}{r}, \tag{18}$$

and from (8) and (9),

$$\lambda+\mu=\kappa\int (T_4^{\,4}-T_1^{\,1})\, r\, e^{\lambda}\, dr \tag{19}$$

This $\lambda(r)$ and $\mu(r)$ satisfy (10) and the nonlinearity of (10) does not enter into the calculation. In fact, one obtains from (18) and (19), for $T_1^{\,1}(r)=T_4^{\,4}(r)=0$, the Schwarzschild solution (14) without having to solve the nonlinear equation (10).

III. A SPECIAI MODEL

We shall consider a model for which (12) holds and the energy density $T_4^{\,4}(r)$ is of the form

$$T_4^{\,4}(r)=\frac{B}{r^2}e^{-r/\rho} \tag{20}$$

where ρ is a parameter. B, ρ and the total mass M of the star are related by

$$4\pi\int_0^\infty T_4^{\,4}(r)\, r^2dr=M\,c^2. \tag{21}$$

We introduce the unit of length 2m

$$2m = 2MG/c^2, \quad G = 6.67 \times 10^{-8} \text{ c.g.s.} \tag{22}$$

and the dimensionless x and ξ

$$r = 2mx, \quad \rho = 2m\ \xi. \tag{23}$$

The exact solution of Equ. (9) is then

$$e^{-\lambda} = 1 + \frac{1}{x} e^{-x/\xi} - \frac{1}{x}. \tag{24}$$

If, with (20), we assume

$$T_1^1(r) = \frac{A}{r^2} e^{-r/\rho}, \tag{25}$$

then, from (19), we obtain

$$-g_{11}g_{44} = e^{\lambda+\mu} = \exp\left(\frac{b}{\xi}\int \frac{e^{-x/\xi}}{x + e^{-x/\xi} - 1} dx\right), \tag{26}$$

where

$$b = 1 - \frac{A}{B}. \tag{27}$$

Asymptotically for large x, $e^{-\lambda}$ and e^{μ} in (24), (26) approach the Schwarzsehild (15), but differ from it in essential ways for various of the parameter ξ.

For $\xi \geq 1$, the function $e^{-\lambda}$ in (24) does not have a zero for $x > 0$ and g_{11} does not have a singularity sphere of the Schwarzschild kind. $e^{-\lambda}$ increases monotonically from $x = 0$ and approaches the Schwarzschild (15) asymptotically at large x.

At $x = 0$,

$$e^{\lambda} \simeq \begin{cases} \dfrac{2}{x}, & \xi = 1 \\ \dfrac{\xi}{\xi - 1}, & \xi > 1. \end{cases}$$

$$e^{\lambda+\mu} \simeq \begin{cases} e^{-2b\xi/x}, & \xi = 1 \\ x^{b/(\xi-1)}, & \xi > 1 \end{cases} \tag{28}$$

From these, it is seen that e^{μ} vanishes at $r = 0$ for all $\xi \geq 1$, and e^{λ} is finite at $r = 0$ for $\xi > 1$, and e^{λ} has pole at $r = 0$ for $\xi = 1$.

For $\xi < 1$, the function $e^{-\lambda}$ in (24) has a zero at x_0, $0 < x_0 < 1$, and g_{11} has a singularity similar to the Schwarzschild $x = 1$ (i.e., $r = 2m$ in (15).) At x_0, the integral in (26) is logarithmic, Let $x = x_0 + y$. Then

$$\lambda+\mu \simeq \ln\, y^s - \frac{b(1-x_0)^2}{2\xi[\xi+x_0-1]^2}y+\cdots \tag{29}$$

$$s=\frac{b(1-x_0)}{\xi+x_0-1}>0 \quad \text{if } b>0\,.$$

so that

$$g_{11}(x_0)g_{44}(x_0)=0 \quad \text{for } b>0\,. \tag{30}$$

At $x=0$,

$$e^{\lambda} \simeq -\frac{\xi}{1-\xi}, \quad \xi<1$$

$$e^{\lambda+\mu} \simeq x^{-b/(1-\xi)}, \quad \xi<1$$

IV. THE GEODESIC OF LIGHT IN A STAR

From the equations of the geodesic for the coordinate s and t, one obtains the first integrals

$$r^2\frac{d\varphi}{ds}=\text{constant}=h\,, \tag{31}$$

$$e^{\mu}\frac{dt}{ds}=\text{constant}=a\,. \tag{32}$$

From (1) one obtains the equation of the geodesic of light $ds=0$

$$e^{\lambda}\left(\frac{dr}{d\varphi}\right)^2+r^2=A^2\,r^4\,e^{-\mu}, \quad r>0 \tag{33}$$

where

$$A=\frac{a}{h}=\frac{e^{\mu}}{r^2}\,\frac{dt}{d\varphi} \tag{34}$$

is a finite constant of the dimension of length.*

With the e^{λ} and e^{μ} obtained in the preceding section, the light path "inside" the star (i.e., where $T_4^4 \neq 0$, especially for $r<2m$) can be obtained on a numerical integration of (33). But a qualitative idea of the path is furnished by the radius of curvature σ of the path

* The equation of a straight line $r=p/\cos\varphi$, where p is the perpendicular distance from the origin $r=0$ to the line, is

$$\left(\frac{dr}{d\varphi}\right)^2+r^2=\frac{1}{p^2}r^4.$$

For Schwarzschild's case, equ (31) becomes

$$\left(\frac{dr}{d\varphi}\right)^2+r^2=A^2r^4+2mr.$$

Thus A has the approximate meaning of the classical 1/p.

$$\sigma = r\frac{2[1-e^{-\lambda}+A^2r^2e^{-\lambda-\mu}]^{3/2}}{3(1-e^{-\lambda})-\frac{1}{\xi}(A^2r^2e^{-\mu}+1)e^{-x/\xi}} \tag{35}$$

The integration of (26) and (33) for various parameters A and ρ will be continued and the results reported in the future.

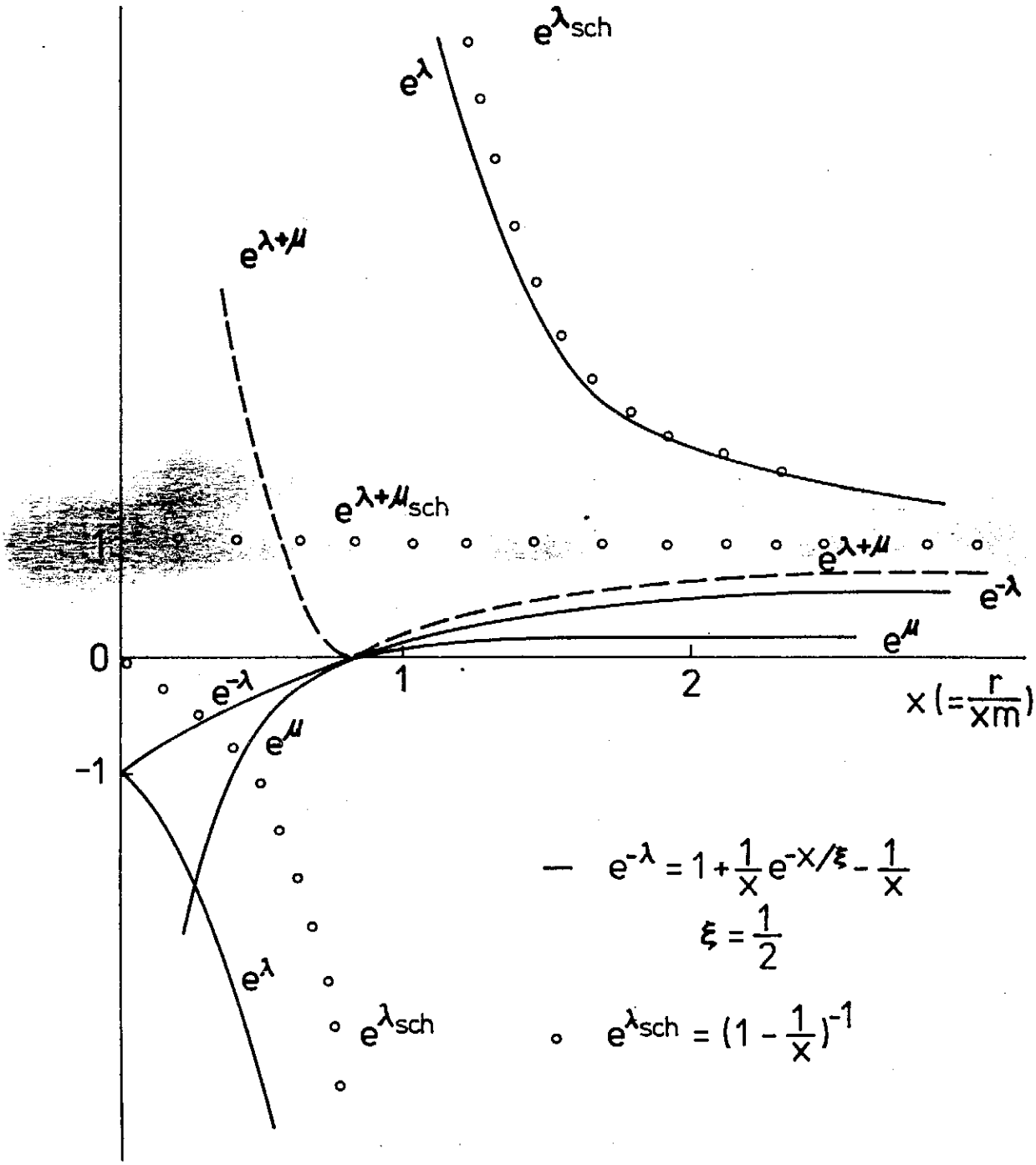

ELASTIC SCATTERING OF ALPHA PARTICLES FROM THE ^{6}Li, ^{9}Be, ^{12}C, ^{19}F, ^{27}Al AND Si^{28} TARGETS AT E_{α}=4.−6. MeV

C. W. Wang (王建萬), G. C. King (江紀成), L. P. Liang (梁靈平),
M. W. Lee (李明威), D. Wang (王 定), M. Wen, E. K. Lin (林爾康)

The phase shift analysis of the α-^{12}C elastic scattering has been studied by Clark et. al.[1] at low energies. Optical-Model parameters of the α-nucleus interactions have been obtained by authers that listed in the compilation by Perey and Perey[2]. Recently, we have measured the angular distributions of the alpha particles scattered from the ^{6}Li, ^{9}Be, ^{12}C, ^{19}F, ^{27}Al and ^{28}Si targets at the energy range E_{α}=4.−6. MeV.

The alpha beam was produced by the 7 MV van de Graaff accelerator at INER. The energy resolution of the incident particles was better than 2 keV. The beam currents used in the experiment ranged from 100 nA to 600 nA depending on the scattering angles. A current integrator was used for measuring the total beam charge that collected by the Faraday cup. Two SSD were used for the particle detection, one for the angular distribution measurements another for monitoring. The angular acceptance of the detector was about 0.08 msr and the angular steps ranged from 2° to 5°.

Both carbon and silicon targets were self-supporting with a thickness of 20 ± 1 $\mu g/cm^2$. The ^{6}Li and ^{19}F measurements were performed by using a lithium flouride thin foil of 20 ± 1 $\mu g/cm^2$ with 20 ± 1 $\mu g/cm^2$ aluminum backing. The outgoing alpha particles scattered from the 20 ± 1 $\mu g/cm^2$ beryllium foil with 20 ± 1 $\mu g/cm^2$ aluminum backing were also measured. The electronic setups that used for the signal processing are shown in Fig. 1. No particle identification was found to be necessary. Some contaminations were also found but proved to be unharmful.

The ^{12}C (α, α) ^{12}C data deduction works have been finished. The absolute differential cross sections and the angular distributions are found to be consistent with that shown in ref. (1) quite nicely in the range of coincident. However, our data have larger angular ranges and more prominent structures. These data are shown in Figs. 2-4. Further deduction works and data analysis are in process.

REFERENCES

(1) G. J. Clark et. al., *Nuclear Physics*, A110, P. 481 (1968).
(2) C. M. Perey and F. G. Perey, *Atomic Data and Nuclear Data Tables*, Vol. 17, P. 1 (1976).

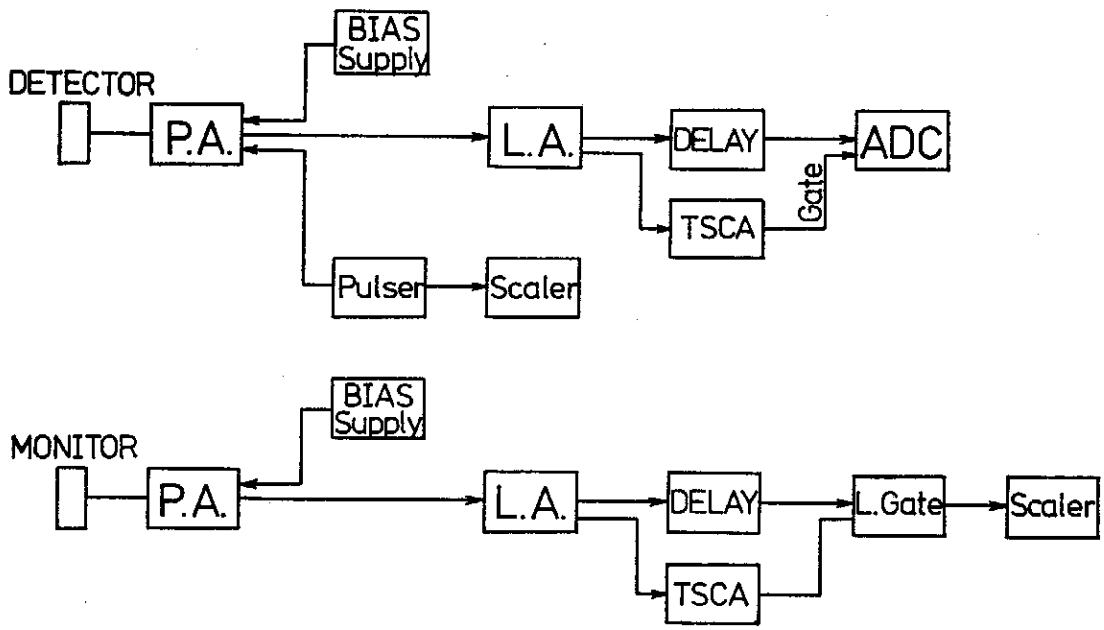

FIG. 1. Electronics

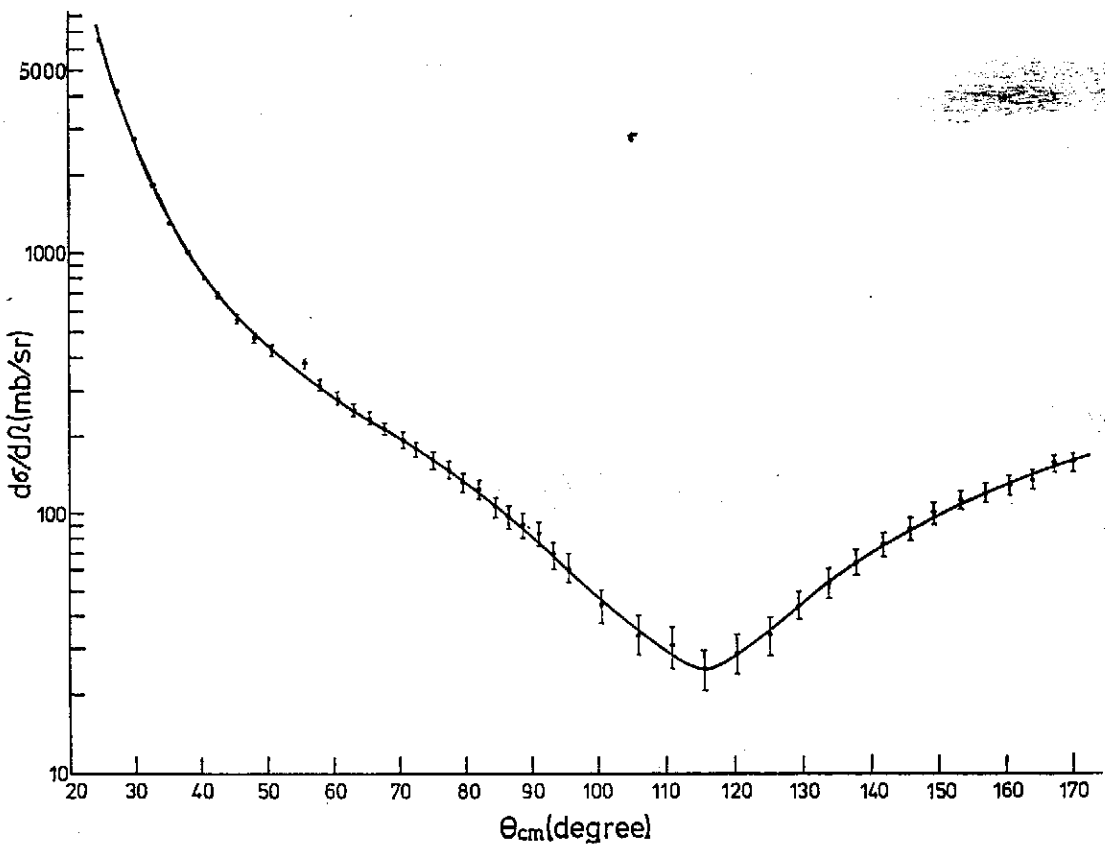

FIG. 2. $^{12}C(\alpha, \alpha)^{12}C$ $E_\alpha = 4.0$ MeV

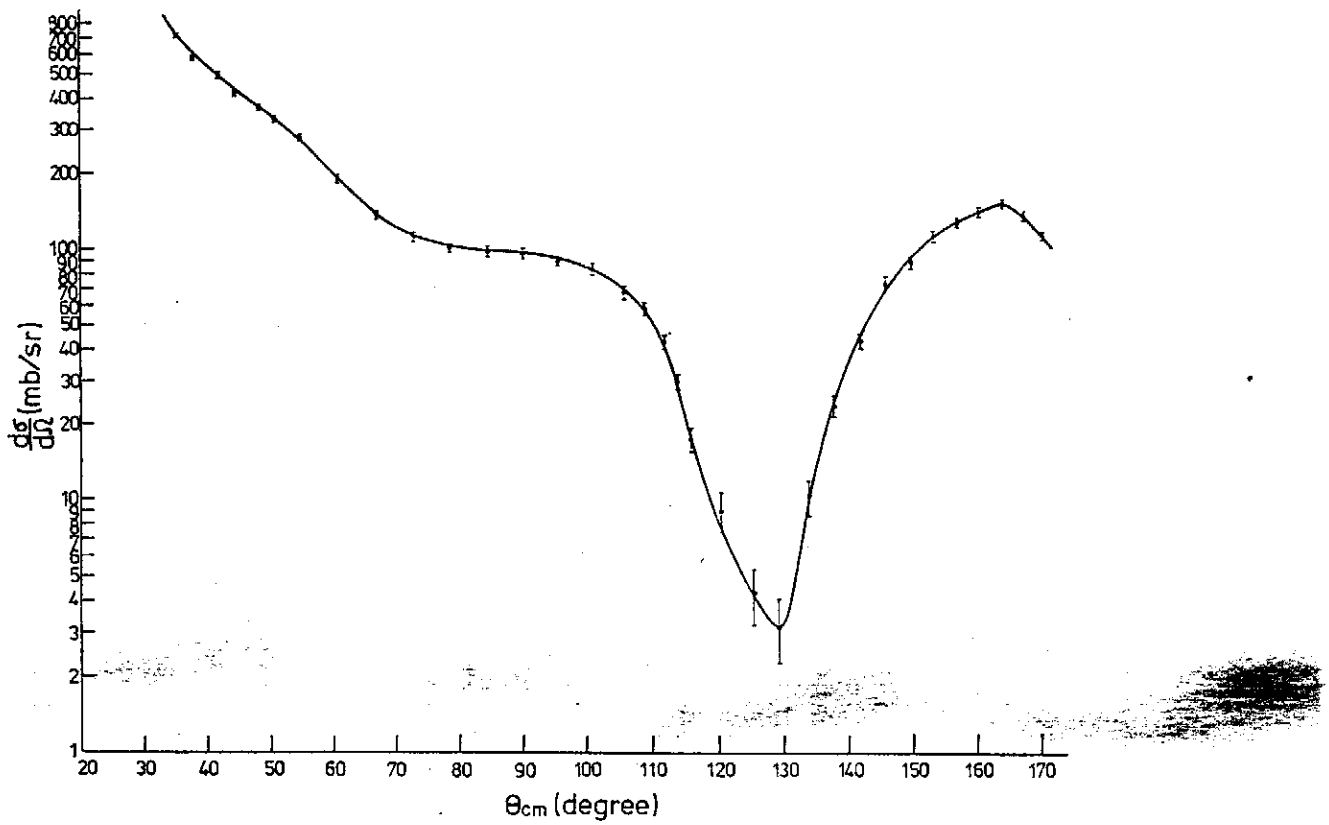

FIG. 3. $^{12}C(\alpha, \alpha)^{12}C$ E_α = 5.0 MeV

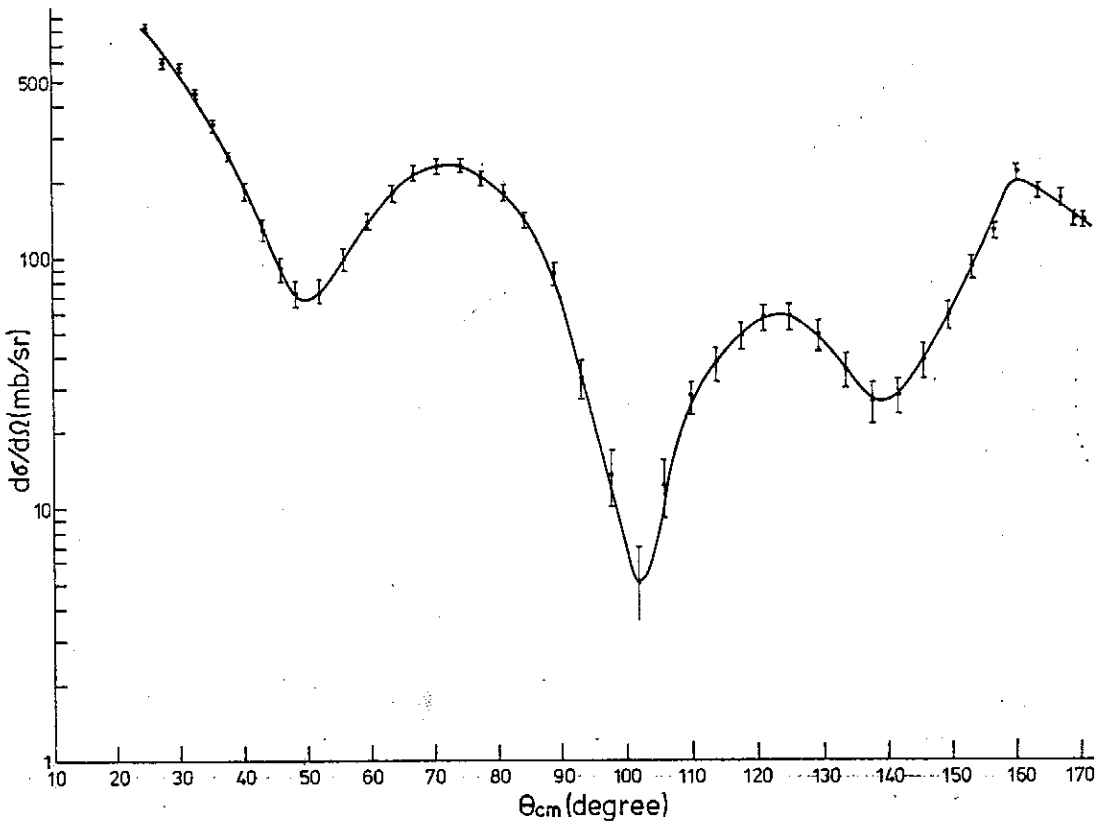

FIG. 4. $^{12}C(\alpha, \alpha)^{12}C$ $E_\alpha = 6.0$ MeV

ELECTRICAL RESISTIVITY OF NICKEL-RICH NICKEL-COPPER ALLOYS BETWEEN 78 AND 700 K

YEONG DER YAO (姚永德)

Institute of Physics, Academia Sinica
Nankang, Taipei, Taiwan, The Republic of China

Abstract

Electrical resistivity ρ of nickel-copper alloys containing 0.0, 4.6, 9.3, 14.0 and 18.8 at. % Cu has been measured as a function of the absolute temperature T between 78 and 700 °K. The Curie temperatures of this set of binary alloys are determined by the deviation from Matthiessen's rule method. The agreement with other methods is excellent.

INTRODUCTION

In a previous publication[1], we reported on a study of the electrical resistivity of a set of nickel-rich nickel-copper alloys between 300 °K and 700 °K. We have found that the temperature dependent part of the electrical resistivity follows a $T^{1.74\pm0.05}$ variation in the ferromagnetic region and increases more slowly than T in the paramagnetic region. The Curie temperature T_c was obtained from the temperature of the diverge of the temperature derivative of the electrical resistivity, $d\rho/dT$, which was computer generated from our $\rho(T)$ data. In this paper, I will report all the electrical resistivity data of five nickel-copper alloys containing 0.0, 4.6, 9.3, 14.0 and 18.8 at. % copper, and the analyses basing on the deviation from Matthiessen's Rule, DMR, etc..

EXPERIMENTAL PROCEDURES

Five nickel-copper alloys containing 0.0, 4.6, 9.3, 14.0 and 18.8 at. % copper were prepared as described before[1]. The electrical resistivity of the above samples was determined using the conventional four-probe technique. Temperatures between 78 °K and 300 °K were achieved in a cryostat; temperatures between 300 °K and 700 °K were achieved in a Marshall furnace.

ANALYSES AND RESULTS

Figure 1 shows the values of the electrical resistivity at 78 °K of the Ni-Cu alloys used in this study. It is a useful check on the good quality of our Ni-Cu binary system of solid solutions. The increase in the electrical resistivity is about 0.86 $\mu\Omega$-cm per 1 at. % Cu, Figure 2 reports the electrical resistivity of our Ni-Cu alloys containing 0.0, 4.6, 9.3, 14.0 and 18.8 at. % Cu between 78 °K and 700 °K. The electrical resistivity of pure nickel between 4 °K and

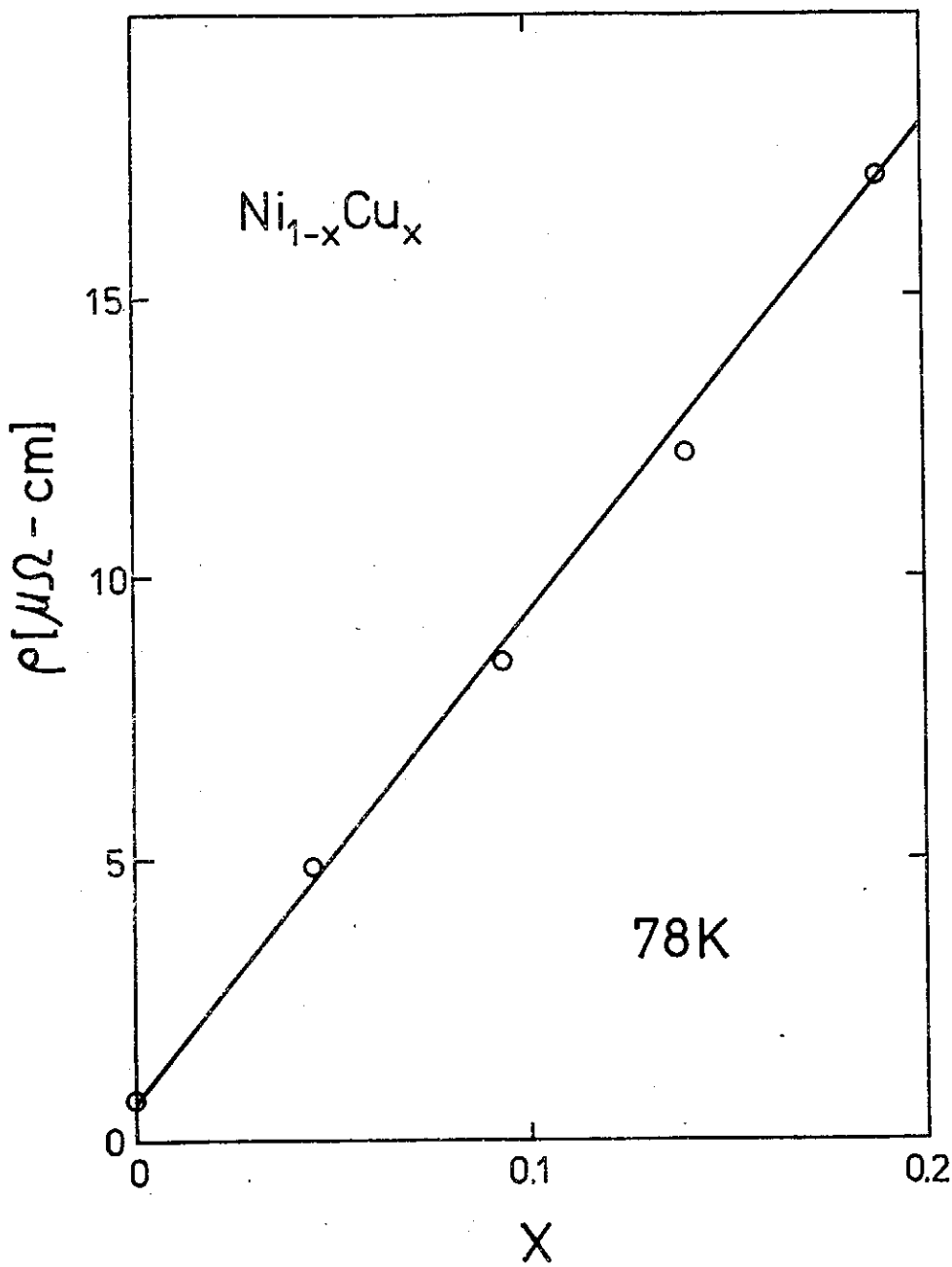

FIG. 1. Electrical resistivity of Ni-Cu alloys as a function of copper concentration at 78 °K.

78 °K is also plotted in figure 2 using the data reported before[2]. This shows that the data above 78 °K of pure nickel in this study matches very well with the low temperature data of pure nickel reported before. The ρ vs. T curves undergo a slope change near the ferromagnetic-paramagnetic phase transition. In the previous publication[1], it has been shown that the temperature

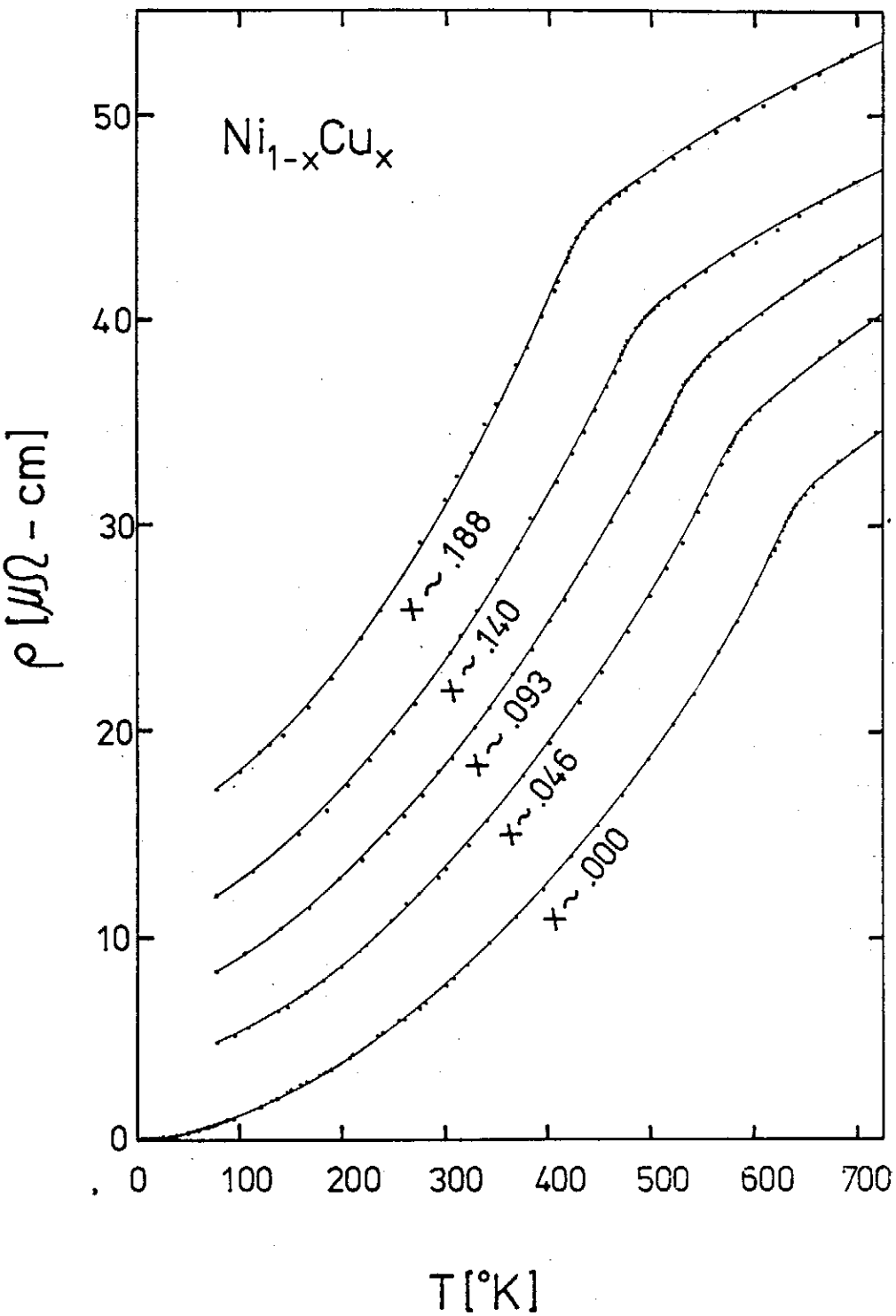

FIG. 2. Electrical resistivity of Ni-Cu alloys as a function of absolute temperature between 78 °K and 700 °K.

dependent part of the electrical resistivity follows a $T^{1.74\pm0.05}$ variation in the ferromagnetic region, and in the paramagnetic region it follows a $T^{0.9\pm0.05}$ variation for pure nickel and gradually changes to follow a $T^{0.6\pm0.05}$ variation for Ni-Cu alloy containing 18.8 at. % Cu. In the critical region, the temperature derivative of the resistivity is divergent positively. The Curie temperature was determined experimentally from the plot of $(d\rho/dT)$ vs. T at which $d\rho/dT$ diverges.

According to the theory by Fisher and Langer[3], it is predicted that in the vicinity of T_c the behavior of $d\rho/dT$ should be the same as that of the specific heat. However, this theory does not take into account the potential scattering of the conduction electrons. Therefore, proper modification must be made when we apply it to consider the random alloy system experimentally.

Recently, Yao and Arajs[4] reported that Curie temperature of a set of ferromagnetic binary alloys with different concentration can be determined by means of the difference between the resistivities of two samples at the same temperature. Now I would like to do further analysis of this Ni-Cu system basing on the deviation form Matthiessen's concept.

Figure 3 shows the temperature dependence of the deviation from Matthiessen's rule, DMR or $\Delta\rho(x, T)$, for four nickel-copper alloys containing 4.6, 9.3, 14.0 and 18.8 at. % copper. Where x is the concentration of copper. Values of $\Delta\rho(x, T)$ were obtained by subtracting the electrical resistivity of the pure Ni from the electrical resistivity of the particular Ni-Cu alloy. Mathematically, I will introduce three functions as follows:

$$\Delta\rho'(T_c) = \left[\frac{d\Delta\rho(T)}{dT}\right]_{T=T_c} = \lim_{\delta T \to 0} \frac{\Delta\rho(T_c+\delta T) - \Delta\rho(T_c)}{\delta T} \qquad (1)$$

$$\Delta\rho'_+(T_c) = \lim_{\delta T \to 0^+} \frac{\Delta\rho(T_c+\delta T) - \Delta\rho(T_c)}{\delta T} \qquad (2)$$

$$\Delta\rho'_-(T_c) = \lim_{\delta T \to 0^-} \frac{\Delta\rho(T_c+\delta T) - \Delta\rho(T_c)}{\delta T} \qquad (3)$$

These three functions are called, respectively, the derivative, the derivative on the right, and the derivative on the left of $\Delta\rho(T)$ at $T=T_c$. And $\Delta\rho'(T_c)$ does not exist means means that $\Delta\rho'_+(T_c) \neq \Delta\rho'_-(T_c)$. From figure 3, $\Delta\rho(x, T)$ exhibits that $(d\Delta\rho/dT)$ does not exist at T_c. The arrows in figure 3 indicate T_c determined by the $d\rho/dT$ method. The crossed arrow shows the value of T_c for pure nickel by the $d\rho/dT$ method. Below T_c of the particular alloy, $\Delta\rho(x, T)$ increases smoothly with increasing T. Above T_c of the particular alloys, $\Delta\rho(x, T)$ decreases smoothly with increasing T. However, between T_c

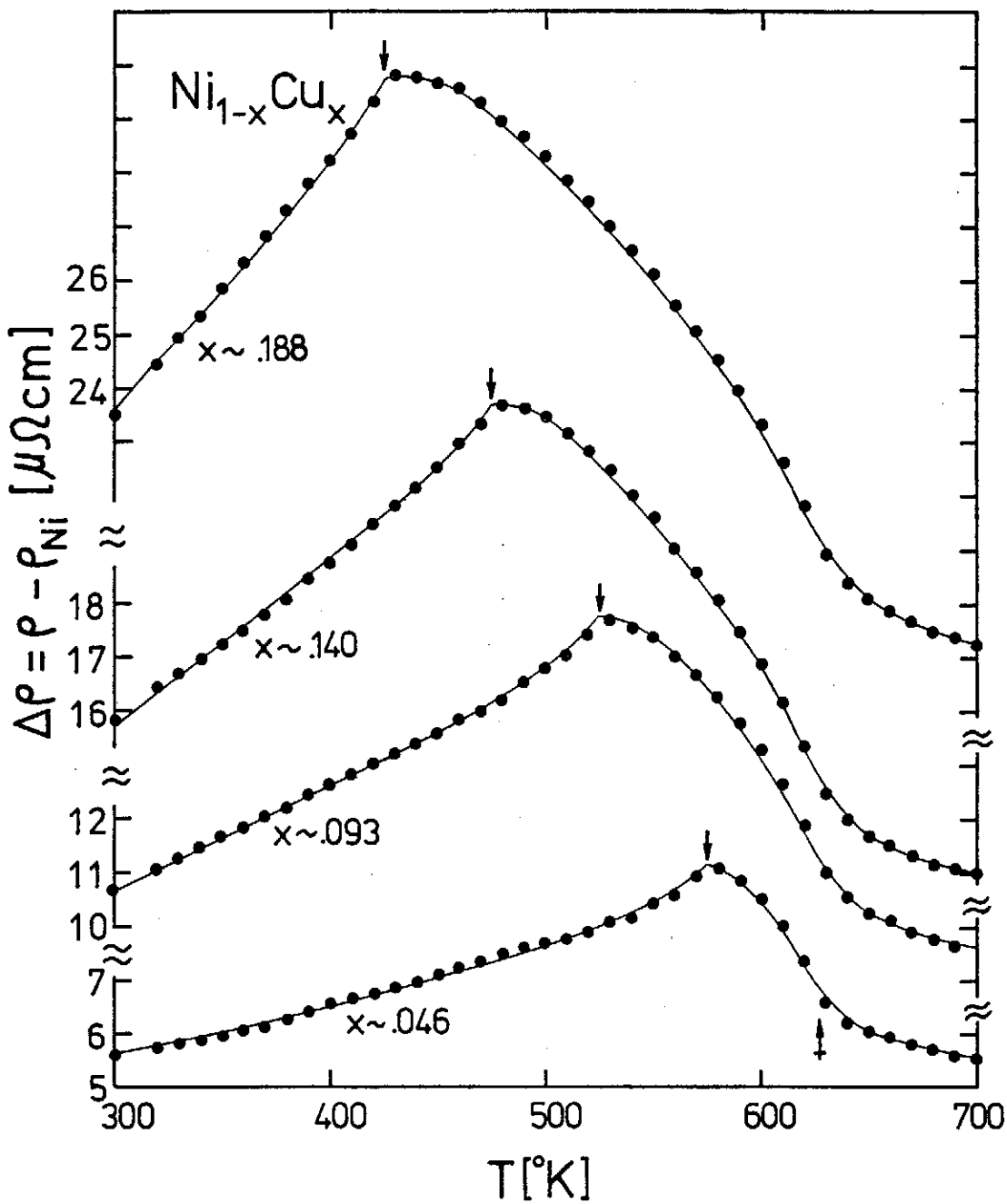

FIG. 3. $\Delta\rho(x, T)$ as a function of T for Ni-Cu alloys between 300 °K and 700 °K.

of pure nickel and T_c of the particular alloy, $\Delta\rho(x, T)$ decreases much much faster with increasing T than that above T_c of pure nickel. It is clear that $\Delta\rho$ is continuous through the Curie temperatures, even $\Delta\rho'_+(T_c) \neq \Delta\rho'_-(T_c)$. Figure 3 tells us that the DMR can be used to determine T_c of ferromagnetic binary alloys.

In this paper, I would like to emphasize that the temperature derivative of the DMR is a powerful method to determine T_c of ferromagnetic binary alloys. Figure 4 shows the temperature dependence of the temperature derivative of the DMR, $d\Delta\rho/dT$, of our nickel-copper system. For each curve, $d\Delta\rho/dT$ was obtained from the $\Delta\rho(T)$ data by point-by-point differentiation using a computer. On each curve, there are two points that $\Delta\rho'_+(T_c) \neq \Delta\rho'_-(T_c)$, one point is the Curie temperature of the particular Ni-Cu alloy and the other is

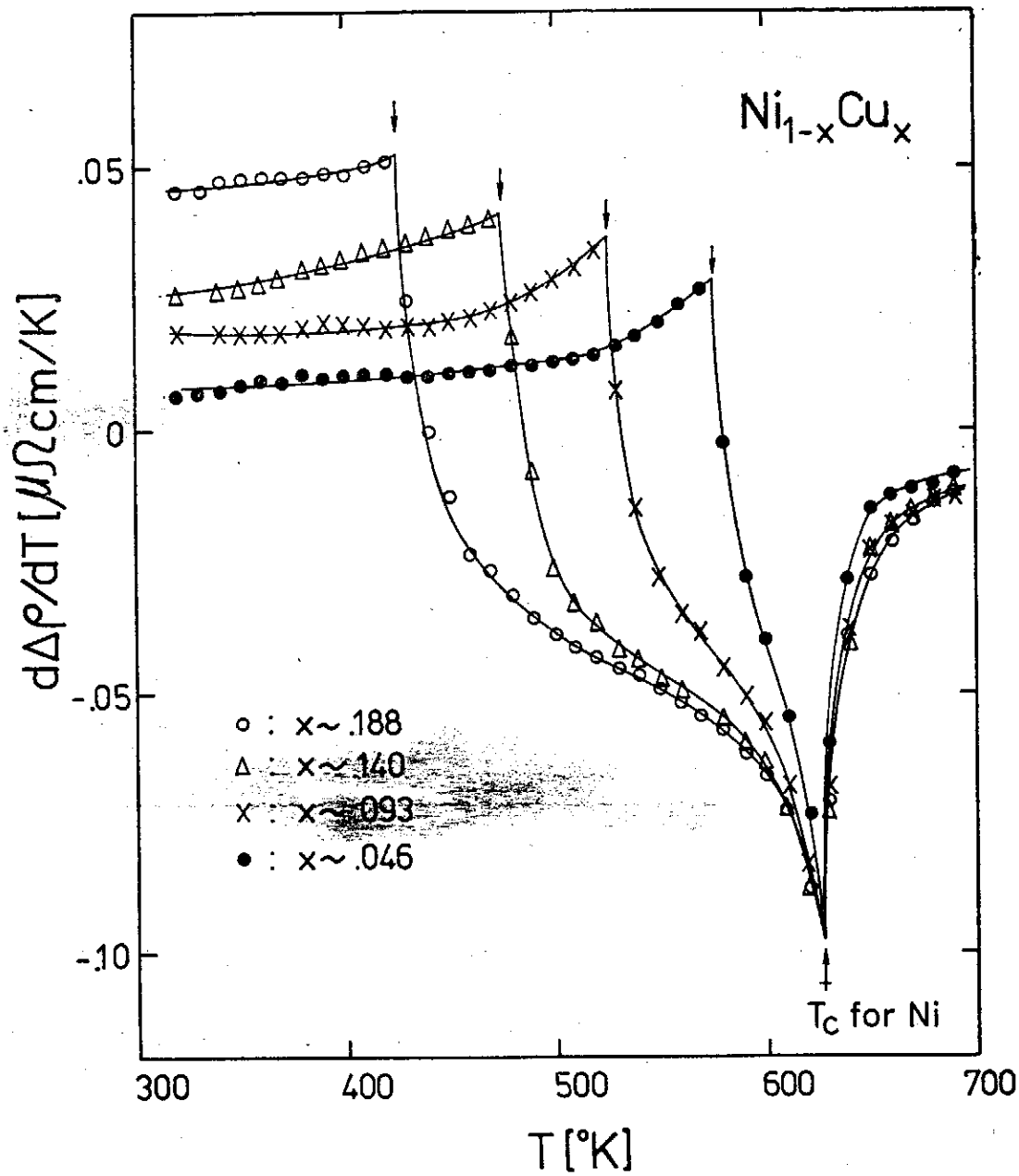

FIG. 4. $d\Delta\rho(x, T)/dT$ as a function of T for Ni-Cu alloys between 300 °K and 700 °K.

the Curie temperature of pure Ni, Basing on the experimental point of view, or from figure 4, we can say that the two points of T_c occur at the maximum and minimum of each $d\Delta\rho/dT$ vs. T curve, respectively. In figure 4, the arrow indicate T_c of each particular alloy and the crossed arrow indicates T_c of the pure Ni. These T_c were determined by the $d\rho/dT$ method[1]. Evidently, we can conclude that the $d\Delta\rho/dT$ method gives results identical to those obtained by conventional methods.

In summary, the result of this analysis shows that the DMR and the first derivative of the DMR are useful methods for the determination of T_c of ferromagnetic binary alloys.

REFERENCES

(1) Y. D. Yao and J. H. Tsai, Chin. J. Phys. to be published.
(2) Y. D. Yao, S. Arajs and E. E. Anderson, J. Low Temp. Phys. **21**, 369 (1975).
(3) M. E. Fisher and J. S. Langer, Phys. Rev. Lett. **20**, 665 (1968).
(4) Y. D. Yao and S. Arajs, Phys. Stat. Sol. (b) to be published.

ELECTRICAL RESISTIVITY OF IRON-RICH IRON-PALLADIUM ALLOYS BETWEEN 78 AND 1150 K

YEONG DER YAO (姚永德)

Institute of Physics, Academia Sinica
Nankang, Taipei, Taiwan, The Republic of China

Abstract

Electrical resistivity ρ of iron-palladium alloys containing 0.5, 1.0, 3.0, 7.9, 10.0 and 11.9 at.% Pd has been measured once as a function of the absolute temperature T between 78 and 1150 °K. The results of the samples containing 0.5, 1.0 and 3.0 at.% Pd are quite reasonable. However, puzzled anomaly happens for the samples containing 7.9, 10.0 and 11.9 at.% Pd. Further study about this anomaly is in progress and will be reported later.

INTRODUCTION

The magnetic behavious of palladium-rich binary alloys has been a subject of extensive study in recent years[1]. Of special interest is the electron scattering as measured by the transport coefficients in these magnetic systems. It is well-known that the palladium-rich iron-palladium alloys exhibit a long-range ferromagnetic behavior even down to very low concentrations. This behavior is quite different with that of the nickel-palladium alloys; in a palladium-rich palladium-nickel system, no long-range ordering exists for less than 2 at. % of nickel. The transport properties in palladium-rich palladium-iron alloys have been studied by a variety of methods. Between them, the electrical resistivity study in particular, has received a good deal of attention[2-8]. However, relatively little work has been done on the iron-rich iron-palladium alloys.

The high temperature magnetic susceptibility of iron-rich iron-palladium alloys has been measured by Arajs[9]. In this paper, we will report a study of the electrical resistivity of a series of iron-rich iron-palladium alloys ranging in composition from 0.5 to 11.9 at. % Pd as a function of the absolute temperature T between 78 and 1150 °K.

EXPERIMENTAL PROCEDURE

Except the sample containing 0.5 at. % Pd, the iron-rich iron-palladium alloys used in this study are the same used for the high temperature magnetic susceptibility study before[9]. These alloys were prepared by levitation melting using 99.8% carbonyl iron (Antara Chemicals) and 99.9% palladium (Engel-

hard Industries, Inc.). Melting was done in purified helium atmosphere. The samples were prepared from these ingots by fast quenching. It was annealed at 1,000°C for 1 hour and 30 minutes, and then quenched in ice water. This gives α phase. The samples were out in the form of rectangular parallelepipes. The surfaces of these samples were polished by using files and sand-papers. Typical sample dimensions were roughly $2.3 \times 2.3 \times 20$ (units in mm^3).

The electrical resistivity data of the above samples was measured by means of the standard four-point probe technique. Temperatures between 77°K and 300°K were achieved in a cryostat; temperatures between 300°K and 1,150°K were achieved in a Marshall furnace. The dc current was maintained constant to about one part in 10^5 and the voltage was measured with a precision of 10^{-7} volts. Between 77°K and 300°K, two Pt resistance thermometer was used to measure the temperature and from 300°K upwards two chromal-alumel thermocouples were used. These were placed near the two ends of the sample. The temperature was maintained constant for every reading to within a few m-deg. The data for the electrical resistivity were recorded at various small temperature intervals in the vicinity of the magnetic phase transition, and large temperature intervals in the remainder of the temperature range studied. Two days were spanned for each sample to finish a complete high temperature run. This means that the electrical resistivity of each samples was measured with increasing and decreasing temperatures between room temperature and 1,200°K within two days.

RESULTS AND DISCUSSION

Fig. 1 shows the residual electrical resistivity measured at 4.2°K before this study. This plot can be explained according to Nordheim's rule. The value of the increase in the electrical resistivity is gradually changed roughly from 2.3 $\mu\Omega$cm/at. % for very dilute Fe-Pd alloys to 0.7 $\mu\Omega$cm/at. % for Fe-Pd alloys containing 12 at. % Pd.

Fig. 2 shows the electrical resistivity data of our Fe-Pd alloys containing 0.5, 1.0, 3.0, 7.9, 10.0 and 11.9 at. % Pd with increasing and decreasing temperatures between 77 and 1,200°K. In this figure, the dots represent the heating runs and the crosses show the cooling runs. It is clear that the electrical resistivity data for the Fe-Pd samples containing 0.5, 1.0 and 3.0 at. % Pd is consistent for both heating and cooling runs. However, the electrical resistivity data of the heating and cooling runs are not matched for these Fe-Pd samples containing 7.9, 10.0 and 11.9 at. % Pd. The anomalous behavior of these electrical resistivity data can be explained by the ferromagnetic-paramagnetic transition and the α-γ transition.

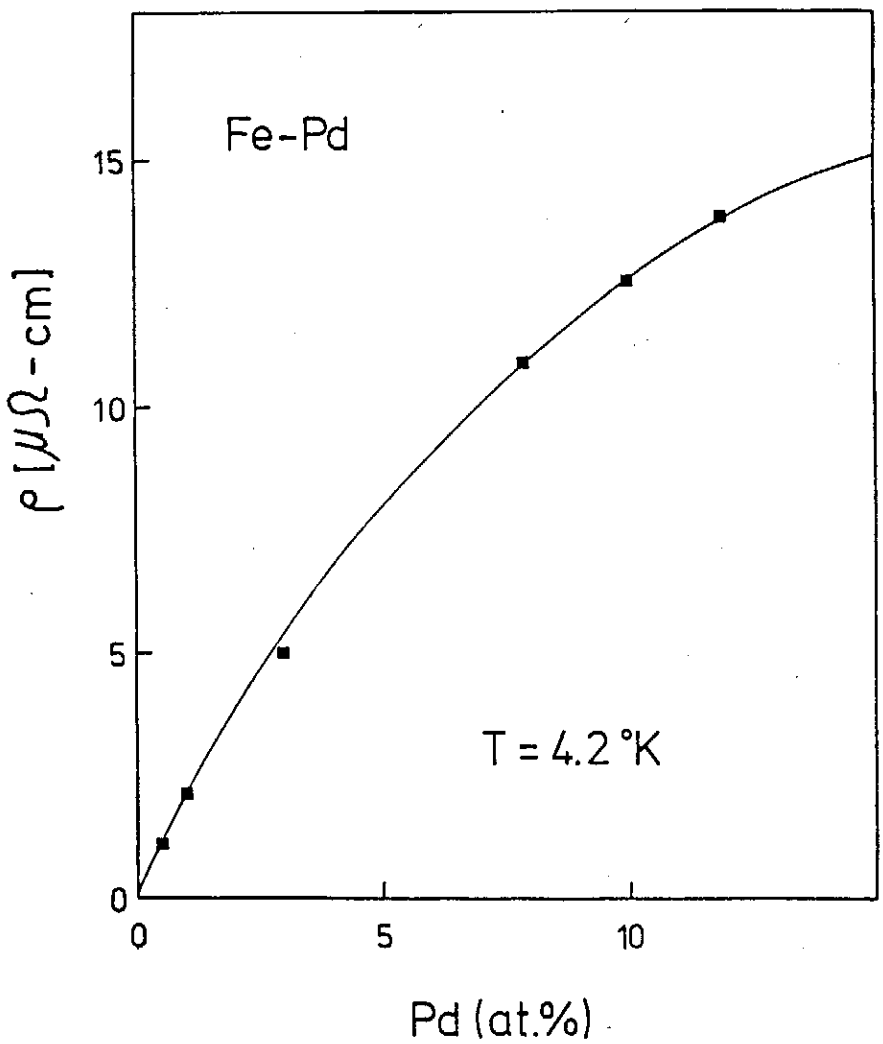

FIG. 1. Residual electrical resistivity of iron-palladium alloys as a function of palladium concentration.

For pure metallic iron, there exists two different crystal structures; the B.C.C. (α or δ phases) and F.C.C. (γ phase) structures. It is well-known that the α-γ phase transformation in iron drastically changes its magnetic properties. Roughly speaking, the α-phase is stable below 910°C; γ-phase is stable between 910°C and 1,390°C; above 1,390°C up to the melting point of iron ($\sim$1534°C) δ-phase is stable. The α-phase iron is ferromagnetic below the Curie temperature, and is paramagnetic above the Curie temperature. The γ-phase iron is a quite mysterious metal whose magnetic properties are not quite clear yet. As far as we know, the γ-Fe has a quite different atomic moment than those of α-Fe. γ-Fe can have two different electronic structures which are separated by about 0.0355 eV in energy[9]. The lower one would be antiferromagnetic

with about 0.5 μ_B (Bohr Magneton) per iron atom and the upper one would be ferromagnetic with the magnetic moment of 2.8 μ_B. The δ-phase iron is essentially the same as the α-phase iron.

According to our experimental results, the anomalous behavior of the Fe-Pd samples containing 7.9, 10.0 and 11.9 at. % Pd could be due to the γ-phase which is partially retained in the α-phase. The anomaly occurs above 700°K. It is noticed that[10] the magnetic transformation of Fe-Pd alloys falls from ~450 to ~350°C as Pd content increases. The magnetic studies done on the same alloys indicate that Pd decreases the antiferromagnetic interactions in F.C.C. iron. From the viewpoint of the metallurgical phase diagram and the electronic structure of the Fe-Pd alloys, our experimental data can be understood quite well. Further analyses will be continued after the annealing and quenching works on our samples. These works are in progress now and will be reported later together with Prof. Arajs.

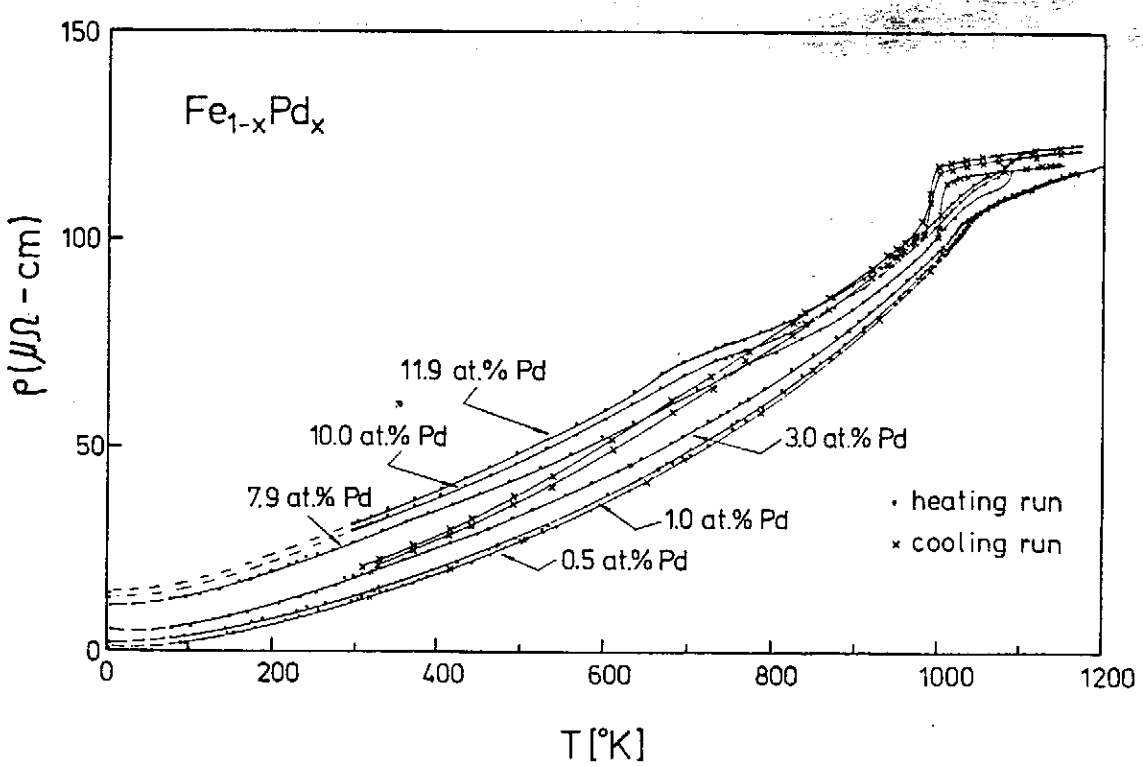

FIG. 2. Electrical resistivity of iron-palladium alloys with increasing and decreasing temperatures between 77 and 1200°K.

REFERENCES

(1) G. J. Nieuwenhuys, *Adv. Phys.* **24**, 515 (1975).

(2) G. Longworth and C. C. Tsuei, *Phys. Lett.* A**27**, 258 (1968).

(3) J. A. Mydosh, J. I. Budnick, M. P. Kawatra and S. Skalski, *Phys. Rev. Lett.* **21**, 1346 (1968).

(4) G. Williams and J. W. Loram, *J. Phys. Chem. Solids* **30**, 1827 (1969).

(5) M. P. Kawatra, S. Skalski, J. A. Mydosh and J. I. Budnick, *J. Appl. Phys.* **40**, 1202 (1969).

(6) S. Skalski, M. P. Kawatra, J. A. Mydosh and J. I. Budnick, *Phys. Rev.* **B2**, 3613 (1970).

(7) M. P. Kawatra, J. I. Budnick and J. A. Mydosh, *Phys. Rev.* **B2**, 1587 (1970).

(8) Y. C. Wu, J. Chen and S. H. Fang, *Chin. J. Phys.* **11**, 130 (1973).

(9) S. Arajs, *Phys. Stat. Sol.* **15**, 501 (1966).

(10) R. P. Elliott, *Constitution of Binary Alloys, First Supplement*, (McGraw-Hill, New York, 1965).

CLUSTER MODEL IN SUBSTITUTIONAL BINARY ALLOY: I. SIMPLE CUBIC SYSTEM

YEONG DER YAO (姚永德)

Institute of Physics, Academia Sinica
Nankang, Taipei, Taiwan, R. O. C.

Abstract

The statistical cluster and its binding energy are presented for simple cubic binary substitutional alloy. Both the electronic configuration and the statistical distribution of cluster are very important factors to influence the physical behavior of binary alloy.

INTRODUCTION

In the last few years, there has been an increasing interest in the study of the cluster phenomenon in binary alloys[1-4]. Most of the work done has been based on the cluster-Bethe-lattice method[1,2] and pseudopotential theory[5] etc.. The cluster-Bethe-lattice method is to treat a cluster of atoms exactly and replace the rest of the system by a proper Bethe lattice. Recently, Yao et al[6] presented a method of calculating the probability of a special cluster group in substitutional binary alloy system. Basing on this concept, this paper is concerned with the description of clusters in a simple cubic substitutional binary alloy system.

THE CLUSTER MODEL

Let us consider a simple cubic substitutional binary alloy, whose constituent are atoms of class A and class B with concentration $(1-x)$ and x, respectively. Under the tight-binding approximaton, we can write the Hamiltonian as

$$H = \sum_{n} | n > \varepsilon_n < n | + \sum_{n \neq m} | n > V_{nm} < m | \qquad (1)$$

where $| n >$ is the single atomic orbital associate with site n. ε_n are the atomic levels which take the values ε_A and ε_B depending on whether an atom A or B occupies the site n. V_{nm} is the hopping integral between sites n and m. If we assume that the atomic sites are occupied at random, then each site can be occupied by an A atom with the probability $(1-x)$, and by a B atom with the probability x. Generally, it is found that small clusters are randomly formed throughout the binary substitutional alloy system. We choose a particular B atom as origin and having the i-th nearest-neighbor coordination number N_i. Then the clusters must satisfy the following three conditions: (i) There

are at least n_i ($n_i \leq N_i$) B-type atoms in the i-th nearest-neighbor shells; (ii) The largest i (or say k) can be zero or any positive integer (here, zero means that only one B-type atom at the origin); (iii) Outside the cluster core shell, say in the j-th shell, where $k+1 \leq j \leq S$, the number of the B-type atoms, m, should be no more than ℓ_j, where ℓ_j can be zero or any positive integer. Let $P^{k,s}_{s.c.}$ (n_i; ℓ_j; x) be the probability of this event. Then,

$$P^{k,s}_{s.c.}\ (n_i;\ \ell_j;\ x) = \left[\prod_{i=0}^{k}\ \sum_{n=n_i}^{N_i} C^n_{N_i}\ x^n\ (1-x)^{N_i-n}\right] \left[\prod_{j=k+1}^{s}\ \sum_{m=0}^{\ell_j} C^m_{N_j}\ x^m\ (1-x)^{N_i-m}\right] \qquad (2)$$

where $C^n_N = N!/n!\ (N-n)!$

Equation 2 is valid, if we assume that the size of the cluster is much smaller than the whole binary alloy system. In a simple cubic system, the coordination numbers are $N_0=1$, $N_1=6$, $N_2=12$, $N_3=8$ and $N_4=6$ etc.. Equation 2 has been evaluated with the aid of a computer for some simple cases. Among these computer results, I would like to mention here two typical cases that should help us to understand more complicated cases.

The first case is $P^{0.1}_{s.c.}$ (1; ℓ_1; x). This is the probability of a single B-type atom with the first nearest-neighbor shell having no more than ℓ_1 B-type atoms, where ℓ_1 is varied from 0 to 5. We have

$$P^{0.1}_{s.c.}\ (1;\ \ell_1;\ x) = x \sum_{m=0}^{\ell_1} C^m_6 \times^{m}\ (1-x)^{6-m} \qquad (3)$$

The value of $P^{0.1}_{s.c.}$ (1; ℓ_1; x) is a function of ℓ_1 and x. Table I tell us the relation between the maximum value of $P^{0.1}_{s.c.}$ (1; ℓ_1; x) and x at which $P^{0.1}_{s.c.}$ (1; ℓ_1; x) is maximum. Obviously, the increasing of the concentration of B-type atoms causes both the size and the probability increasing of the cluster.

TABLE I: The relation between P_{max} and $X_{P_{max}}$ for $P^{0.1}_{s.c.}$ (1; ℓ_1; x) system.

ℓ_1	P_{max}	$X_{P_{max}}$	ℓ_1	P_{max}	$X_{P_{max}}$
0	.057	14	3	.335	46
1	.134	24	4	.462	58
2	.227	34	5	.620	72

The second case is presented by a B-type atom with the first nearest-neighbor shell having at least n_1 B-type atoms and its second nearest-neighbor shell having

no more than 6 B-type atoms, where n_1 is varied from 1 to 6. We have

$$P^{1,2}_{s.c.}\ (1,\ n_1;\ 6;\ x) = \times [(1-x)^{12} + 12x(1-x)^{11} + 66x^2(1-x)^{10} + 220x^3(1-x)^9 + 495x^4(1-x)^8 + 792x^5(1-x)^7 + 924x^6(1-x)^6] \sum_{n=n_1}^{6} C_6^n\ x^n(1-x)^{6-n} \quad (4)$$

The value of $P^{1,2}_{s.c.}$ $(1,\ n_1;\ 6;\ x)$ is dependent on the values of n_1 and x. Table II shows the relation between the maximum value of $P^{1,2}_{s.c.}$ $(1,\ n_1;\ 6;\ x)$ and the x at which $P^{1,2}_{s.c.}$ $(1,\ n_1;\ 6,\ x)$ is maximum. The difference between first case and second case is that the maximum value of $P^{1,2}_{s.c.}$ $(1,\ n_1;\ 6;\ x)$ decreased with respect to increasing the concentration of B-type atoms. However, it is still true that the value of the probability is proportional to the size of the cluster.

TABLE II: The relation between P_{max} and $X_{P_{max}}$ for $P^{1,2}_{s.c.}$ $(1,\ n_1;\ 6;\ x)$ system.

n_1	P_{max}	$X_{P_{max}}$	n_1	P_{max}	$X_{P_{max}}$
1	.3310	40	4	.1150	56
2	.2822	46	5	.0469	60
3	.2020	50	6	.0104	66

The above two examples show that a special B-type cluster group will exist at a special concentration of B-type atoms. Experimentally, it is well known that for the non-dilute Ni-Cu alloys, atomic cluster occurs near the critical concentration for the onset of ferromagnetism ($\sim$55 at % Cu) and in varying degrees depending on the annealing temperature[7] etc.. Beside the statistical distribution effect, the binding energy of a cluster with N B-type atoms is also an important factor to vary the situation of cluster. We can write the binding energy, E_N, of a cluster with N B-type atoms by

$$E_N = C \sum_{\substack{\text{whole} \\ \text{cluster}}} E_{BB}\ (r) \quad (5)$$

where C is the proportional constant; E_{BB} is the binding enery between two B-type atoms separated by distance r. The summation is made over the whole cluster. Under the assumption that the B-type cluster is surrounded completely by A-type atoms. The binding energy E_{BB} can be considered as the combination of the band-structure energy[8] and electrostatic energy[9] over the Fermi surface. Using the pseudopotential theory[5], E_{BB} can be easily shown as follows:

$$E_{BB}(r) = \frac{1}{2\pi r}\int_0^\infty dq \left\{ \frac{V_A^2\, q^3 \sin qr}{4\pi^2 e^2}\left(\frac{1-E(q)}{1-[1-E(q)][1-g(q)]}\right) \right.$$
$$< k+q \mid \omega_B - \omega_A \mid k > < k \mid \omega_B - \omega_A \mid k+q > + \qquad (6)$$
$$\left. 4e^2 (Z_B - Z_A)^2 \exp\left(\frac{-q^2}{f}\right)\frac{\sin qr}{q} \right\}$$

Where V_A is the atomic valume of A-type atom; q is the allowed wave number in k space; ω_A and ω_B are the pseudopotentials for A and B atoms, respectively, Z_A and Z_B are the valences of A-type and B-type atoms, respectively; e is the electronic charge; E(q) is the Hartree dielectric function; g(q) is the Hubbard-Sham exchange and correlation correction[10]; and f is a convergence factor. Eq. (6) can be calculated to find the minimum energy configuration for each simple cubic substitutional binary alloy system.

A stable configuration of cluster can be presented by

$$\frac{dE_N}{dN} \approx 0 \text{ (or minimum)} \qquad (7)$$

under the assumption that N is much smaller than the number of whole atoms in the binary alloy system. The stable configuration for cluster to occur in a binary alloy is then the optimum situation between the statistical distribution and the electronic structure of the system.

In conclusion, we have analysed the cluster in the simple cubic substitutional binary alloy system. Both the electronic configuration and the statistical distribution of cluster are very important factors which influence strongly the physical behavior of binary alloy. Of course, this conclusion can be also applied to body center cubic, face center cubic and many other complicated substitutional binary alloys.

Acknowledgement: The author wishes to thank the "Computer Center" of Academia Sinica for allowing to use their computer for this research, and also to thank Messrs. Ni and Ueng for their assistance in computer calculation.

REFERENCES

(1) F. Yndurain, J. D. Joannopoulos, M. L. Cohen and L. M. Falicov, Solid st. Comm. **15,** 617 (1974).
(2) J. D. Joannopoulos and F. Yndurain, Phys. Rev. B**10,** 5164 (1974).
(3) K. Binder, D. Stauffer, H. Müller-Krumbhaar, Phys. Rev. B**12,** 5261 (1975).
(4) K. Binder, Phys. Rev. B**15,** 4425 (1977).
(5) W. A. Harrison, *Pseudopotentials in the Theory of Metals,* Benjamin, New York (1966),

(6) Y. D. Yao, S. Arajs and E. E. Anderson, Phys. Stat. Sol. (b) **82,** 343 (1977).
(7) J. Vrijen, C. Van Dijk and S. Radelaar, *Proc. Conf. on Neutron Scattering,* Edited by R. M. Moon, p. 92 (1976).
(8) G. K. Straub, A. R. Ducharme and J. R. Holland, Solid St. Comm. **15,** 1901 (1974).
(9) A. R. Ducharme and H. T. Weaver, Phys. Rev. B**5,** 330 (1972).
(10) D. C. Wallace, Phys. Rev. **187,** 991 (1969).

FURTHER STUDY ON NI-RICH NI-TI ALLOYS

YEONG DER YAO (姚 永 德)

Institute of Physics, Academia Sinica
Nankang, Taipei, Taiwan, The Republic of China

Abstract

Further study of the electrical resistivity of Ni-rich Ni-Ti alloys shows that the temperature dependent part of the electrical resistivity follows a $T^{1.73\pm0.05}$ variation in the ferromagnetic region and a $T^{0.89\pm0.05}$ variation in the paramagnetic region. The derivative of DMR of this system shows that it is a powerful method to determine the Curie temperatures of binary nickel-base ferromagnetic alloys.

INTRODUCTION

This paper is a continuation of investigations of the electrical resistivity of the nickel-rich nickel-titanium alloys published before[1]. The characteristic feature of a metallic system is the presence of conduction electrons. Electrical resistivity is one of the most important properties, essentially depending on the electronic structural, compositional and magnetic situations of the metallic system. In other words, the electrical resistivity of a given metal or alloy depends not only on its electronic structure, but also on the mechanisms of the relaxation of the conduction electrons which are due to the scattering by structural defects of the lattice, phonons, magnons and also due to the scattering arising from electron-electron interactions. The electrical resistivity of simple non-transition metals is mainly determined by the first two mechanisms of scattering. For non-magnetic transition metals, especially at low temperatures, the last mechanism is essential. For magnetic transition metals, all the above-mentioned mechanisms of scattering make contributions to the electrical resistivity.

The linear response theory formula by Kubo[2] for the electrical conductivity is exact in the sense that no assumption is made about the rate at which the charge carriers are scattered. And the approach based on the Boltzmann transport equation for the distribution of charge carriers is an approximation valid in the limit where the rate of scattering of the charge carriers is small[3]. Neither of these two approaches is a practical tool for calculating the electrical transport properties of systems with a large scattering rate, for example, in the disordered alloy system or in the liquid metal system. In recent years a number of attempts have been made to find an exact formula for the electrical resistivity. Even several different formulae have been derived[4,5,6,7], the search

for formulae of the electrical resistivity does not seem to be fruitful for many systems. This is mainly due to many complicated scattering factors included.

In this paper, I am interested to analyse experimentally the temperature dependent part of the electrical resistivity of the nickel-rich Ni-Ti system between the ferromagnetic and paramagnetic regions. Besides, the temperature derivative of the deviation from Matthiessen's Rule analysis is also carried out for this Ni-Ti system.

ANALYSES AND RESULTS

The data reported before[1] were fitted to the empirical formula:

$$\rho(T) = \rho_{4.2} + AT^n,$$

where $\rho_{4.2}$ is the residual electrical resistivity measured at 4.2 K for each particular Ni-Ti alloy[8], A is a constant independent on temperature, and n is the power of T or the index which can be any positive or negative numbers. A naturally logarithmic plot of the $(\rho - \rho_{4.2})$ against the absolute temperature T is shown in figure 1, which includes all the samples that we have measured before[1]. It should be remarked here that the titanium concentration in Ref. 1 labelled as at. % were actually expressed in wt. %. This error was made during the long-oversea-communication with Prof. Arajs, and this error has been corrected later in Ref. 8. Analysing from figure 1, we easily see that the index n comes out to be 1.73 ± 0.05 in the ferromagnetic region; and in the paramagnetic region n appears to become 0.89 ± 0.05 for all the samples. It is evident that the temperature-dependent part of the electrical resistivity increases faster than T in the ferromagnetic region and it increases more slowly than T in the paramagnetic region. These behaviors are consistent with the Ni-Cu system[9]. In ferromagnetic region, there is always a T^2 contribution to the total electrical resistivity due to ferromagnetism[10,11]; and the contribution to the total electrical resistivity due to phonon at high temperature is roughly proportional to T. Therefore, the combination of these interactions contributes to the temperature-dependent electrical resistivity a T^n term, where n has the value between 1 and 2. In paramagnetic region, the behavior can be explained in terms of the band concept which has already been described in Ref. 9. Following Eq. (5) in Ref. 9, the departure of the resistivity from linearity with temperature is determined by the magnitudes and signs of N_d and $(dN_d/dE)_{E_F}$ etc.. In this dilute Ni-Ti system, the Ti concentration is low enough that the change of magnitudes of N_d and $(dN_d/dE)_{E_F}$ is not manifest. Therefore, the value of the index n is roughly equal to 0.89 from pure nickel to Ni-Ti alloy containing 1.9 at. % Ti.

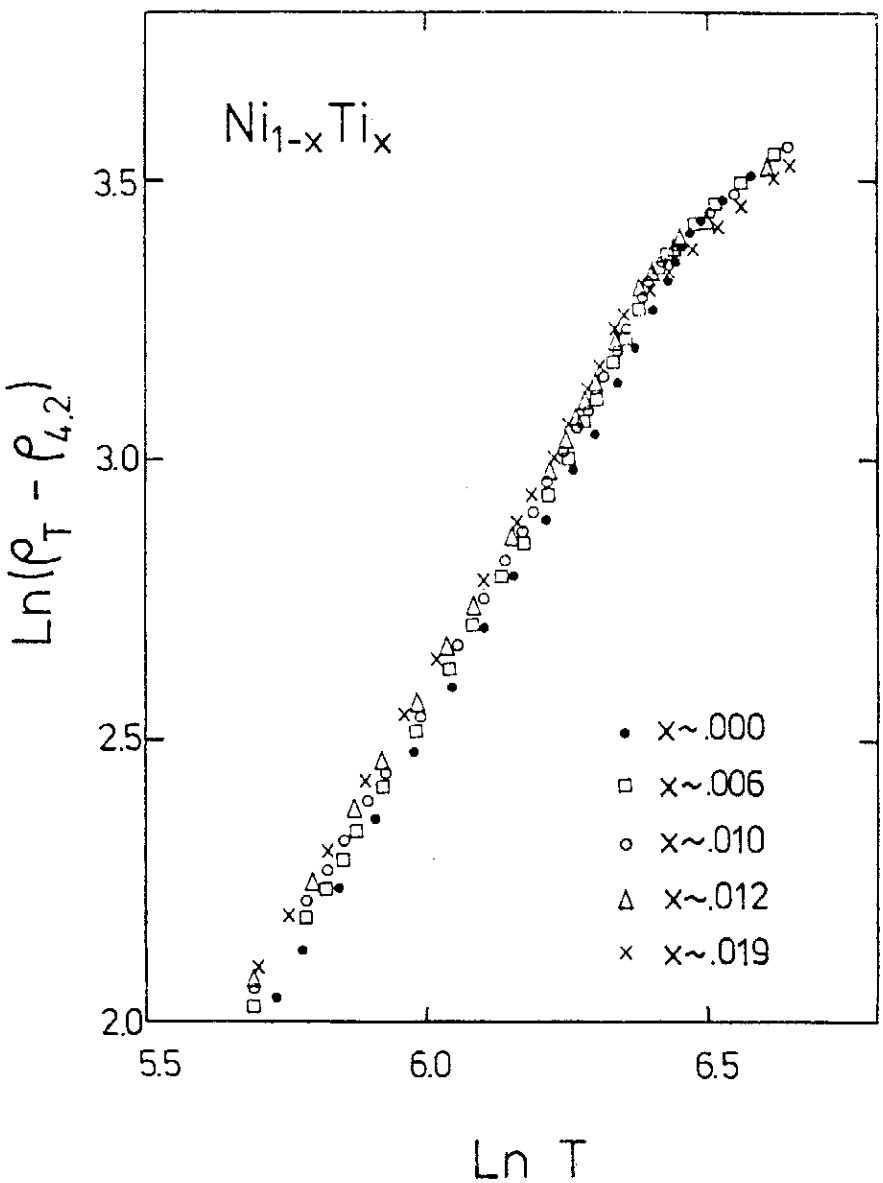

FIG. 1. $(\rho-\rho_{4.2})$ against T on a ℓn-ℓn plot.

The temperature dependence of the deviation from Matthiessen's rule, $\Delta\rho(x, T)$, for this Ni-Ti alloy system has been shown in Ref. 8. Where x represents the concentration of Ti. Even $\Delta\rho(x, T)$ is a continuous function through the Curie temperatures, the derivative of $\Delta\rho(x, T)$ with respect to T does not exist at the Curie temperature T_c. In other words, the derivative on the right is not equal to the derivative on the left of $\Delta\rho(x, T)$ at $T=T_c$.

Figure 2 shows the temperature dependence of the temperature derivative of the DMR, $d\Delta\rho/dT$, for four nickel-titanium alloys containing 0.61, 0.98,

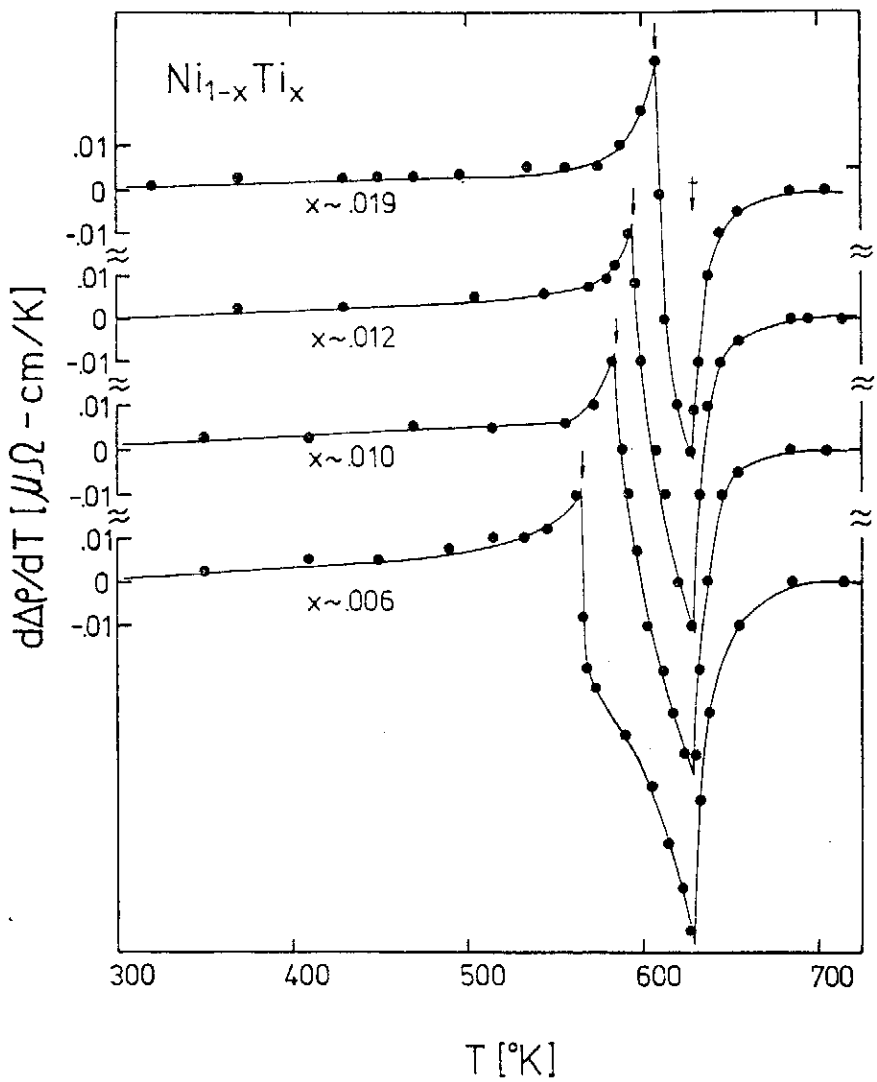

FIG. 2. $d\Delta\rho(\times, T)/dT$ as a function of T for Ni-Ti alloys between 300°K and 720°K.

1.22 and 1.89 at. % titanium. This plot was constructed from the $\Delta\rho(x, T)$ data by point-by-point differentiation using a computer. On each $d\Delta\rho/dT$ curve, there are two points that the derivative on the right is not equal to the derivative on the left; one point is the Curie temperature of the particular Ni-Ti alloy and the other is the Curie temperature of Ni. The arrows and the crossed arrow in figure 2 indicate the Curie temperatures determined by the $d\rho/dT$ method[1]. From figure 2, we are convinced that the two points of T_c occur at the maximum and minimum of each $d\Delta\rho/dT$ vs. T curve, respectively. Below the Curie temperature of the particular alloy, $d\Delta\rho/dT$ increases slowly with increasing T. Between the Curie temperatures of the particular alloy and the pure nickel, $d\Delta\rho/dT$ decreases very fast with increasing T. Above

the Curie temperature of the pure nickel, $d\Delta\rho/dT$ increasing very fast within a quite short temperature range and appears to become quite flat thereafter. Evidently, we have proved that the $d\Delta\rho/dT$ method gives results identical to those obtained by other methods.

REFERENCES

(1) Y. D. Yao, S. Arajs and K. V. Rao, *Chin. J. Phys.* **15**, 1 (1977).
(2) R. Kubo, *Can. J. Phys.* **34**, 1274 (1956).
(3) W. Kohn and J. M. Luttinger, *Phys. Rev.* **108**, 590 (1957).
(4) S. F. Edwards, *Proc. Phys. Soc.* **86**, 977 (1965).
(5) V. M. Kenkre and M. Dresden, *Phys. Rev.* **A6**, 769 (1972).
(6) P. Argyres and J. Sigel, *Phys. Rev. Lett.* **31**, 1397 (1973).
(7) P. Argyres and J. Sigel, *Phys. Rev.* **B9**, 3197 (1974).
(8) Y. D. Yao and S. Arajs, *Phys. Stat. Sol.* (b), **B89**, K201 (1978)
(9) Y. D. Yao and J. H. Tsai, *Chin. J. Phys.*, Vol. 16, No. 4 (1978)
(10) G. K. White and R. J. Tainsh, *Phys. Rev. Lett.* **19**, 165 (1967).
(11) F. C. Schwerer and J. Silcox, *Phys. Rev. Lett.* **20**, 101 (1968).

THE DERIVATIVE OF DMR ON FE-RICH FE-V ALLOYS

YEONG DER YAO (姚 永 德)

Institute of Physics, Academia Sinica
Nankang, Taipei, Taiwan, The Republic of China

Abstract

Results of the first temperature derivative of the deviation from Matthiessen's Rule (DMR) on Fe-rich Fe-V alloys are reported. The present analysis shows that the first temperature derivative of DMR is a useful method for the determination of the Curie temperatures of binary iron-base ferromagnetic alloys.

INTRODUCTION

From the previous work devoted to the deviation from Matthiessen's rule, DMR (see the review articles of Bass[1] and Cimberle et al[2]), the existence of the DMR in various metallic alloy systems involving defects other than substitutional impurities is demonstrated. In most nonmagnetic alloy systems, the DMR at sufficiently high temperature is well described by a linear function of the temperature. Usually, linearity is good down to the Debye temperature or a fraction thereof. Up to now, much less effect has been expended in examining the DMR in magnetic alloy systems.

Recently, Yao and Arajs[3] reported that the Curie temperature T_c of a set of ferromagnetic binary alloys with different concentrations can be determined by means of the DMR. In this paper, I will emphasize the DMR near the neighborhood of the ferromagnetic-paramagnetic phase transition of a binary ferromagnetic alloys. Specifically, basing on the iron-rich iron-vanadium alloys, I will show that the first temperature derivative of the DMR can be used to determine the Curie temperatures of a set of binary ferromagnetic alloys.

ANALYSES AND RESULTS

The electrical resistivity of a binary alloy at the absolute temperature T can be written as

$$\begin{aligned}\rho(c, T) &= \rho(0, T) + \Delta\rho(c, T) \\ &\equiv \rho(0, T) + \rho(c, 0) - \rho(0, 0) + \Delta(c, T) \qquad (1)\end{aligned}$$

with the assumption that

$$\Delta(0, 0) = \Delta(c, 0) = \Delta(0, T) = 0 \qquad (2)$$

In this expression, the electrical resistivity of the binary alloy with solute concentration c, $\rho(c, T)$, is written in terms of the electrical resistivity of the

pure base metal, $\rho(0, T)$, and the increment $\Delta\rho(c, T)$ due to the introduction of the solute impurity. According to Matthiessen's rule, $\Delta\rho(c, T)$ should be temperature independent and $\Delta\rho(c, T) = \rho(c, 0) - \rho(0, 0)$ always. However, the existence of a non-zero DMR has been know for a long time. The recent interest in Matthiessen's rule was caused by analysing the physical meaning of the DMR in many different alloys and also in different temperature regions. The term $\Delta(c, T)$ is defined as the DMR of the alloy with impurity concentration c. Evidently, the DMR is not exist for pure metals and the binary alloys at absolute zero; i.e. $\Delta(0, 0) \equiv \Delta(0, T) \equiv \Delta(c, 0) \equiv 0$.

According to Eq. (1), the DMR can be denoted as follows:

$$\Delta(c, T) = \rho(c, T) - \rho(0, T) + \rho(0, 0) - \rho(c, 0) \qquad (3)$$

where $\rho(0, 0)$ and $\rho(c, 0)$ are the residual resistivity of pure metal and the alloy with impurity concentration c, respectively. They are constants and independent on temperature. Let us consider the temperature-dependent part of the DMR for a set of binary ferromagnetic alloys. At first, we assume that the electrical resistivity is the sum of the resistivities due to magnetic scattering and other effects except magnetism. Mathematically, we have

$$\rho(c, T) = \rho_{N.F.}(c, T) + \rho_{Oth.}(c, T) \quad \text{in ferromagnetic region} \qquad (4\text{-a})$$
$$\rho(c, T) = \rho_{C.F.}(c, T) + \rho_{Oth.}(c, T) \quad \text{in Critical region} \qquad (4\text{-b})$$
$$\rho(c, T) = \rho_{N.P.}(c, T) + \rho_{Oth.}(c, T) \quad \text{in paramagnetic region} \qquad (4\text{-c})$$

Here, the meaning of the abbreviations are: N.F.: normal ferromagnetic region; C.F.: critical fluctuation region; N.P.: normal paramagnetic region, Oth.: other effects except the magnetic effect. The critical fluctuation region is usually within a few degrees of T_c.

According to the Fe-V alloy system reported by Teoh et al[4], the Curie temperature increases with increasing the concentration of V, until the concentration of V is about 10 at. %. Let us analyse the temperature-dependent part of the DMR in the neighborhood of the Curie temperature of pure iron. The Fe-V alloy with V concentration c is in the normal ferromagnetic region. We have

$$\rho(c, T) - \rho(0, T) = \rho_{N.F.}(c, T) - \rho_{C.F.}(0, T) + \rho_{oth.}(c, T) - \rho_{Oth.}(0, T) \qquad (5)$$

The sum of the first temperature derivative of all the electrical resistivities due to other effects except the critical fluctuation effect is a smooth and continuous function with respect to the absolute temperature T in this critical fluctuation temperature region of Fe, in case there are no other anomalies happened in this region. According to Fisher and Langer[5], $d\rho_{C.F.}(0, T)/dT$ above T_c should vary like the magnetic specific heat, or it is proportional to $\varepsilon^{-\alpha}$, where $\varepsilon = |T - T_c|/T_c$ and α is the specific heat critical exponent. Below T_c, $d\rho_{C.F.}$

$(0, T)/dT$ should be proportional to $\varepsilon^{2\beta-1}$, where β is the critical index for the spontaneous magnetization. However, it was shown by Richard and Geldart[6] that $d\rho_{C.F.}(0, T)/dT$ varies as the magnetic specific heat for $T < T_c$ as well as $T > T_c$. Anyway, this divergence is positive both above and below T_c. The above analysis shows that $d\Delta(c, T)/dT$ is divergent negatively at T_c of pure Fe.

In the neighborhood of the Curie temperature T_c of the particular Fe_{1-c} V_c alloy, the Fe_{1-c} V_c alloy is in the critical fluctuation region, and Fe is in its normal paramagnetic region. We can find

$$\rho(c, T) - \rho(0, T) = \rho_{C.F.}(c, T) - \rho_{N.P.}(0, T) + \rho_{Oth.}(c, T) - \rho_{Oth.}(0, T) \quad (6)$$

Again, the sum of the temperature derivative of all the electrical resistivities due to other effects except the critical fluctuation effect is a smooth and continuous function with respect to T in the neighborhood of T_c of Fe_{1-c} V_c alloy, in case there are no other anomalous effects in this small temperature region. Following the same reason[5, 6] analysed for Eq. (5), the temperature derivative of $\rho_{C.F.}(c, T)$ is divergent positively at T_c of Fe_{1-c} V_c. Therefore, we can conclude that $d\Delta(c, T)/dT$ is divergent positively at T_c of Fe_{1-c} V_c.

Except the Curie temperatures of Fe and Fe_{1-c} V_c are equal or very closed to each other, the derivative of DMR can be used to determine the Curie temperatures of Fe and Fe_{1-c} V_c. Even if the two Curie temperatures are closed enough that both are in the critical fluctuation temperature region, however the separation of the two Curie temperatures is not ambiguous, we can still do the same analysis as above and find that $d\Delta(c, T)/dT$ to exhibit a negative cusp at the T_c of pure Fe and a positive cusp at the T_c of Fe_{1-c} V_c.

Generally speaking, it is interesting to note that the temperature derivative of the difference in the electrical resistivity of ferromagnetic binary alloys with different concentrations can also be used for the determination of their T_c. Specifically, let

$$\Delta\rho_{ij}(T) = \rho(c_i, T) - \rho(c_j, T), \quad (7)$$

$$d\Delta\rho_{ij}(T)/dT = d[\rho(c_i, T) - \rho(c_j, T)]/dT \quad (8)$$

where c_i and c_j are different solute concentrations. Then the behavior of $d\Delta\rho_{ij}(T)/dT$ is completely similar to the behavior of $d\Delta\rho(c, T)/dT$ described above. Of course, it can be expected that the quantity $d\Delta\rho_{ij}(T)/dT$ should exhibit anomalies at the values of T_c associated with each composition as described for $d\Delta\rho(c, T)/dT$.

Fig. 1 shows the temperature dependence of the temperature derivative of the DMR, $d\Delta(c, T)/dT$, for four iron-vanadium alloys containing 0.5, 0.9, 2.7 and 6.1 at. % vanadium. This plot was constructed from the $\Delta\rho(c, T)$ data

by point-by-point differentiation using a computer. On each $d\Delta/dT$ curve, there are two points that $d\Delta/dT$ is divergent positively or negatively. The arrows and crossed arrow in figure 1 indicate the Curie temperatures determined by the $d\rho/dT$ method[4]. From the above analysis, we conclude that two points of T_c occur at the maximum and minimum of each $d\Delta/dT$ vs. T curve, respectively. Below the Curie temperature of pure iron, $d\Delta/dT$ decreases slowly with increasing T. Between the Curie temperatures of pure iron and the particular alloy, $d\Delta/dT$ increases very fast with increasing T. Above the Curie temperature of the particular alloy, $d\Delta/dT$ decreasing very fast within a small temperature region and appears to become quite flat thereafter. From this plot, we have again experimentally proved the results of the above analysis.

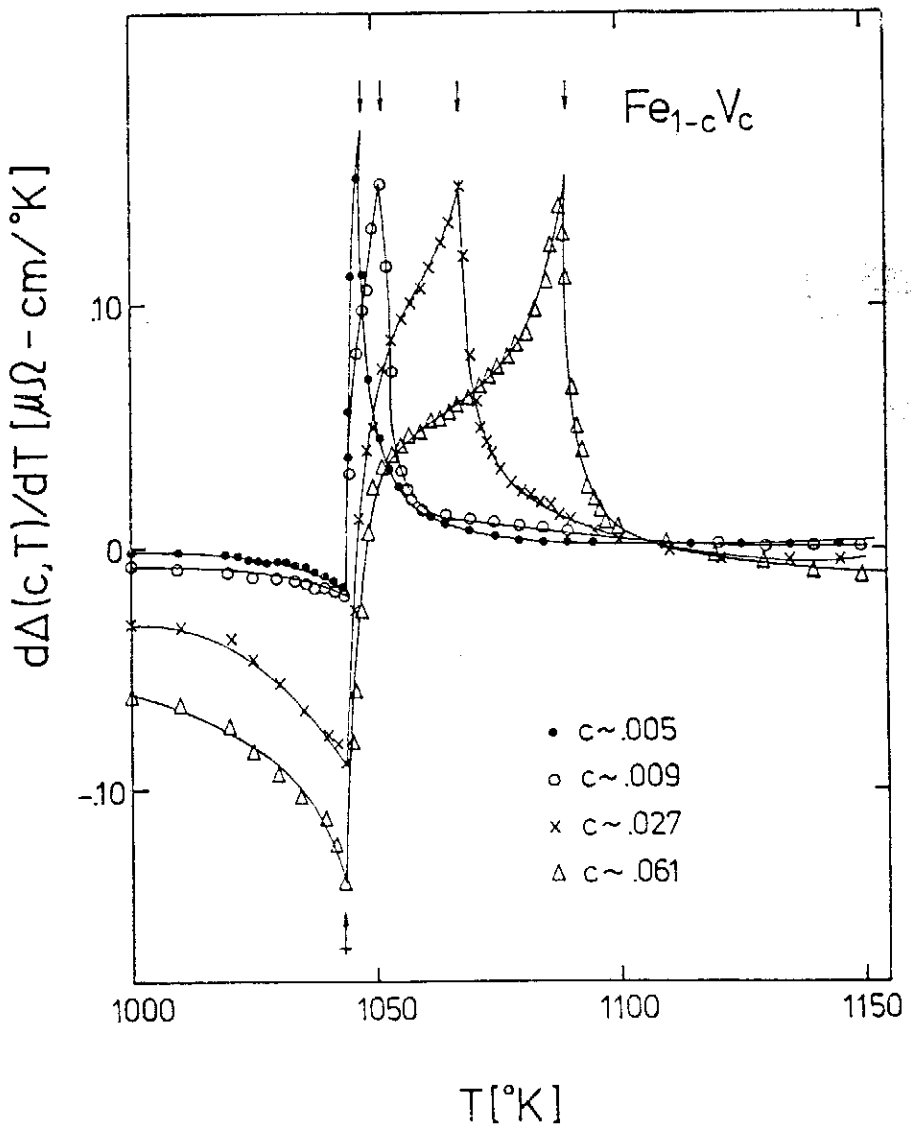

FIG. 1. $d\Delta(c, T)/dT$ as a function of T for Fe-V alloys between 1000°K and 1150°K.

In summary, the above conclusion provide a practical method to determine the Curie temperatures of a set of isotropic type-I ferro-magnetic alloys[7]. Applications to more complex system will be reported later.

REFERENCES

(1) J. Bass, *Adv. Phys.* **21**, 431 (1972).

(2) M. R. Cimberle, G. Bovel and C. Rizzuto, *Adv. Phys.* **23**, 639 (1974).

(3) Y. D. Yao and S. Arajs, *Phys. Stat. Sol.* (b), to be published.

(4) W. Teoh, S. Arajs, D. Abukay and E. E. Anderson, *J. Mag. Mag. Materials* **3**, 260 (1976).

(5) M. E. Fisher and J. S. Langer, *Phys. Rev.* Lett. **20**, 665 (1968).

(6) T. G. Richard and D. J. W. Geldart, *Phys. Rev.* Lett. **30**, 290 (1973).

(7) D. J. W. Geldart and T. G. Richard, *Phys. Rev.* **B12**, 5175 (1975).

ELECTRICAL RESISTIVITY OF POLYCRYSTALLINE SM AND SM - 3 AT.% DY BETWEEN 15 AND 300 °K

Y. D. YAO, (姚永德) L. T. HO (何俐民) and C. Y. YOUNG (楊占元)

Institute of Physics, Academia Sinica
Nankang, Taipei, Taiwan, The Republic of China

Abstract

Electrical resistivity ρ of polycrystalline Sm and Sm-Dy containing 3 at.% Dy has been measured as a function of the absolute temperature T between 15 and 300 °K. Basing on the criterion that at the Néel temperature T_N, $d\rho/dT$ is minimum, it has been determined that the values of T_N are 105.8± .5 K and 102.8± .5 K for the hexagonal sites of Sm and Sm-3at. % Dy respectively.

INTRODUCTION

In recent years, considerable interest has been centered on the understanding of the magnetic and structural properties of samarium[1-9]. It is well-known now that two allotropic forms are existed in metallic samarium; i.e. α-Sm and β-Sm. The structural transformation occurs near 1197 °K. Two magnetic transitions have been quite sure to occur near 13 and 106 °K. Another anomalies have been observed in the temperature intervals from 560 to 700 °K and from 800 to 920 °K. The nature of these behaviors is mainly due to the complicated crystal structure and magnetic interactions of metallic samarium.

Dysprosium is a hexagonal closed-packed structure and has been extensively studied. The magnetic behavior of dysprosium is quite understood now. Two magnetic transitions have been confirmed[10] to occur near 85 and 180 °K. Below 85 °K, dysprosium is in the ferromagnetic state with the magnetic moments parallel or closely parallel to the hexagonal layers. Between 85 and 180 °K, it is a spiral spin antiferromagnetic state with moments confined to the basal plane of the hexagonal structure. The moments in each basal plane were ferromagnetically ordered but the direction of magnetisation rotated from plane to plane by a turn angle which decreased from 43.2° at the Néel temperature to 26.5° at the Curie temperature[11]. Above 180 °K, Dy is converted into the paramagnetic state.

However, it is quite unexplored on the samarium-dysprosium alloy system from both experimental and theoretical points of view. Therefore, we decided to start the studies on Sm-Dy alloy system by measuring the electrical resistivity of polycrystalline Sm and Sm-Dy containing 3 at. % Dy between 15 and 300°K. Our results and their significance are presented in this paper.

EXPERIMENTAL CONSIDERATIONS

The polycrystalline Sm and Sm-Dy containing 3 at. % Dy were prepared by an electric arc melter using 99.9% samarium (Research Chemicals) and 99.5% dysprosium (St. Eloi Corporation). Melting was done in purified argon atmosphere. The ingot of Sm-Dy containing 3 at. % Dy was repeated melting several times. This is trying to get a better homogenized sample. From these ingots samples in the form of rectangular parallelpipeds were cut by hand using a diamond saw. The surfaces of the samples were polished using files and sandpaper. Typical sample dimensions were roughly $0.7 \times 3 \times 20$ mm^3. Four copper electrodes were lightly spot-welded to each sample. The center two copper electrodes were used as the potential leads; the other two were used as the current leads.

The electrical resistivity of the samples was determined using the conventional four-probe technique. Temperatures between 15 and 300 °K were achieved by a Displex closed-cycle refrigeration system (Model CS-202, Air Products and Chemicals Inc.). The temperature is controlled by a proportional plus rate cryogenic temperature controller (Model 3610, Air Products and Chemicals Inc.). The short-term stability of this temperature controller is within ± 0.01 °K and the long-term stability is within ± 0.1 °K. Two temperature sensors were placed beneath and above the sample. The average of this two temperature readings was supposed to be the temperature of the sample. A dc current was maintained constant to about one part in 10^5 and the voltage was measured with a precision of a few nanovolts. The sample was in a good thermal contact with the large high-conductivity copper base. For this purpose, a GE adhesive (No. 7031) or the equivalent had to be used between the sample and the copper base to ensure electrical insulation and good thermal conduction.

RESULTS AND DISCUSSION

Figure 1 shows the electrical resistivity of our polycrystalline Sm and Sm-3 at. % Dy samples between 15 and 300 °K. The anomaly has been shown to occur near 105.8 ± 0.5 °K and 102.8 ± 0.5 °K for Sm and Sm-3 at. % Dy respectively. The detailed temperature variation of the electrical resistivity in the neighborhood of this anomaly for Sm and Sm-3 at. % Dy is presented in Figs. 2 and 3 respectively. The temperature derivative of the electrical resistivity is also plotted in these two figures. The Néel temperatures are determined from these plots as the temperatures at which $d\rho/dT$ shows a minimum. We determined that the values of T_N for polycrystalline Sm and Sm-3 at. % Dy are 105.8 ± 0.5 °K and 102.8 ± 0.5 °K respectively.

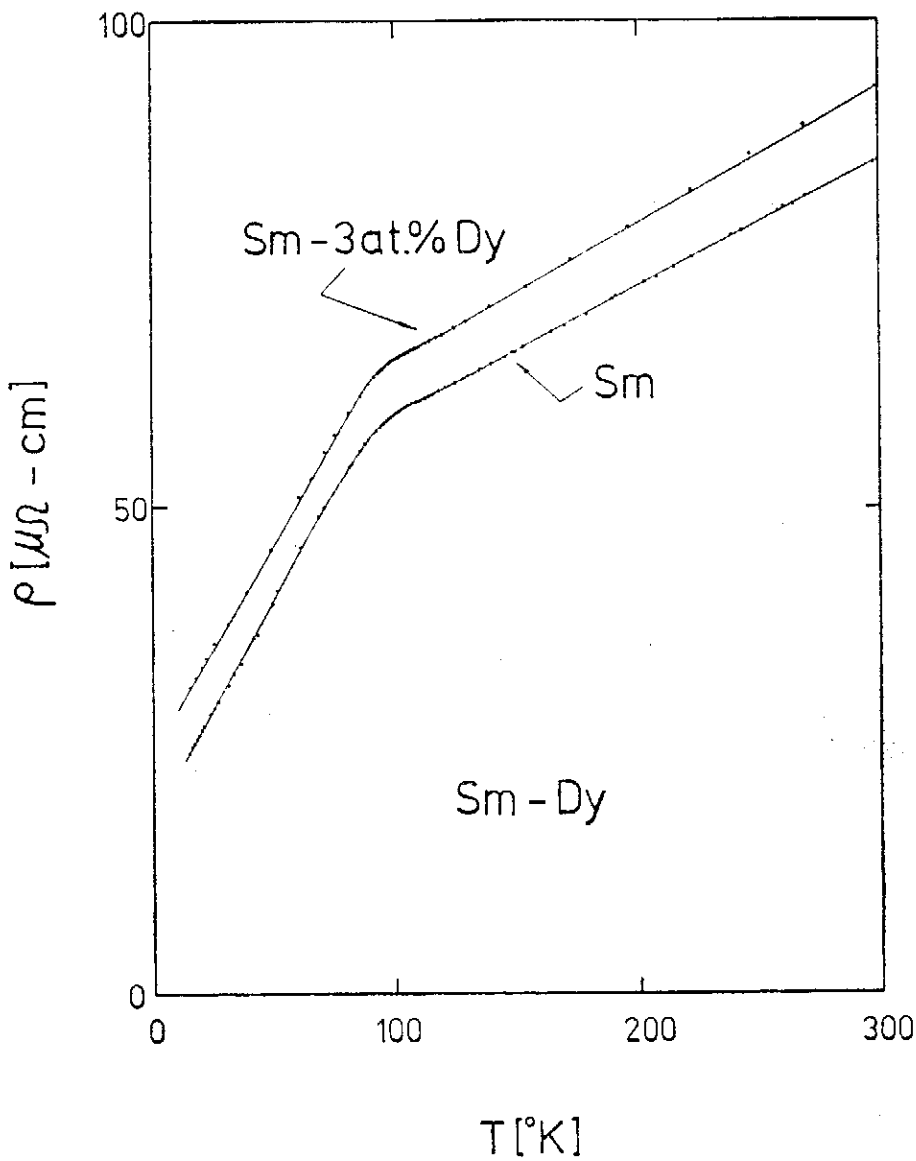

FIG. 1. Electrical resistivity of Sm and Sm-3 at.% Dy as a function of absolute temperature between 15 and 300°K.

Unfortunately, due to the limitation of our closed-cycle refrigeration system, the anomaly near 13°K for Sm is not considered here. Our electrical resistivity data do not clearly shown maximum and minimum near the Néel temperature. However, from Figs. 2 and 3, it is clear that the ρ vs. T curves undergo a concave downward smooth change below T_N and is almost a straight line above T_N. The general behavior of the electrical resistivity near T_N for Sm and Sm-3 at. % Dy is very similar to that of a typical antiferromagnetic metal, e. g. Cr, except the maximum and minimum behaviors.

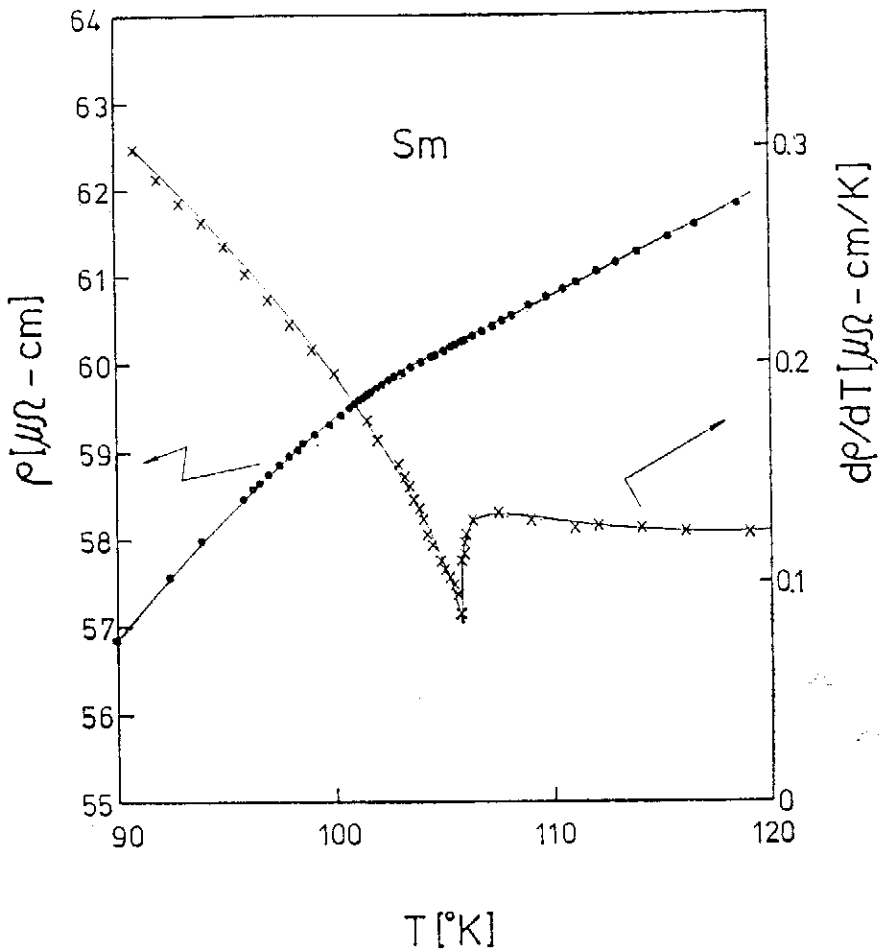

FIG. 2. Electrical resistivity of Sm and its temperature derivative in the neighborhood of 105.8°K.

The temperature derivative of the electrical resistivity was computer differentiated, point by point, at every temperature. The behavior of $d\rho/dT$ near T_N tell us that it is exactly a normal antiferromagnetic-paramagnetic phase transition. It is well-known that the crystal structure of Sm below 1197°K is rhombohedral, and may be considered as a nine-layer stacking sequence, i. e. ABABCBCAC, of closed-packed layers. Two thirds of the atoms have near-neighbor layer corresponding to the simple hexagonal structure, i. e. ABAB . . . , and the remaining atoms have near-neighbor layer similar to the cubic close packing, i. e. ABCABC . . . ; it will be convenient to refer to these as hexagonal and cubic sites respectively, even though the site symmetries are not exactly those of the ideal hexagonal and cubic close packing. Basing on the neutron diffraction study[6] on a single crystal of Sm, the moments on both types of sites align along the c direction to form separate simple antiferromagnetic structures. On the hexagonal sites, the ferromagnetic sheets are normal to the c axis; on the

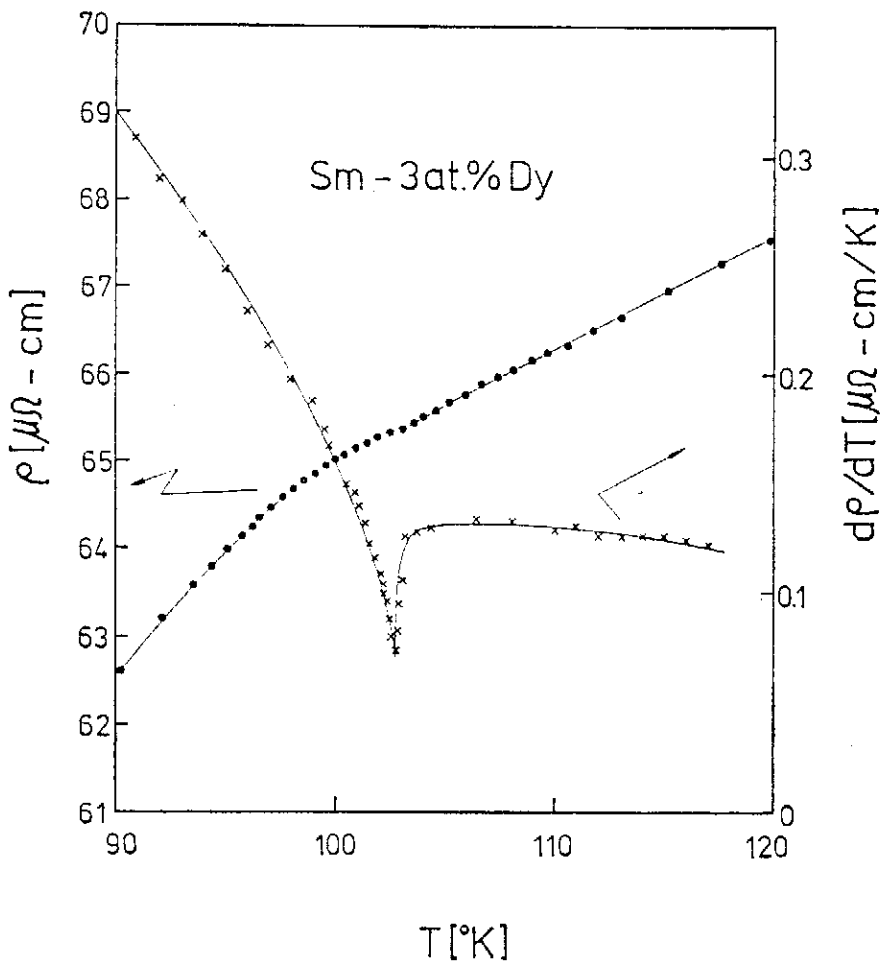

FIG. 3. Electrical resistivity of Sm-3 at.% Dy and its temperature derivative in the neighborhood of 102.8°K.

cubic sites, the sheets are parallel to $(10\bar{1}1)$ planes. The higher Néel temperature, T_{NH}, is a antiferromagnetic-paramagnetic phase transition for the hexagonal sites, and in this paper we have shown that $T_{NH} = 105.8 \pm 0.5$°K for Sm and $T_{NH} = 102.8 \pm 0.5$°K for Sm-3 at. % Dy. The lower Néel temperature, $T_{NC} \approx 13$°K, has been shown to be an antiferromagnetic-paramagnetic transition for the cubic sites. According to this study, because no evident anomaly happens between 15 and 100°K, we conclude that T_{NC} should be below 15°K for both Sm and Sm-3 at. % Dy.

Furthermore, we notice that the value of T_{NH} of Sm is almost about 3°K higher than that of Sm-3 at. % Dy. This may be explained as a result of weak interactions between that tripositive ions of Sm and Dy. The outermost electronic configuration for Sm^{3+} and Dy^{3+} is $4f^5 5S^2 5P^6$ and $4f^9 5S^2 5P^6$ respectively. In Sm-3 at. % Dy alloy, there is a possibility that the spiral spin

antiferromagnetic Dy ions substitute some Sm ions at hexagonal sites. This produces an additional magnetic Brillouin zone whose planes further incise and contort the Fermi surface and causes a little drop of T_{NH}. From the different configuration of the 4f shell electrons between Sm and Dy ions, the drop of T_{NH} by Dy impurities can be explained as owing to a weak delocalization of the f-wave functions.

To clarify the physical situation about the spiral spin antiferromagnetic Dy dissolved in rhombohedral Sm, further experimental and Theoretical works are definitely necessary. These works are in progress in our laboratory and will be reported later.

REFERENCES

(1) J. M. Lock, *Proc. Phys. Soc. Lond.* B**70**, 566 (1957).
(2) L. C. Jennings, E. D. Hill and F. H. Spedding, *J. Chem. Phys.* **31**, 1240 (1959).
(3) S. Arajs, *Phys. Rev.* **120**, 756 (1960).
(4) S. Arajs and G. R. Dunmyre, *Z. Nat.* A**21**, 1856 (1966).
(5) M. Schieber, S. Foner, R. Doclo and E. J. McNiff, *J. Appl. Phys.* **39**, 885 (1968).
(6) W. C. Koehler and R. M. Moon, *Phys. Rev. Lett.* **29**, 1468 (1972).
(7) A. S. Bulatov and V. A. Finkel, Zh. Eksp. *Teor. Fiz.* **63**, 213 (1972).
(8) R. B. Beeken and Wm. R. Savage, *Phys. Rev.* B**15**, 5307 (1977).
(9) Ya. A. Kraftmakher and T. Yu. Pinegina,*Phys. Stat. Sol.* (a) **47**, K81 (1978).
(10) D. R. Behrendt, S, Legvold and F. H. Spedding, *Phys. Rev.* **109**, 1544 (1958).
(11) M. K. Wilkinson, W. C. Koehler, E. O. Wollan and J. W. Cable, *J. Appl. Phys.* **32**, S48 (1961).

INTERNAL RESISTANCES OF SOLAR CELL

YU-TUNG YANG (楊 毓 東)

Physics Institute, Academia Sinica
Nankang, Taipei, Republic of China

Abstract

If a solar cell is well designed and made, the exact solar cell equation $I = I_{sc} - I_o [\exp(qV/kT) - 1]$ is satified. The internal resistances of such a solar cell are determined by $R_s = (kT/qI_{sc})[\exp(qV_{oc}/kT) - 1]/\exp(qV_{oc}/kT)$, and $R_{sh} = (kT/qI_{sc})[\exp(qV_{oc}/kT) - 1]^2/\exp(qV_{oc}/kT) = R_s [\exp(qV_{oc}/kT) - 1]$. If a p-n junction solar cell agrees with the solar cell equation, then the calculated internal series resistance R_s is small, and is usually of the order of 10^{-1} ohm, and the internal shunt resistance R_{sh} is usually very large, and is of the order of 10^9 ohms or more, (all on one cm^2 basis). They may be calculated accurately according to the above formulae and the experimental values of V_{oc} and I_{sc}. If $V_{oc} \gg kT/q$, then R_s approaches kT/qI_{sc}, and R_{sh} approaches $(kT/qI_{sc})\exp(qV_{oc}/kT)$. If $V_{oc} \ll kT/q$ under illumination, the solar cell is poor, and then, R_s approaches kT/qI_o, and R_{sh} approaches zero which means there is heavy leakage. The solar cell equation is not designed for the solar cells with back surface fields.

INTRODUCTION

The basic solar cell equation is[1-3]

$$I = I_{sc} - I_o [\exp(qV/kT) - 1] , \qquad (1)$$

where I is the measured current output by light stimulation. I_{sc} is the measured short-circuit current, I_o is the dark current which can be obtained from known values of V_{oc} and I_{sc}. $V = V_{oc}$ and $I = 0$ when the circuit is open.

In the past, many authors had tried to modify (1) in order to satisfy the experimental I-V curves[4-5], but the difficulty remains.

Since (1) is an exact socution of the (differential) equation of continuity, therefore, any solar cell which is well designed and made should satisfy (1). When $V = V_{oc}$, $I = 0$, then,

$$I_{sc} = I_o [\exp(qV_{oc}/kT) - 1] . \qquad (2)$$

The above equation (2) contains all the necessary descriptions of a solar cell and also the relations among the parameters. The derivation of the internal series- and shunt-resistance maybe done by using (2) alone. For instance, the internal series resistance may be defined as

$$R_s = (\partial V_{oc}/\partial I_{sc}) . \qquad (3)$$

Thus,

$$R_s = (kT/qI_{sc}) [\exp(qV_{oh}/kT) - 1]/\exp(qV_{oc}/kT) . \qquad (4)$$

The above expression is considered reasonable because R_s is the only resistance which may keep I_{sc} from going to infinity if the conductor is or nearly is ideal, and

$$V_{oc} = \int dV_{oc} = \int R_s dI_{sc} = (kT/q) \int dI_{sc}/(I_{sc} + I_o) + C_1$$
$$= (kT/q) \ln(I_{sc} + I_o) + C_1 . \quad (5)$$

The constant of integration C_1 is determined from the initial condition: In darkness, $V = V_{oc} = 0$, and $I = I_{sc} = 0$. Thus (5) shows

$$C_1 = -(kT/q) \ln I_o . \quad (6)$$

When (6) is combined with (5),

$$I_{sc} = I_o [\exp(qV_{oc}/kT) - 1] , \quad (7)$$

which is (2).

When the solar cell circuit is open, I_{sc} is not functioning, but the recombination processes must go on to keep equilibrium, therefore, $-I_o$ is functioning, and it goes through a shunt (or leakage) resistance R_{sh} in the cell. From (2) we may define

$$V_{oc} = \int dV_{oc} = \int -R_{sh}\, dI_o = (kT/q) \int dI_o [-I_{sc}/I_o(I_{sc} + I_o)]$$
$$= (kT/q) [-\ln I_o + \ln(I_{sc} + I_o)] + C_2 , \quad (8)$$

where C_2 is a constant of integration, and R_{sh} is defined as

$$R_{sh} = (-\partial V_{oc}/\partial I_o) . \quad (9)$$

Again, in darkness, $V = V_{oc} = 0$, and $I = I_{sc} = 0$, therefore, (8) shows

$$C_2 = 0 . \quad (10)$$

Thus, (8) also goes back to (2) after integration.

(5) shows that V_{oc} maybe determined under short-circuit condition by letting I_{sc} go through R_s, and (8) shows the same V_{oc} may also be obtained under open-circuit condition by letting $-I_o$ go through R_{sh}. As far as V_{oc} is concerned, (5) and (8) are equivalent. Under short-circuit condition, only I_{sc} exists.

Finally, from (2)

$$R_s = (kT/q) [\exp(qV_{oc}/kT) - 1]/I_{sc} [\exp(qV_{oc}/kT)]$$
$$= (kT/q) (I_{sc} + I_o)^{-1} = (\partial V_{oc}/\partial I_{sc}) . \quad (11)$$

and similarly,

$$R_{sh} = (kT/q) [\exp(qV_{oc}/kT) - 1]^2/I_{sc} [\exp(qV_{oc}/kT)]$$
$$= (kT/q) [(1/I_o) - (1/(I_{sc} + I_o))] = -(\partial V_{oc}/\partial I_o) . \quad (12)$$

(11) and (12) show that the R_s and the R_{sh} of a solar cell are dependent,

$$R_{sh} = R_s [\exp(qV_{oc}/kT) - 1] . \quad (13)$$

(13) is considered reasonable because both the resistances are in the same solar cell made of one single crystal.

In the past, R_{sh} and R_s were estimated by measuring the slopes at $(V_{oc}, 0)$ and at $(0, I_{sc})$ respectively. (11) and (12) represent the same idea but only more analytical and more accurate, and no circuit theory is required.

EVIDENCES

A thin (50μ) horizontal N/P solar cell constructed by Lindmayer and Wrigley (LW)[6] is selected as an example. From (1) we observe that the LW solar cell is made of almost perfect crystal, and it was also briefly mentioned in their report[6]. The I-V curve of the LW solar cell deviates only very slightly from the curves constructed according to (1). (In which case, the measured V_{oc} and I_{sc} are used for the construction of the upper-bound theoretical I-V curve, and the measured $V_{opt.}$ and $I_{opt.}$ (optimum) values are used for the construction of the lower-bound theoretical I-V curve. The experimental I-V curve should run between the theoretical upper- and lower-bound. If a solar cell is ideal, then, the upper- and lower-bound theoretical IV curves should coincide. However, if a solar cell is not well made, then the gap between the two bounds becomes wide. Fig. 1 shows the experimental I-V curve of a not-very-effective solar cell (N/P, 2×2 cm$^2\times0.5$ mm), and the gap is wide between the lower- and upper-bound. Fig. 2 shows the I-V curve of the LW solar cell which is almost ideal. The gap is very narrow. Table I shows the results of calculations of the parameters.

TABLE I. Parameters of solar cells and range of variations

Solar cell	V_{OC}		I_{SC}		I_O		R_S	
	lower	upper	lower	upper	upper	lower	upper	lower
No. 1, (N/P, 2×2cm², thickness=0.5mm).	0.483v	0.574v	0.128a	0.134a	1.16×10^{-9}a	3.34×10^{-11}a	0.20Ω	0.194Ω
LW, (N/P, 2×2cm², thickness=50μ)	0.579v	0.583v	0.128a	0.129a	2.803×10^{-11}a	2.357×10^{-11}a	0.203Ω	0.202Ω

R_{sh}		$V_{oPt.}$		$I_{oPt.}$		Efficiency, per cm²	Figure
lower	upper	lower	upper	lower	upper		
$2.24\times10^{7}\Omega$	$7.66\times10^{8}\Omega$	0.42v	0.49v	0.121a	0.126a	9.6% (AM1)	1
$0.93\times10^{9}\Omega$	$1.10\times10^{9}\Omega$	0.500v	0.505v	0.122a	0.123a	11.3% (AM0)	2

Acknowledgement: I am grateful to Li-Hue Chen for his helpful discussions and the preparation of the computer program.

REFERENCES

(1) H. J. Hovel, "Solar cells", in "Semiconductors and semimetals". Ed. by R. K. Willardson and A. C. Beer, Vol. 11, pp. 58-65, Academic Press, New York, 1975
(2) R. Cummerow, Phys. Rev., **55**, 16, 1954
(3) J. P. Mckelvey, "Solid state and semiconductor physics", Harper and Row, New York, 1971, pp. 461-468
(4) C. T. Sah, N. Noyce, and W. Shockley, Proc. IRE, **45**, 1228, 1957
(5) M. B. Prince, J. Appl. Phys., **26**, 534, 1955
(6) J. Lindmayer and C. Wrigley, IEEE Photo. Spec. Conf., 12th, Baton Rouge, Louisiana, 1976, p. 53

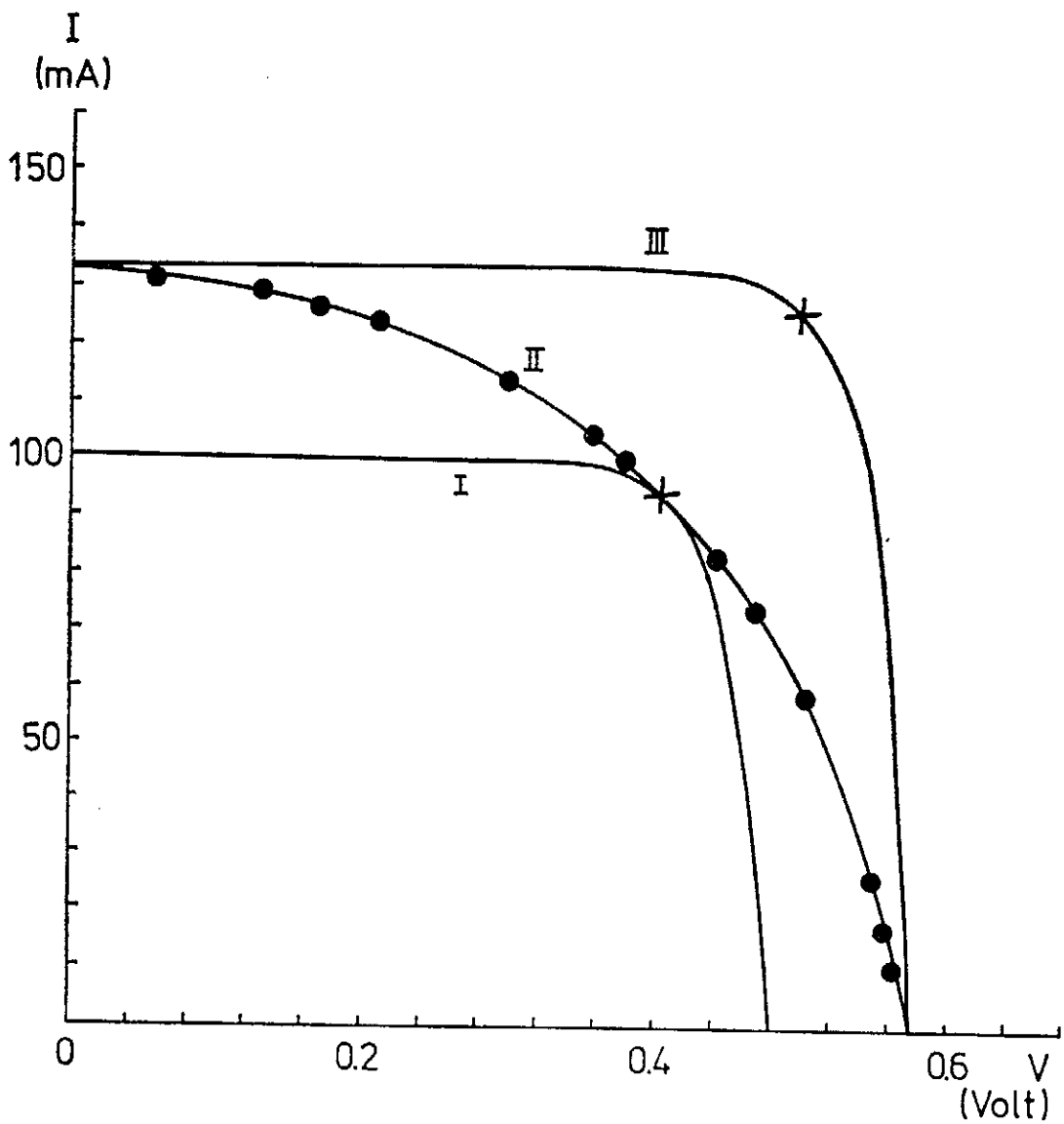

FIG. 1 Solar cell in horizontal position. Curve I is the theoretical lower-bound I-V curve, curve II is the experimental curve, and curve III is the theoretical upper-bound. (N/P, frontal area=2×2 cm², and thickness=0.5 mm).

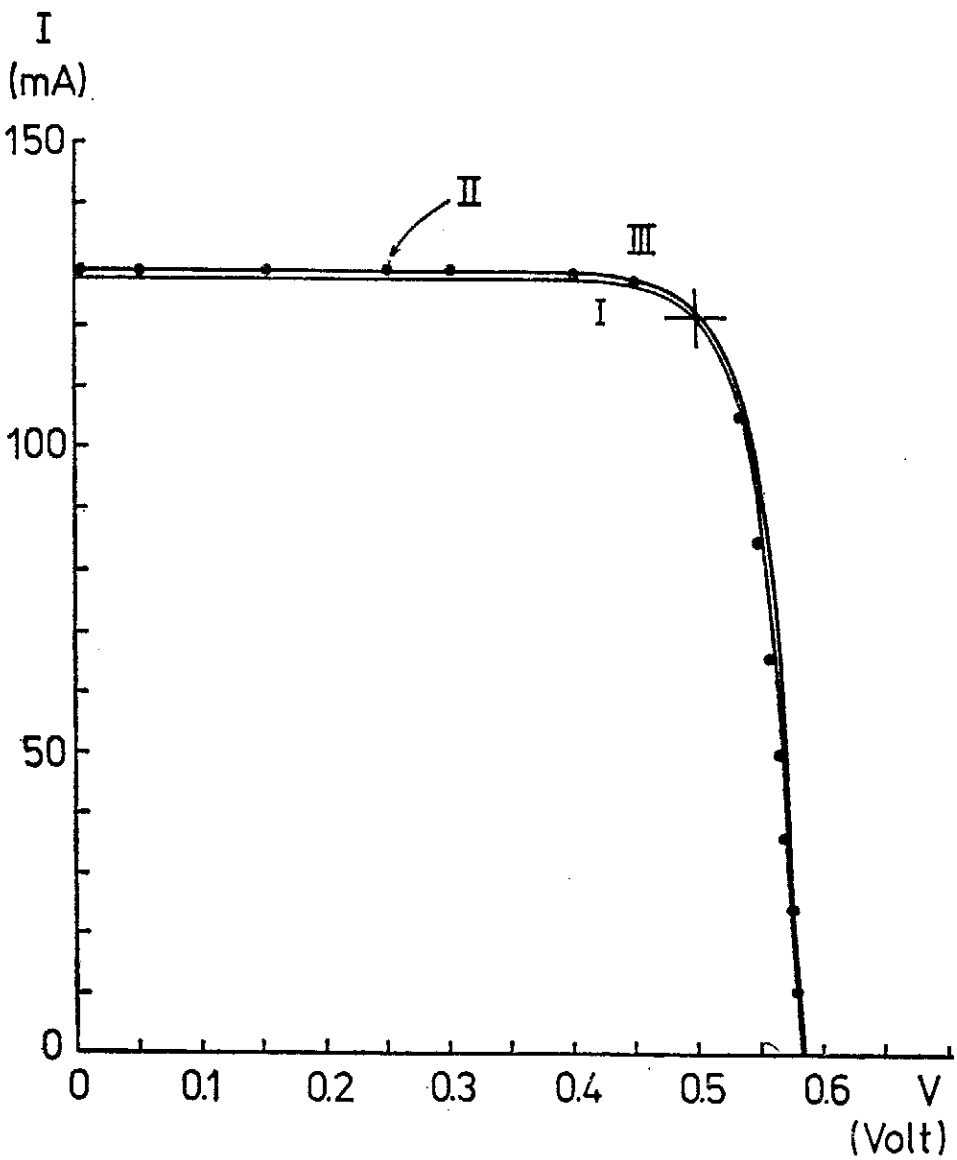

FIG. 2 Thin solar cell I-V curve reported by Lindmayer and Wrigley[6]. The theoretical lower- and upper-bound are only barely distinguishable. It is found that the basic solar cell equation (1) is almost strictly obeyed. (Dots are the original I-V values by Lindmayer and Wrigley). (N/P, frontal area=2×2 cm^2, and thickness = 50 μ).

A THEORY OF THRESHOLD SWITCHING IN AMORPHOUS THIN FILM*

CHUN CHIANG (蔣 忻 儒)

Institute ef Physics Academia Sinica
Nankang, Taipei, Taiwan, The Republic of China

Abstract

Using the concept that two reversible forms exist in amorphous thin film and that the transition between them may be activated by the current, and these two forms have different conductivities, the threshold switching phonomenon may be explained. The threshold switching equation and time delay equation are also derived.

Threshold switching in amorphous thin film has recently attracted great attention[1, 2, 3, 4, 5]. Despite its intensive research no electronic switching theory has been developed to the stage that quantitative calculation and prediction can be made. Recently, a quantitative switching theory[6] has been given for the organic thin film with dipoles, and a quantitative theory has also been given for the nerve excitation and action potential[7, 8].

This letter proposes some conditions in the amorphous thin film for showing the threshold switching, and furthermore, threshold switching equation and time delay equation are derived and predictions are made.

The conditions required for the amorphous thin film are: (i) there are two stable and reversible configurations (configuration I and configuration II) co-existing in approximately equilibrium in the amorphous film. These two configurations may transform to each other through an energy barrier under electric excitation. The difference between configuration I and configuration II may either be due to the positional variation of the atoms, the variation of the number of the bonding atoms, the changing of the bonding state such as from p-orbital to d-orbital or from lone pair to bonding[9], or from neutral dangling bond to positive and negative dangling bond[10, 11] or a combination of the above situations, (ii) the conductivity of configuration II is much higher than that of configuration I, (iii) the energy level of the configuration I and II may be elavated by current I with the amount k_1 I and k_2 I respectively, the elevation of the energy is due to the fact that the kinetic energy of the current may dissipate and excite the system within the film (see Fig. 1). Thus k_1 and k_2 represent respectively the extent of electronic exitation of the energy level for configuration I and configuration II in the system by the current, and are temperature dependent. This exitation is electrical in origin and may not necessarily be thermal. Also, the electronic energy may be elevated

* To be published in Physica Status Solidi

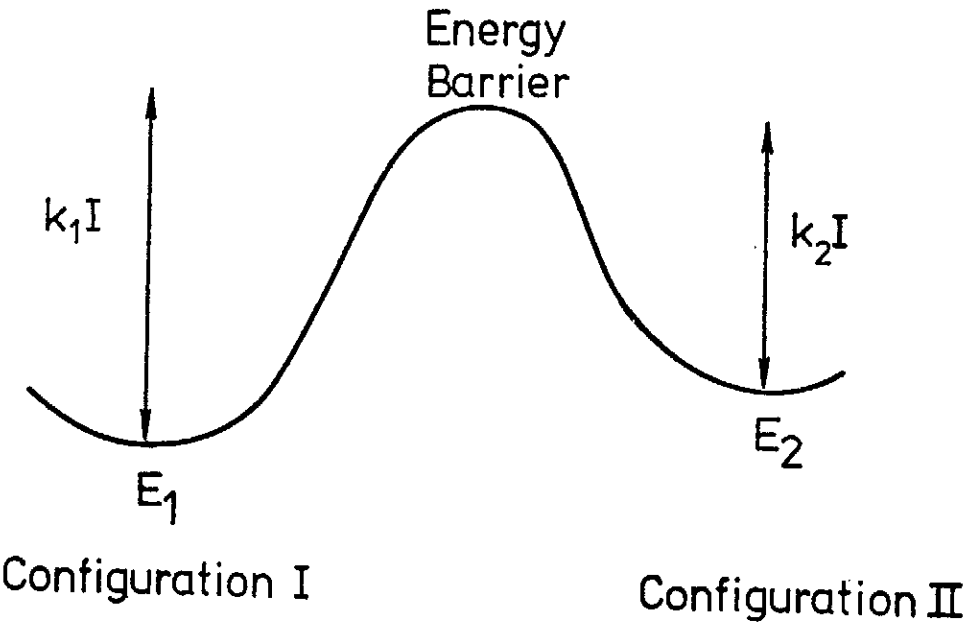

FIG. 1. Energy diagram of two reversible configurations in amorphous thin film. The transition is seperated by the barrier and may be activated by the current.

to such an extent that ionization may result and representing the occurrence of avalanche.

For a quantitative calculation, we write

$$\frac{dN_1}{dt} = -AN_1 e^{-(u-E_1-k_1|I|)/KT} + AN_2 e^{-(u-E_2-k_2|I|)/KT}$$
$$\frac{dN_2}{dt} = AN_1 e^{-(u-E_1-k_1|I|)/KT} - AN_2 e^{-(u-E_2-k_2|I|)/KT} \qquad (1)$$

where N_1 or N_2 is respectively the number density of configuration I or configuration II per unit length within the film. A is collisional frequency and k_1, k_2 are constant. E_1 or E_2 is the energy of configuration I and configuration II respectively, u is the barrier energy. Equation (1) says that the changing of N_1 per unit time is proportional to the number of transformation from configuration II to configuration I minus the number of transformation from configuration I to configuration II. The number of transformation from configuration I to configuration II is equal to the number of N_1 multiplied by the collisional or vibrational frequency A and the probability of transformation per collision. The probability of transformation per collision from configuration I to configuration II is $\exp-[u-(E_1+k_1|I|)]/KT$, where $u-(E_1+k_1|I|)$ is the energy difference between the barrier and the configuration I. The number of transformation from configuration II to configuration I is equal to AN_2 exp−

$[u-(E_2+k_2|I|)]/KT$. Similar reasoning applies to the changing of N_2 per unit of time.

Equation (1) may be solved to give

$$N_1 = \frac{N\, e^{(E_2+k_2|I|)/KT}}{e^{(E_1+k_1|I|)/KT}+e^{(E_2+k_2|I|)/KT}} + \left[N_1^0 - \frac{N\, e^{(E_2+k_2|I|)/KT}}{e^{(E_1+k_1|I|)/KT}+e^{(E_2+k_2|I|)/KT}}\right] \times \exp-\left[A\, e^{-(u-E_1-k_1|I|)/KT} + A\, e^{+(u-E_2-k_2|I|)/KT}\right] t \quad (2)$$

$$N_2 = \frac{N\, e^{(E_1+k_1|I|)/KT}}{e^{(E_1+k_1|I|)/KT}+e^{(E_2+k_2|I|)/KT}} - \left[N_1^0 - \frac{N\, e^{(E_2+k_2|I|)/KT}}{e^{(E_1+k_1|I|)/KT}+e^{(E_2+k_2|I|)/KT}}\right] \times \exp-\left[A\, e^{-(u-E_1-k_1|I|)/KT} + A\, e^{-(u-E_2-k_2|I|)/KT}\right] t,$$

where N_1^0 is the initial number of configuration I and N is the total number of configuration I and configuration II at any time, being a constant for a given film. Starting from the OFF state, configuration I predominates in the film and $N_1^0=N$.

Also, if part of the area on the surface of electrode has been activated to the state of configuration II by the current, then the current in that area will be activated and propagate along the way to the other electrode forming a filament of configuration II. Pearson and Miller[16] and Weirauch[17] have reported evidence for conducting filaments on the ON state, Uttecht et al.[18] and Sie[19] have directly observed filament formation on the surface of the film. Thus, if G is the conductance of the film and g_1 or g_2 is respectively the conductivity of the film in the pure state of configuration I or configuration II, then

$$G = (N_1/N)(a/d)g_1 + (N_2/N)(a/d)g_2 \quad (3)$$

and

$$I = VG, \quad (4)$$

where a is the area and d is the thickness of the film.

From equations (2), (3), (4) and $N_1^0=N$, we have

$$\frac{I}{V} = \frac{g_1\, e^{(E_2+k_2|I|)/KT} + g_2\, e^{(E_1+k_1|I|)/KT}}{e^{(E_2+k_2|I|)/KT}+e^{(E_1+k_1|I|)/KT}} \frac{a}{b} + \frac{a(g_1-g_2)}{d}\left[1 - \frac{e^{(E_2+k_2|I|)/KT}}{e^{(E_1+k_1|I|)/KT}+e^{(E_2+k_2|I|)/KT}}\right] \times \exp-\left[A\, e^{-(u-E_1-k_1|I|)/KT} + A\, e^{-(u-E_2-k_2|I|)/KT}\right] t. \quad (5)$$

The steady value is

$$V = \frac{e^{(E_1+k_1|I|)/KT}+e^{(E_2+k_2|I|)/KT}}{(a/d)g_1\, e^{(E_2+k_2|I|)/KT} + (a/d)g_2\, e^{(E_1+k_1|I|)/KT}} I. \quad (6)$$

This is the threshold switching equation for amorphous thin film. This equation shows that the threshold voltage is proportional to the thickness d in agreement with the experiment[13], whereas the "injection model" such as that proposed by Lucas[14] and Wright and Ibrahim[15] predits it to be proportional to d^2. Equation (6) may also be transformed to be

$$V = \frac{1+\exp[(\Delta E+\Delta k|I|)/KT]}{(ag_2/d)+(ag_1/d)\exp[(\Delta E+\Delta k|I|)/KT]}\, I \qquad (6)'$$

If we let $ag_1/d = 0.\times 10^{-4}\Omega^{-1}$, $ag_2/d = 1.7\times 10^{-3}\Omega^{-1}$, $\Delta E = 0.2$ ev, $\Delta k = -7.5\times 10^{-2}$ev/Amp, then equation (6)′ appears as shown in Fig. 2. Independently, I suggest that measurements of absorption spectrum and emmision spectrum of the film under electric excitation be performed, and the intensity of the spectrum of the film in ON state and OFF state be compared, to have an independent check of ΔE and Δk. This may be experimentally difficult, and also the identification of the spectrum with the structure of the film itself is a difficult task; nevertheless, the possibility exists that such works in optics and electronics may correlate and may be complementary to each other. From

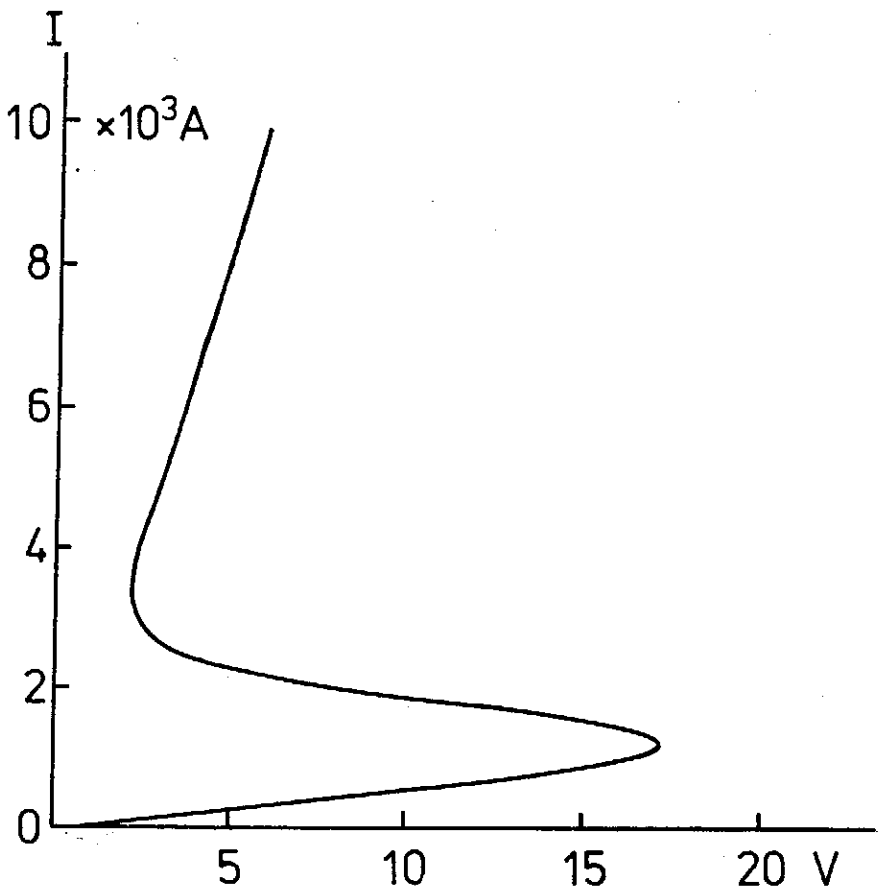

FIG. 2. I-V switching curve calculated according to equation (6)′

this theory, it would not be surprising to find that photo effect can also cause switching and structure change in thin film.

In the derivation of equation (6), it is assumed that the excitation of the energy level by current is proportional to I, however, it should be noted that the process of the imact of molecules by electrons is very complicated, being structure dependent and may even vary from sample to sample. Thus, the excitation of the energy level is a complicated function of current. However, regardless of the exact form of the current dependence, the major switching property in equation (6) is not appreciably changed, and the functional form of the current in the exponential term in equation (6) will only change the range of current for which the switching takes place.

For a given voltage V, which is larger than the threshold voltage V_t by an amount ΔV, the delay time is the period required for the current to reach the threshold value I_t. Thus from Eq. (5), we have

$$t = C_1 \{\ell n\, C_2 - \ell n\, \Delta V\} \tag{7}$$

where

$$C_1 = [A \exp(E_1 + k_1|I_t| - U)/KT + \exp(E_2 + k_2|I_t| - U)/KT]^{-1}$$
$$C_2 = [1 - \exp(E_2 + k_2|I_t|)/KT]\,[\exp(E_1 + k_1|I_t|)/KT + \exp(E_2 + k_2|I_t|)/KT]^{-1} \times a(g_2 - g_1)V_t^2/d|I_t|$$

and approximation has been used that $\Delta V < V_t$, also the relation that

$$V_t = \frac{d}{a}\,\frac{e^{(E_1+k_1|I_t|)/KT} + e^{(E_2+k_2|I_t|)/KT}}{g_1\, e^{(E_2+k_2|I_t|)/KT} + g_2\, e^{(E_1+k_1|I_t|)/KT}}\, I_t \tag{8}$$

has been used.

Eq. (7) is the time delay equation and shows that the delay time decreases with increasing voltage, and if the voltage is at the threshold voltage, the delay time is infinity. However, the applied voltage is difficult to be fixed exactly at the threshold voltage, so slight variation will cause a spread of the delay time. This fact is indeed observed by the experiment[12]. By comparison of Eq. (7) with the experimental data of time delay, E_1, E_2 and k_1, k_2 may also be estimated.

In conclusion, we have specified the conditions for the amorphous film to show the threshold switching behavior, and quantitative relationspip has been derived for the threshold behavior and the delay time, which no other electronic switching theory seems to be able to accomplish yet. I have also pointed out the way in which independent systematic experiments may be performed to check this theory.

REFERENCES

(1) A. Szymanski, D. C. Larson and M. M. Labes, *Apyl. Phys.* Lett. **14**, 88 (1969).
(2) I. Balberg, Appl. *Phys. Lett. 16*, 491 (1970).
(3) M. Saji, C. H. Leurg and K. C. Kao, *J. Non-Crystalline Solids*, **23**, 147 (1977).
(4) W. Van Roosbroeck, *Phys. Rev. Lett.* **28**, 1120 (1972).
(5) S. H. Lee and H. K. Henisch, *Appl. Phys.* Lett. **22**, 230 (1973).
(6) C. Chiang, *Appl. Phys. Lett.* **31**, 554 (1977).
(7) C. Y. Lee and C. Chiang; *Bull. Math. Biol.* **38**, 59 (1976).
(8) C. Chiang, Bull. Math. Biol. **40**, 247 (1978).
(9) M. Kastner, D. Adler and H. Fritzsche, *Phys. Rev. Lett.* **37**, 1504 (1976).
(10) P. W. Anderson, *Phys. Reu. Lett.* **34**, 953 (1975).
(11) R. A. Street, and N. F. Mott, *Phys. Rev. Lett.* **35**, 1293 (1975).
(12) S. H. Lee and H. K. Henisch, *J. Non-Cryst. Solids* 8-10, 422 (1972).
(13) A. E. Owen and J. M. Robertson, *IEEE transactions on Electron Devices*, Vol. ED-20, 105 (1973).
(14) I. Lucas, *J. Non-Cryst. Solids.* **6**, 136 (1971).
(15) G. T. Wright and A. F. Ibrahim, *Electron, Lett.*, **4**, 597 (1968).
(16) A. D. Pearson and G. E. Miller, *Appl. Phys. Lett.*, **14**, 280 (1969).
(17) D. E. Weirauch, *Appl. Phys. Lett.*, **16**, 72 (1970).
(18) R. Uttecht et al., *In Proc. Symp. Semiconductor Effects in Amorphous Solids (New York, N. Y.)* May 1969, pp. 358.
(19) C. H. Sie, *In Proc. 3rd Int. Conf. Amorphous and Liquid Semiconductors*, Cambridge, England, Sept. 1969, pp. 548.

GEOMETRICAL ORIENTATION AND POLYMERIZATION IN ANTHRACENE THIN FILM AS A SWITCHING AND MEMORY DEVICE

CHUN CHIANG (蔣 忻 儒)

Institute of Physics, Academin Sinica
Nankang, Taipei, Taiwan, The Republic of China

Abstract

The switching and memory phenomenon in anthracene thin film is explained on the basis of polymerization of anthracene molecule to graphite-like polymer. When the voltage is at threshold point, the energetic electron and the secondary ionization may initiate the polymerization. Since the polymer has graphite-like structure, it has higher conductivity thus the film is switched to ON state. Since the molecule in thin film can not rotate as freely as in liquid, the polymer formed is under great bond strain, thus the polymer may readily switch back to monomer anthracene molecule. However, if with repeated cycles, the polymer is at a relatively stable configuration with less bond strain, then it is in the memory state. Many experimental data of Elsharkawi and Kao may be explained with this model. A simple derivation for threshold switching equation is given.

I. INTRODUCTION

Switching and memory device is of keen interest. Ordinarily we can observe this phenomenon in inorganic thin film[1, 2]; recently, organic thin films also have been shown to exhibit this phenomenon[3–7]. However, the mechanism for this phenomenon is not clear. Chiang[16] recently proposes a flip-flop model of organic thin film with dipoles as a mechanism for switching and negative resistance phenomenon. Theoretically any bistable structure conversion with different conductivity, which can be activated by voltage, may show the switching and memory phenomenon. In the past, the amorphous-crystalline conversion has been suggested as the mechanism in inorganic thin film[15]. However, for the organic molecule and polymer with large volume, the number of molecules per unit of thickness of the film is greatly reduced, thus the contribution of amorphous-crystalline conversion is less. In this paper I propose the polymer-monomer conversion as the cause for switching and memory phenomenon in thin film of anthracene, and in other aromatic thin film such as tetracene film. The data in the existing literature[4, 5, 7] seem consistent with this model as will be shown in the following.

II. MECHANISM

When the organic crystal such as anthracene is sublimated onto a flat glass substrate, a thin amorphous film is formed; when the film is not very thick, the

molecule may enjoy a relatively large space due to its large plannar structure and the random deposition in coating, thus it may be regarded as an intermediate state between liquid state and crystalline solid state.

The characteristics of the amorphous state is that the structure is neither as regular and rigid as crystalline state, nor as loose as in liquid state. Thus the atoms or molecules in the amorphous state have better freedom than those in the crystalline state and yet maintain certain definit form. Perhaps, it is this property which renders amorphous thin film particularly susceptable for switching phenomenon.

With applied electric field, the current is first limited by the space charge. As the electric field becomes stronger, the anthracene molecule becomes ionized, which increases the current. As the electric field is further increased, secondary ionization may also be initiated, furthermore, the increased current provides sufficient heat to loose the barrier for rotation and translation of the molecule, thus anthracene molecule may orient itself to a geometrical position suitable for polymerization and the molecule is polymerized. The polymer formed has a graphite-like structure with low resistivity and represents the "ON" state. Due to the fact that the amorphous film does not provide a large free space for molecule to orient itself as freely as in liquid, the polymer formed is under great bond strain and is not stable, thus the polymer readily switches back to monomer form, the "OFF" state, as the voltage is decreased. However, with repeated cycles, the monomer may gradually orient itself to a steady position which is suitable for polymerization with less strain, then the film may be switched to "ON" state and remain in that state for some period, even without the applied field, namely, the "Memory" state. Nevertheless, this state is less stable than "OFF" state and a large current pulse of either polarity will break the polymer and erase the "Memory" state, and the film is switched back to "OFF" state. If the polarity is opposite to that of the applied field, the erase is more effective. This is because the polymer formed under an applied field with strain is easier to shift to its monomer state by taking a path which is reversal to its original path rather than the opposite path which has to pass through a maximum barrier.

At the threshold voltage for switching, since the molecules can not orient themself simutaneously to form a polymer, thus the current is unstable. With excess current in the "ON" state or with repeated cycles, the hydrogen atoms may escape from the film and oxygen in the air may interact with the film, thus other product may be formed; furthermore, the switching involves a relatively drastic geometric orientation in space, which may profondly affect the contact electrode, thus the film will gradually loss its switching property.

In the thick film, the molecule packing is more compact, thus it provides less space for the molecules to rotate and polymerize, thus the energy of the injected electrons and holes is released in the form of electroluminescence, while in the thin film, the energy is consumed in the translation and rotation to form the polymer, thus exhibiting the switching phenomenon and electroluminescence is less likely to be observed[7], however, if the energy is not completely consumed, then there is still chance to show some electroluminescence[5]. The conductance of the "ON" state in anthracene film is found to decrease with increasing of the temperature, then rise again[7]; this is probabily due to the fact that increasing the temperature may break the strained bond of the metastable polymer, thus decreasing the conductance, however further increasing the temperature facilate the transport of the carrier thus the conductance increase again. The relative insensitivity of tetracene on temperature over a wide temperature range[4] is probabily due to the fact that there is more fused ring in tetracene, and the polymer formed has more resemblance to the graphite, whose conductance is found to be weakly dependent on the temperature[16].

This model predicts and explains most of the experimental facts observed in anthracene thin film in particular and the aromatic thin film in general[4, 5, 7], and it seems that no other theory[8] may explain the data to such detail. To further strengthen the proposal that the polymer-monomer conversion is the cause for switching and memory in some organic thin film, we note that:

(1) Normally, the virgin film formed is in the OFF-state, however, the virgin polymer film formed by electron beam bombardment[12] is in the ON-state. Since the conductivity of the polymer is higher than that of the monomer, this supports the view that the ON-state is the polymer form and the OFF-state is the monomer form.

(2) The ionization potential for styrene, anthracene and tetracene is around 8.9 ev, 8.2 ev and 7.7 ev respectively[13, 14], this is about the same order of magnitude and sequence observed for switching voltage in styrene[5], anthracene[7] and tetracene[4] thin film.

(3) Polymerization in liquid state by electric ionization has been established[9, 10, 11] and polymerization in solid state by radiation and electron bombardment is also well known, thus it should not be surprised that meta-stable polymer could be formed by electric ionization in solid thin film, forming the "Memory" state; also due to the bond strain formed in the amorphous thin film, the meta-stable polymer is relatively easy to switch to the monomer "OFF" state.

(4) Photo-induced optical changes in amorphous As-S films has been explained by DeNeufville et al.[18] as due to photo polymerization and has been patially confirmed by Raman scattering experiments[19]. This explaination by photo-polymerization is compatible to the present explaination of electric-polymerization.

III. THRESHOLD SWITCHING EQUATION

Suppose for current passing through a unit area, the distribution of polymer and monomer in equilibrium in that area follows the Boltzmann relationship, then

$$\frac{\eta_1}{\eta_2} = e^{-\frac{(E_1+k_1|I|)}{KT}} \Big/ e^{-\frac{(E_2+k_2|I|)}{KT}} \tag{1}$$

where η_1 and η_2 are the number of polymer and monomer in that area, E_1 and E_2 are the potential energy of the polymer and monomer, k_1 and k_2 are constant and represent the extent of energy excitation by the current, K the Boltzmann constant and T the temperature. Suppose we have

$$\frac{I}{V} = G = \frac{\eta_1}{\eta_1+\eta_2} G_1 + \frac{\eta_2}{\eta_1+\eta_2} G_2 \tag{2}$$

where G_1, G_2 or G represents respectively the conductance of a film with polymer, monomer or a mixture of polymer and monomer, V the voltage, then, combining (1) and (2), we have the threshold switching equation as follows:

$$V = \frac{e^{-\frac{(E_1+k_1|I|)}{KT}} + e^{-\frac{(E_2+k_2|I|)}{KT}}}{G_1 e^{-\frac{(E_1+k_1|I|)}{KT}} + G_2 e^{-\frac{(E_2+k_2|I|)}{KT}}} I \tag{3}$$

Note that G_1 and G_2 may not necessary be constant and is usually a function of I or V in organic film.

REFERENCES

(1) M. A. Lampert, *Proc. IRE.* **50**, (1962) 1781.

(2) M. A. Barnett, and A. G. Milnes, *J. Appl. Phys.* **37**, (1966) 4215.

(3) J. Kevorkian, M. M. Labes, D. C. Larson, and D. C. Wu, *Disc. Faraday Soc.* **51**, (1971) 139.

(4) A. Szymanski, D. C. Larson, and M. M. Labes, *Appl. Phys. Letters* **14**, (1969) 88.

(5) H. Carehano, R. LaCoste, and Y. Sequi, *Appl. Phys. Letters* **19**, (1971) 414.

(6) V. I. Stafeev, V. V. Kuznetsova, V. P. Malchanov, S. S. Serov, V. V. Pospelov, E. I. Karakashan, S. B. Airapetyants, and L. S. Gasanov, *Sov. Phys. Semiconductors* **2**, (1968) 642.

(7) A. R. Elsharkawi and K. C. Kao, *J. Phys. Chem Solids*, **38**, (1977) 95.

(8) A. E. Owen and J. M. Robertson, *IEEE transactions on electron devices*, Vol. Ed.-20, (1973) 105.

(9) J. W. Breitenback and C. Srna. *Pure Appl. Chem.* **4**, (1962) 245.

(10) H. Z. Friedlander. Encykl. *Polymer Sci. Technol.* **5**, (1966) 629.

(11) B. L. Funt, *Macromol. Rev.* **1**, (1967) 35.

(12) W. P. Ballard, J. *Non-Crystalline Solids* **17**, (1975) 81.

(13) M. E. Wacks and V. H. Dibeler, *J. Chem. Phys.*, **31**, (1959) 1557.

(14) A. Streitwiser, Jr., *Molecular orbital theory*, John Wiley & Sons, Inc., New York, (1962) 191.

(15) S. H. Sie, M. P. Dugan and S. C. Moss, J. Non-Cryst. *Solids 8-10*, (1972) 877.

(16) I. L. Spain, A. R. Ubbelohde and D. A. Young, Phil. Trans Roy. Soc. (London), **A262**, (1967) 1128.

(17) C. Chiang, Appl. Phys. Lett. **31**, (1977) 553.

(18) J. P. DeNeufville, S. C. Moss and S. R. Ovshinsky, J. Non-Cryst. Solids, **13**, (1973) 191.

(19) S. A. Solin, Bull. Am. Phys. Soc., Ser. II, 19 (1974) 212.

ON THE GATING CURRENTS AND THE DIPOLE TRANSITIONS*

CHUN CHIANG (蔣 忻 儒)

Institute of Physics, Academia Sinica
Nankang, Taipei, Taiwan, The Republic of China

Abstract

Gating current is considered to be due to the transitions of dipoles, which are coupled with the membrane matrix. Based on previous theory of nerve excitation, the equation for gating current is derived; the charge displacement equation and the time constant of the gating current are also derived. Agreement with experimental data is good.

INTRODUCTION

Hodgkin and Huxley (1952) predicted about 20 years ago that there should be a gating current associated with opening and closing of the gates through which the Na ions can pass. However, only recently it has been discovered experimentally by Armstrong and Bezanilla (1973, 1974, 1975, 1977), Bezanilla and Armstrong (1975), Rojas and Keynes (1975), Meves (1974), Nonner et al (1975), Keynes (1975), Keynes and Rojas (1974, 1976). They show convincingly that the current observed was the gating current.

Recently, Wei (1969, 1971, 1972), Lee and Chiang (1976), Hodsen and Wei (1976) promoted the dipole theory to explain nerve excitation; Chiang (1978) further derives the nerve action potential equation and the voltage clamp equation utilizing the idea of dipole-phonon interaction and Newton's law of motion. The derived equations agree with the experiments very well. The dipole transition in that theory should give rise to the "gating current". The purpose of this article is to derive the equation for this gating current based on the previous Chiangs' theory of nerve excitation (1978) and to make some comparisons with the experimental data.

THE GATING CURRENT EQUATION

We assume that dipoles may be excited by the phonons from state I, which has population N_1 with energy E_1, to state II, which has population N_2 with energy E_2; and dipoles in state II may also transit to state I with emission of photons, which may be absorbed by the membrane matrix, thereby producing phonons. The rate equation may be written as follows (Chiang, 1978):

* To be published in Bull. Math. Biol.

$$\frac{dN_1}{dt} = -\omega_{12}N_1 + \omega_{21}N_2 - b(P - P_0) \quad (1)$$

$$\frac{dN_2}{dt} = \omega_{12}N_1 - \omega_{21}N_2 + b(P - P_0) \quad (2)$$

$$\frac{dP}{dt} = \beta\frac{dN_1}{dt} - b'(P - P_0) \quad (3)$$

where ω_{12} or ω_{21} is respectively the rate constant for the dipole to jump from state I to state II or vice versa, P is the number of phonons at a given time, P_0 is the number of phonons in equilibrium, b and b′ are constant, and β is the percentage of photons, emitted due to transition of dipoles from state II to state I, which will be absorbed to produce phonons. β will be positive if $E_2 > E_1$ and negative if $E_2 < E_1$.

Let $N_1 - N_2 = \Delta N$, $N_1 + N_2 = N$, where N is the total number of dipoles, then ΔN and P may be found from equations (1), (2) and (3) to be

$$\Delta N = C_1 e^{-\lambda_1 t} + C_2 e^{-\lambda_2 t} + \frac{\omega_{21} - \omega_{12}}{\omega_{21} + \omega_{12}} N \quad (4)$$

$$P = -\frac{C_1}{2b}(\lambda_2 - b\beta - b')e^{-\lambda_1 t} - \frac{C_2}{2b}(\lambda_1 - b\beta - b')e^{-\lambda_2 t} + P_0, \quad (5)$$

where

$$\lambda_{1,2} = \tfrac{1}{2}[(\omega_{21} + \omega_{12} + b\beta + b') \pm \sqrt{(\omega_{21} + \omega_{12} + b\beta + b')^2 - 4b'(\omega_{21} + \omega_{12})}] \quad (6)$$

and ω_{12}, ω_{21} may be determined by using the Boltzmann distribution (Lee & Chiang, 1976) to be

$$\omega_{12} = \frac{1}{2\tau}\exp[-(UW - pV)/WKT], \quad \omega_{21} = \frac{1}{2\tau}\exp[(UW - pV)/WKT], \quad (7)$$

where τ the average time for the dipole to jump from one state to the other, $U = (E_2 - E_1)/2$, W is the width of the membrane, V is the voltage difference (inside positive), k is the Boltzmann constant, T is the absolute temperature, and p is the dipole moment.

C_1 and C_2 may be determined by the initial condition $\Delta N(0)$, $P(0)$ to be

$$C_1 = \frac{2b[P(0) - P_0] + (\lambda_1 - b\beta - b')\{\Delta N(0) - N\tanh[(WU - pV)/WKT]\}}{\lambda_1 - \lambda_2} \quad (8)$$

$$C_2 = -\frac{2b[P(0) - P_0] + (\lambda_2 - b\beta - b')\{\Delta N(0) - N\tanh[(WU - pV(/WKT]\}}{\lambda_1 - \lambda_2} \quad (9)$$

Suppose each dipole has g charge; then the gating current I_g may be calculated by using equation (4) to be:

$$I_g = g\frac{d\Delta N}{dt} = -g(\lambda_1 C_1 e^{-\lambda_1 t} + \lambda_2 C_2 e^{-\lambda_2 t}). \quad (10)$$

Suppose the membrane voltage is clamped at V_2 from an initial steady value V_1; with the initial conditions that $P(0)=P_0$ and $\Delta N(0)=N\tanh(WU-pV_1)/WKT$; and substituting equations (8), (9) into equation (10), we have

$$I_g=\frac{-gN}{\lambda_{1,V_2}-\lambda_{2,V_2}}\{\tanh(WU-pV_1)/WKT-\tanh(WU-pV_2)/WKT\}$$
$$\{\lambda_{1,V_2}(\lambda_{1,V_2}-b\beta-b')e^{-\lambda_{1,V_2}t}-\lambda_{2,V_2}(\lambda_{2,V_2}-b\beta-b')e^{-\lambda_{2,V_2}t}\}, \quad (11)$$

where λ_{1,V_2}, λ_{2,V_2} can be seen from equations (6) and (7) to be

$$\lambda_{1,V_2;\ 2,V_2}=\frac{1}{2}\left\{\left[\frac{\cosh(WU-pV_2)/WKT}{\tau}+b\beta+b'\right]\right.$$
$$\left.\pm\sqrt{\left[\frac{\cosh(WU-pV_2)/WKT}{\tau}+b\beta+b'\right]^2-\frac{4b'}{\tau}\cosh(WU-pV_2)/WKT}\right\}. \quad (12)$$

Equation (11) shows that the gating current has two components. However, due to the difficulty of the experiments and the small magnitude of the current, it is not easy to measure and analyze the gating current accurately. Meves (1974) does report that two phases, initial fast phase and a second phase with a 2-3 times larger time constant are often observed. The work of Armstrong & Bezanilla (1975) for squid axons and the work of Nonner, Rojas and Stämpfli (1978) for nodes of Ranvier also indicate that the gating current consists of

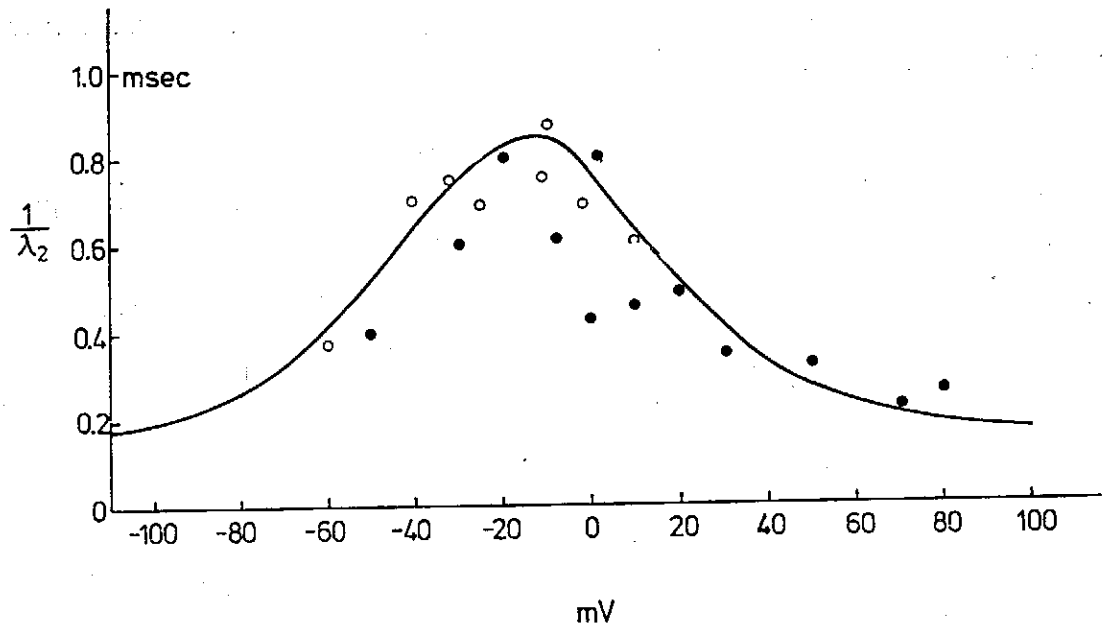

FIG. 1. The time constant of the current calculated according to equation (12)', together with the data of Meves. The open circles represent the measurements at holding potential of -102 mV, and the filled circles represent the measurements at holding potential of -88 mV.

two components. Goldman and Hahin (1978) established firmly that three time constants are observed in the sodium tail current. In terms of Chiang's equation of the sodium current (1978), the time course of the sodium current should consist of three time constants, namely $1/\lambda_1$, $1/\lambda_2$ for the gating current and one additional time constant, for the drag force. The experimentai data seem to agree satisfactorily with the prediction of the theory.

THE DEPENDENCE OF THE TIME CONSTANT ON VOLTAGE

The time constant $1/\lambda$ of the gating current can be calculated from equation (12) to be

$$\frac{1}{\lambda_{1,2}}=\frac{1}{2b'}\{1+\tau(b\beta+b')\mathrm{sech}(WU-PV)/WKT$$

$$\pm\sqrt{[1+\tau(b\beta+b')\mathrm{sech}(WU-PV)/WKT]^2-4b'\tau\,\mathrm{sech}(WU-PV)/WKT}\}. \quad (12)'$$

With $\tau=0.7$ msec, $\beta=0.3$, $b'=6$, $b=3$, $1/\lambda_2$ is plotted in Fig. 1 and shown to agree with experimental data (Meves, 1974). Keynes and Rojas (1974) apply the idea of a voltage-dependent Boltzmann distribution of charges between two states and derive the relaxation time constant of the distribution. As remarked by them, their equation predicts that the time constant would decay to zero as the absolute magnitude of the voltage becomes very large; however, the experimental finding is that the time constant approaches a constant value as the absolute magnitude of the voltage becomes large. Thus the present theory shows a better agreement with the data.

CHARGE DISPLACEMENT

The total charge movement Q associated with a change from voltage V_1 to voltage V_2 may be obtained by integrating equation (11):

$$Q=\int_0^{T'} I_g\,dt=-gN\{\tanh(WU-pV_1)/WKT-\tanh(WU-pV_2)/WKT\}$$

$$\left\{\frac{(\lambda_{1,V_2}-b\beta-b')e^{-\lambda_1 T'}}{\lambda_{1,V_2}-\lambda_{2,V_2}}-\frac{(\lambda_{2,V_2}-b\beta-b')e^{-\lambda_2 T'}}{\lambda_{1,V_2}-\lambda_{2,V_2}}-1\right\}. \quad (13)$$

It T' is large, then

$$Q=gN\{\tanh(WU-pV_1)/WKT-\tanh(WU-pV_2)/WKT\}. \quad (14)$$

The experimental data of charge distribution from various authors are different. If we choose Meves' (1974) data, then $gN=-800$ charges/μm^2, $W=70$ Å, $U=+11$ mev, $p=-50$ eÅ, $T=273$, $V_1=-88$ mV. Equation (14) is plotted in Fig. 2, together with the data of Q_{on} (open circles) and Q_{off} (filled circles); the inflection point is the voltage for which $WU-pV=0$. Any

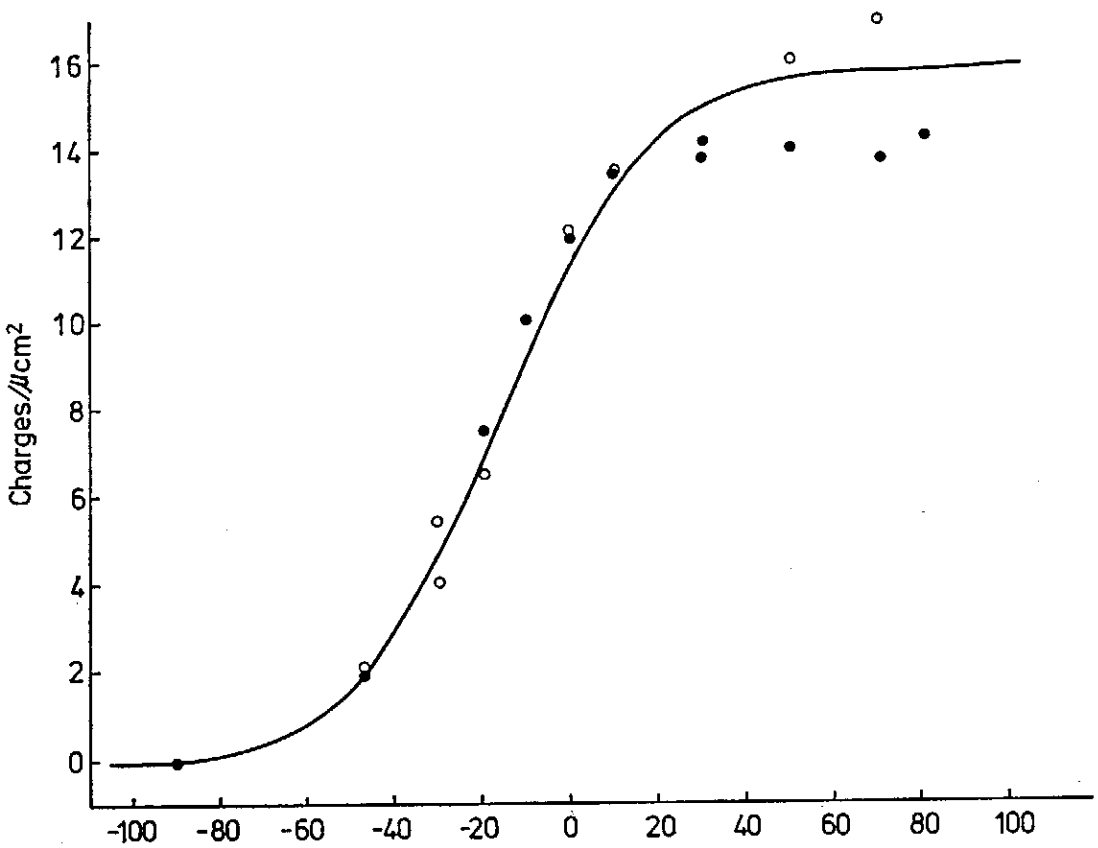

FIG. 2. The charge displacement calculated according to equation (14) together with data of Meves. The open circles are for the on-reponse and the filled circles are for the off-response.

chemicals such as Ca^{++}, which may affect U or p, will shift the inflection point of the charge displacement curve or the point for maximum value of the time constant τ in Fig. 1. Thus this theory can be tested by investigating the effect of Ca^{++} on the membrane dipoles. Indeed, Keynes & Rojas (1974) have found that the Ca^{++} concentration can reversibly shift the maximum point of τ without changing its absolute magnitude.

In the experiments of Meves (1974) and Meves & Vogel (1977), $T'=3$ msec. This is quite large compared with the value of the time constants; thus equation (14) is compatible with his experimental conditions. Bezanilla and Armstrong (1975) report that the ratio of Q_{off} to Q_{on} approaches unity for short pulses, but decreases for long pulses. Their short pulse for T' is also relatively large compared with the time constant; thus, Q_{off}/Q_{on} should be approximately equal to unity in agreement with equation (14). For long pulses, Q_{off}/Q_{on} deviates from unity and decreases to about one-third (Armstrong & Bezanilla, 1977); thus, equation (14) alone cannot explain this decrease and

some additional mechanism must be operative here. Armstrong & Bezanilla (1977) suggest that part of the charge has been immobilized in the case of long pulses, therefore Q_{off}/Q_{on} is less than unity.

DISCUSSION

In trying to understand the behavior of gating current, Keynes and Rojas (1974, 1976) propose the "two state model", which asserts that the gating current originates from the charge distribution between two states. Neumcke, Nonner and Stämpfli (1976) find that this "two-state model" can not account for their experimental findings, such as the voltage-dependent delay of sodium current, and suggest a multiple transition of gating particles before and after the opening of sodium channels. Meves (1974), Nonner, Nuemcke and Stämpfli (1977), Keynes & Kimura (1977) also propose various forms of multi-state models to account for the gating current. Also, for the behavior of sodium current there are many multi-state coupled kinetic models (see the review of Goldman 1976). However, none of those models has given sufficient detail of the molecular process involved in the gating process and agreement with experiments is only moderate.

The present calculation of gating current has been derived from Chiang's theory of nerve excitation and sodium activation. The calculated charge displacement and time constants agree satisfactorily with the experimental data. However, Meves (1974), Keynes and Rojas (1976) found that the off-time constant depends on the depolarizing pulse. Neither the multi-state model nor the present model can account for this dependence. However, a closer inspection of the data (Fig. 2 of Keynes and Rojas 1976) reveals that the off-gating current may consist of two components with two fixed time constants with varying weighting factors, instead of one component with varying time constant. This interpretation is strengthencd by the finding from other workers (Armstrong & Bezanilla, 1975; Nonner, Rojas & Stämpfli, 1978) that the gating current indeed consists of two components. Recently, Goldman and Hahin (1978) reported that there are three time constants in the sodium tial current which do not vary with the initial conditions. This finding also strengthens the above interpretation of two components in off-gating current. In terms of Chiangs' (1978) theory, the sodium current consists of three components, two of which have the same time constants, $1/\lambda_1$ and $1/\lambda_2$, as that for the gating current. Since the weighting factor of the component depends on the experimental conditions, one component may be too small to be detected. Thus in comparing the time constant of the sodium current and the gating current, if the same time constant $1/\lambda_1$ or $1/\lambda_2$ is found in both cases, then of course the ratio of

the time constant for the sodium current to that for the gating current is unity; if different time constants are found, for example $1/\lambda_1$ for the sodium current and $1/\lambda_2$ for the gating current, then the ratio of the time constants is different from unity. This may explain why the ratio of the time constant for sodium tail current to that for the off-gating current is unity in some instances (Bezanilla & Armstrong, 1975; Keynes & Rojas, 1974), and is different from unity in others (Keynes & Rojas, 1976).

In summary, the calculation of the charge displacement and the time constant of the gating current from the previous theory of nerve excitation agrees satisfactorily with the experimental data. The possible reason for the discrepency of experimental data from different authors is suggested. It is hoped that this theory may stimulate new designs of experiments in this field.

The author is grateful to the reviewer for many helpful comments and for his efforts to improve this manuscript.

REFERENCES

Armstrong, C. M. and F. Bezanilla. 1973. "Currents related to the movement of the gating particles of the sodium channels". *Nature* (London.) **242**, 459-461.

Armstrong, C. M. and F. Bezanilla. 1974. "Charge movement associated with the opening and closing of the activation gates of the Na channels". *J. Gen. Physiol.* **63**, 533-552.

Armstrong, C. M. and F. Bezanilla. 1975. "Currents associated with the ionic gating structures in nerve membrane. Ann. N.Y. Acad. Sci. **264**, 265-277.

Armstrong, C. M. and F. Bezanilla. 1977. "Inactivation of the sodium channel, II. Gating current experiments." J. Gen. Physiol. **70, 567-590.**

Bezanilla, F. and Armstrong, C. M. 1974. "Gating currents of the Sodium channels: three ways to block them". Science (Wash. D.C.) **183, 753-754.**

Bezanilla, F. and Armstrong, C. M. 1975. "Kinetic properties and inactivation of the gating currents of the sodium channels in squid axon. Phil. Trans. R. Soc. B**270**, 449.

Bezanilla, F. and Armstrong, C. M. 1975. "Inactivation of gating charge movement". Biophys. J. **15**, 163 a.

Chiang, C. 1978. "On the nerve impulse equation: the dynamic responses of nerve impulse". Bull. Math. Biol. **40, 247-255.**

Goldman, L. 1976. "Kinetics of channel gating in excitable membranes". Q. Rev. Biophys. **9, 491-526.**

Goldman, L. and R. Hahin. 1978. "Sodium tail currents in Myxicola". Biophys. J. **21,** 41 a.

Hodgkin, A. L. and A. F. Huxley, 1952. "A quantitative description of membrane current and its application and exitation in nerve". J. Physiol. (Lond.). **117**, 500-544.

Hodson, H. and Wei, L. Y. 1976. "Comparative evaluation of quantum theory nerve excitation". Bull. Math. Biol. **38**, 277-293.

Keynes, R. D. 1975. "Organization of the ionic channels in nerve membranes." In *The Nervous System, Vol. 1: Basic Neurosciences,* Ed.: D. B. Tower, Raven Press, New York.

Keynes, R. D. & Rojas, E. 1974. "Kinetics and steady-state properties of the charged system controlling conductance in the squid giant axon". J. Physiol. **239, 393-434.**

Keynes, R. D. & Rojas, E. 1976. "The temporal and steady-state relationships between activation of the sodium conductance and movement of the gating particles in the squid giant axon." J. Physiol **255**, 157-189.

Keynes, R. D. and Kimura, J. E. 1977. "Opening and closing ionic channels in nerve". Int. Congress. Paris, P. 194.

Lee, C. Y. and Chiang, C. 1976. "Nerve excitation by the coupling of dipoles and membrane matrix", Bull. Math. Biol. **38**, 59-70.

Meves, H. 1974. "The effect of holding potential on the asymmetry currents in squid axons". J. Physiol **243**, 847-867.

Meves, H. and Vogel, W. 1977. "Inactivation of the asymmetrical displacement current in giant axons of Loligo Forbesi." J. Physiol. **267**, 377-393.

Neumcke, B., Nonner, W. and Stämpfli, R. 1976. "Asymmetrical displacement current and its relation with the cativation of sodium current in the membrane of frog myelinated nerve". Pflügers Arch. **363**, 193-203.

Nonner, W., Rojas, E. and Stämpfli, R. 1975. "Displacement currents in the node of Ranvier", Pflügers Arch. **354**, 1-18.

Nonner, Rojas & Stämpfli, 1978. "Asymmetrical displacement currents in the membrane of frog myelinated nerve: early time couse and effects of membrane potential". Pflügers Arch. **375**, 75-85.

Nonner, W., Neumcke, B. and Stämpfli, R. 1977. "Gating current and activation of Na current in myelinated nerve". Inst. Congress. Paris. pp. 197.

Rojas, E. and Keynes, R. D. 1975. "On the relation between displacement currents and activation of the sodium conductance in the squid giant axon". Phil. Trans. R. Soc. Lond B. **270**, 459-482.

Wei, L. Y. 1969. "Molecular mechanisms of nerve excitation and conduction." Bull. Meth. Biophys., **31**, 39-58.

_____, 1971. "Possible origin of action potential and birefringence change in nerve axon." Ibid., **33**, 521-537.

_____, 1972. "Dipole theory of heat production and absorption in nerve axon." Biophys. J., **12**, 1159-1170.

PYRUVATE METABOLISM IN DORSAL ROOT GANGLIA OF CHICKEN EMBRYO

YUAN-YANG LAI

Department of Science and Mathematics Education
Taiwan Provincial College of Education

WEI-KUNG WANG (王 唯 工)

Biophysics Laboratory, Institute of Physics
Academia Sinica, Taipei, Taiwan, R.O.C.

Abstract

Dorsal root ganglia of chich were incubated in McCoy 5A medium with (1-^{14}C) pyruvate. $^{14}CO_2$ output were measured continuously. When 100 $\mu\ell$ of incubation medium were used and glucose depletion were not significant, $^{14}CO_2$ output as a function of incubation time had a monotonic decreasing curve. When 20 $\mu\ell$ of incubation medium were used, the $^{14}CO_2$ output had a much faster decrease followed by a slow increase. This suggested pyruvate may be used in different pathways to produce $^{14}CO_2$ depended on the environment condition.

Preliminary chromatography data of the tissue after incubation also indicated that when 20 $\mu\ell$ of incubation medium were used to incubate 14 days ganglia, more peaks were found and the quantity were also much larger than that incubated in 100 $\mu\ell$ of incubaton medium. For 10 days ganglia, the volumn of incubation medium did not have such significant effect, all showed simpler peaks with smaller quantity. These results were consistant with the conclusion that more carbon might be recycled in pentose cycle in 14 day's ganglia.

INTRODUCTION

Glucose is the most essential energy source in nervous system. Metabolism of glucoae has two different pathways in animal, the glycolysis and pentose phosphate shunt (also known as hexose monophosphate pathway or pentose cycle).

The traditional way to distinguish the two pathways is to measure the $^{14}CO_2$ or ^{14}C-lactate from different lobelled glucose.

A model using the time course of liberated $^{14}CO_2$ was first introduced by Wang[1] and later refined by Larrabee[2]. In the refinement of Larrabee's model, he used the data of smaller volume of incubation medium and claim the discovery of changing recycle coefficient according to the volumn of incubation medium.

Here, we use (1-^{14}C) pyruvate as the precusor to measure the $^{14}CO_2$ output as a function of incubation time as well as the volumn of incubation medium. It is found that when the volumn of incubation medium was not

enough to keep the concentration of glucose, pyruvate would be used by different pathway, supposely the reverse of glycolysis, therefore, the assumption of uniform metabolic rate by Wang is not held, and the equation derived according to such assumption can not be used.

The intermediate found in the tissue of 14 day's ganglia also suggested that the pentose cycle were activated during the age of 10 to 14 day's of age.

MATERIALS AND METHODS

Fertile eggs were obtained from nearby farm, a few eggs were put into the incubator every day. Age was defined as the number of days of incubation at 37°C, usually it takes 21 day's for an egg to hatch.

Ringer's solution was prepared with 8.39 g of NaCl, 0.44 g of KCl and 1.26 mℓ of 2 molar $CaCl_2$ made up to 1 liter with distilled water, McCoy's 5A modified medium and antibiotic-antimyotic solution (100 x; 1,000 unit/mℓ penicillin, 10,000 mcg/mℓ streptomycin and 25 mcg/mℓ fungizone) were obtained from Grand Island Biological CO., Grand Island, N. Y., Labelled pyruvate was obtained from New England Nuclear, Boston, Massachusetts.

Whatman, No. 1 filter paper was used for paper chromatography. The developing solution was prepared with methanol: formic acid: water = 80 : 15 : 5 (v/v).

10 day's and 14 day's chicken embryo were put into the petri dishes, a forceps were used to open the abdomen then pinched out the spinal nerves; cut the spinal column and transferred the spinal column into another petri dish which contained some cold Ringer's solution. The dorsal root ganglia were removed from this part of spinal column (25-29). After the ganglia were picked out, the surrounding membrane and associated sciatic nerve were cut as close to the ganglion as possible.

The prepared ganglia were incubated for 24 hrs at 37°C in two different volume of incubation medium. One is containning 100 μℓ of McCoy's 5A modified medium and 1 μCi of 1-^{14}C pyruvate, another is containning 20 μℓ of McCoy's 5A modified medium and 0.2 μCi 1-^{14}C pyruvate. During the incubation, the 95% O_2—5% CO_2 gas were flow over a large volume (5 mℓ) of bath medium before being passed over incubation solution. The flow rate of the carrier gas was set to about 1 mℓ/min. Labelled CO_2 was counted continuously with low background α and β counting system from Canberra Industries, Meriden, Connecticut.

RESULTS

From Fig. 1 it was found that for a large incubation volumn the $^{14}CO_2$ output from $(1-^{14}C)$ pyruvate reached maximum in about 80 minutes than slowly reduced. However for small incubation volumn there are some fine structure for this $^{14}CO_2$ output, it reduced slowly at beginning, then the reduction rate are suddenly enhanced, for a short time the $^{14}CO_2$ output reach a minimum then it increased slowly. The rate of increase for 14 day's ganglia are higher than that of 10 day's ganglia.

The paper chromatograph results are more interesting, because we detected only that labelled compound that was from $(1-^{14}C)$ pyruvate. There were only one continuous peak for 10 day's ganglia besides the origin, no matter it was incubated in 100 $\mu\ell$ medium or 20 $\mu\ell$ medium (Fig. 3A). However there are at least 3 important peaks for 14 day's ganglia incubated 100 $\mu\ell$ medium (Fig. 3C). For 14 day's ganglia incubated in 20 $\mu\ell$ medium (Fig. 3B), there were even more peaks and the magnitute was also significantly higher than that shown in Fig. 3C.

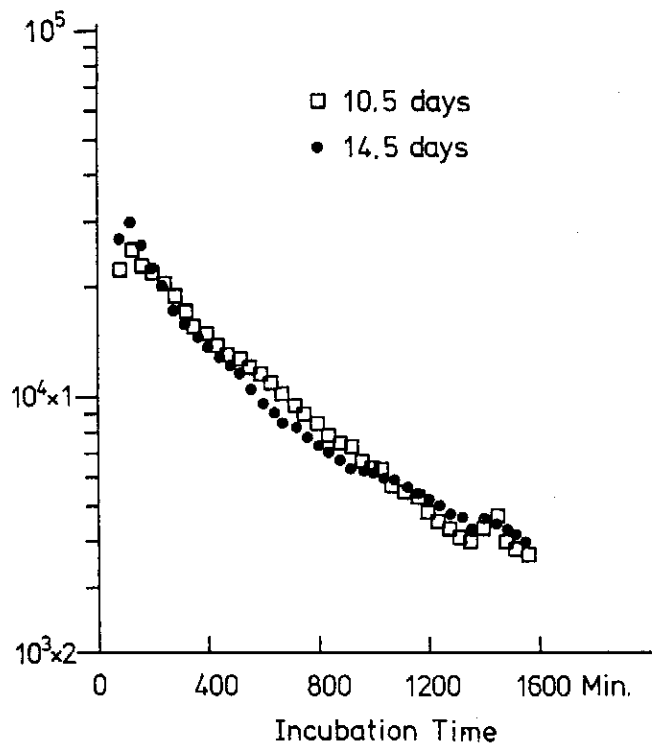

FIG. 1. Output of labelled $^{14}CO_2$ from dorsal root ganglia (25-29) in the presence of $(1-^{14}C)$ pyruvate. Incubation medium was 100 $\mu\ell$. The amount of released $^{14}CO_2$ are presented as counts/40 minutes.

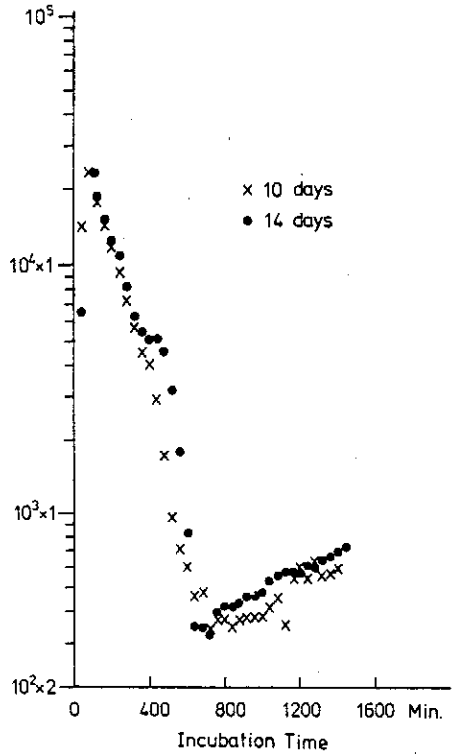

FIG. 2. Output of labelled $^{14}CO_2$ from dorsal root ganglia (25-29) in the presence of $(1-^{14}C)$ pyruvate. Incubation medium was 20 $\mu\ell$. The amount of released $^{14}CO_2$ are presented as counts/40 minutes.

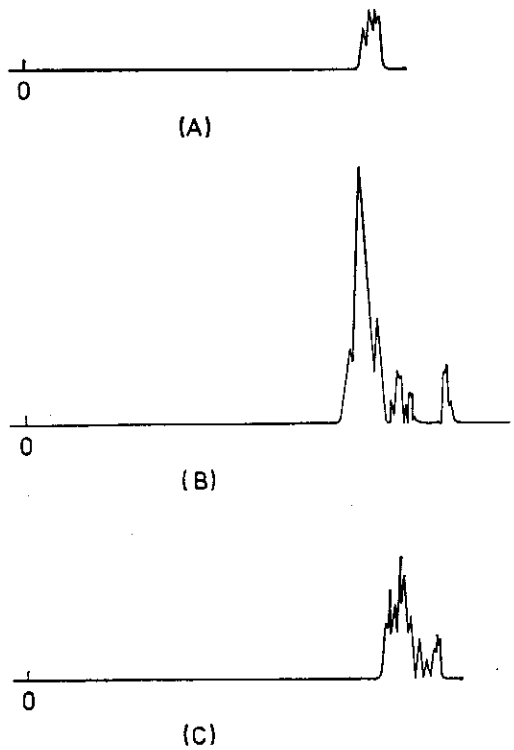

FIG. 3. Paper chromatagraphy of labelled compound from dorsal root ganglia after incubation
0: represent origin.
(a) 10 day's old chicken embryo
(b) 14 day's old chicken embryos incubated in 20 $\mu\ell$ of medium.
(c) 14 day's old chicken embryos incubated in 100 $\mu\ell$ of medium.

DISCUSSION

For $(1-{}^{14}C)$ pyruvate to produce $^{14}CO_2$, there are two major pathways

(1) $(1-{}^{14}C)$ pyruvate $\rightarrow$ Acetyl CoA $+ {}^{14}CO_2$

(2) Reverse the pathway of glycolysis to generate some hexose, these hexose may go through Hexose-Monophosphate shunt or pentose cycle to produce $^{14}CO_2$.

The advantage to use $(1-{}^{14}C)$ pyruvate is that the ^{14}C will liberated as $^{14}CO^2$ at the time that pyruvate was converted to acetyl-CoA and the possibility of the incorporation of ^{14}C into TCA cycle or lipid are reduced to minimum. The ^{14}C in the tissue will be greatly reduced and the peaks we found in paper chromatagraph will mainly be intermediates in glycolysis and pentose cycle.

Glycolysis is a reversible reaction, it is suggested that three enzymes, pyruvate carboxylase, phosphopyruvate carboxylase, and fructose 1.6 diphosphatase are needed for gluconeogensis[1]; Pentose cycle may be a cycle[4] or a reversible shunt[2] too.

In our result, labelled $^{14}CO_2$ output from $(1-{}^{14}C)$ pyruvate are mainly from the pathway 1, because of the fast on-set and the large quantity.

For large volumn of incubation medium, the glucose concentration will be kept within 90%[4], the $^{14}CO_2$ were mainly from pathway 1, and therefore the $^{14}CO_2$ output has a monotonic decreasing curve, however, when the volumn of incubation medium was reduced to 20 $\mu\ell$, the depletion of glucose would be about 50% in 7 hours incubation. The $^{14}CO_2$ output reduced suddenly and decrease to a very low level, the interesting point is that the $^{14}CO_2$ output gradually increased again after reach this minimum. Since the ^{14}C are from pyruvate, this increase are probably due to the pathway (2). The reverse of the glycolysis, the increase of liberated $^{14}CO^2$ were most possibly through pentose cycle.

Larrabee pointed out that the recycle in pentose cycle are more complete when the volumn of incubation medium was small. While the efficiency of recycling is down to 60% while the volumn of incubation was large. According to pressented results, the apparent higher recycle coefficient found by Larrabee was probably due to glucogenesis instead of recycle. When incubated in small volumn of incubation medium, the glucose depletion was significant and the lactate produced at the beginning of incubation might reverse the glycolysis and produce glucose. More information might be find in the chromatograph data. According to figure 3(A) there were not many labelled intermediates of large quantity in the ganglia at 10 day's of age. However, at 14 day's of age, the number of labelled intermediates increased and the quantity also became much higher, especially when the incubation medium were small and the glucogenesis were more active. A few large new peaks found in 14 day's of ganglia are missing from that of 10 day's. These new peaks may be related to the intermediates in pentose cycle which Wang[4] had found to be more active at 14 day's ganglia. More detailed chromatagraphy data will be needed to prove this.

DEFERENCES

(1) Quadflieg, K. H., and Brand, K., *Time-dependent partition of glucose carbons metabolized by the superior cervical gnaglion from calves J. Neurochem.* **31**, 211-215, 1978.

(2) Krebs, H. A., and Woodford, M., *Fructose 1.6-diphosphatose in striate muscle.* J. Biochem. **94**, 436, 1965.

(3) Larrabee, M. G., *A new mathematics approach to the metabolism of* [^{41}C] *glucose. with application to sensory ganglia of chicken embruos.* J. Neurochem. **31**, 461-491, 1978.

(4) Wang, W. K., *Glucose metabolism in developing nervous system. Ph.D. thesis, Johns Hopkins University,* 1973.

DIFFUSION OF PLANE TURBULENT BUOYANT JETS IN DENSITY - STRATIFIED AMBIENT FLUID*

ROBERT R. HWANG (黃榮樾) and C. S. FU (傅志申)

Institute of Physics
Academia Sinica
Taipei, Taiwan, ROC.

Abstract

In this study initial diffusion of a plane turbulent buoyant jet discharged into a linearly density-stratified environment was investigated theoretically and experimentally. An integral approach using a variable entrainment coefficient deduced from the incorporation of the mass conservation into the kinetic energy conservation works to predict the gross features of a vertical buoyant jet numerically.

In the laboratory experiment, a filling salt solution process was designed to generate a linearly density-stratified environment. Variations of velocity and density defect across the jet as well as along the axial centerline were measured and analyzed. Spreading ratio obtained from the experimental measurements was between 1.10 and 1.40. It was adopted as 1.30 in proceeding the numerical calculations. It is found that the comparisons between the numerical calculation and the laboratory experiment were favorable.

INTRODUCTION

Disposals of sewage and heated water into the ocean and estuaries have been practiced by many coastal cities around the world. In the design of submarine outfalls, the engineer is faced with the problem of determining the dilution necessary to meet disposal objectives. A fundamental problem of ocean disposal is then to know the dilution of effluent in the vicinity of the outfall. A typical outfall diffusion structure contains many discharge ports on the pipe to release power-plant discharges and treated municipal and industrial waste into ocean. It has renewed interest in two-dimensional buoyant jets. The buoyant jet formed when the individual jets of a multiport diffuser merge is a good approximation to a plane jet. It also noted that during the summer months the sun often heats the surface waters of the ocean causing a temperature gradient which results in a density gradient. Hence an understanding of the mechanism and mixing processes of such a jet in a density-stratified ambient is necessary to permit optimal design of such diffusers.

Initial diffusion of a vertical buoyant jet into the environment has been studied previously by several investigators (for a review see Koh and Brooks 1975), each of them adopting a different approach. One of the early attempts to understand the influence of density variation in plumes was the work of Rouse, Yih and Humphreys (1952) who studied experimentally both plane and

* Also presented at 2nd Conf. on Theo. Appl. Mechanics held at Tainan, Taiwan, R.O.C., Dec. 16-17, 1978

round vertical plumes in uniform surroundings. Morton, Taylor and Turner (1957) analized the plume flow using integral forms of the equations governing the mean quantities and, to close the problem, they intorudced a constant coefficient for the entrainment of fluid into the plume. Other subsequent studies based on the entrainment concept were carried out by many researchers. Using a universal constant of entrainment coefficient obtaided from experimental results of laboratory experiments on simple plumes (Rouse, Yih and Humpheys 1952), Fan ann Brooks (1969) analyzed the trajectory, widths, and dilution ratios of turbulent buoyant jets discharged into a uniform or density-stratified environment. Fox (1970) deduced the form of entrainment in a variable coefficient on the basis of incorporating the conversation equation for the kinetic energy. Abraham (1963) replaced the entrainment assumption by essentially assuming a rate of spread of the jet. List and Imberger (1973) and Kotsovinos & List (1977), through dimensional reasoning, and experimental results deduced that the entrainment coefficient must be a linear function of the local Froude number in the case of a vertical buoyant jet for both round jet and plane jet in a uniform density environment. Although the study on a turbulent buoyant jet into a uniform ambient fluid is numerous, the study on the diffusion of a buoyant jet into stratified fluids, for example a vertical buoyant jet into a linearly density-statified fluid, seems to be relatively unexplored.

In this study, initial diffusion of a plane turbulent buoyant jet discharged into a linearly density-stratified environment was investigated theoretically and experimentally. An integral approach using a variable entrainment coefficient deduced from the incorporation of the mass conservation into the kinetic energy conservation works to predict the gross features of a vertical buoyant jet such as the axial variation of centreline velocity as well as the density defect in linearly stable density stratified environment. These results are compared with laboratory experiments to verify the basic ideas.

FORMULATION OF THE PROBLEM

The flows induced by vertical turbulent line jets with varying levels of buoyancy flux discharged into linearly density stratified ambient were studied and shown in figure 1. The fluids are assumed to be incompressible and the ambient fluid to be stably linear stratification in density and to have only motion induced by the jet itself. A flow geometry is chosen in which an x, y co-ordinate system is oriented with the x axis vertically upwards and coincident with the jet axis. Fluid local mean velocities in the x and y directions are denoted by $\bar{u}(x, y)$ and $\bar{v}(x, y)$ respectively. It is further assumed that the flow is fully turbulent and that the viscous and molecular transport of momentum

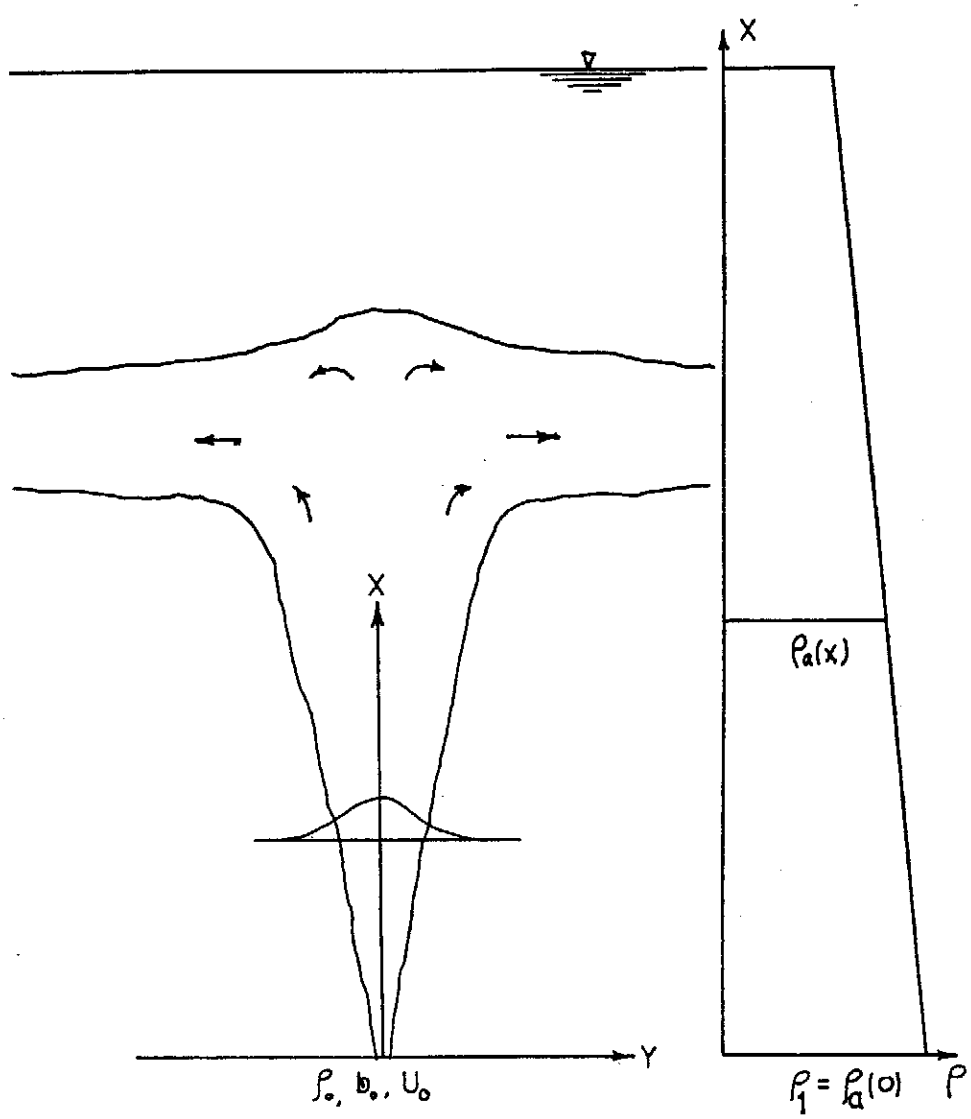

FIG 1. Vertical jet discharged into a linearly density-stratified environment.

and tracer respectively can be neglected relative to the turbulent transport. With these definitions and assumptions the time-averaged equations for two-dimensional incompressible motion of a turbulent fiow with small density variations are obtained:

$$\frac{\partial \bar{u}}{\partial x} + \frac{\partial \bar{v}}{\partial y} = 0 \qquad (1)$$

$$\bar{u}\frac{\partial \bar{u}}{\partial x} + \bar{v}\frac{\partial \bar{u}}{\partial y} = -\frac{1}{\bar{\rho}}\frac{\partial p}{\partial x} + \frac{\rho_a - \bar{\rho}}{\bar{\rho}}g - \frac{\partial \overline{u'^2}}{\partial x^2} - \frac{\partial \overline{u'v'}}{\partial y} \qquad (2)$$

$$\bar{u}\frac{\partial(\rho_1 - \bar{\rho})}{\partial x} + \bar{v}\frac{\partial(\rho_1 - \bar{\rho})}{\partial y} = \frac{\partial \overline{u'\rho'}}{\partial x} + \frac{\partial \overline{v'\rho'}}{\partial y} \qquad (3)$$

Here u', v' and ρ' are the deviations in velocity and density from the time-averaged mean values, ρ_1 is the reference density chosen as the ambient density at the plane jet orifice, $\bar{p}$ the pressure difference from the hydrostatic ambient pressuae, g is the gravitational acceleration. The difference between the time-averaged local fluid density at any point $\bar{\rho}(x, y)$ and the ambient density at the orifice ρ_1 is small, so that there is little error in using the ambient density at the orifice ρ_1 to replace the local density $\rho(x, y)$ in the description of the inertia force. With the usual boundary layer approximation, it is known that the gradients of turbulent transports in the axial direction are small in compare with that in its normal direction. It is also assumed that the turbulent flux of tracer is much less than the advective flux (Corrsin & Uberoi 1950). With these assumptions, equations (2) and (3) can be reduced to

$$\bar{u}\frac{\partial \bar{u}}{\partial x}+v\frac{\partial \bar{u}}{\partial y}=\frac{\rho_a-\bar{\rho}}{\rho_1}g+\frac{1}{\rho_1}\frac{\partial \overline{\rho u'v'}}{\partial y} \tag{4}$$

$$\frac{\partial}{\partial x}(\bar{u}(\rho_1-\bar{\rho}))+\frac{\partial}{\partial y}(\bar{v}(\rho_1-\bar{\rho}))=0 \tag{5}$$

Integration of equations (1), (4) and (5) over the whole jet cross-section yields the following integral equations:

$$d\mu(x)/dx=-2\bar{v}(x,\ b(x)) \tag{6}$$

$$dm(x)/dx=\int_{-b(x)}^{b(x)} g\ \frac{\rho_a-\bar{\rho}}{\rho_1}dy \tag{7}$$

$$d\beta(x)/dx=0 \tag{8}$$

where $$\mu(x)=\int_{-b(x)}^{b(x)}\bar{u}(x, y)\ dy,\ m(x)=\int_{-b(x)}^{b(x)}\bar{u}^2(x, y)\ dy,$$

$$\beta(x)=\int_{-b(x)}^{b(x)}\bar{u}(x, y)\ (\rho_1-\bar{\rho}\ (x, y))\ dy$$

are the fluxes of specific mass, momentum and buoyancy respectively.

The preceding equations define the rate of change of the integral properties of jet. The actual distributions of velocity and density across the jet are unknown since they are the solutions of the full equations of motion while it is not known precisely how the Reynolds stresses are related to the mean motion of the fluid. To close the problem, previous investigators (Morton et al (1956), Fan & Brooks (1969) etc.) have made about the entrainment of ambient fluid into the turbulent buoyant jet and assumed that the entrainment velocity was directly proportional to the velocity on the axis of jet. That is

$$\lim_{b(x)\to\infty}-2\bar{v}\ (x, b(x))=2\alpha\bar{U}_m(x) \tag{9}$$

here α is the entrainment coefficient. Based on the experimental evidence, it is further assumed that lateral distributions of axial velocity and density deficiency with respect to the ambient density to be Gaussian. Conventient distributions are

$$\bar{u}(x, y) = \bar{U}_m(x) \exp(-y^2/b_u^2) \tag{10}$$

$$\rho_a(x) - \bar{\rho}(x, y) = (\rho_a(x) - \bar{\rho}_m(x)) \exp(-y^2/b_d^2) \tag{11}$$

where b_u and b_d are the characteristic lengths of the velocity and density deficiency profiles respectively and $\bar{U}_m(x) = \bar{u}(x, 0)$, $\rho_m(x) = \bar{\rho}(x, 0)$. It is also assumed that $b_d(x)/b_u(x) = \lambda$, is a universal constant.

Under these assumptions and taking b(x) to infinite the system of equations (5)-(7) becomes

$$d(\bar{U}_m b_u)/dx = \frac{2}{\sqrt{\pi}} \alpha \bar{U}_m \tag{12}$$

$$d(\bar{U}_m^2 b_u)/dx = \sqrt{2}\, g\, \alpha\, b_u(\rho_a - \bar{\rho}_m) \tag{13}$$

$$d[\bar{U}_m b_u(\rho_a - \bar{\rho}_m)]/dx = \frac{\sqrt{1+\lambda^2}}{\sqrt{\lambda^2}} b_u \bar{U}_m \frac{d\rho_a}{dx} \tag{14}$$

Equations (12)-(14) are tnen the governing equations for a plane turbulent buoyant jet flow through a stagnant, stably linear density-stratified ambient.

In view of the above approach, a very important parameter using the entrainment concept in the analysis of buoyant jet is the entrainment coefficient. Many investigators have shown that there is no unique entrainment coefficient for turbulent buoyant jets. The expression for the entrainment coefficient derived in this study is similar to the analysis of Fox. With multiplication of each term of Eq. (4) by $\bar{u}$ and integration in both sides over the whole jet cross-section yields the following form of the kinetic energy relationship:

$$de(x)/dx = \int_{-b(x)}^{b(x)} g\bar{u}\left(\frac{\rho_a - \rho(x, y)}{\rho_1}\right) dy - \frac{1}{\rho_1}\int_{-b(x)}^{b(x)} -\rho\,\overline{u'v'}\,\frac{\partial \bar{u}}{\partial y} dy \tag{15}$$

where $e = \frac{1}{2}\int_{-b(x)}^{b(x)} \bar{u}^3\, dy$ is the kinetic energy flux.

The last term of Eq. (15) represents the rate at which energy is lost to the mean motion through the generation of turbulence. With the customary hypothesis of dynamic similarity of the mean (and turbulent) motion at all elevations permits the profiles of Reynolds stresses as well as velocity and density definiency to be considered of the same form for every value of x. It is thus assumed that

$$-\rho\,\overline{u'v'} = \rho_1 \bar{U}_m(x)\, h\,(y/b_u) \tag{16}$$

Substitution of Eq. (16) into Eq. (15), the latter can be rewritten as

$$d(\bar{U}_m^3\, b_u)/dx = \frac{2}{\sqrt{3}} \frac{\lambda}{\sqrt{1+\lambda^2}} g\, b_u\, \bar{U}_m \frac{\rho_a - \rho_m}{\rho_1} + \frac{2\sqrt{3}}{\sqrt{\pi}} \bar{U}_m I \qquad (17)$$

where $$I = \int_{-b(x)}^{b(x)} 2\eta\, e^{-\eta^2} h(\eta)\, d\eta.$$

From the relationship between Eq. (13) and Eq. (17) can obtain:

$$d(\bar{U}_m\, b_u)/dx = 2\left(\frac{\lambda}{\sqrt{2}} - \sqrt{3}\frac{\lambda}{\sqrt{1+\lambda^2}}\right) \frac{g\, b_u(\rho_a - \bar{\rho}_m)}{\rho_1 \bar{U}_m} + \frac{2\sqrt{3}}{\sqrt{\pi}} I\, \bar{U}_m \qquad (18)$$

Comparison of Eq. (18) with Eq. (12) yields

$$\alpha = \alpha_1 + \alpha_2/F_L \qquad (19)$$

herein $F_L = \bar{U}_m^2 \Big/ \frac{g\, b_u(\rho_a - \bar{\rho}_m)}{\rho_1}$, is the local densimetric Froude number along the jet axis, $\alpha_1 = \sqrt{3}\, I$ and $\alpha_2 = \sqrt{\pi}\left(\frac{\lambda}{\sqrt{2}} - \sqrt{3}\, \frac{\lambda}{\sqrt{1+\lambda^2}}\right)$.

In view of the above expression for the entrainment coefficient, the first term α_1 is the integral parameter due to turbulence features while the second term is the integral prameter due to the buoyancy effect. This expression leads to the conclusion that the entrainment function is linearly depend on the inverse of the local jet Froude number thus confirming the results obtained by many researchers.

SNLUTION OF EQUATIONS

Equations (12)-(14) are the governing equations for a two-dimensional slot buoyant jet in a linearly density-stratified ambient fluid with the introduction of α in the form of Eq. (19). In order to transform the system of equations into simple normalized form, dimensionless parameters are defined as follows:

Specific mass flux:

$$Q = \left\{\frac{32\sqrt{2(1+\lambda^2)}\ \alpha_1^2 T_0^4}{\pi\, S^3}\right\}^{-1/3} (\bar{U}_m^2 b_u^2)$$

Momentum flux:

$$M = \{S/[2\sqrt{2(1+\lambda^2)}\ T_0^2]\}\ (\bar{U}_m^2\, b_u)^2 \qquad (21)$$

Buoyancy flux:

$$B = \left(\frac{\sqrt{\lambda^2}}{\sqrt{1+\lambda^2}}/T_0\right)\ g\, \bar{U}_m\, b_u\, (\rho_a - \bar{\rho}_m)/\rho_1 \qquad (22)$$

Coordinate:

$$\xi = \left[\frac{32\sqrt{2(1+\lambda^2)}\alpha_1\, S^3}{\pi\, T_0^2}\right]^{1/6} x \qquad (23)$$

where $S=-\frac{g}{\rho_1} d\rho_a/dx$ and $T_0=\frac{\sqrt{\lambda^2}}{\sqrt{1+\lambda^2}} g b_0 U_0 \frac{\rho_1-\rho_0}{\rho_1}$ are stratified parameter and initial buoyancy parameter respectively which are not dimensionless.

In the substitution of Eqs. (20)-(23) into Eqs. (12)-(14), the system of governing equations then becomes

$$dQ/d\xi=\frac{\sqrt{2}}{\lambda\sqrt{\pi}}\alpha_2\frac{BQ^{3/2}}{M}+M^{\frac{1}{2}} \tag{24}$$

$$dM/\xi=BQ^{\frac{1}{2}} \tag{25}$$

$$dB/d\xi=-Q^{\frac{1}{2}} \tag{26}$$

The corresponding initial conditions are

$$Q(0)=Q_0,\quad M(0)=M_0,\quad \text{and}\quad B(0)=1\quad \text{at}\ \xi=0 \tag{27}$$

Here, we assume that the zone of established flow of the buoyant jet is started at $\xi=0$.

The solution to the system of differential equations cannot be obtained in closed analytical form. A numerical schemes based upon Runge-Kutta method was carried out by direct step-by-step integration and the computations were obtain on a CDC CYBERNET computer.

EXPERIMENTAL APPARATUS AND PROCEDURE

The objective of the experimental investigation was to study the mechanics of a plane vertical turbulent jet discharge in a linearly density-stratified ambient for some range of densimetric Foude numbers. The results of the experiments will use to compare with the computational results obtained in the numerical solutions. Some description of the experimental procedures and techniques is given as follows.

The experiments were performed in a Plexiglas test tank 178 cm long, 85 cm deep and 20 cm wide, filled with a linearly stratified salt solution. The laboratory facilites were shown schematically in Fig. 2. A two-dimensional vertical buoyant jet was generated by discharging fresh water from a chamber containing flow-straightening elements through a slot whose width could be varied from 2 mm to 10 mm. A constant-head source supplied the jet through a calibrated flowmeter. At sides of the test tank, over-flow sluice gates were provided to control the amount of water coming from the jet discharged into the test tank. The water depth of ambient can then be maintained constant depth during the experiments.

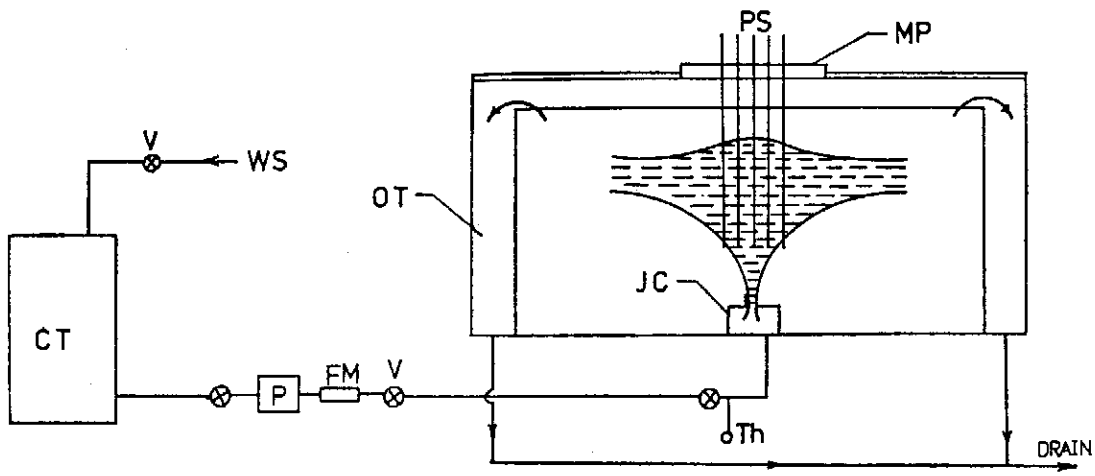

CT	CONSTANT TEMPERATURE TANK	P	CONSTANT HEAD PUMP
FM	FLOW METER	PS	PROBE SYSTEM
JC	JET CHAMCER	Th	THERMOMETER
MP	MOUNTED PANEL	V	ADJUSTABLE VALVE
OT	OVERFLOM TANK	WS	WATER SOURCE

FIG. 2. Schematic diagram of experimental facilities.

The test tank was filled with 16 distinct layers of salt water, each with a different density, to a total of 80 cm. The equipment used for this process included a floater, so designed that it always floated freely on the surface during the filling process. In making the salt solution, the relationship between the density and the salinity of the salt solution used is Knudsen's simple formula as

$$\rho_a = 1 + (-0.093 + 0.8149\ \sigma - 0.000482\ \sigma^2 + 0.0000068\ \sigma^3) \times 10^3$$

herein σ is the salinity of the salt solution. Approximately 6h were needed to complete the filling process. An elapsed time of about 36h permitted the diffusion process to smooth out the abrupt density differences between adjacent layers, and therefore promoted the establishment of the desired linear density distribution.

After the over-day and night diffusion period, the density distribution was measured by the conductivity probe. The results verified that a continuous linear distribution profile from the original discrete distribution is established (see fig. 3). The jet with constant-head source then discharged into the test tank to study the mechanics of a plane vertical turbulent jet in a linearly density-stratified ambient fluid. In all the experiments the tracer concentration measured was the density definiency of the jet fluid below the ambient fluid. Six micro-cell conductivity probes were used for density measurements and six hot-film probes were arranged for velocity measurements. A multi-channel switch allowed the placement of the probes, one at a time, into the output of

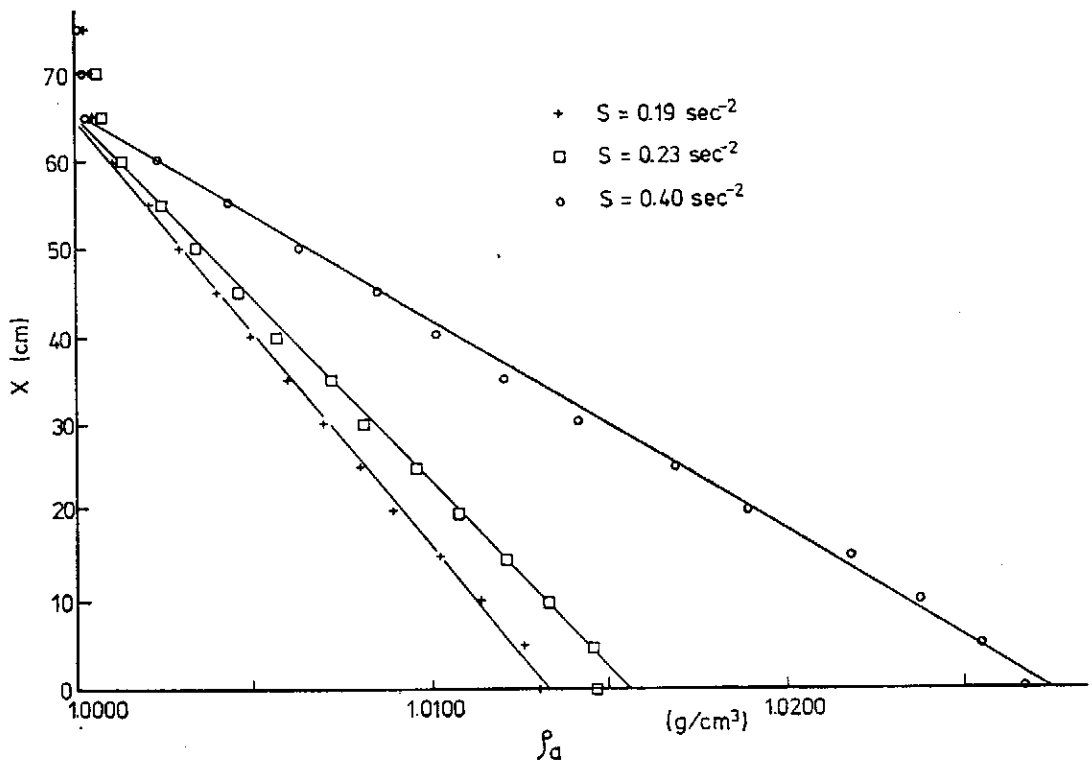

FIG. 3. Measurements of linearly density-stratified environment.

the conductivity meter and the hot-film anemometer for the measurements of conductivity and velocity respectively.

RESULTS AND DISCUSSION

As mentioned preciously, in order to obtain solutions for the integral quantities, μ, β and m, two important parameters, the entrainment coefficient, α, and the spread ratio, λ, are introduced in solving the problem theoretically. In this study, a variable entrainment coefficient was deduced from the incorporation of the kinetic energy conservation and the spread ratio was obtained from the ratio of the half-widths of the mean density defect and velocity profiles across the jet. A series of experiments on plane buoyant jets, in different density-stratified ambient were performed using the apparatus and techniques described in the previous section. Figure 4 shows the measurements of the mean density defect and velocity probiles at $X/D=35$ for the case of $F_0=20$ and $S=0.23$ sec^{-2}. It can be seen that the mean velocity and density defect probiles across the jet are closely approximated by Gaussian distribution. A Gaussian curve was then fitted to each of the experimental data and the half-widths of the mean velocity and density defect determined from these fitted

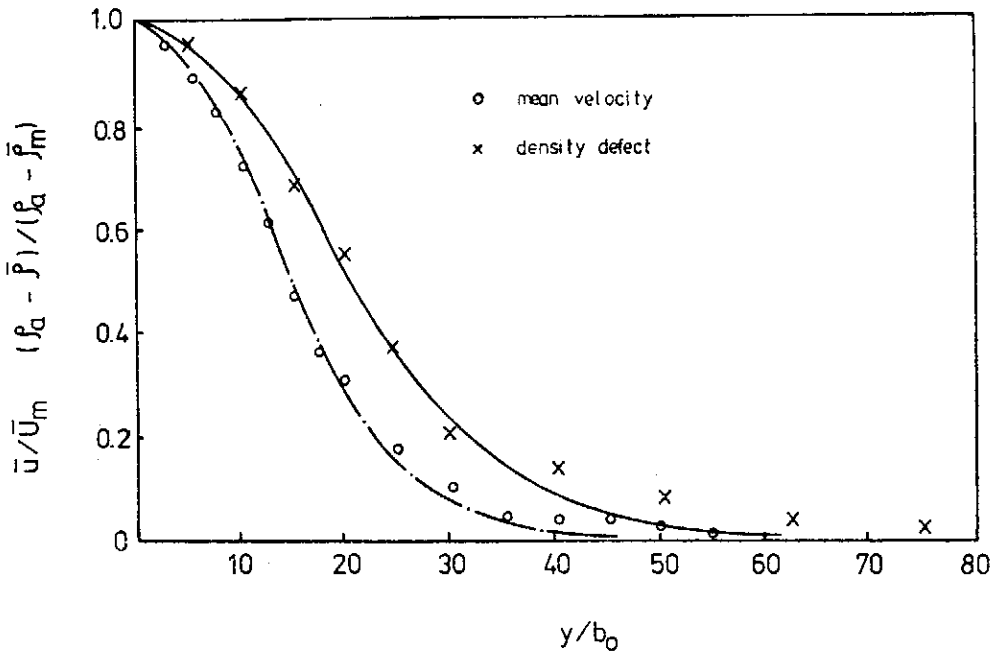

FIG. 4. Measurements of mean Velocity and density defect across the jet at $x/b_o=85$ ($F_o=20$, $S=0.23$ sec^{-2}).

curves given by equations (10) and (11). Numerous experiments in this study show the spreading ratio, $\lambda=b_d/b_u$, lies in the rang of 1.10 to 1.40. An acceptable value for λ appears to be about 1.30 and is used in the analyzing calculations. This value is close to the experimental result of $\lambda=1.35$ obtained by Kotsovinos & List (1977) in their study on plane buoyant jets discharged into homogeneous ambient.

In order to verify the theoretical results, a substantial number of experiments were designed to obtain information of the depressions of the mean velocity and density defect on the center-line at different discharges and ambient conditions. The jet densimetric Froude number, $F_0=U_0/\sqrt{(\rho_1-\rho_0)g\ b_0}\ /\rho_1$, and a dimensionless stratified parameters, $S_0=-(\rho_1-\rho_0)/(b_0\frac{d\rho_a}{dx})$ were used to characterized the jet and the ambient conditions. Figures 5 and 6 present results experimentally and theortically on the decay of the mean velocity and the density defect along the center-line respectively for $S_0=350$ with $F_0=9.5$ and $F_0=20$. Obviously, the center-line mean velocity and density, measured at any axial position, lower for the increasing F_0 before the jet reaches its terminal height. The experimental results were compared with two theoretical methods for prediction of buoyant jet development—one, developed by Fan on the basis of using a universal constant entrainment coefficient and the other,

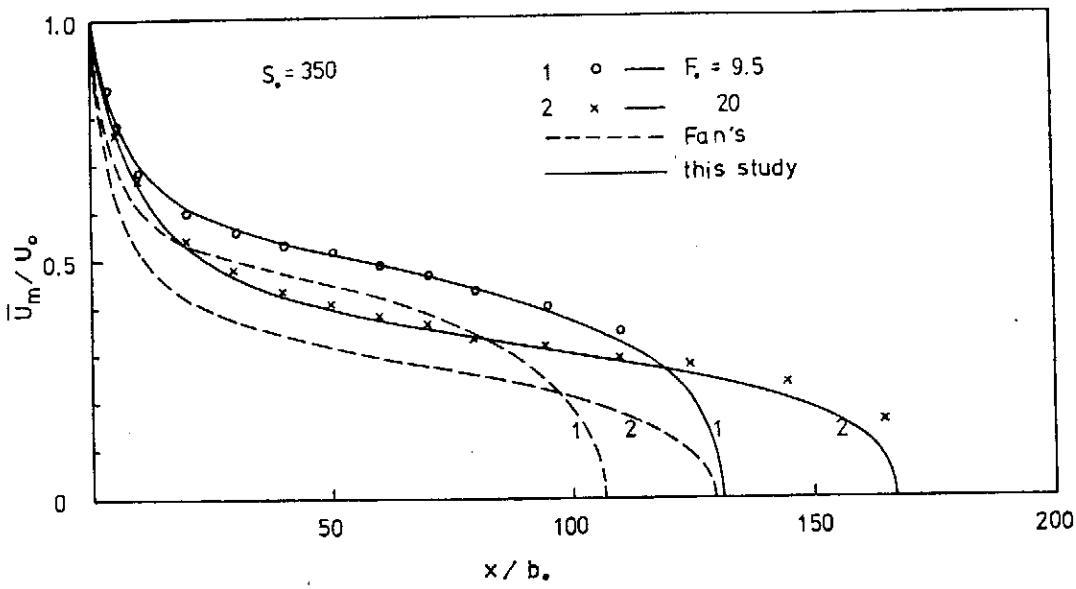

FIG. 5. Comparison of experimental and theoretical results of center-line mean velocity.

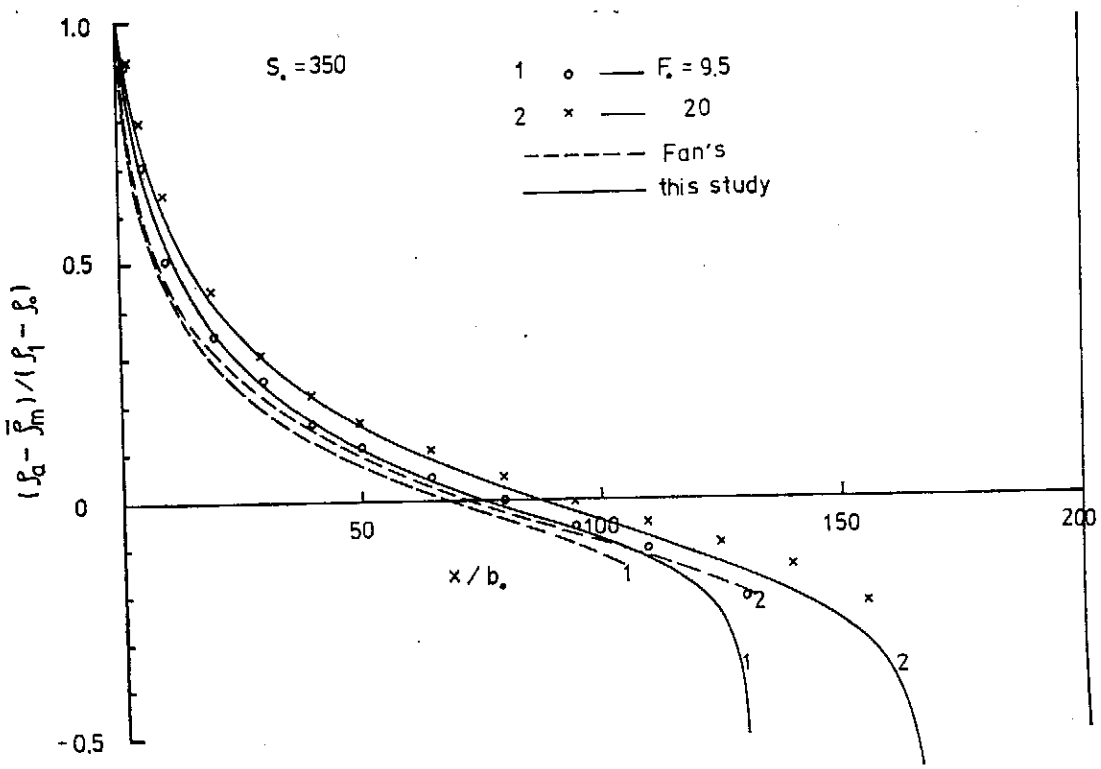

FIG. 6. Comparison of experimental and theoretical results of center-line density defect.

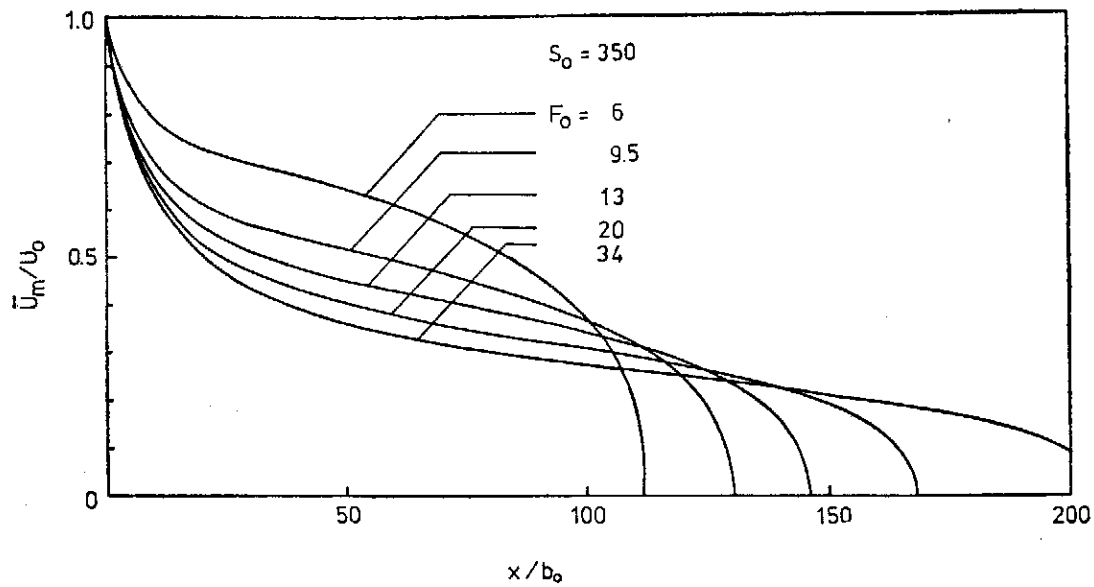

FIG. 7. Dependence of center-line mean velocity on discharge Froude number with S_o=350.

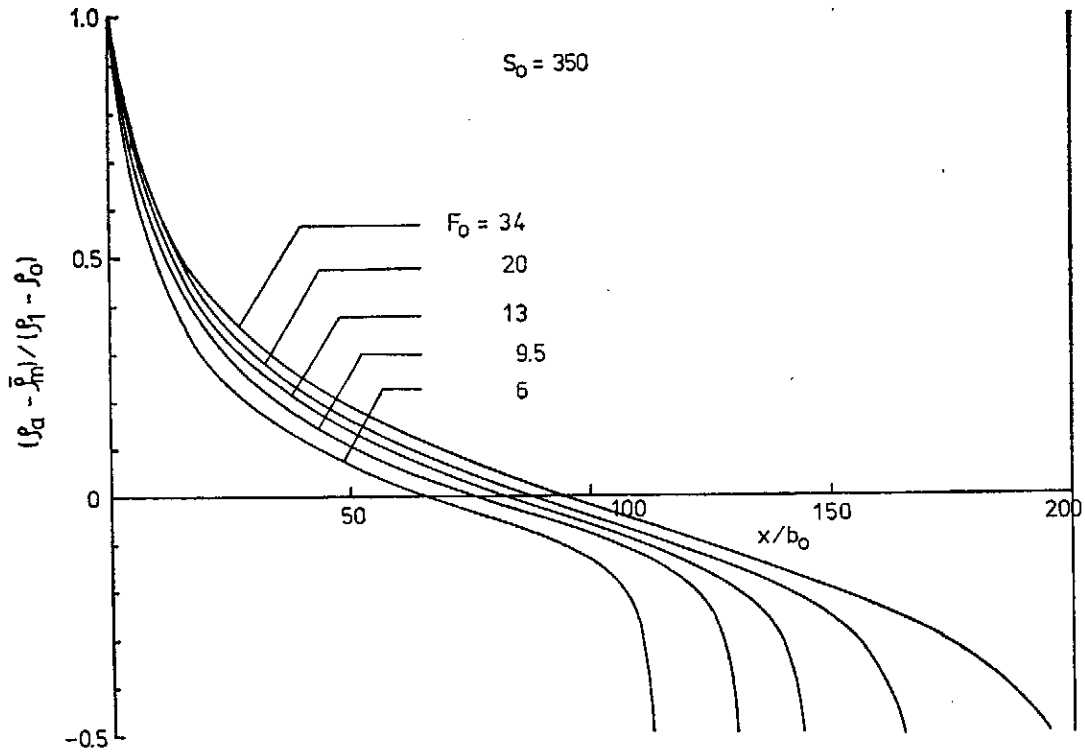

FIG. 8. Dependence of center-line density defect on discharge Froude number with S_o=350.

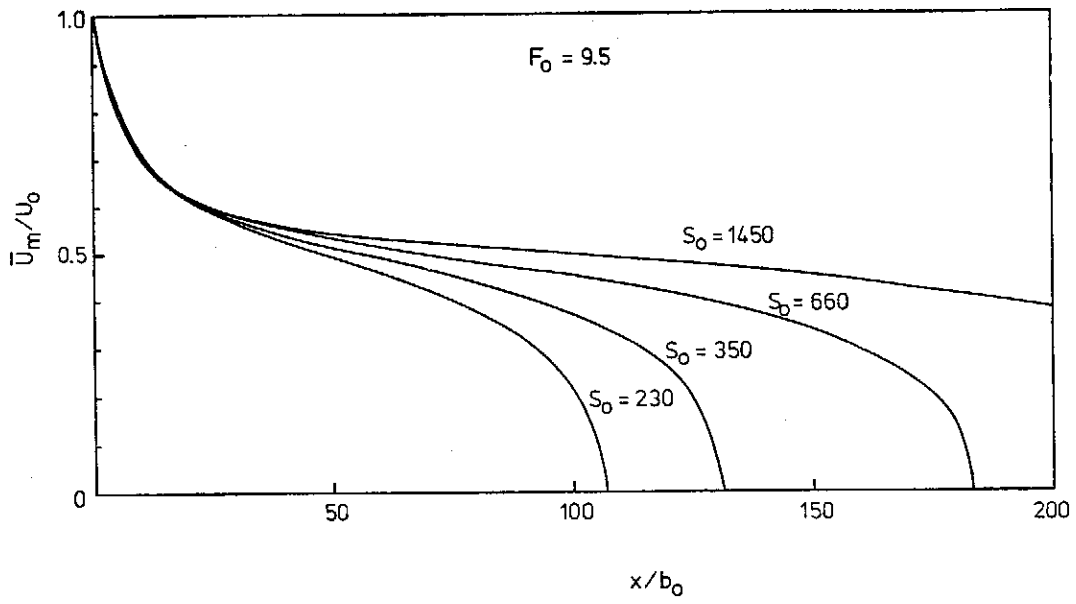

FIG. 9. Dependence of center-line mean velocity on ambient stratified parameter with F_o=9.5.

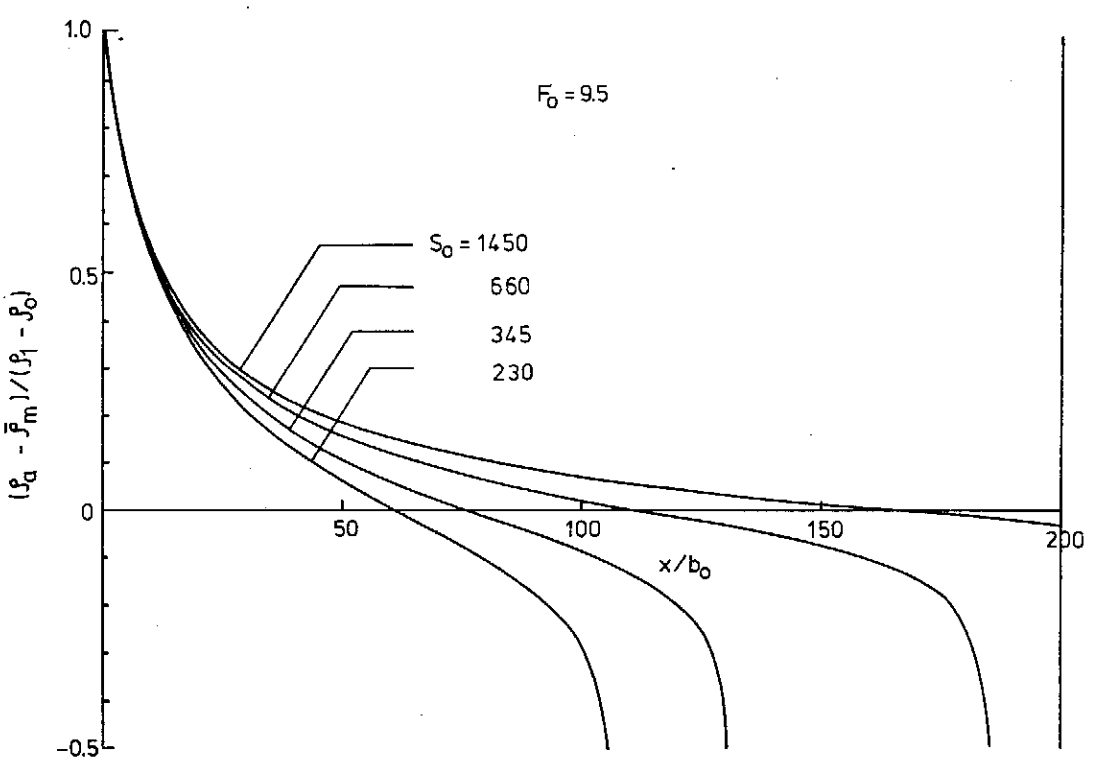

FIG. 10. Dependence of center-line density defect on ambient stratified parameter with F_o=9.5

presented in this paper using a variable entrainment coefficient. The dotted lines denoted Fan's results and solid lines were computational results obtained from solving equations (20)-(22) in this study. In general, solutions of the present study agree more favorably with experimental results than Fan's solutions.

To complete this study a substantial number of computations were carried out in solving equations (20)-(22) with different discharge and ambient conditions. Figures 7 and 8 show the decay of the mean velocity and the density defect on the center-line respectively as a function of F_0 for a given $T_0=350$. Both of the rate changes of the center-line mean velocity and density defect are dependent on the initial jet condition. The center-line mean velocity and density defect, measured along the center-line, lower for the increasing F_0 in a given ambient stratification. In the case of a buoyant jet discharged vertically, the increasing F_0 is increasing the initial momentum flux. From the view point of the variable entrainment concept, the great momentum flux will induce a great amount of entrainment from the surrounding ambient into the jet and cause the jet expanded rapidly. Hence, in the development of the jet the center-line velocity lowers and the terminal height of rise increases with increasing the densimetric Froude number F_0. As a buoyant jet discharged vertically into the density stratified ambient fluid the decreasing density of the ambient in the vertical direction will cause the buoyancy flux of the jet to be decreased in the jet direction and finally to be negative at somewhere the mean density defect is become negative. Under the interaction of the negative buoyancy, the momentum flux of the jet finally vanishes at a terminal point where the mean velocity is zero. Figures 9 and 10 show the decay of mean velocity on the center-line and the density defect along the center-line respectively as a function of S_0 for a given $F_0=9.5$. Clearly the decay of these axial properties lowers for the decreasing S_0 before the jet reaches its terminal height. The terminal height of the rise also noted that increases with increasing the stratified parameter S_0.

The gross features of a vertical buoyant jet in a linearly density-stratified environment were also computated from solving equations (20)-(22) in using a variable entrainment coefficient. Fig. 11 shows the variations of gross jet characteristics Q, M and B along the ξ-corrdinate for the case $M_0=0.4$, $Q_0=0.03$. The momentum flux parameter M first increases with ξ and reaches its maximum at the point where B changes sign and then decreases under negative buoyance and finally vanishes at the terminal point. The buoyancy flux parameter B decreases monotonically from unity to a minimum at the terminal point. The volume flux parameter Q first increases with ξ and reaches its maximum at the point where the negative buoyancy dominates the entrainment and then decreases

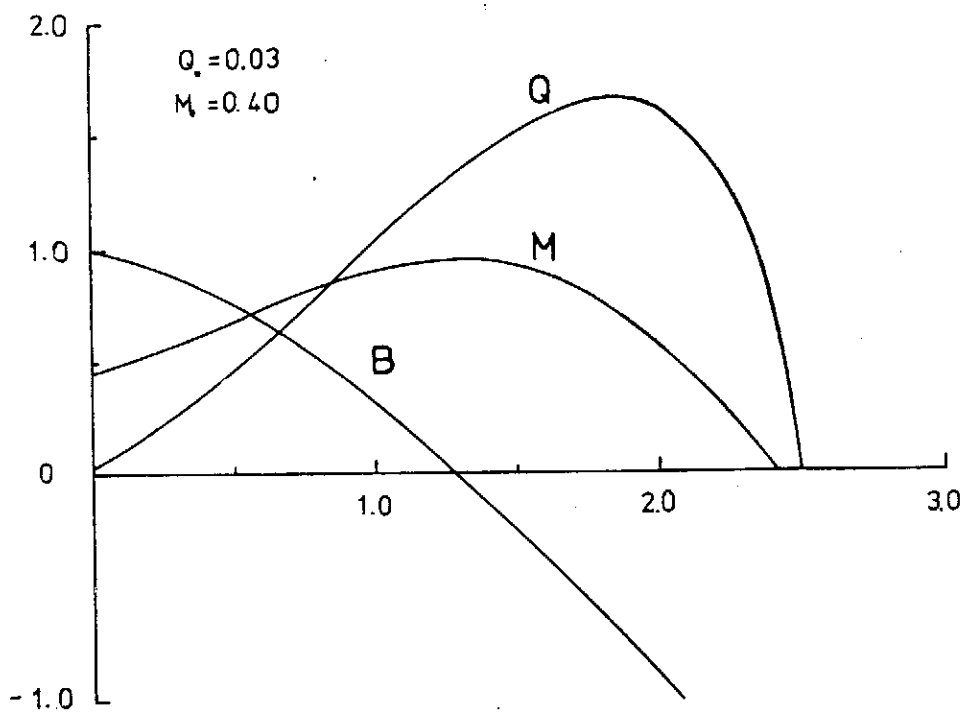

FIG. 11. Variation of volume flux, buoyancy flux and momentum flux along §-coordinate with $Q_o=0.03$ and $M_o=0.4$.

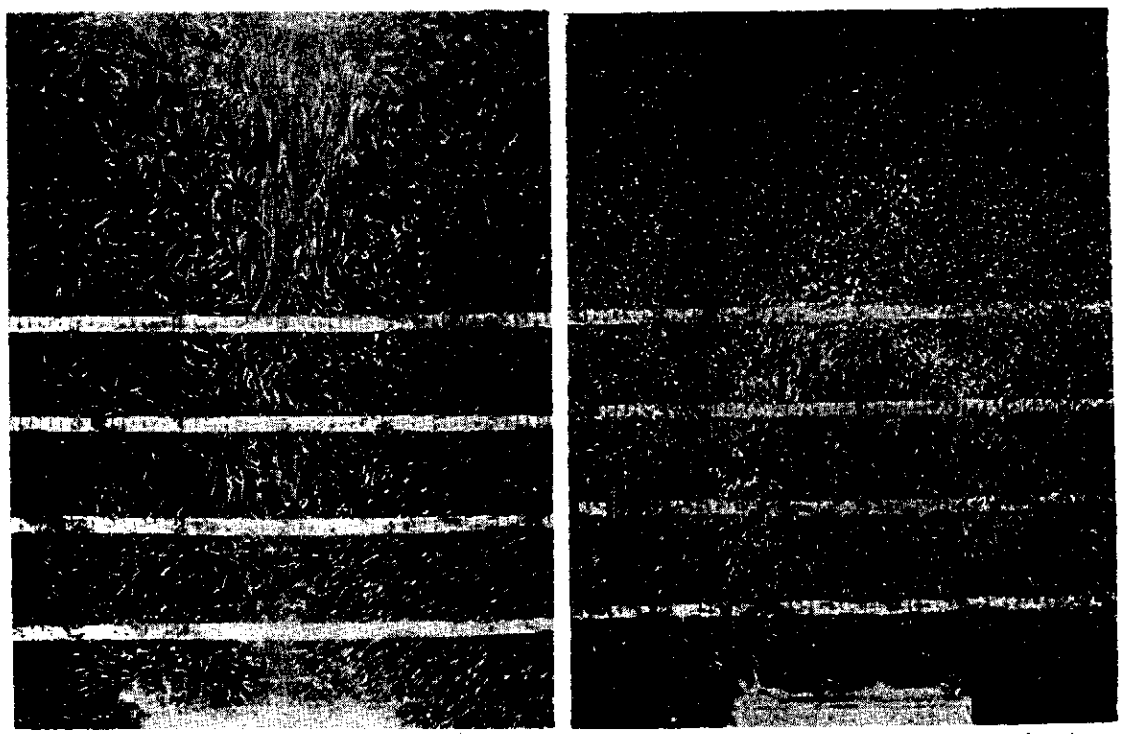

(a) In auniform environment

(b) In a linearly density-stratified environment ($S_o=300$)

FIG. 12. Photographs of a plane buoyant jet with $F_o=20$.

under the inverse entrainment from the jet into the ambient. It is different from using a universal constant of entrainment coefficient that the volume flux parameter increases monotonically with ξ.

For application to practical problems, it is necessary to determine the jet center-line dilution ratio along the jet direction. From the continuity of a tracer, $\bar{U}_m$ bc = constant, the jet centerline dilution C_0/C can be determined from the ratio of the volume flux parameter and the initial valume flux parameter Q_0 as $C_0/C=(Q/Q_0)^{\frac{1}{2}}$. The dilution value along the jet axier can then be computed from solving the system of equations (24) to (26). It can be seen that the problem of a vertical plane buoyant jet in a linearly stratified environment is characterized by the flux parameters Q_0 and M_0, because of the solutions found are independent on α_1, α_2 and λ values chosen. But in practical application it is more convenient to use the jet densimetric Froude number F_0 and a dimensionless stratified parameter S_0. The relationships between the set of parameters F_0, S_0 and the set M_0, Q_0 are

$$M_0=\frac{\sqrt{2(1+\lambda^2)}}{4\lambda^2}F_0^2/S_0 \tag{28}$$

$$Q_0=\frac{\sqrt{2(1+\lambda^2)}}{4(\lambda^2\alpha_1)^{2/3}}F_0^{2/3}/S_0 \tag{29}$$

It should be noted that the jet centerline dilution computed from $(Q/Q_0)^{\frac{1}{2}}$ can only apply up to the point where the variation of Q reaches the maximum. After that the expression $C_0/C=(Q/Q_0)^{\frac{1}{2}}$ is not suitable in applying to compute the center-line dilution, because the ambient density stratification prevents the jet from reaching the surface to spread out horizontally and the inverse entrainment from the jet into the ambient is not considered in the calculation. Since the dilution ratio is the square root of the ratio of the terminate and the initial volume flux parameters, an increase in the initial mixing can be obtained by decreasing Q_0 (such as by using a long diffuser to decrease the value of F_0).

Acknowledgements: This work was supported by the National Science Council of ROC under Grant No. NSC-66E-0304-03(01).

DEFERENCES

1. Abraham, G., *"Jet Diffusion in Stagnant Ambient Fluid,"* Delft Hydraulics Lab. Publ. No. 29, 193 pp. (1963).
2. Albertson, M. L. et al, *"Diffusion of Submerged Jets,"* Tans. ASCE, Vol. 115, pp. 639-664 (1950).
3. Chen, C. J. & Rodi W., *"A Mathematical Model for Stratified Turbulent Flows and Its Application to Buoyant Jets,"* 16th IAHR Congress, Sao Panlo, Brazil (1975).

4. Fan, L. N., *"Turbulent Buoyant Jets into Stratified or Flowing the Ambient Fluids,"* Report KH-R-15, California Inst. Tech. Pasadena, Calif. (1967).
5. Fan, L. N. & Brooks, N. H., *"Numerical Solutions of Turbulent Buoyant Jet Problems,"* Report KH-R-18, California Inst. Tech. Pasadena, Calif. (1969).
6. Fox, D. G., *"Forced Plume in a Stratified Fluid,"* J. of Geophysical Research 75, 33, 6818-6835, (1970).
7. Kotsovinos, N. E. & List, E. J., *"Plane Turbulent Buoyant Jets. Part 1. Integral Properties,"* J. Fluid Mech., Vol. 81, pp. 25-44. (1977).
8. List, E. J. & IMberger, J., *"Turbulent Entrainment in Buoyant Jets Y. Plumes,"* ASCE, J. of Hy. Div., HY9, 1461-1474, (1973).
9. Morton, B., Taylor, G. I. & Turner, J. S., *"Turbulent Gravitational Convenction from Maintained and Instantancous Scources,"* Proc. Royal Society, Vol. A234, 1056, pp. 1-23 (1956).
10. Rouse, H. et al, *"Gravitational Convection from a Boundary Source,"* Tellus, 4, pp. 201-210 c1952ɔ.
11. Sneck, H. J. & Brown, D. M., *"Plume Rising fram Large Thermal Sources such as Dry Colling Towers,"* ASME, J. of Heat Transfer, 232-248, (1974).
12. Taylor, G. I.., *"Flow Induced by Jets,"* J. Aero/Space Science, Vol. 25, pp. 464-465 (1958).
13. Hwang, R.R., & Cheng, Y.K., *"Rise of Buoyant Jets in Density-Stratified Environments: A Laboratory Study,"* Annual Rep. of the Inst. of Phy., Academia Sinica, Vol. 8, 1978.

Annual Report of the Institute of Physics, Academia Sinica, Vol. 8, 1978

密度層變水域中浮昇射流的擴散探討

黃榮鑑　傅忠申

中央研究院物理研究所

摘　要

本文藉實驗及理論的數值計算，探討線性密度層變水域中一垂直二維浮昇射流的擴散性。浮昇射流之擴散理論由質量、動量、動能量及浮量守恒方程，利用斷面積分法設定速度與密度差剖面呈高氏分佈，並引用捲增概念導出一常微分控制方程組。捲增係數則由動能量守恒推導出與反局部密度 Froude 數成線性的關係式而非一通用常數。流場中各物理總量之變化由此控制方程組與啓始條件解出。

實驗方面，使用鹽水分層填加方法，填製綫性密度層變水域。擴散比由實驗中對速度及密度差的剖面分佈之量測定出，介於 1.10～1.40 之間。本文之數值計算取定 1.30。比較實驗測定之縱向軸中心速度及軸中心密度差分佈與數值之計算結果以印證理論之分析。

RISE OF BUOYANT JETS IN DENSITY-STRATIFIED ENVIRONMENTS: A LABORATORY STUDY

ROBERT R. HWANG[1] (黃榮鑑) and Y. K. CHENG[2] (鄭永康)

Abstract

The maximum height of rise of plane turbulent buoyant jets dischared vertically into stratified ambient fluid is studied experimentally. By using the dimensional analysis the ceiling height of rise of jet is related functionally to the discharge configurations and stratification of environments. In the laboratory experiments, a filling salt solution process is designed to generate a linearly density-stratified environment and a photographic technique is used to trace the development of the flow. It is found that the maximum height of rise of a plane vertical jet is proportional to $F_0^{2/3}$ and $S^{1/2}$.

I. INTRODUCTION

The use of submerge outfalls to return sewage and heated water into the ocean and estuaries has been practiced by many coastal cities around the world. Inadequate disposal of the pollutants has often created a serious contamination in the coastal areas. Controlling of such pollution problems relies on the requirement that the waste disposal not be detrimental to public health, aesthetics, and wildlife. In nearly all practical cases dilution takes an important index in the meeting of these disposal objective.

The practice of submerge disposal is to discharge the waste matter of water-borne in jets. Significant contributions to the understanding of submarine outfall dilution have been made by many investigators (for a review see Koh & Brooks[4]). For jets discharging into homogeneous media, results of their analysis showed that the dilution in the vertical jet can be expressed in the form as

$$S_s = f_1\left(\frac{H_s}{b_0}, F_0\right) \tag{1}$$

in which S_s is the dilution factor at the point at which the jet axis meets the air-liquid surface, defined as the ratio of the concentration of effluent to the concentration of jet axis; H_s denotes the depth of liquid over the discharge point; b_0 is the diameter or the width of the jet orifice at discharge; F_0 describes the initial Froude number, defined as $U_0/\sqrt{b_0 g(\rho_j-\rho_0)/\rho_0}$; U_0 is the velocity of discharge of the jet at orifice; ρ_j and ρ_0 are densities of jet and ambient fluid respectively. For density-stratified environments, the density gradient of the ambient can influence the establishment of sewage fields. The

1. Research Fellow, Institute of Phy., Academic Sinica, Taipei, R.O.C..
2. Research Assistant.

sewage jets mix with so much dense bottom water that they become neutrally buoyant in the water column and spread at this level before rising to the surface. In this case, the maximum height of rise of the waste-water jet must be determined in obtaining the terminal dilution.

The literature in determining the rise of buoyant jets in stably stratified environment is not abundant. Using an integral technique and constant-entrainment description for the analysis of turbulent jets, Fan and Brooks[1, 2] obtained a formulate of rise of the waste-water plume discharged vertically into a uniformly stratified environment (G=constant) given by

$$Y_{max}=2.84(g_0'U_0b_0)^{1/3}G^{-1/2} \qquad (2)$$

in which, Y_{max} is the maximum height of rise of the waste-water plume; $g_0'=(\rho_1-\rho_0)g/\rho_1$, the initial description of buoyancy force; $G=(-\frac{g}{\rho_1})(d\rho_a/dy)$, the stratified parameter of ambient fluid.

Hwang[3] deduced the form of entrainment in a variable coefficient on the basis of incorporating the conservation equation for the kinetic energy and studied the initial diffusion of a plane turbulent buoyant jet discharged into a linearly density-stratified environment. These results of determining the rise of plane buoyant jets were compared with the data cbtained from laboratory experiments. It showed (as shown in Fig. 1) that both of them fit well only in some flow configurations. Therefore, it is necessary to obtain a jet-rise formula fitted a wide range of discharge conditions at the jet source and ambient conditions to determine the maximum height of rise for practical applications. This study is then to obtain such a formula from correlating a substantial series of experimental data according to simple theoretical considerations such as dimensional analysis. The height of rise was obtained in terms of the initial desimetric Froude number of buoyant jets and the stratification parameter of the surrounding environment.

II. DIMENSIONAL ANALYSIS

The disposal of waste matter through submarine jets subjects the mechanic effects of the jet momentum and buoyancy. Near the source, differences in velocity and volume flux between the effluent and the ambient fluid produce mixing due to the instability of the interface and due to the turbulent energy contained in the jet. Buoyancy causes rise of the submerged jet. In a stably stratified environment, the density stratification of ambient fluid can prevent the rise of sewage jets from reaching the surface by inducing rapid mixing of the buoyant jets with heavy bottom water, thus produing a neutrally buoyant cloud.

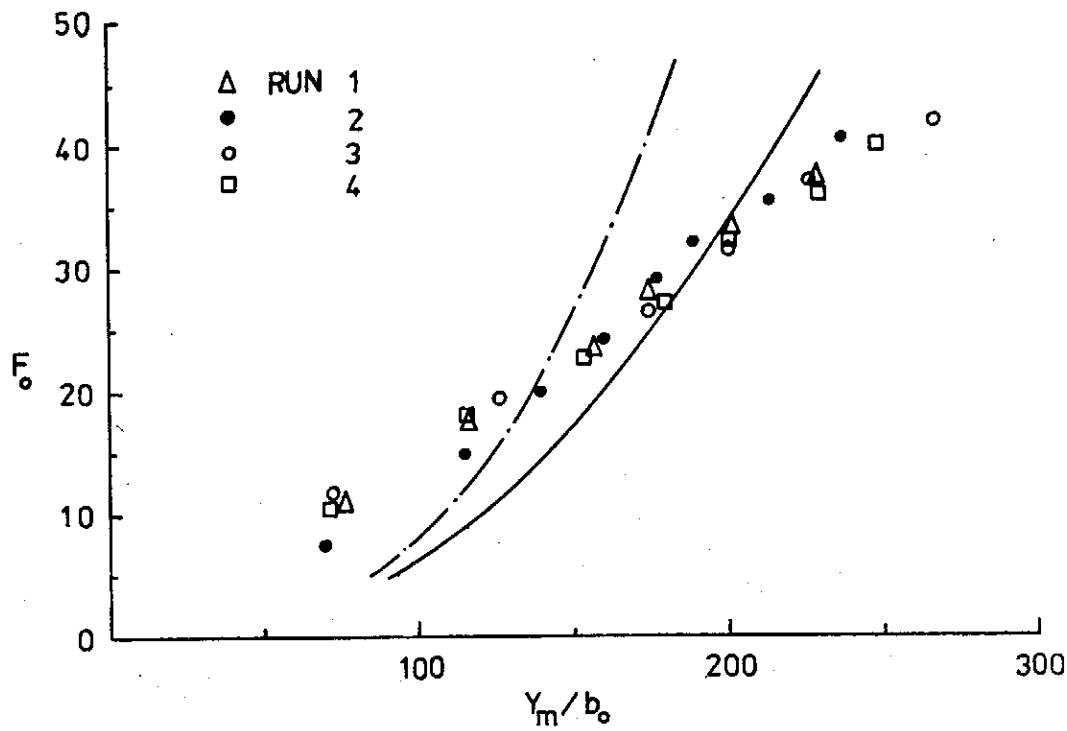

FIG. 1. Comparison of experimental and theoretical results on the rise of vertical buoyant Experts. imjental reseults. △ — S = 310, ● — ○ = S 320, — S = 303, □ — S = 300, theoretical results:. Brooks (1, 2), Hwang (3) for S = 320.

Fig. 2 shows a plane buoyant jet issuing vertically into a stably stratified environment in which the ambient density decreases with elevation. The jet first behaves like the buoyant jet that its density deficit reduced continuously and becomes zero at a certain height (point of neutral buoyancy). From here on the buoyancy force is negative and the jet behaves similar to a negative buoyant jet. The flow decelerates, reaches a maximum height Y_m and then turns downward and spreads sideways. Therefore, the functional relationship which exists between the maximum height of rise of the plane buoyant jet and the other variables involved, may be written in the form

$$Y_m = \phi_1 (\mu_0,\ m_0,\ \beta_0,\ G) \tag{3}$$

in which, $\mu_0 = U_0 b_0$, $m_0 = U_0^2 b_0$, and $\beta_0 = \frac{\rho_1 - \rho_0}{\rho_1} g\ U_0 b_0$ are the initial fluxes of specific volume, momentum and buoyancy respectively; $G = -\frac{g}{\rho_1} d\rho_a/dy$, is the parameter described the stratification of the environment.

By dimensional anslysis[5], the functional relationship can be written as

$$\phi_2 (Y_m\ \beta_0^{-1/3}\ G^{1/2},\ m_0^{-1}\ \beta_0^{1/3}\ \mu_0,\ m_0^2\ \beta_0^{-3} G) = 0 \tag{4}$$

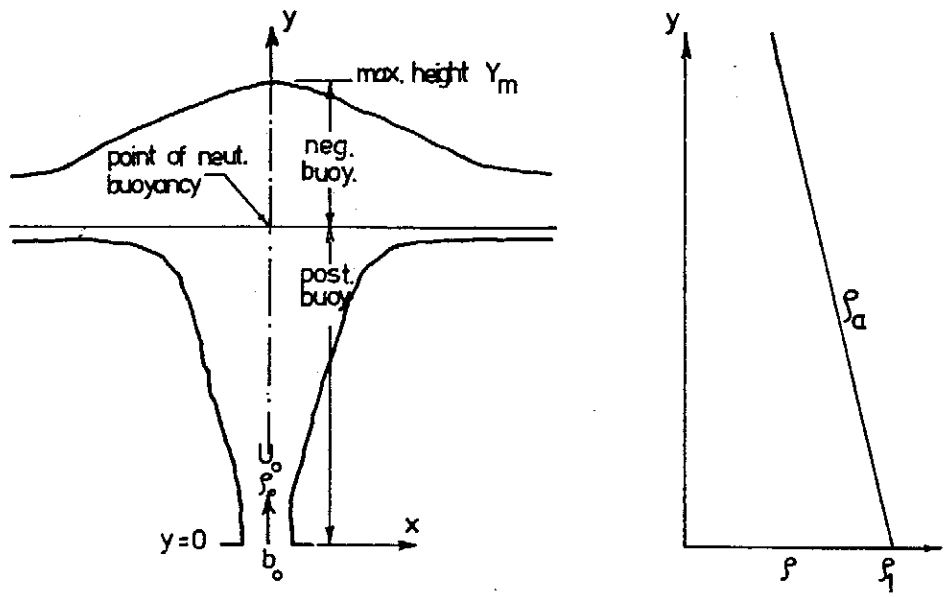

FIG. 2. Vertical buoyant jet in stably stratified environments.

The first term indicates the normalized length scale of the height of rise of plane buoyant jet; the second term is the ration of buoyant to inertial forces at the jet orifice and can be simplified to a form of $F_0^{-2/3}$; while the last term can be formed as $F_0^2S^{-1}$ in which $S=[(\rho_1-\rho_0)/b_0]/(-d\rho_a/dy)$, is a dimensionless parameter of stratification of the ambient fluid. Equation (4) can then be rewritten as

$$\zeta_m=\phi_3(F_0^{-2/3}, F_0^2S^{-1}) \tag{5a}$$

or

$$F_0^{-2}\zeta_m=\phi_4(F_0^{-8/3}, S^{-1}) \tag{5b}$$

in which, $\zeta_m=Y_m\beta_0^{-1/3}G^{1/3}$. The program of the study was therefore designed to determine the functional relationship which exists between ζ_m and the other variables involved experimentally.

III. EXPERIMENTAL APPARATUS AND PROCEDURE

Apparatus.—The laboratory experiments were performed in a plexiglas test tank 178 cm long, 85 cm deep and 20 cm wide, filled with a linearly density-stratified salt solution. A detailed sketch of the experimental apparatus is shown schmatically in Fig. 3.

As shown in the sketch, a two-dimensional vertical buoyant jet was generated by discharging fresh water from a chamber containing flowstraightening elements through a slot of width 2 mm. A constant-head source supplied the

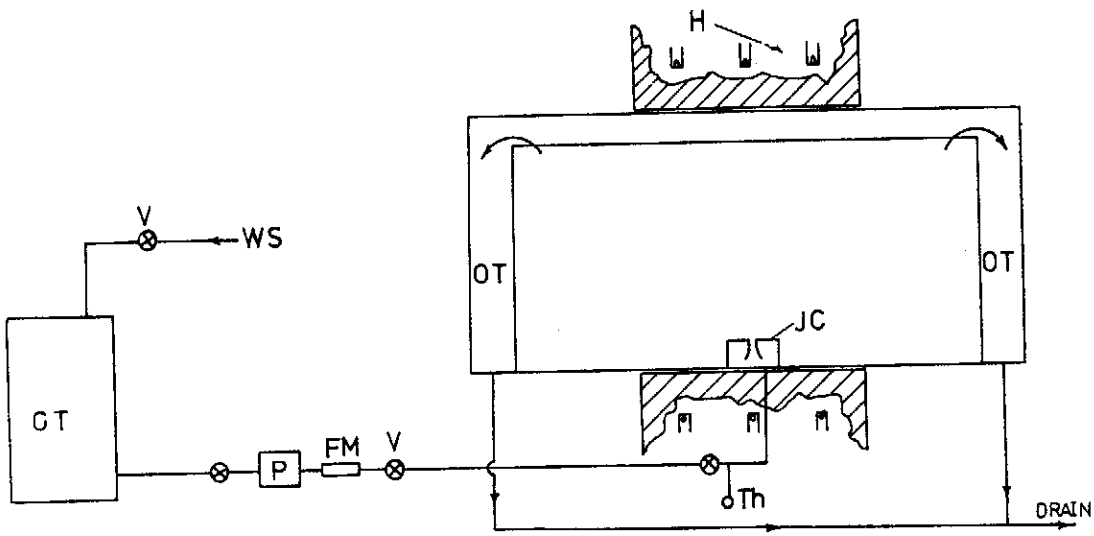

CT CONSTANT TEMPERATURE TANK
FM FLOW METER
H LIGHT BOX
JC JET CHEMBER
OT OVERFLOW TANK
P CONSTANT HEAD PUMP
Th THERMOMETER
V ADJUSTABLE VALVE
WS WATER SOURCE

FIG. 3. Schematic diagram of experimental apparatus.

jet through a calibrated flowmeter. At sides of the test tank, over-flow sluice gates were provided to maintain the constant depth of fluid in the test tank during the experiments. Two light boxes were installed providing for illumination; one on the top and another from the low position of the test tank. A Nikon F2 camera of 50 mm lens was mounted at the front of the test section for recording the development of the flow.

Procedure.—The test tank was filled with 16 distinct layers of salt water, each with a different density, to a total of 80 cm. The equipment used for this process included a floater, so designed that it always floated freely on the surface during the filling process. Approximately 6 hours were needed to complete the filling process. An elapsed time of 24 to 36 hours permitted the diffusion process to smooth out the abrupt density differences between adjacent layers, and therefore promoted the establishment of the desired linear density distribution.

After the over-day and night diffusion period, the density distribution was measured by the conductivity probe. The results verified that a continuous linear distribution profile from the original discrete distribution is established. The jet with constant head source then discharged into the test tank at a determined flow rate. The flow was made visible by a suspension of small

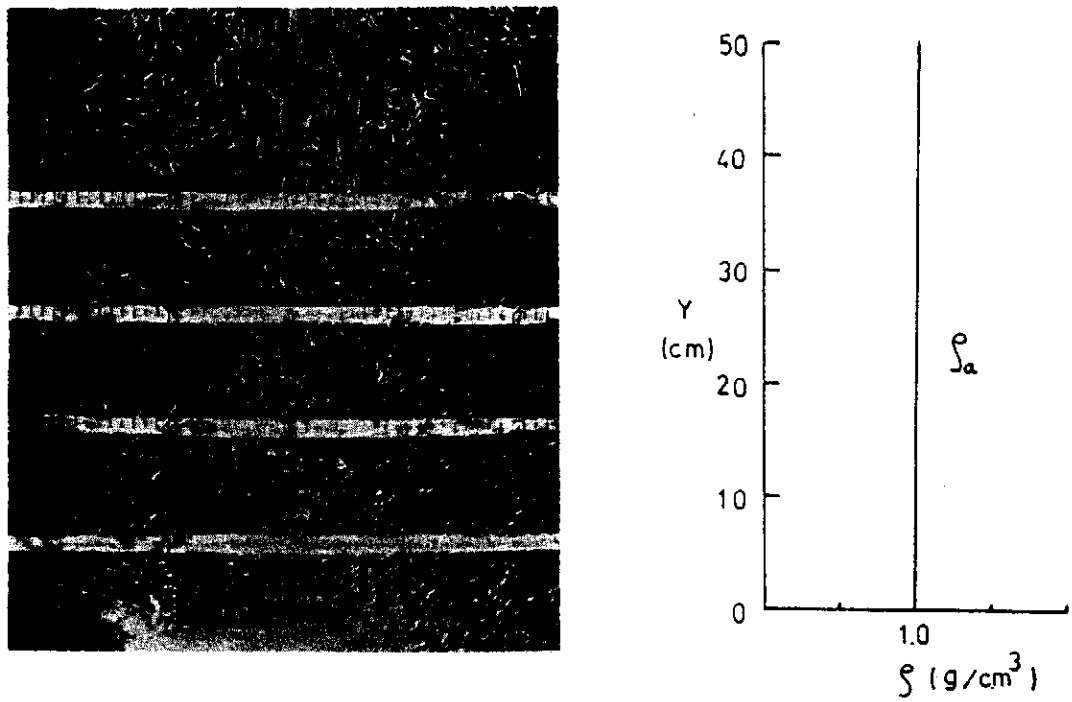

(a) $F_o = 10.$, $G = 0$, $S = \infty$

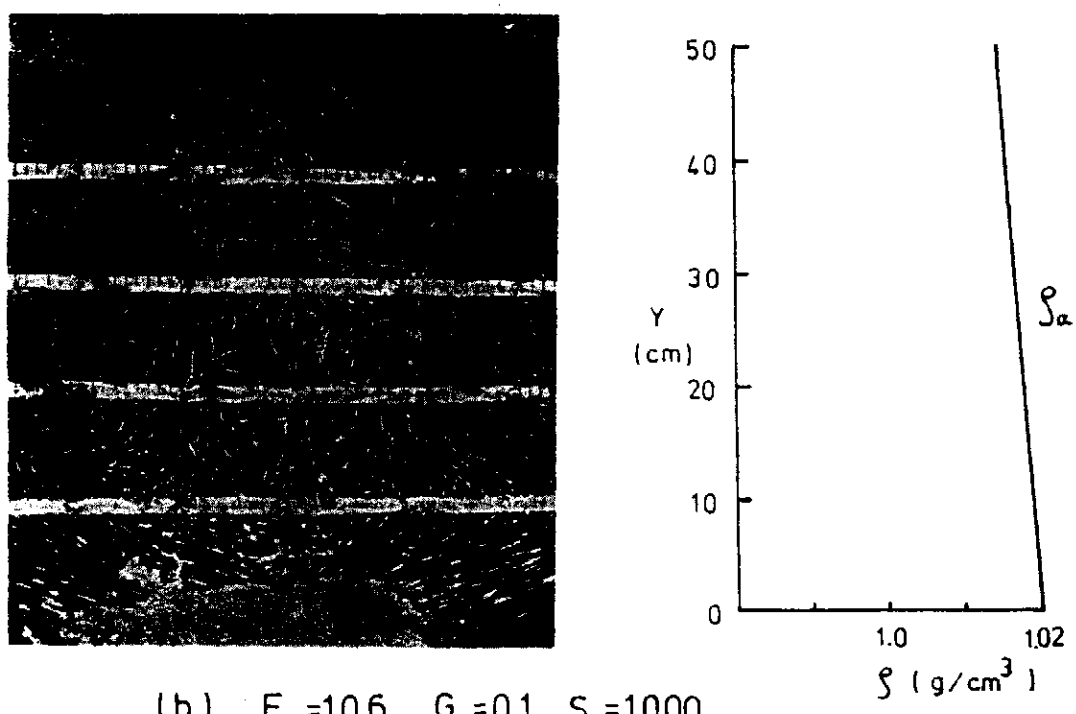

(b) $F_o = 10.6$, $G = 0.1$, $S = 1000$ (sec^{-2})

FIG. 4. Laboratory experiments of vertical buoyant jets into their corresponding environments.

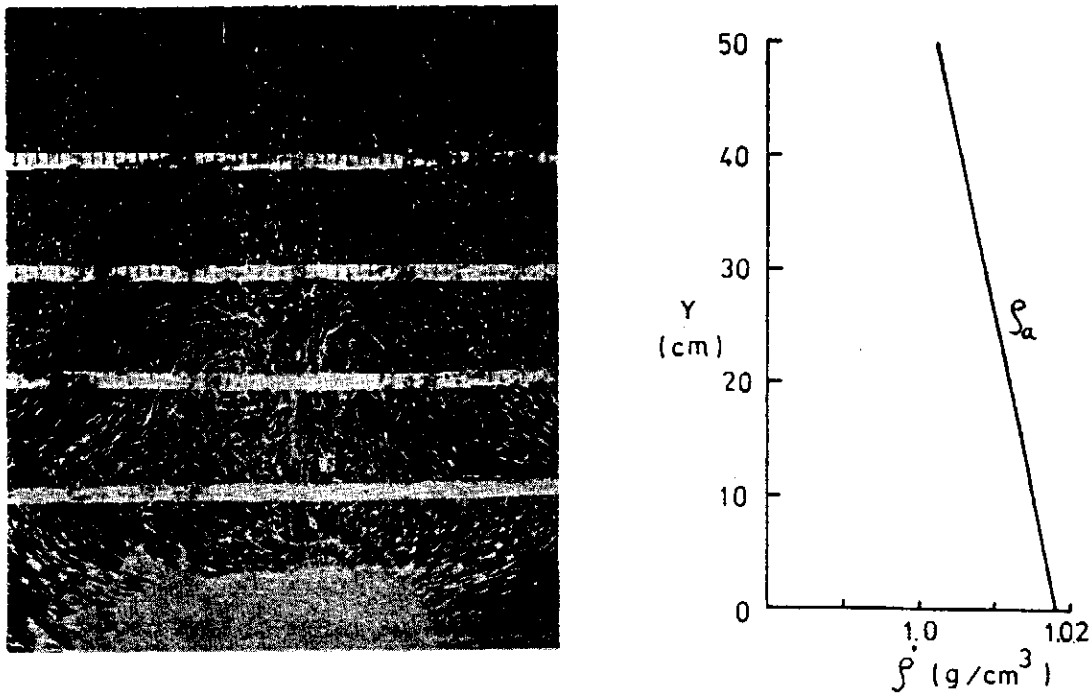

(a) F_o =23.8, G =0.29 (sec^{-2}), S =320

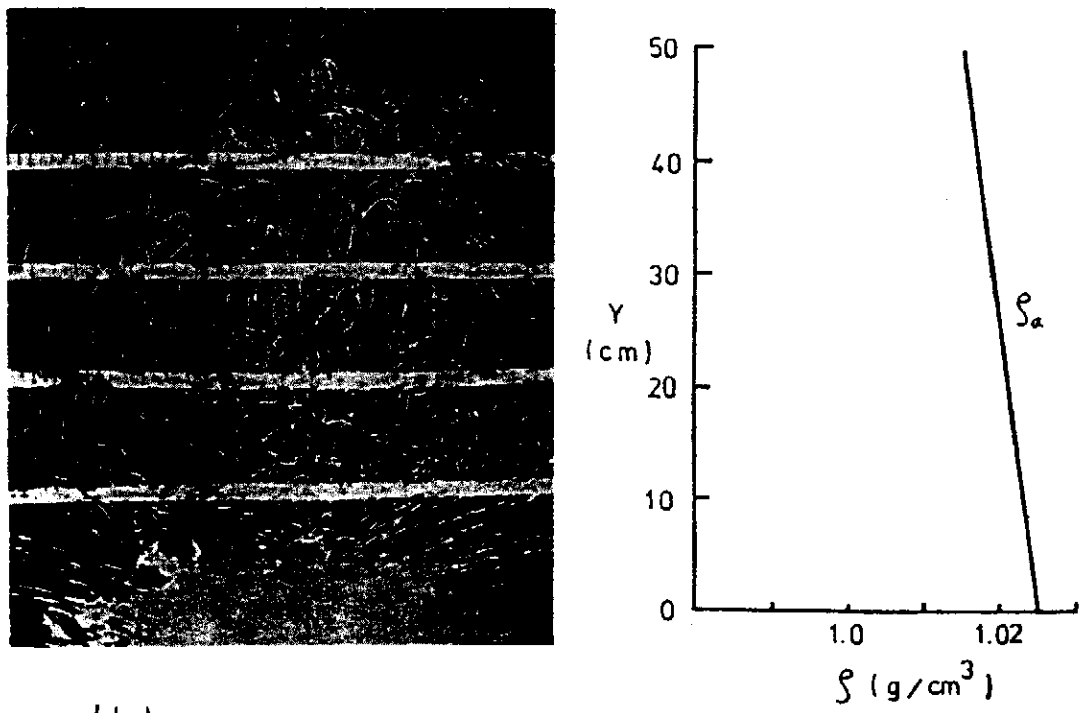

(b) F_o =25., G =0.19 (sec^{-2}), S =625

FIG. 5. Laboratory experiments of vertical buoyant jets into their corresponding environments.

Pliolite S-5 beads (0.05—0.5 mm) which were illuminated by the sheath light from both of the upper and the lower light boxes. A Nikon F2 camera of 50 mm wide lens installed at the front of the test section was then used to record the establishment of the flow pattern. In order to give particle streaks clearly and to show the flow pattern effectively, the shutter time was set at 1/2 sec. It was found that good quality streakline pictures can be obtained at f. 11 with a film speed of ASA 400 (Kodak Trix Pan). Some specimen photographs with their corresponding density profiles of the environment from the experiments are shown in Fg. 4 and 5.

IV. EXPERIMENTAL RESULTS

A substantial number of experiments on plane buoyant jets were performed using the apparatus and techniques described in the previous section. The objective of the experimental investigation was to obtain the maximum height of rise of a plane vertical turbulent jet for a wide range of flow configurations and ambient stratifications. In these experiments, maximum heights of rise were measured from flow pictures for jets with different initial densimetric Froude numbers and stratified parameters. Fig. 6 shows some of the experimental results on the maximum rise of jets as a function of F_0 for different stratified parameters in the environment. It is then seen that the height of rise of jets varies with both of flow configurations and ambient stratifications.

In order to obtain a simplified result of the functional relationship, the experimental data obtained from the laboratory study were plotted in a full-logarithmic coordinates according to the dimensional analysis of equation(5). Fig. 7 presents a dimensionless plot of the ceiling height of rise against with initial Froude number, F_0. The exist Froude numbers are ranged from 6 to 42.5 and the dimensionless stratified parameters are in the range of 300 to 1,000 obtained in this experimental study. The data points in Fig. 7 show a simplified relationship between dimensionless variables $F_0^{-2}\zeta_m$ and $F_0^{-8/3}$ in despite of the variations of S and it can be represented approximately by a line shown in the figure. Thus the ceiling height of rise in any plane vertical buoyant jets discharged into any linearly stratified environments can be described by

$$\zeta_m = 1.05\, F_0^{1/3} \tag{6}$$

Since the dimensionless height of rise, ζ_m, can be written in a form of $\zeta_m = F_0^{-1/3} S^{-1/2} Y_m/b_0$, the result is then obtained in a simple form as

$$Y_m/b_0 = 1.05\, F_0^{2/3} S^{1/2} \tag{7}$$

The result, therefore, suggests that the ceiling height of rise of a plane vertical buoyant jet is proportional to $F_0^{2/3}$ and $S^{1/2}$.

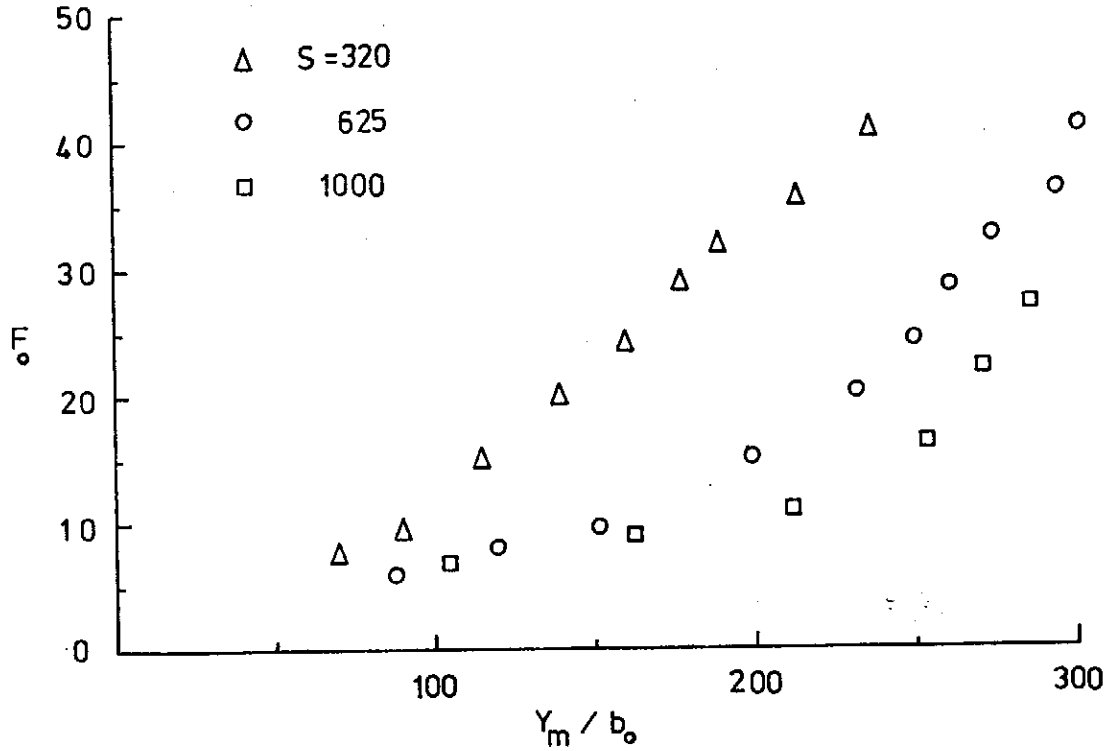

FIG. 6. Dependence of discharge Froude number and surrounding stratified parameter on the rise of vertical buoyant jets.

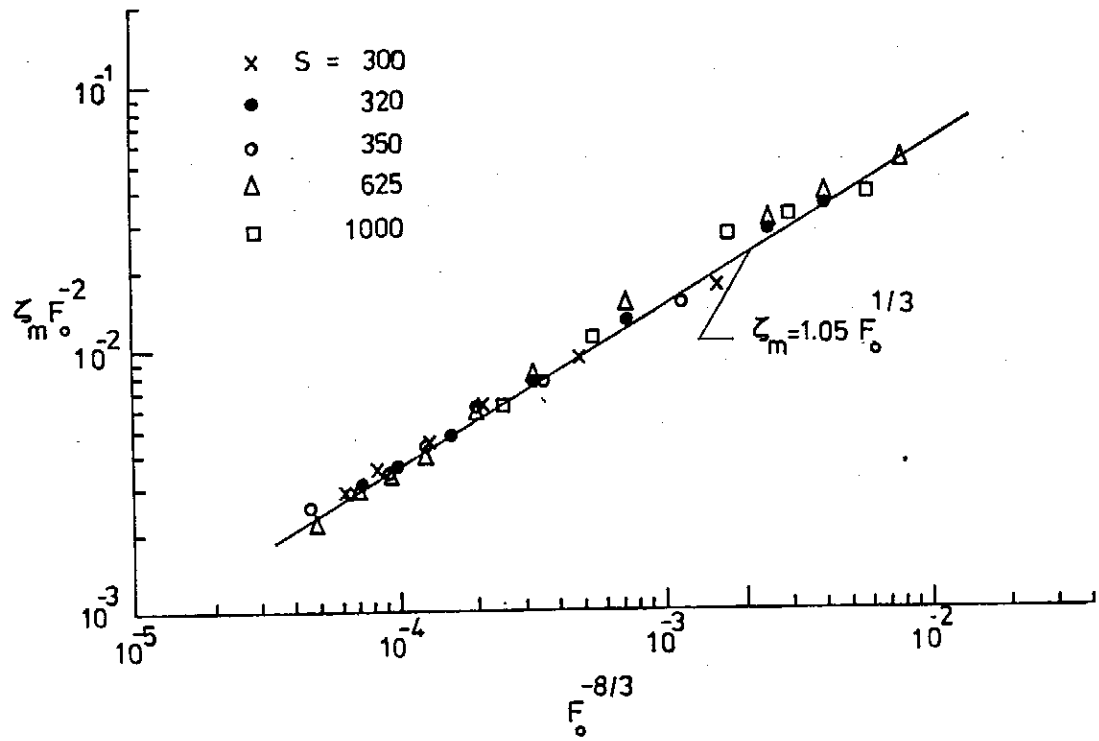

FIG. 7. The maximum height of rise of vertical buoyant jets in linearly density-stratified environments.

V. CONCLUDING REMARKS

A laboratory tecnique is developed for study the rise of plane buoyant jets discharged vertically in the density-stratified environments. The maximum height of rise of buoyant jets is related functionally to the discharge configuration of environments on the basis of dimensional analysis. Although some numerical computations are available in predicting the ceiling height of buoyant jets discharged in the density-stratified environment, those models were obtained underlying that the velocity profiles as well as profiles of buoyancy and concentration of any tracer are assumed to be similar at all cross sections normal to the jet trajectory throughtout the flow field. It is seen that the density deficit of a buoyant jet issuing into a stably stratified environment reduces continuously and becomes zero at the point of neutral buoyancy. From here on and after it, the flow decelerates and spreads sideways, and the flow is no more similar. The detailed structure of flow field at this intermediate mixing region is not clear at the present. Therefore, the functional result relating the maximum height of rise to the discharge configurations of buoyant jets and the surrounding ambient stratification obtained in this study provides a powerful result.

DEFERENCES

(1) Brooks, N. H., *"Dispersion in Hydrologic and Coastal Environments,"* Rep. No. KH-R-29, W. M. Keck Laboratory of Hydraulics and Water Resources, California Inst. of Technology, Pasadena, Calif., 1972.

(2) Fan, L. N., and Brooks, N. H., *"Numerical Solutions of Turbulent Buoyant Jet Problems,"* Rep. No. KH-R-18, W. M. Keck Lab. of Hydraulics and Water Resources, California Inst. of Technology Pasadena, Calif., 1969.

(3) Hwang, R. R., and Fu, C. S., *"Diffusion of Plane Turbulent Buoyant Jets in Density-Stratified Ambient Fluid,"* presented at the Dec. 16-17, 1978, 2nd Conf. on Theo. & Appl. Mechanics, held at Tainan, Taiwan, R.O.C..

(4) Koh, R. C. Y., and Brooks, N. H., *"Fluid Mechanics of Waste-water Disposal in the Ocean,"* Annual Review of Fluid Mechanics, Vol. 7, 1975, pp. 187-211.

(5) Rouse, H., Advanced Mechanics of Fluids, ch. I, John Willey & Sons, Inc., 1968.

FLOW PAST AN IMPULSIVELY STARTED CIRCULAR CYLINDER

L. C. CHIEN (簡來成)

Institute of Physics, Academia Sinica, Taipei, Taiwan, Republic of China

Abstract

Because of the impulsively start, there is a singularity at the time $t=0^+$. This paper gives the accurate solution in the neighberhood of the singularity by analytic solution obtained by inner-outer expansion method to the third order. The viscous layer considered stream function and vorticity obtained by the method of asymptotic expansion at the small time are employed as initial conditions for numerical integration. An efficient numerical method, hopscotch method, is described for integrating the Navier-Stokes equations. The time development of the flow preperties are obtained and plotted. Second bubble was found for Reynold number, based on diameter, greater than 500.

I. INTRODUCTION

Although there has been a large number of numerical computations on the unsteady viscous flow over an impulsively started circular cylinder, the existing solutions agree neither quantitatively nor qualitatively with one another. Because no analytical solution was the available, Payne (1958), and later others used potential flow as their initial conditions for numerical integration. They computed the vorticity on the cylinder for $t=0+$ by using the stream function obtained from potential flow theory. The finite difference formulation assumes a uniform thickness of one grid of vortex sheet around the cylinder. However, the vorticity already diffused 4 or 5 grids away from the cylinder surface for $Re=50$ at $T=0.02$ (Chien, 1977). Therefore, the potential flow started solution is a poor one near the singularity. Physically, the potential flow started integration of the Navier-Stokes equations does not take into account the initial structure of the flow (Collins and Dennis, 1973b). The solution is inaccurate initially. The effect of the inaccuracy on the later time probably leads to the lack of agreement among various investigations.

In this study, the analytic solution, obtained by inner-outer expansion method to the third order (Chien, 1977), is used as initial conditions for numerical computation. The hopscotch method is used to integrate the vorticity equation. And the Poisson equation is solved by successive over-relaxation.

Because of the thin viscous layer and fast diffusion of vorticity for less viscous flow, it is more difficult to carry out the compuation at higher Reynolds

number. In this paper, we choose Re=50 and 250 in our study.

II. BASIC EQUATIONS AND METHOD OF ANALYSIS

Consider the unsteady viscous incompressible flow past a circular cylinder of radius a when the flow starts at time t=0+ with a constant velocity U. The governing equation of motion in polar coordinates are

$$\frac{\partial\omega}{\partial T}+\frac{\partial\psi}{\partial\theta}\frac{\partial\omega}{\partial r}-\frac{\partial\psi}{\partial r}\frac{\partial\omega}{\partial\theta}=\frac{1}{Re}\left[\frac{\partial^2\omega}{\partial r^2}+\frac{1}{r}\frac{\partial\omega}{\partial r}+\frac{1}{r^2}\frac{\partial^2\theta}{\partial\theta^2}\right] \quad (1)$$

where the terms has been normalized using the radius a, and the velocity U. The Reynolds number is defined as $Re=aU/\nu$. The angle θ is measured from the front of the cylinder. The stream function ψ, the vorticity ω and the velocity components u_r and u_θ in the r and θ directions are

$$\omega=\frac{\partial^2\psi}{\partial r^2}+\frac{1}{r}\frac{\partial\psi}{\partial\theta}+\frac{1}{r^2}\frac{\partial\psi^2}{\partial\theta^2}. \quad (2)$$

$$u_r=-\frac{1}{r}\frac{\partial\psi}{\partial\theta},\quad u_\theta=\frac{\partial\psi}{\partial r}. \quad (3)$$

The boundary conditions are

$$\psi=\omega=0 \qquad \text{when } \theta=0 \text{ and } \pi. \quad (4)$$

$$\psi=\frac{\partial\psi}{\partial r}=0 \qquad \text{when } r=1. \quad (5)$$

$$\psi\to r\sin\theta,\ \omega\to 0 \text{ for } r\to\infty \quad (6)$$

The vorticity on the cylinder is given by Roach (1976)

$$\omega_{iw}=\frac{2(\psi_{iw+1}-\psi_{iw})}{\Delta r^2} \quad (7)$$

Since it is desirable to have finer meshes near the cylinder and more coarse ones far away, modified polar coordinates is used to transform the circular arc into a flat boundary,

$$\zeta=\ln r \text{ or } r=\exp(\zeta), \quad (8)$$
$$\text{and } \theta=\theta.$$

The defining equations then become

$$\exp(2\zeta)\frac{\partial\omega}{\partial T}+\frac{\partial\psi}{\partial\theta}\frac{\partial\omega}{\partial\zeta}-\frac{\partial\psi}{\partial\zeta}\frac{\partial\omega}{\partial\theta}=\frac{1}{Re}\left[\frac{\partial^2\omega}{\partial\zeta^2}+\frac{\partial^2\omega}{\partial\theta^2}\right] \quad (9)$$

$$\frac{\partial^2\psi}{\partial\zeta^2}+\frac{\partial^2\psi}{\partial\theta^2}=\exp(2\zeta)\omega \quad (10)$$

$$u=-\exp(-\zeta)\frac{\partial\psi}{\partial\theta},\quad u_\theta=\exp(-\zeta)\frac{\partial\psi}{\partial\zeta} \tag{11}$$

$$\psi=\omega=0 \qquad \text{for } \theta=0 \text{ and } \pi \tag{12}$$

$$\psi=\frac{\partial\psi}{\partial r}=0 \quad \text{for } r=1 \tag{13}$$

$$r\to r\sin\theta \quad \omega\to 0 \qquad \text{for } r\to\infty \tag{14}$$

$$\omega_{iw}=\frac{2(\psi_{iw+1}-\psi_{iw})}{\Delta\zeta^2} \quad \text{for cylinder surface.} \tag{15}$$

Let n denote the number of time steps and ΔT the size of time increment. The scheme for advancing the solution from time $n\Delta T$ to time $(n+1)\Delta T$ consisting of calculating new values of the vorticity, ω_{ij}^{n+1} at all grid points via the vorticity equation (9) by finite-difference approximation of the boundary conditions, the values of vorticity ω_{ij}^{n} and the stream function ψ_{ij}^{n} from the previous time step.

Hopscotch method, developed by Gourley (1970) is used to compute the vorticity at the new time step. The method divides each time step in two sweeps of the mesh. In the first and subsequent odd-number time steps, the points with i+j equal to odd are calculated based on the current values of neighboring points. For vorticity equation (9), the new values of vorticity ω_{ij}^{n+1} is given by

$$\omega_{ij}^{n+1}=\omega_{ij}^{n}+\Delta T\ \exp(-2\zeta_{ij})\left[-\frac{\psi_{i+1,j}^{n}-\psi_{i-1,j}^{n}}{2\Delta\theta}\ \frac{\omega_{ij+1}^{n}-\omega_{ij-1}^{n}}{2\Delta\zeta}\right.$$
$$+\frac{\psi_{i,j+1}^{n}-\psi_{i,j-1}^{n}}{2\Delta\zeta}\ \frac{\omega_{i+1,j}^{n}-\omega_{i-1,j}^{n}}{2\Delta\theta}\Big]+\frac{1}{Re}\left[\frac{\omega_{i+1,j}^{n}+\omega_{i-1,j}^{n}-2\omega_{ij}^{n}}{\Delta\theta^2}\right.$$
$$\left.+\frac{\omega_{ij+1}^{u}+\omega_{i,j-1}^{n}-2\omega_{ij}^{n}}{\Delta\zeta^2}\right],\quad \text{for } j+j=\text{odd}. \tag{16a}$$

The second sweep at the same time level, the points (i+j) equal to even are calculated using the new values of the neighboring points obtained in the first sweep,

$$\omega_{ij}^{n+1}=\omega_{ij}^{n}+\Delta T\ \exp(-2\zeta_{i,j})\left[-\frac{\psi_{i+1,j}^{n}-\psi_{i-1,j}^{n}}{2\Delta\theta}\ \frac{\omega_{ij+1}^{n+1}-\omega_{ij-1}^{n+1}}{2\Delta\zeta}\right.$$
$$+\frac{\psi_{i,j+1}^{n}-\psi_{i,j-1}^{n}}{2\Delta\zeta}\ \frac{\omega_{i+1,j}^{n+1}-\omega_{i-1,j}^{n+1}}{2\Delta\theta}\Big]+\frac{1}{Re}\left[\frac{\omega_{i+1,j}^{n+1}+\omega_{i-1,j}^{n+1}-2\omega_{ij}^{n+1}}{\Delta\theta^2}\right.$$
$$\left.-\frac{\omega_{i,j+1}^{n+1}+\omega_{i,j-1}^{n+1}-2\omega_{i,j}^{n+1}}{\Delta\zeta^2}\right],\quad \text{for } i+j=\text{even}. \tag{16}$$

The first sweep consists of forward-time-central-space differencing for (i+j) odd, whilst the second sweep is fully implicit in the sense that the new values

are required at (i, j), (i ± 1, j), and (i, j ± 1) but this implicitness involving no simultaneous algebraic solutions.

New values of stream function ψ_{ij}^{n+1} are computed for all grid points by using finite-difference approximation of the Poisson equation (10), the boundary conditions, the new values of vorticity ω_{ij}^{n+1} and the old values of the stream function ψ_{ij}^{n}. The most popular numerical method solving this elliptic equation is the successive over-relaxation method.

For numerical solution of equation (10), we take the difference approximation as

$$\frac{\psi_{i+1,\,j}+\psi_{i-1,\,j}-2\psi_{i,\,j}}{\Delta\theta^2}+\frac{\psi_{i,\,j+1}+\psi_{i,\,j-1}-2\psi_{i,\,j}}{\Delta\zeta^2}=\exp(2\zeta_{jj})\,\omega_{ij} \tag{17}$$

To use successive over-relaxation procedure, we replace this equation by

$$\psi_{i,\,j}^{k+1}=\psi_{i,\,j}^{k}+\frac{\gamma}{2(1+\beta^2)}\Big[\psi_{i+1,\,j}^{k}+\psi_{i-1,\,j}^{k+1}+\beta^2(\psi_{i,\,j+1}^{k}+\psi_{i,\,j-1}^{k+1})$$

$$-2(1+\beta^2)\psi_{i,\,j}^{k}-\Delta\theta^2\exp(2\zeta_{ij})\,\omega_{ij}\Big] \tag{18}$$

where β is $\Delta\theta/\delta\zeta$, γ is the over-relaxation factor, and the super-script k and $k+1$ indicate the number of the $k-$th and $(k+1)-$th interation respectively. The optimum over-relaxation factor is investigated by many scholors (Carrier and Person, 1976, Section 14-10). Jain and Rao (1969) chose $\gamma=1.85$. After some tests for different values of γ, we found the optimum over-relaxation factor $r=1.80$.

The successive over-relaxation method consists of applying equation (18) at every interior mesh point in regular succession. The points are scanned row by row from left to right starting from the row next to the boundary and going up the column. This completes one interation. The procedure is repeated until a sufficient convergence obtained. The convergence criterion is

$$\max_{i,\,j}\left|\frac{\psi_{i,\,j}^{k+1}-\psi_{i,\,j}^{k}}{\psi_{i,\,j}^{k+1}}\right|<0.01\,. \tag{19}$$

III. COMPUTATIONAL PROCEDURE

The numerical solution of the flow over an impulsively started cylinder is an initial-boundary value problem. Besides the boundary conditions, the stream function and vorticity distribution must be know at the initial time in order to carry out the finite difference computation.

The boundary conditions are described in Section 2. The initial values of stream function and vorticity are obtained from following equations at every interior grid point for a given Reynolds number and time (Chien, 1977).

$$\psi(r,\theta,t)=\left\{r-r^{-1}-\frac{4}{\sqrt{\pi}}\frac{\sqrt{T}}{\sqrt{Re}}(r^{-1}+\sqrt{\pi}\,\eta\,\mathrm{erfc}\eta\right.$$
$$-e^{-\eta^2})-\frac{T}{Re}\left[r^{-1}-(6\eta^2+1)\ \mathrm{erfc}\eta\right.$$
$$\left.+\frac{6}{\sqrt{\pi}}e^{-\eta^2}\right]-2\left(\frac{T}{Re}\right)^{\frac{3}{2}}\left[\left(\frac{16}{3}\eta^3+\eta\right)\ \mathrm{erfc}\eta\right.$$
$$\left.\left.-\frac{1}{\sqrt{\pi}}\left(\frac{16}{3}\eta^2-\frac{1}{6}\right)e^{-\eta^2}-\frac{1}{6\sqrt{\pi}}\right]\right\}\sin\theta$$
$$+8\frac{T\sqrt{T}}{\sqrt{Re}}\left[\int_0^\eta f(\zeta)d\zeta-\frac{1}{\sqrt{\pi}}\left(1+\frac{4}{9\pi}-\frac{4\sqrt{2}}{3}\right)\right.$$
$$(r^{-2}+2r-3)+2\frac{\sqrt{T}}{\sqrt{Re}}\int_0^\eta g_3(\zeta)d\zeta\Big]$$
$$\sin\theta\cos\theta+16\frac{T^2\sqrt{T}}{\sqrt{Re}}\left[\int_0^\eta F_3(\zeta)d\zeta\right.$$
$$\left.\sin\theta\cos^2\theta-\int_0^\eta f_3(\zeta)\,d\zeta\sin^3\theta\right] \qquad (20)$$

$$\omega(r,\theta,t)=\frac{\partial^2\psi}{\partial r^2}+\frac{1}{r}\frac{\partial\psi}{\partial r}+\frac{1}{r^2}\frac{\partial^2\psi}{\partial\theta^2} \qquad (2)$$

where $f(\zeta)$, $g_3(\zeta)$, $F_3(\zeta)$ and $f_3(\zeta)$ are palynomials of error function.

Numerical integration of equation (9) and (10) is carried out according the following steps:

1) Time is stepped ΔT, and new values of vorticity are computed from equation (16).

2) Iterative computation for new values of stream function ψ using equation (18), is continued until a sufficient convergence condition (19) is satisfied.

3) Compute the values of the vorticity on the cylinder surface using equation (15).

The above procedure is repeated for subsequent time steps.

IV. RESULTS FOR $Rd=2Re=100$

The study of the case for $Re=50$, i.e. $Rd=100$, is motivated to see if the second bubble exists for Rd less than 550. We use the same grid structure as that we study for the case $Rd=500$, and have the same conclusions of the

experiments of Honji and Taneda (1969) and the numerical computations of Pantel (1976). No secondary bubble was found for Rd less than 500.

The initial conditions for the computation are the stream function and vorticity at T=0.02 obtained from equations (19) and (2). A small bubble was first observed at T=0.54 located on the cylinder surface from $\theta=171°$ to 180°, where the angle is measured from the front stagnation point. We can infer that the initial separation time is about T=0.52. Comparing the results of the existing solutions in Table 2-7 of Chien (1977), we see that the present numerical solution agrees excellently with that of Collins and Dennis (1973b) T=0.513.

The stream function and velocity profiles at early time, T=0.2, coincide with that obtained from the analytic solution of Chien (1977) as shown his Figures 2-1(c), 2-6(c) and 2-7(c).

The development of the flow pattern at various time is shown in Figure 1. Those for the tangential velocity is in Figures 2 Figure 3 shows the development of vorticity distribution on the surface of the cylinder with time from T=0.6 to T=6.0.

Although we can continue the computation for even larger times, the results after T=2.5 are not accurate because the far field boundary condition, namely zero vorticity, does not hold at r=exp (1.0). The vorticity diffused far away from the cylinder especially in the neighborhood of the rear stagnation point. Numerical solutions by Kawaguti and Jains (1966), Collins and Dennis (1973b), and experimental measurement by Honji and Taneda (1972) show that the wake length grows continuously to T=24 to a length of S=7d$\sim$8d. See Collins and Dennis (1973b) Figure 2. Because of the limit of the computer capacity, we should have another attempt to study this problem in the future.

Figure 3 shows that the vorticity distribution over the surface of the cylinder remains smoot up to T=2.0. A little bit time later, the curve shows a kink in the separation region, $\theta_s < \theta < \pi$. The kink continues to be present as T increases. Although it never becomes sufficiently pronounced as it does for higher values of Reynolds numbers, Figures 6. The vorticity within the separation region grows less negative and never increases to positive. This implies the non-existence of the secondary bubble. Moreover, as T goes on further, the kink eventually becomes less pronounced which signified the approach of a steady-state solution. The trend agrees with that of Collins and Dennis (1973b) which approaches steady-state solution at T=25.

The flow patterns, Figures 1(a) to 1(d), show that as time increases, the recirculation region is enlarged and the streamlines are displaced outward. The

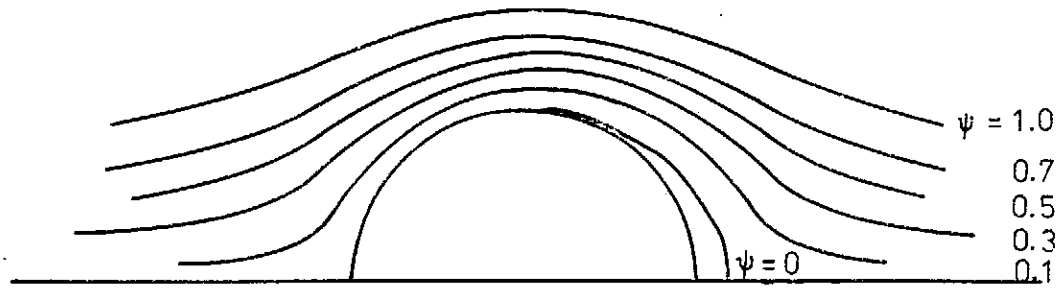

FIG. 1(a). Flow Pattern at Re=50 for T=0.6

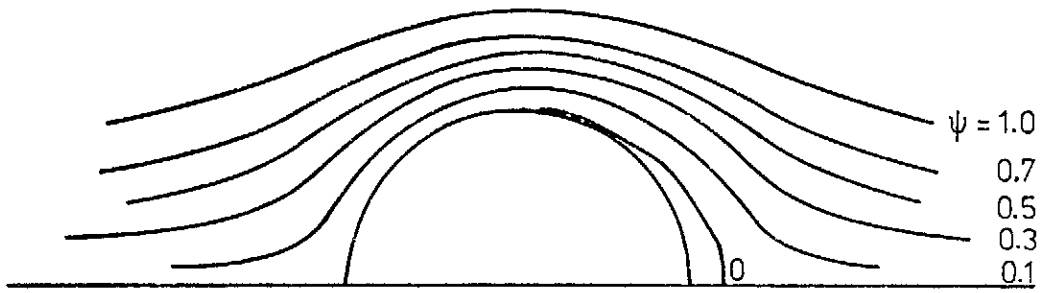

FIG. 1(b). Flow Pattern at Re=50 for T=1.0

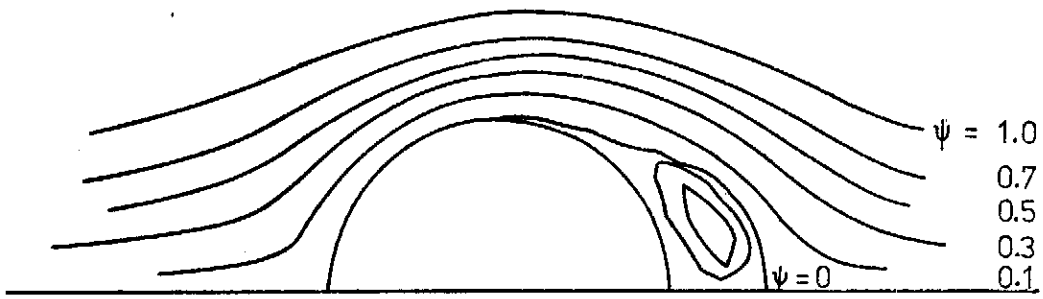

FIG. 1(c). Flow Pattern at Re=50 for T=2.0

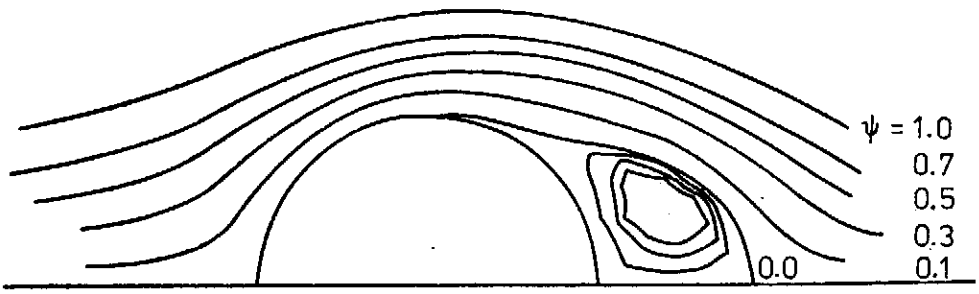

FIG. 1(d). Flow Pattern at Re=50 for T=3.0

larger the time, the more negative becomes the stream function in the recirculation region. Consequently, the region of negative velocity becomes larger. We plot the tangential velocity profiles up to r=1.5. The radial range is large enough to depict the velocity profiles at T=0.6, Figure 2(a). In Figure 2(d), T=3.0, from $\theta=120°$ to 165°, the radial range is not adequate to describe the velocity profiles that asymptotically approach to potential flow at outer rangion.

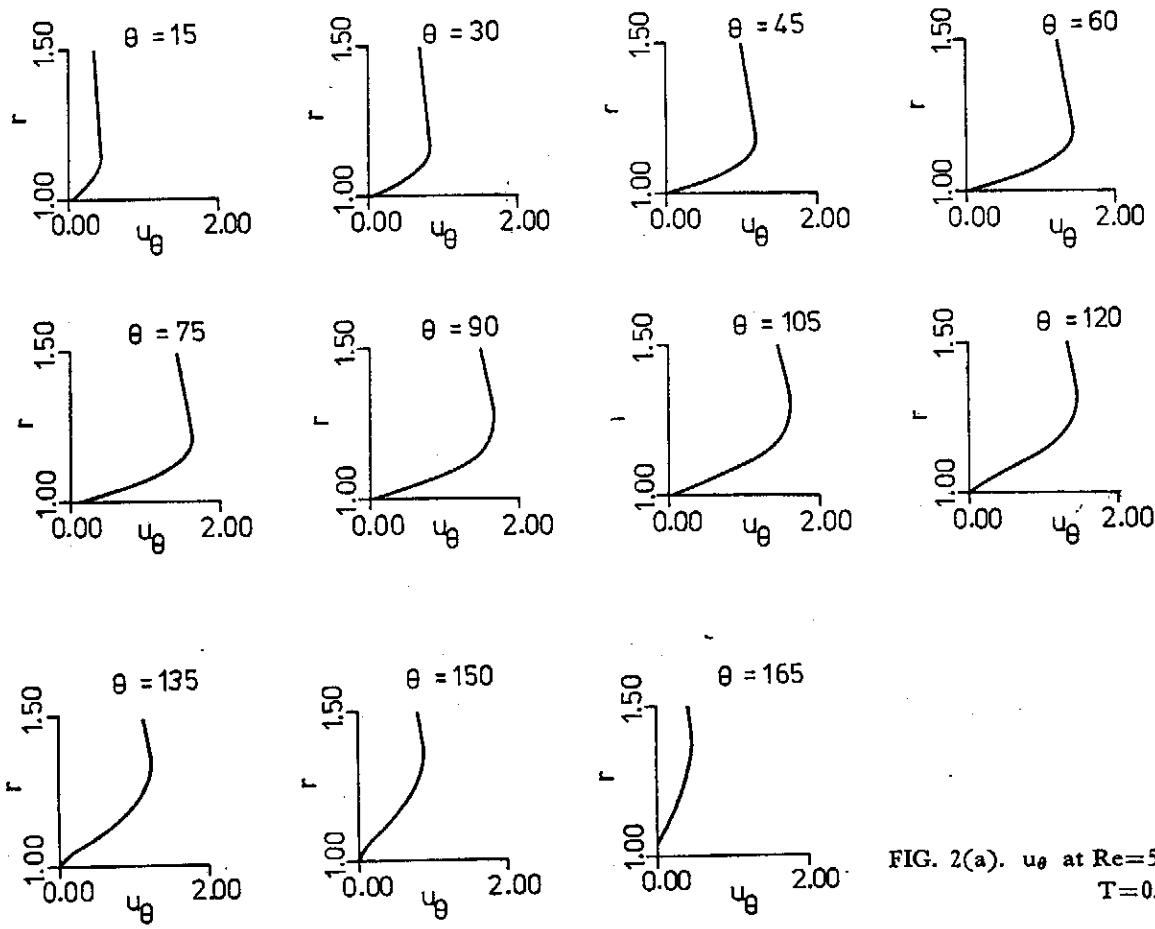

FIG. 2(a). u_θ at Re=50 T=0.6

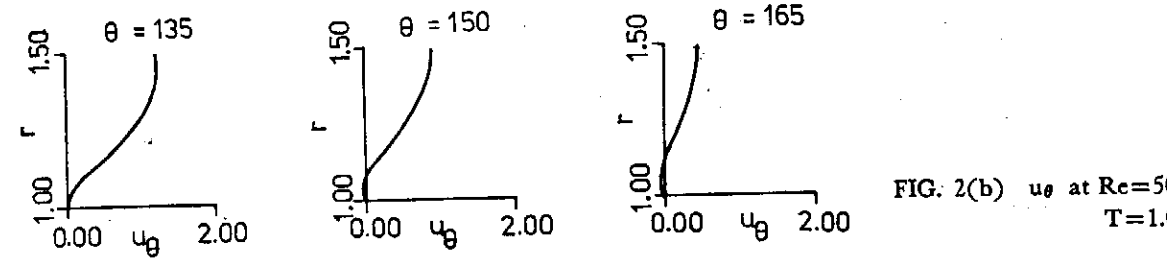

FIG. 2(b) u_θ at Re=50 T=1.0

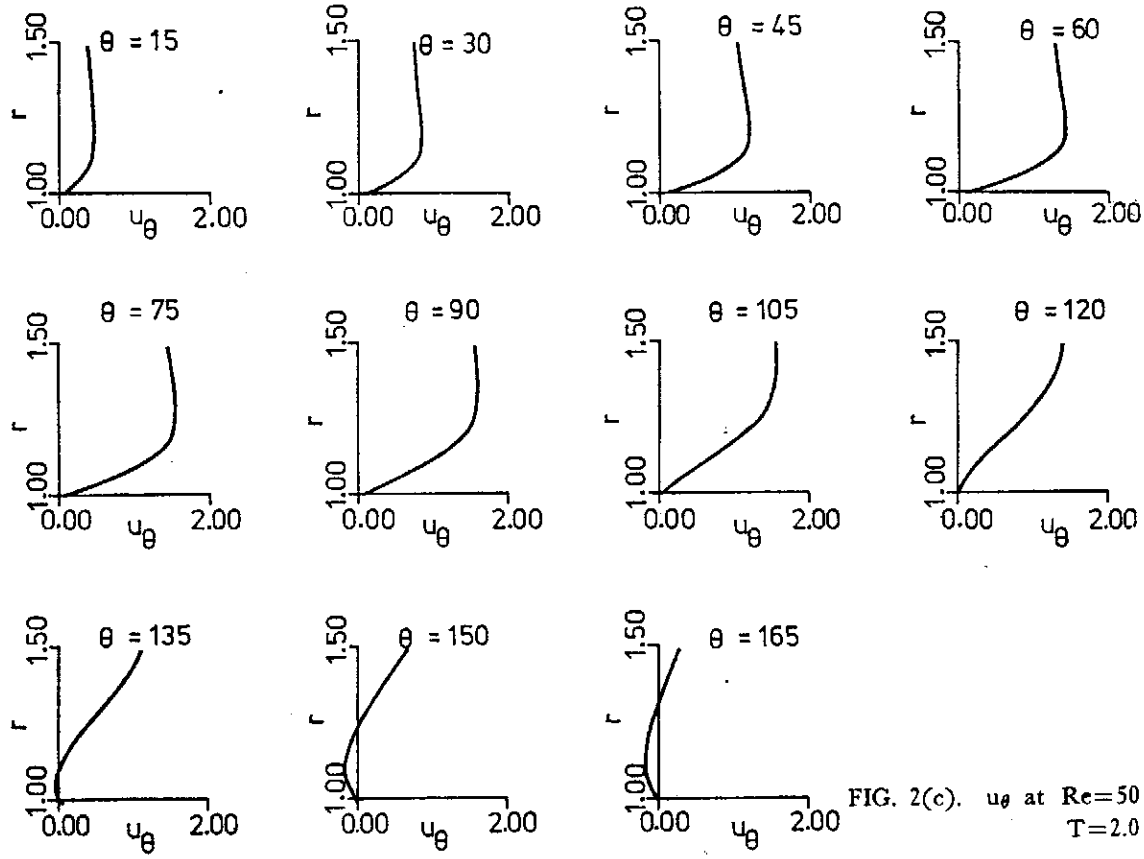

FIG. 2(c). u_θ at Re=50 T=2.0

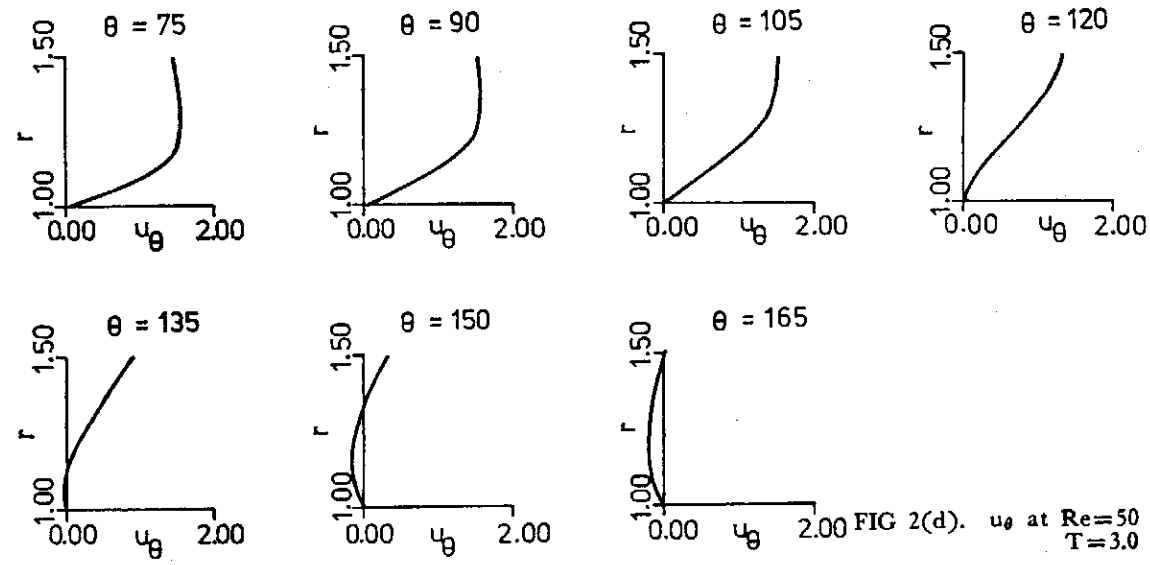

FIG 2(d). u_θ at Re=50 T=3.0

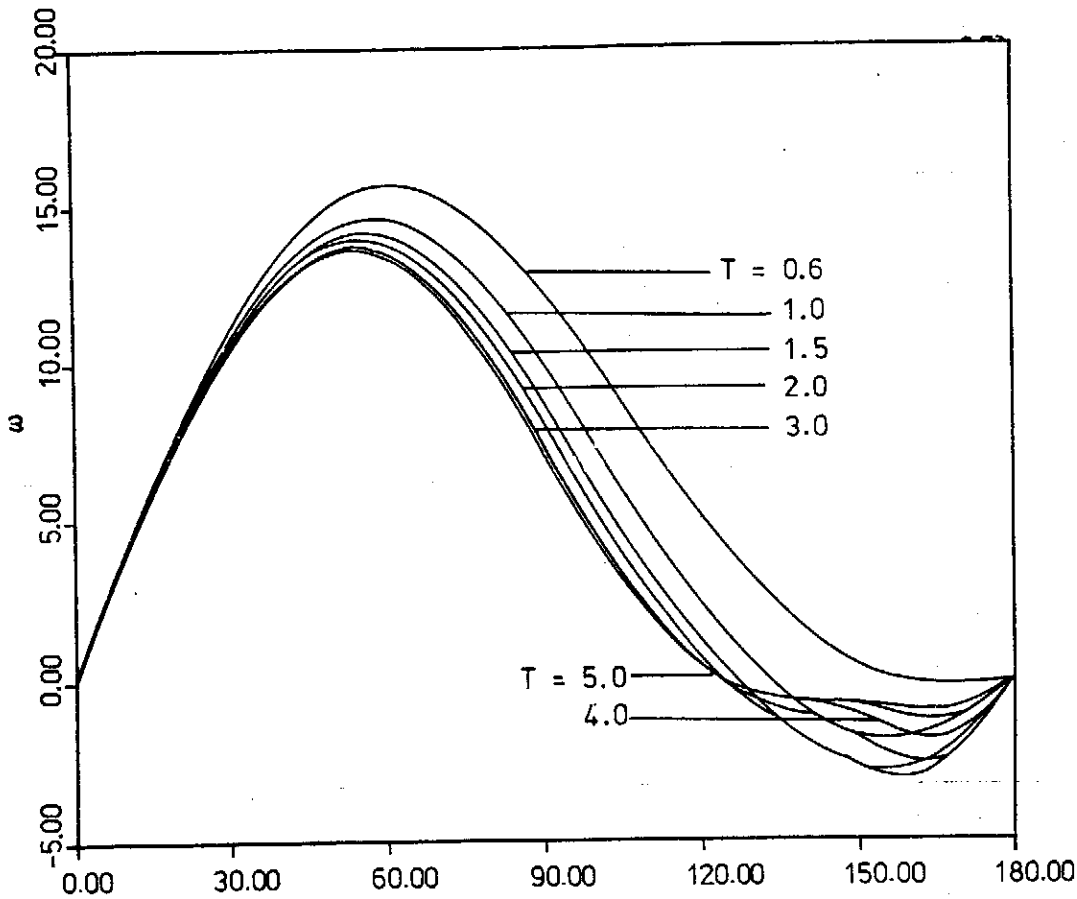

FIG. 3. Vorticity Distribution on the Cylinder at Re=50 for Moderate Time.

V. RESULTS FOR Rd=2Re=500

One of the reasons for finding a solution at Re=250, Rd=500, is to compare the results of Son aud Hanratty (1969), Collins and Dennis (1973b). The experiments of Honji and Taneda (1969) indicated that at Rd=550 a pair of secondary vortices are found on the surface of the cylinder at the ahead of the main vortices. They appear at about T=4.8. The calculation of Son and Hanratty (1969) also indicated the appearance of o pair of secondary vortices at Rd=500. They first appeared at about T=2.78 which is much smaller than the corresponding value of T for the experiment at Rd=550 and eventually decrease in size. Collins and Dennis (1973b) reported that the secondary vortices first appear at T=2.75· Patel (1976) calculated T=10.12, which is not accurate because his initial separation T=0.54 is too large compared to the existing solutions. The present study confirms these calculations for the early stages of the flow in that the secondary vortices first appear at about T=2.56.

The computation can not be continued beyound T=6.6, while Collins and Dennis (1973b) stopped their computation at T=4.8, at which stage the procedure broke down.

The initial flow pattern used for numerical computation is at T=0.1. The development of the flow patterns with time until T=4.8 are shown in Figures 4(a) to 4(e). Appearance of the first bubble at about T=0.4 agrees with the present analytic solution at T=0.375. The corresponding T for Collins and Dennis (1973b) is 0.394. Figure 4(d) and (e) show that the secondary bubble appears at $\theta=145°$ from the front stagnation point. In the bubble, the fluid rotates in a direction opposite to that of the main vortex. This is shown in Figure 6 at T=2.5 to 3.2. The vorticity within the separation region grows from negative to positive. The tangential velocity in the separation region is negative, while in the secondary bubble it is positive, Figure 5(f) at $\theta=150°$.

The development of tangential velocity profiles are shown in Figure 5 from T=0.6 to T=3.2. The variation is more pronounced than those at Re=50, Figure 2.

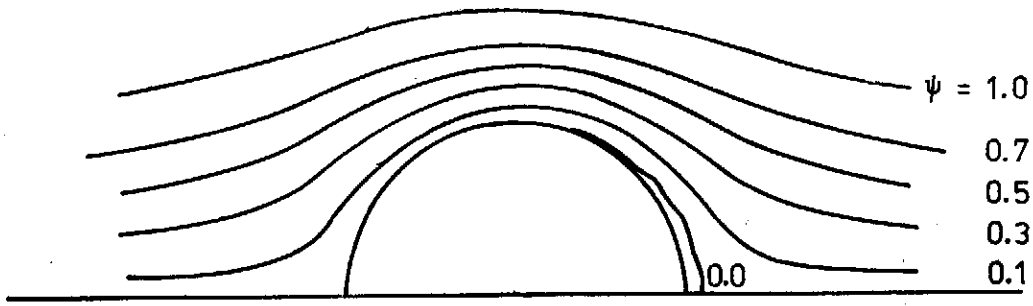

FIG. 4(a). Flow Pattern at Re=250 for T=0.6

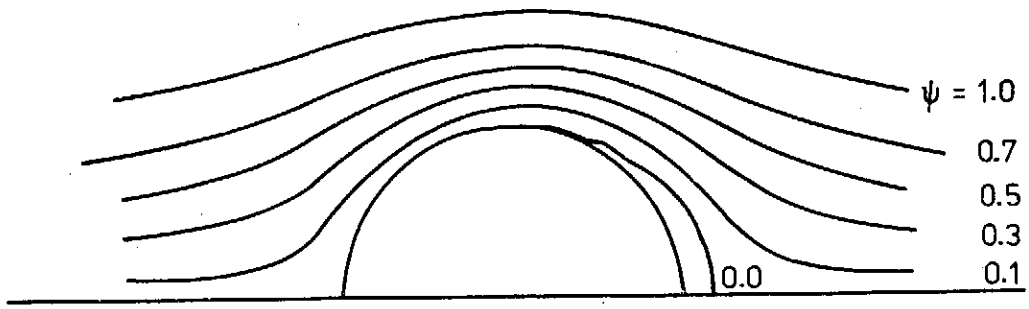

FIG. 4(b). Flow Pattern at Re=250 for T=1.0

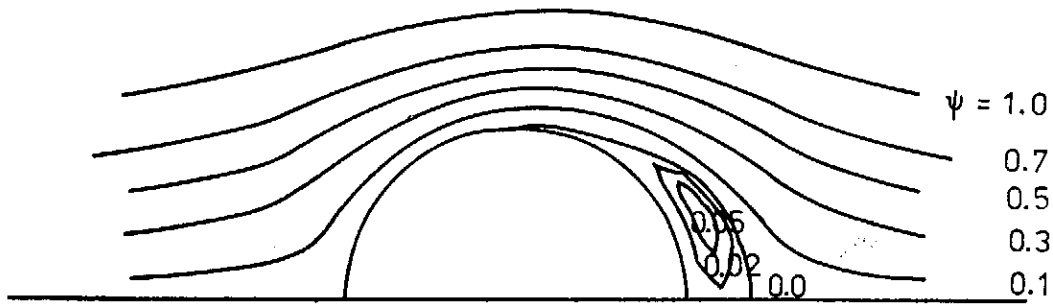

FIG. 4(c). Flow Pattern at Re=250 for T=1.5

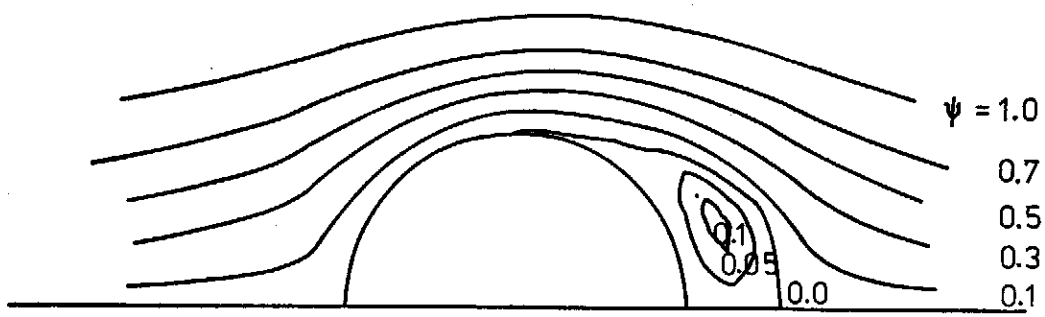

FIG. 4(d). Flow Pattern at Re=250 for T=2.0

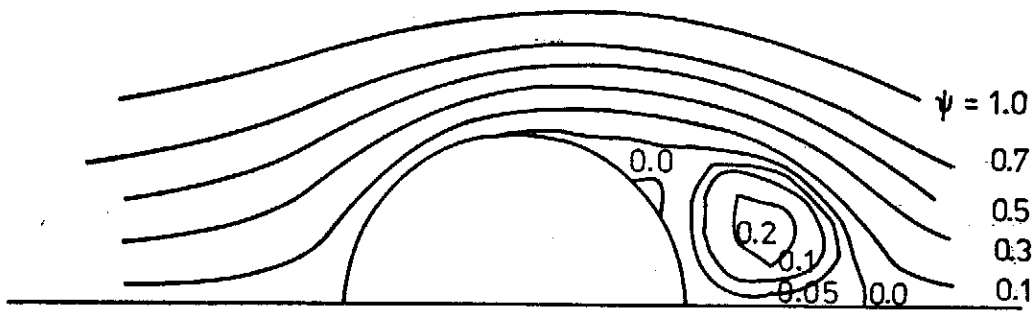

FIG. 4(e). Flow Pattern at Re=250 for T=3.2

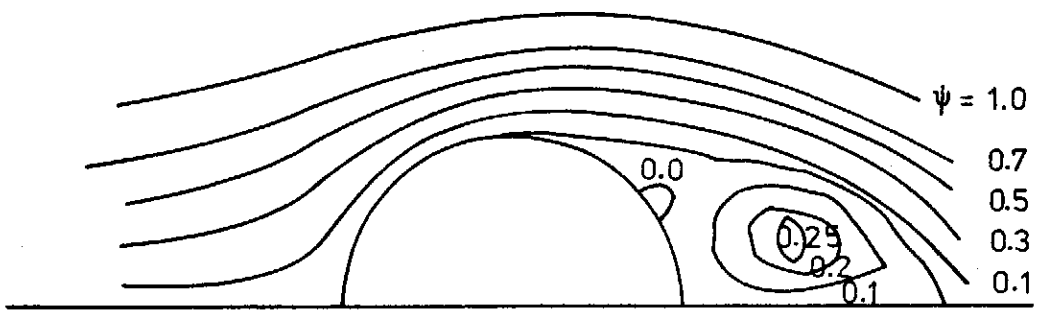

FIG. 4(f). Flow Pattern at Re=250 for T=4.8

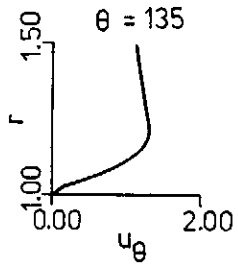

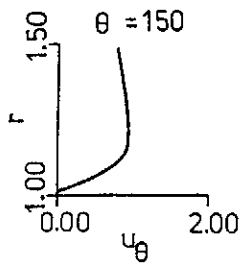

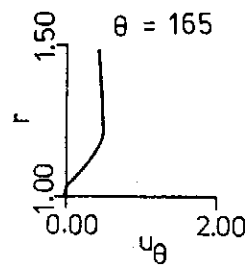

FIG. 5(a). u_θ at Re=250 T=0.6

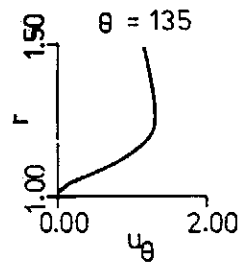

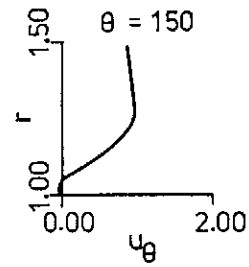

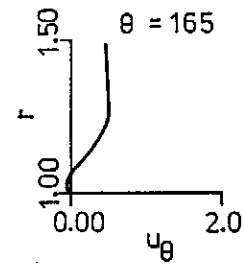

FIG. 5(b). u_θ at Re=250 T=0.8

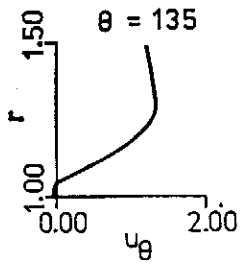

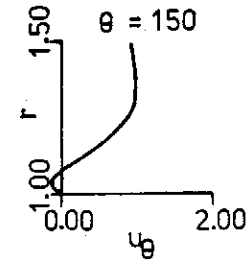

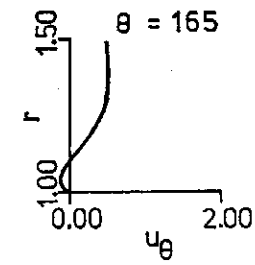

FIG. 5(c). u_θ at Re=250 T=1.0

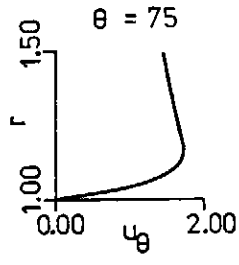

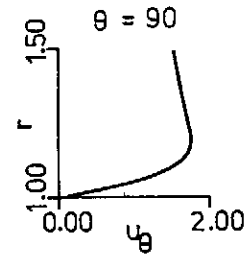

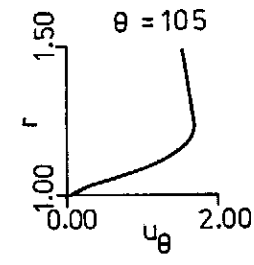

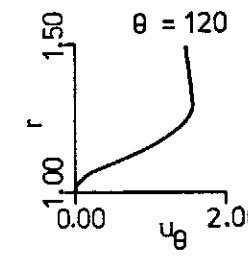

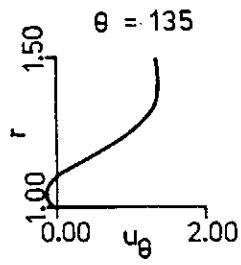

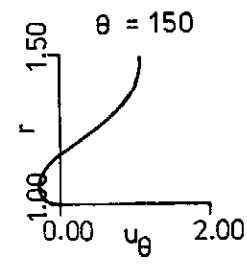

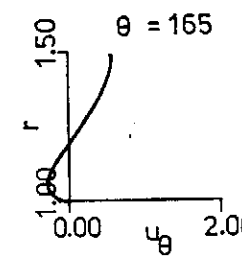

FIG. 5(d). u_θ at Re=250 T=1.5

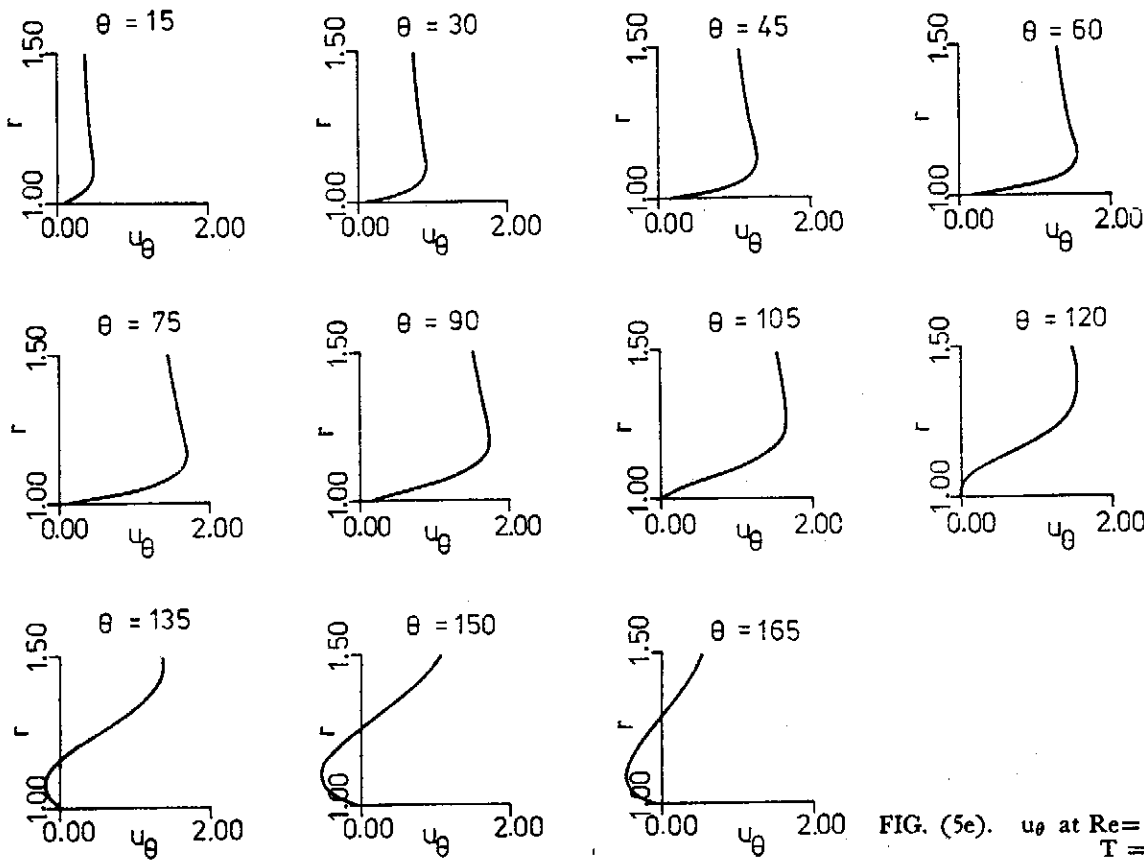

FIG. (5e). u_θ at Re=250 T =2.0

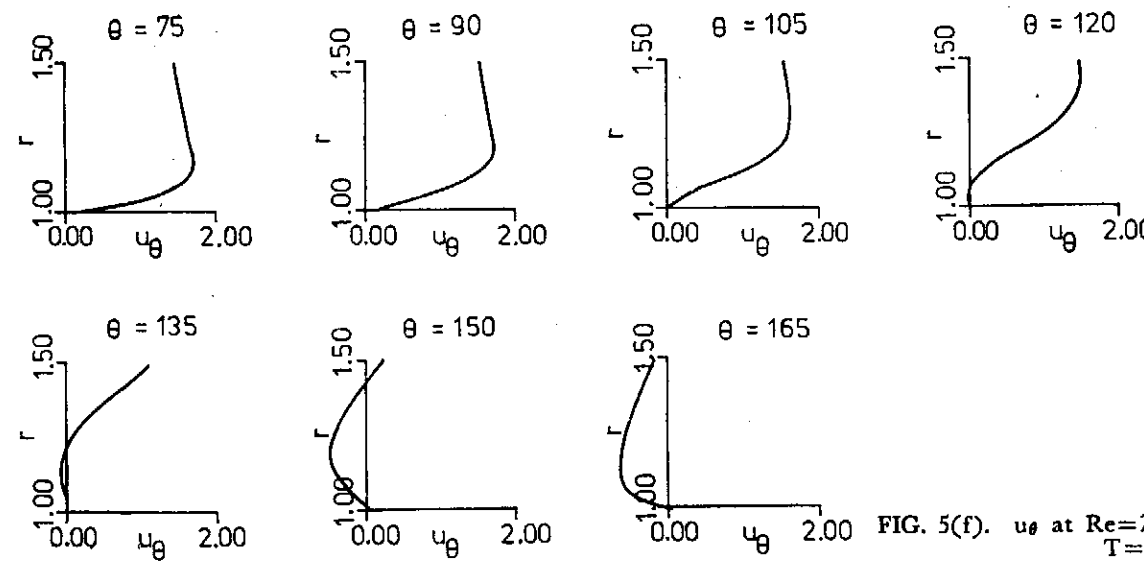

FIG. 5(f). u_θ at Re=250 T=3.2

The vorticity distribution over the surface of the cylinder is shown in Figure 6. The comparison of the vorticity distribution on the cylinder between Son and Hanratty (1969), Collins and Dennis (1973b) is made in Table 1.

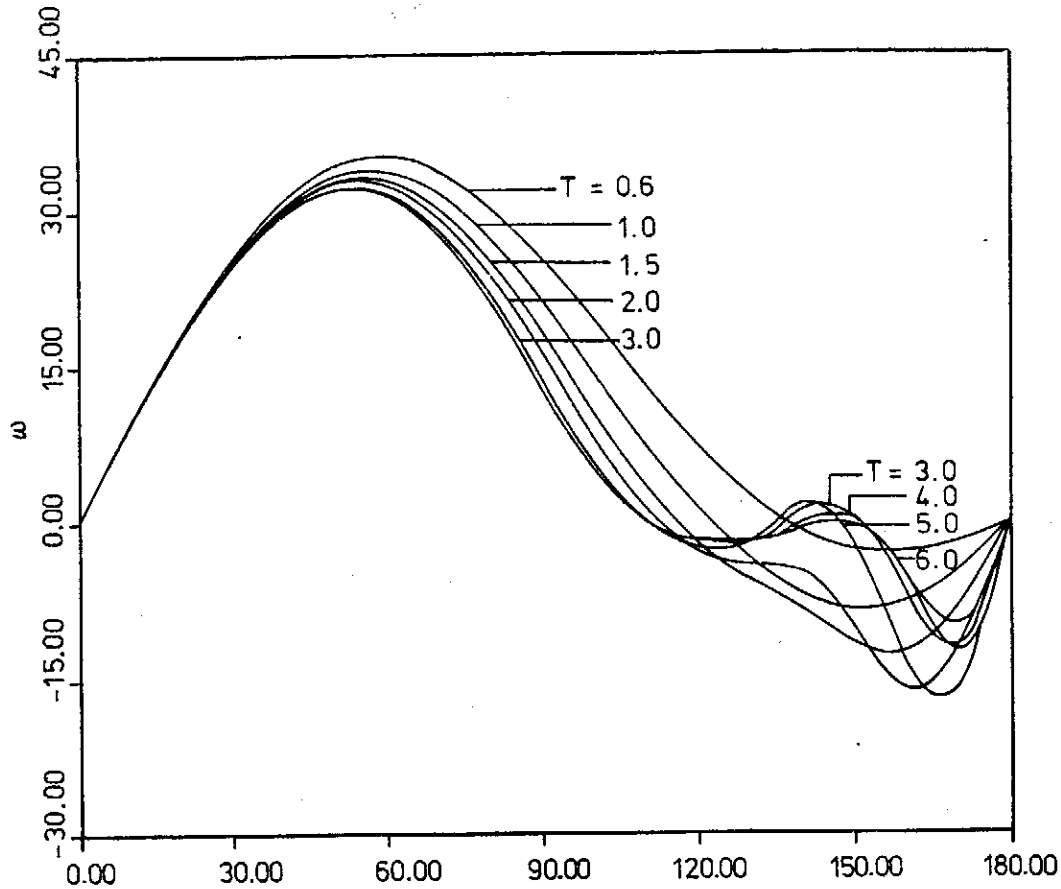

FIG. 6. Vorticity Distribution on the Cylinder at Re=250 for Moderate Time.

TABLE 1. Comparison of Verticity Distribution on the Cylinder at Rd = 2Re = 500 for Moderate Time

θ	45	90	135
		T=1.1	
Sons & Hanratty (1969)	33.0	20.0	−8.3
Collins & Dennis (1973b)	31.6	20.0	−7.08
Present	32.15	20.47	−6.41
		T=2.0	
Sons & Hanratty (1969)	32.0	15.0	−4.2
Collins & Dennis (1973b)	30.4	15.0	−4.38
Present	31.67	16.10	−4.27
		T=3.18	
Sons & Hanratty (1969)	30.5	10.0	0.80
Collins & Dennis (1973b)	28.8	10.0	0.88
Present	31.34	13.30	0.17

Collins and Dennis (1973b, Figure 11, P. 124) confirmed that the results of Son and Hanratty (1969) coincided exactly with theirs. We read the Figure of Son and Hanratty (1969, Figure 14, P. 381) and listed in the table. There are some difference. For $T=1.1$ and $T=2.0$, the three results agree closely, while at $T=3.18$, the agreement is not good enough, probably because of the smaller computation domain in our study.

The length of wake behind the circular cylinder is a function of time. At $T=1.0$, we get the wake length $S=0.16r$. Panikker and Lavan (1975) obtained $S=0.21r$, and $S=0.26r$ measured by Honji and Taneda (1969) experiment for $Rd=550$. At $T=2.0$, we got $S=0.57r$ for $Rd=500$, and Honji and Taneda (1969) has $S=0.65r$ for $Rd=550$ by experiment.

VI. CONCLUSION

The major objective of this study is to solve the problem of the unsteady viscous flow over an impulsively started cylinder. The analytic solution obtained by the method of matched asymptotic expansion to the third order is used as initial conditions for numerical integration. In this study, we compare our results with the existing solutions. The initial separation time and the vorticity distribution on the surface of the cylinder agree with the computations of Collins and Dennis (1973a, b).

The flow patterns, tangential velocity profiles and vorticity distribution over the cylinder surface were plotted and studied at various time. By the figures, we can see the development of these flow properties.

From this study, the following major conclusions can be drawn.

1) Separation of the viscous layer starts at the rear stagnation point and progresses along the cylinder asymptotically to a steady separation angle. The higher the Reynolds number, the sooner the separation angle reaches its steady value.

2) No second bubble was found for Reynold number less than 250. For $Re=250$, the second bubble appears at $T=2.56$ and 2.08 respectively.

3) The numerical solutions with viscous layer initial conditions, namely Collins and Dennis (1973b) and this study, broke down for $Re=250$ at $T=4.8$ and 6.6 respectively. While the potential flow started solution can be continued to large time, Son and Hanratty (1969), Jain and Rao (1969) and others. The experimental results of Honji and Taneda (1969, Figure 7, P. 171) indicate that a transition from a laminar to a turbulent wake takes place at $T=11$ for $Re=250$. Therefore, the laminar equations would not be expected to apply for large value of Re and T.

REFERENCES

Chien, L. C. (1977). Impulsively Started Viscous Flow Over a Circular Cylinder. Ph. D. Dissertation, Department of Aerospace Engineering, University of Southern California.

Collins, W. M. and Dennis, S. C. R. (1973a). The Initial Flow Past an Impulsively Started Circular Cylinder. *Quarterly Journal of Mechanics and Applied Mathematics*, Vol. 26, pp. 53-75.

Collins, W. M. and Dennis, S. C. R. (1973b). Flow Past an Impulsively Started Circular Cylinder. *Journal of Fluid Mechanics*, Vol. 60, Part 1, pp. 105-127.

Carrier, G. F. and Person, C. E. (197b). Partial Differential Equation Theory and Technique, *Academic Press*, New York.

Gourley, A. R. (1970). Hopscotch: A Fast Second-order Partial Differential Equation Solver, *Journal of Institute of Mathematics and Applications*, Vol. 6, pp. 375-390.

Honji, H. and Taneda, S. (1969). Unsteady Flow Past a Circular Cylinder. *Journal of Physics Society of Japan*, Vol. 27, pp. 1668-1677.

Honji, H. and Taneda, S. (1972). Starting Flow Past Spheres and Elliptic Cylinders, *Report of Research Institute of Applied Mechanics*, Kyushu University, Vol. 19, 265.

Jain, P. C. and Rao, K. S. (1969). Numerical Solution of Unsteady Viscous Incompressible Fluid Flow Past a Circular Cylinder, *Physics of Fluids*, Vol. 12, pp. II-57 to II-64.

Jain, P. C. and Goel, B. S. (1976). Shielding of Vortices Behind a Circular Cylinder. *Computers and fluid*, Vol. 4, pp. 137-142.

Kawaguti, K. and Jain P. C. (1966). Numerical Study of a Viscous Fluid Past a Circular Cylinder. *Journal of Physics Society of Japan*, Vol. 21, pp. 2055-2062.

Payne, R. B. (1958). Calculation of Unsteady Viscous Flow Past a Circular Cylinder, *Journal of Fluid Mech.* 4, pp. 81-86.

Panikker, P. K. G. and Lavan, Z. (1975). Flow Past Impulsively Started Bodies Using Green's Function. *Journal of Computational Physics*, Vol. 18, pp. 46-65.

Pantel, V. A. (1976). Time-dependent Solutions of the Viscous Incompressible Flow Past a Cirular Cylinder by the Method of Series Trancation. *Computers and* Vol. 4, pp. 13-27.

Roache, P. J. (1976). *Computational Fluid Dynamics.* Hermosa Publishers, New Mexico.

Son, J. S. and Hanratty, T. J. (1969). Numerical Solution of Flow Around a Cylinder at Reynolds Number of 40, 200 and 500. *Journal of Fluid Mechanics*, Vol. 35, Part 2, pp. 369-386.

大氣垂直速度計算之研究

A Comparative Study of Vertical Motion Computations

曾　忠　一

中央研究院物理研究所
國立臺灣大學大氣科學系

摘　　要

垂直速度在從事大氣的診斷和預報研究以及大氣物理過程的參數化研究方面是很重要的參數，可是在大氣大幅度運動中其數值很小，不易由觀測儀器直接求得，必須由其他氣象變數間接計算求得。一般說來，傳統的垂直速度計算法有三種：即運動學法、絕熱法和動力學法。本研究利用變分最佳化的原理，設計一種新的垂直速度計算法，校正水平風的觀測值，使其滿足連續方程式和熱力學方程式，以維持計算出來的垂直速度和其他氣象變數的內部一致。本研究利用1975年6月10日的梅雨資料來探討這種方法的適用性。研究結果顯示，這種方法求得的垂直速度與天氣系統、衛星圖片符合。

此外本研究比較五種垂直速度計算法的結果。研究結果顯示，準地轉垂直速度方程式所求得的垂直速度在梅雨鋒面處相當微弱。此外兩種變分程式和運動學法所得的垂直速度與天氣系統和衛星圖片顯出的符合。

壹、研究目的與有關文獻之檢討

垂直速度在從事大氣運動的診斷和預報研究以及大氣物理過程的參數化研究方面是很重要的參數，可是在大氣大幅度運動中其數值很小，不易由現有的觀測儀器直接得到，必須由其他氣象變數的觀測值，諸如水平風溫度或壓力分佈間接計算求得。一般說來，較常使用的垂直速度計算法有三種：第一種是運動學法，就是用連續方程式由水平風的觀測值求得。第二種方法是絕熱法，就是利用熱力學方程式由水平風和溫度的觀測值求得。第三種方法是動力學法，利用準地轉方程式組或平衡方程式組的垂直速度方程式只由等壓面上的高度求得。這三稱方法各有其優點和缺點。運動學法計算最簡單，唯一的假設是靜水平衡，可是假如風的觀測或輻散的計算有誤差，在對連續方程式做垂直積分由底層的垂直速度求上層的垂直速度時，誤差就會累積起來，假如不做適當的校正，所得的垂直速度不一定可靠，甚至數量級

會相差太多，而不像是大氣大幅度運動中所應有的垂直速度值。絕熱法的計算也很簡單，唯一的假設是絕熱過程，可是當非絕熱的效應很重要時，由絕熱法所得的垂直速度誤差就會很大，此外當大氣的氣溫遞減率接近乾絕熱遞減率時，垂直速度也不易準確計算得到。動力學法的優點在於只用到等壓面上的高度，而高度是在氣象變數值中觀測值較爲準確的，可是這種方法必須求解一個三維的橢圓型偏微分方程式，而且必須估計摩擦和加熱的影響，因此實際計算起來是很複雜的。

以上談到的垂直速度計算法，只利用一個氣象變數值或一個控制方程式，所得到的垂直速度不能和其他氣象變數值維持內部一致。最淺顯的例子就是由絕熱法或動力學法所得到的垂直速度就不一定和觀測風滿足連續方程式。此外以上的三種垂直速度計算法未能充分利用現有的觀測資訊。由於運動學法所得的垂直速度必須加以校正，而且爲了充分利用現有的觀測資訊，最近幾年有人想到利用變分最佳化的原理來校正垂直速度。利用變分原理來求垂直速度的概念起源於 Sasaki (1958) 的一篇論文。他提出了利用變分原理來從事客觀分析的理論基礎。O'Brien (1970) 提出一種利用變分原理來校正運動學法所得到的垂直速度的方法。McGinley (1973) 利用變分原理來校正水平觀測風，同時求得垂直速度。後來 McFarland (1975) 利用 McGinley 的方法來求垂直速度，以研究暴風環境。Liang (1976) 改進 McGinley 的垂直速度計算法，再加上校正頂層的垂直速度以得到較佳的結果。曾氏 (1977) 又提出兩種利用變分最佳化來計算垂直速度的程式。

在各種垂直速度計算法的比較研究方面，Danard (1964) 發現，假如不考慮潛熱的釋出，在 600mb 以下各層，由準地轉方程式組所得到的垂直速度值只有運動學法所得到的四分之一。Vincent 及其他人 (1976) 曾經比較利用運動學法和準地轉方程式組求垂直速度的結果。他發現用運動學法來求垂直速度結果較佳，用準地轉 ω 方程式所得到的垂直速度場的分佈並不與天氣系統完全符合，而且垂直運動相當微弱，垂直速度的最大值只有運動學法求得的 $^1/_5$。美國國家氣象中心本來同時採用運動學法和準均轉 ω 方程式來求垂直速度，以做爲預報雲量和降水的參考，現在已完全只採用運動學法了。

鑑於垂直速度計算法的重要性，以及變分最佳化法在氣象學上的廣泛用途，本研究利用變分原理，設計一種新的垂直速度計算法，校正水平風的觀測值，使其滿

足連續方程式和熱力學方程式，使計算出來的垂直速度能和其他氣象變數值維持內部一致。這種變分程式採取運動學法和絕熱法的優點，充份利用水平風和溫度的觀測資訊。此外本研究比較五種垂直速度計算法的結果，以探討各種程式的適用性。

貳、研 究 方 法

利用變分最佳化法的原理來求垂直速度，依照使用的動力約束條件和氣象變數的多寡，可分爲三個層次：

(1) 以連續方程式爲約束條件來校正風的觀測值，同時求得垂直速度。McGinley (1973)，McFarland (1975) 以及 Liang (1976，1977) 等人使用的垂直速度計算程式屬於這一類。這種程式必須水平風的觀測值相當準確才能得到正確的垂直速度。

(2) 利用風和溫度的觀測值，使其滿足連續方程式和熱力學方程式的約束條件來求得垂直速度。這種垂直速度計算程式是曾氏 (1977) 提出的。假如風的觀測值較爲準確，則這種程式相當於第一種變分程式；假如溫度的觀測值較爲準確，則這種程式相當於絕熱法。因此這種方法合併了第一種變分程式和絕熱法的優點。

(3) 同時利用風、溫度以及高度的觀測值，使其滿足動量方程式、靜水方程式、連續方程式和熱力學方程式等所謂原始方程式組的約束條件，以求得垂直速度。這種垂直速度計算程式是曾氏 (1977) 提出的。由於這種程式的計算法較爲複雜，必須同時求解兩個連立橢圓型偏微分方程式，因此在本研究中暫不考慮。

以下簡介本研究中採用的垂直速度計算法，然後詳細說明計算步驟。

第一種變分程式

在進行變分最佳化的過程中，我們所做的假設是這樣的：

$$u \simeq \tilde{u} \qquad v \simeq \tilde{v} \tag{1}$$

式中 u 是 x 方向的風速分量，v 是 y 方向的風速分量，加上 "～" 符號代表觀測值，未加 "～" 符號的代表校正以後的值。(1) 式代表經過變分最佳化後所得到的 u、v 與觀測值相差很小。有了這個假設，我們讓誤差變量爲極小，因此變分公式爲

$$\delta\iiint[\tilde{\alpha}\ (u-\tilde{u})^2+\tilde{\alpha}(v-\tilde{v})^2]\ dx\ dy\ dp/m^2=0 \tag{2}$$

其中 δ 是變分算符，m是地圖投影變形因子，$\tilde{\alpha}$ 代表 u、v 的觀測權重。式中多了 m^2 代表權重是在地球上而非地圖上決定的。由於 u、v 不是互相獨立的，必須滿足連續方程式的約束條件

$$m^2\left(\frac{\partial}{\partial x}\frac{u}{m}+\frac{\partial}{\partial y}\frac{v}{m}\right)+\frac{\partial\omega}{\partial p}=0 \tag{3}$$

因此若加上 (3) 式的約束條件，(2) 式的變分公式變爲

$$\delta\iiint\left\{\tilde{\alpha}\ (u-\tilde{u})^2+\tilde{\alpha}\ (v-\tilde{v})^2+2\lambda\left[m^2\frac{\partial}{\partial x}\frac{u}{m}+m^2\frac{\partial}{\partial y}\frac{v}{m}+\frac{\partial\omega}{\partial p}\right]\right\}dx\,dy\,dp/m^2=0$$

其中 2λ 是 Lagrange 乘數，乘上 2 的係數的目的是使分析方程式沒有不必要的常數。由於 Lagrange 乘數在變分最佳化過程中是一未知數，因此權重 $\tilde{\alpha}$ 可以併入 Lagrange 乘數，上式就變爲

$$\delta\iiint\left[\left(\frac{u}{m}-\frac{\tilde{u}}{m}\right)^2+\left(\frac{v}{m}-\frac{\tilde{v}}{m}\right)^2+2\lambda\left(\frac{\partial}{\partial x}\frac{u}{m}+\frac{\partial}{\partial y}\frac{v}{m}+\frac{1}{m^2}\frac{\partial\omega}{\partial p}\right)\right]dx\,dy\,dp=0 \tag{4}$$

(4) 式經過簡單的運算以後，我們可以得到 Euler-Lagrange 方程式

$$u=\tilde{u}+\frac{\partial\lambda}{\partial x} \tag{5}$$

$$v=\tilde{v}+\frac{\partial\lambda}{\partial y} \tag{6}$$

$$\frac{\partial\lambda}{\partial p}=0 \tag{7}$$

$$\frac{\partial}{\partial x}\left(\frac{u}{m}\right)+\frac{\partial}{\partial y}\left(\frac{v}{m}\right)+\frac{1}{m^2}\frac{\partial\omega}{\partial p}=0 \tag{8}$$

以及自然邊界條件

$$\lambda=0 \text{ 在四周的邊界上} \tag{9}$$

$$\delta\omega=0 \text{ 在底層和頂層的邊界上} \tag{10}$$

(8) 式就是原有的連續方程式。(10) 式代表底層和頂層的邊界上垂直速度 ω 必須事先給出，在變分最佳化過程中無法加以決定的。(5) 式和 (6) 式代入 (8) 式我們得到

$$\frac{\partial^2\lambda}{\partial x^2}+\frac{\partial^2\lambda}{\partial y^2}+\frac{\partial}{\partial x}\left(\frac{\tilde{u}}{m}\right)+\frac{\partial}{\partial y}\left(\frac{\tilde{v}}{m}\right)+\frac{1}{m^2}\frac{\partial\omega}{\partial p}=0 \tag{11}$$

由 (7) 式可知，λ 和垂直坐標 p 無關，因此 (11) 式對 p 由底層 p_L 至頂層 p_T 積分可以得到下式

$$\frac{\partial^2\lambda}{\partial x^2}+\frac{\partial^2\lambda}{\partial y^2}+\frac{1}{p_T-p_L}\int_{p_L}^{p_T}\left[\frac{\partial}{\partial x}\left(\frac{\tilde{u}}{m}\right)+\frac{\partial}{\partial y}\left(\frac{\tilde{v}}{m}\right)\right]dp+\frac{\omega_T-\omega_L}{p_T-p_L}=0 \qquad (12)$$

(12) 式就是 λ 的方程式，其邊界條件爲 (9) 式。λ 求出以後，垂直速度 ω 可由 (11) 式由底層積分上去得到。由於 (11) 式對 ω 而言是一階常微分方程式，却有兩個邊界條件 ω_L 與 ω_T，因此由底層積分至頂層時，垂直速度並不一定會等於 ω_T，必須再加以校正。λ 值求出以後，最佳化的 u、v 值可由 (5) (6) 式分別得到。由 (5) (6) 二式可知，λ 值是一種速度勢函數。因爲這種變分程式中，觀測權重 $\tilde{\alpha}$ 可併入 λ，因此無法確知觀測風的可信度，若風的觀測值很準確，得到的 ω 也很準確，反之亦然，這是因爲這個程式只利用風一種氣象變數的觀測值而已。

第二種變分程式

第二種變分程式，除了利用風的觀測值外，也考慮到溫度的觀測值。我們所做的假設是這樣的

$$u\simeq\tilde{u} \qquad v\simeq\tilde{v}$$

$$\frac{\partial T}{\partial t}\simeq 0 \qquad (13)$$

(13) 式的假設代表大氣大幅度運動的準定常特性，有了這個假設可以濾除高頻雜波。現在讓誤差變量爲極小，因此變分公式爲

$$\delta\iiint\left[\tilde{\alpha}\,(u-\tilde{u})^2+\tilde{\alpha}(v-\tilde{v})^2+\beta\left(\frac{\partial T}{\partial t}\right)^2\right]dx\,dy\,dp/m^2=0 \qquad (14)$$

除了和第一種變分程式一樣具有連續方程式的約束條件外，又有下列熱力學方程式的約束條件

$$-\frac{\partial T}{\partial t}=m\,\tilde{u}\,\frac{\partial\tilde{T}}{\partial x}+m\,\tilde{v}\,\frac{\partial\tilde{T}}{\partial t}+\tilde{\sigma}\omega\equiv\tilde{C}+\tilde{\sigma}\omega \qquad (15)$$

其中

$$\tilde{\sigma}=\frac{\tilde{T}}{\tilde{\theta}}\,\frac{\partial\tilde{\theta}}{\partial p}$$

$$\tilde{\theta}=\tilde{T}\left(\frac{1000}{p}\right)^{R/c_p}$$

其他的符號與一般使用的相同。將兩個約束條件入 (14) 式的式的變分公式我們得到

$$\delta\iiint\left\{\tilde{\alpha}\left(\frac{u}{m}-\frac{\tilde{u}}{m}\right)^2+\tilde{\alpha}\left(\frac{v}{m}-\frac{\tilde{v}}{m}\right)^2+2\tilde{\alpha}\lambda\left[\frac{\partial}{\partial x}\left(\frac{u}{m}\right)+\frac{\partial}{\partial y}\left(\frac{v}{m}\right)+\frac{1}{m^2}\frac{\partial\omega}{\partial p}\right]\right.$$
$$\left.+\frac{\beta}{m^2}(\tilde{C}+\tilde{\sigma}\omega)^2\right\}dx\,dy\,dp=0 \tag{16}$$

(16)式經過簡單的運算可以得到下列 Euler-Lagrange 方程式

$$u=\tilde{u}+\frac{\partial\lambda}{\partial x} \tag{17}$$

$$v=\tilde{v}+\frac{\partial\lambda}{\partial y} \tag{18}$$

$$\beta\tilde{\sigma}(\tilde{C}+\tilde{\sigma}\omega)-\tilde{\alpha}\frac{\partial\lambda}{\partial p}=0 \tag{19}$$

$$\frac{\partial}{\partial x}\left(\frac{u}{m}\right)+\frac{\partial}{\partial y}\left(\frac{v}{m}\right)+\frac{1}{m^2}\frac{\partial\omega}{\partial p}=0 \tag{20}$$

以及下列自然邊界條件

$$\lambda=0 \text{ 在四周的邊界上} \tag{21}$$

$$\delta\omega=0 \text{ 在底層和頂層的邊界上} \tag{22}$$

(21) 式和 (22) 式的自然邊界條件和第一種變分程式的自然邊界條件 (9) 式和 (10) 式是一樣的。

(17)、(18) 式以及 (19) 式解出 ω 以後代入 (20) 式我們可以得下列 λ 的方程式

$$\nabla^2\lambda+\frac{\tilde{\alpha}}{m^2\beta}\frac{\partial}{\partial p}\left(\frac{1}{\tilde{\sigma}^2}\frac{\partial\lambda}{\partial p}\right)+\nabla\cdot\left(\frac{\tilde{\mathbf{V}}}{m}\right)-\frac{1}{m^2}\frac{\partial}{\partial p}\frac{\tilde{C}}{\tilde{\sigma}}=0 \tag{23}$$

式中

$$\nabla^2=\frac{\partial^2}{\partial x^2}+\frac{\partial^2}{\partial y^2}$$

$$\nabla=\mathbf{i}\frac{\partial}{\partial x}+\mathbf{j}\frac{\partial}{\partial y}$$

$$\tilde{\mathbf{V}}=\mathbf{i}\,\tilde{u}+\mathbf{j}\,\tilde{v}$$

λ 的四周邊界條件就是 (21) 式，底層和頂層的邊界條件可由 (19) 式得到

$$\frac{\partial\lambda}{\partial p}=-\frac{\beta}{\tilde{\alpha}}\tilde{\sigma}\,(C+\tilde{\sigma}\omega) \tag{24}$$

因此 λ 的四周邊界條件爲 Dirichlet 型邊界條件，而在底層和頂層的邊界條件爲 Neumann 型邊界條件。

將 (23) 式對 p 微分，然後由 (19) 求得 $\partial\lambda/\partial p$ 代入，我們可以得到 ω 的方程式

$$\frac{\beta}{\tilde{\alpha}}\nabla^2\tilde{\sigma}^2\omega+\frac{1}{m^2}\frac{\partial^2\omega}{\partial p^2}+\frac{\partial}{\partial p}\nabla\cdot\left(\frac{\tilde{v}}{m}\right)+\frac{\beta}{\tilde{\alpha}}\nabla^2\tilde{\sigma}\,\tilde{C}=0 \tag{25}$$

其底層和頂層的邊界條件是 (22) 式，也就是說底層和頂層的垂直速度必須事先求得。四周的邊界條件可由 (19) 求得到。由於在四周的邊界上 $\lambda=0$，因此 $\partial\lambda/\partial p=0$，由 (19) 式我們得到

$$\omega=-\frac{\tilde{C}}{\tilde{\sigma}} \quad \text{在四周邊界上} \tag{26}$$

因此 ω 方程式 (25) 式的邊界條件都是 Dirichlet 型的。由(26)式可知，ω 的四周邊界是由熱力學方程式不考慮時間變化和潛熱釋出而得到的。

這種垂直速度計算程式同時利用風和溫度的觀測值，使其滿足連續方程式和熱力學方程式，因此這種程式兼具第一種變分程式和絕熱法的優點。

準地轉垂直速度方程式

準地轉垂直速度方程式的型式如下 (Haltiner 1971)

$$\sigma_s\nabla^2\omega+f_0^2\frac{\partial^2\omega}{\partial p^2}=\frac{\partial}{\partial p}J(\phi,\ f+\zeta)-\frac{1}{f_0}\nabla^2 J\left(\phi,\ \frac{\partial\phi}{\partial p}\right) \tag{27}$$

其中

f_0 平均科氏參數

σ_s 各層平均靜力穩定度

ϕ 重力位

$\zeta=\frac{1}{f_0}\nabla^2\phi$ 渦度

其他符號與一般使用的相同。本研究未考慮摩擦和加熱的效應。(27) 式假如 $\sigma_s>0$ 則爲橢圓型偏微分方程式，可用緩和法來求解。由於這個垂直速度計算程式爲一般人所熟知，在此不加詳細討論。

線型平衡系

線型平衡系的形式如下 (Haltiner, 1971)

$$\nabla\cdot(f\nabla\psi)=\nabla^2\phi \tag{28}$$

$$\nabla^2(\sigma\omega)+f^2\frac{\partial^2\omega}{\partial p^2}=f\frac{\partial}{\partial p}[J(\psi,\ \zeta+f)+\nabla f\cdot\nabla\chi]$$
$$-\nabla^2[J(\psi,\ \frac{\partial\phi}{\partial p})+\nabla\chi\cdot\nabla\frac{\partial\phi}{\partial p}]-\nabla f\cdot\nabla\frac{\partial^2\psi}{\partial p\partial t} \tag{29}$$

$$\nabla^2\frac{\partial\psi}{\partial t}+J(\psi,\ f+\zeta)+\nabla\chi\cdot\nabla f=f\frac{\partial\omega}{\partial p} \tag{30}$$

$$\nabla^2\chi+\frac{\partial\omega}{\partial p}=0 \tag{31}$$

其中

f	科氏參數
ψ	流線函數
$\phi=gz$	重力位
σ	靜力穩定度
$\zeta=\nabla^2\psi$	渦度
χ	速度勢函數

其他符號與一般使用的相同。由於這個垂直速度計算程式爲一般人所熟知，在此不加詳細討論。

參、計　算　步　驟

本研究所使用的資料係取自 Chen and Tsay (1977) 梅雨報告中民國六十四年六月十日格林尼治時間零 (0000Z) 時的天氣資料。此時之天氣概況如圖 1, 2, 3, 4, 5。圖1 是海平面氣壓，圖2, 3, 4, 5 分別爲 850mb，700mb，500mb 以及 200mb 的高度。當時副熱帶太平洋高壓與鄂霍次克高壓間的梅雨鋒面自日本向西南延伸，經過琉球、臺灣到達南中國海，蒙古高壓位於中國大陸北部。本研究所使用的水平網格系統均與梅雨報告相同，計算過程中水平微分項採用中差分法，垂直微分項用不等間距差分法 (Sundqvist and Veronis 1970)，以適應各不等間距定壓層的天氣資料。

本研究的底層邊界定在 850mb，此處吾人以梅雨報告中由摩擦和地形效應所求得的垂直速度做爲邊界條件 (圖7)，因此這層的垂直速度是本研究中五個垂直速

度計算法的底層邊界條件。在頂層的邊界條件中本研究並不採用 Lateef (1968) 以絕熱法求得的 100mb 上的垂直速度。Wilson (1976) 曾比較在 100mb 處以零及絕熱法求得之值做爲頂層邊界條件，結果發現對垂直速度之計算並無甚大差異，故本研究中第一種變分程式得到的 100mb 的垂直速度（圖 15a）當做第二種變分程式以及準地轉和平衡系垂直速度的頂層邊界條件。至於運動學法的頂層邊界條件即 100mb 的 ω 值是用 Lateef (1968) 的絕熱法求得的（圖 15b）。Liang (1976) 曾用變分原理來校正頂層的垂直速度，但本研究未予使用。

以下詳述三種垂直速度計算程式的步驟，此外運動學法的計算步驟在梅雨報告中已詳述說明，在此不再贅述。

第一種變分程式

第一種變分程式計算中網格垂直結構如右圖。首先由 (12) 式可以得 λ 值，然後用(11)式由再底層積上去，可以得到每一層的 ω 值，最後再做線性調整，使最上層的 ω 值恰等於 ω_T。λ 值求出以後，最佳化後的風可以由 (5) (6) 式求得，由於本研究的主題在垂直速度，因此未將 u、v 值列在圖上。由於各層的 ω 值均由底層積上去，因此不需要四周的邊界條件。ω 值求得以後再線性內插到各定壓層上。計算結果列在圖 8a (700mb)，9a (500mb)，10a (400mb)，11a (300mb)，12a (250mb)，13a (200mb)，14a (150mb)，15a (100mb)。

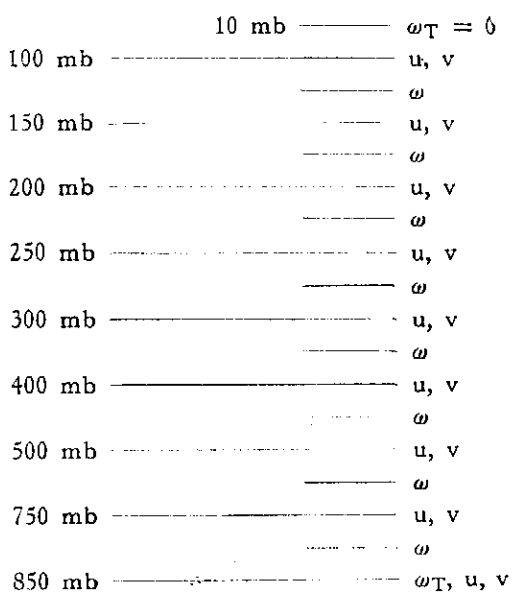

第二種變分程式

第二種變分程式必須用緩和法解兩個橢圓形微分方程式，比較複雜。網格的垂直結構如右圖。頂層的邊界條件是由第一個變分程得到的 100mb 上的 ω 值。首先

必須估計觀測權重 $\tilde{\alpha}$ 和動力權重 β 之值，估計的方法見曾氏(1976與1977)。然後解 λ 的方程式 (23) 式，邊界條件是 (21) 式與 (24) 式。此外必須解 ω 的方程式 (25) 式，邊界條件爲 (26) 式與 ω_T ω_L。λ 值和 ω 值求出以後，可以由 (17) 式和 (18)式分別求出 u、v 值，然後用曾氏 (1976，1977) 的方法重新計算權重 $\tilde{\alpha}$ 與 β。如此周而復始，複做數次，直到 $\tilde{\alpha}$ 與 β 值趨近於一定時才停止。ω 值是在兩定壓層之間計算的，求出以後再用線性內插到各定壓層上。計算結果列在圖 8b (700mb)，圖 9b (500mb)，圖 10b (400mb)，圖 11b (300mb)，圖 13b (200mb)。

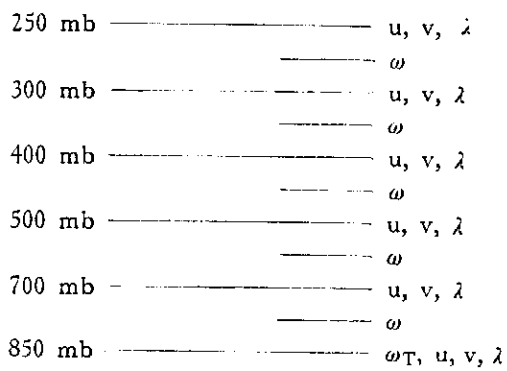

準地轉垂直速度方程式

用準地轉 ω 方程式來求垂直速度必須用緩和法來解一個橢圓型方程式。網格的垂直結構和第二種變分程式的相同，所有的上下四周邊界和第一種變分程式相同。由於準地轉 ω 方程式並不是由變分原理得來的，因此邊界條件可以用任何合理的邊界條件。第一種變分程式和第二種變分程式所使用的邊界條件必須是自然邊界條件，這是一種數學邊界條件，當然這種邊界條件也符合物理的假設。假如這兩種變分程式用其他任何合理的物理邊界條件，而非自然邊界條件，這樣就會違反變分原理，最後得不到正確的垂直速度值。以上所說的是準地轉 ω 方程式邊界條件與其他程式的邊界條件不相同的地方。因此在本研究中的邊界條件（四周的邊界條件）除了準地轉 ω 方程式和第一種變分程式相同以外，其他各種程式的四周邊界都不相同。根據以上所說的，本研究的四種程式中，除了 ω 方程式和第一種變分程式外，無法完全在同樣的四周邊界條件下，比較各程式的垂直速度計算結束。這樣情形在其他各種數值天氣預報問題中也屢見不鮮。準地轉 ω 方程式的計算結果在圖8c(700mb)，圖 9c (500mb)，圖 10c (400mb)，圖 11c (300mb)，圖 12b (250mb)，圖 13c (200mb)，圖 14b (150mb)。

線 性 平 衡 系

線性平衡系比準地轉 ω 方程式複雜，必須用緩和法來解三個橢圓型方程式。網

格的垂直結構和第二種變分程式的相同，所有的上下和四周的邊界條件與第一種變分程式相同。線性平衡系的解法詳見 Haltiner 1971。用線性平衡系求得的垂直速度在圖 8d (700mb)，圖 9d (500mb)，圖 10d (400mb)，圖 11d (300mb)，圖 12c (250mb)，圖 13d (200mb)，圖 14c (150 mb)。

肆、研 究 結 果

由於大氣大幅度運動中其垂直速度是根據某些物理的或數學的假設由其他氣象變數計算得來的，因此垂直速度的準確值無法得知。驗證各種程式所得到的垂直速度的正確性必須依靠和其他氣象參數的相關以及天氣系統的環流型式來決定。本研究的驗證基準是根據下列方法決定的：(1) 天氣系統，諸如槽線或脊線的位置以及 500mb 天氣圖上的環流型式。(2) 濕度參數，諸如雲圖（圖 6）或降水量。(3) 梅雨報告中 (Chen and Tsay 1977) 用運動學法所得到的垂直速度（圖 8e, 9e, 10e, 11e, 12d, 13e, 14d)。

通常上升運動大部分佈在槽線的東方或南方，而下降運動通常在脊線的東方或南方。換句話說上升運動分佈在槽線的前方，而下降運動分佈在槽線的後方。因此五種垂直速度計算法得到的結束大致與這個原理符合。

四種垂直速度計算法得到的結果（自圖 8 至圖14）顯示，上升運動主要分佈在梅雨峰面上，即由日本向西南方延伸，經過琉球臺灣到達南海北部。此外在長江中游、綏遠省也有强烈的上升氣流。在雲南、北越一帶另有微弱的上升運動。下降氣流主要分佈在黃海、韓國以及中國東北一帶，此外在中國大陸西北的新疆省也有旺盛的下降氣流。五種垂直速度計算程式得到的結果顯示，主要的上升氣流和下降氣流的分佈狀況大致相同。最顯著的差異是用準地轉和線性平衡系的 ω 方程式計算出來的垂直速度比較微弱，尤其是梅雨槽線前方以及長江中游的上升氣流，在400mb 以下非常微弱，僅及用另外三種方法得出的垂直速度的 $^1/_4$。

此外觀察各圖（圖 8 至圖14）也可以發現，相似的物理或數學的假設所設計出來的程式，其計算出來的垂直速度分佈型式也比較相似。用準地轉和線性平衡系的 ω 方程式得出來的垂直速度，不論其數值或分佈型式都和其他三種方法計算出來的相差較多，這是因爲用準地轉和線性平衡系的 ω 方程式來求垂直速度，與其他三種

方法不同，只利用等壓面上的高度值而已。此外第二種變分程式和第一種變分程式所得到的垂直速度分佈型式與數值都相差不多，這是因爲兩者的數學假設相似，兩者都用風的觀測值，而第二種變分程式多用了溫度的觀測值。第一種變分程式和運動學法所得到的結果也相似，因爲兩者都是只用風的觀測值而已，此外兩者都只用一個連續方程式。

本頁的表 1 詳細列出 500mb 各上升運動和下降運動最旺盛區域中由五種不同的方法所得到的垂直速度最大值。由表 1 可以顯示，準地轉 ω 方程式求得的垂直速度在梅雨鋒面上諸如琉球群島和長江中游處是相當微弱的，這一點與實際的天氣情況並不符合。由圖 6 的衛星照片中得知，梅雨鋒面處，即由日本向西南延伸，經過

上升或下降氣流發生地區		第一種變分程式	第二種變分程式	準地轉 ω 方程式	運動學法	線性平衡方程組
上升區域	琉球	−5.2	−5.0	−0.8, −1.3	−5.0	1.0
	長江中游	−6.0, −5.2	−3.1	微弱	−3.2, −3.4	微弱
	華遠	−4.5, −4.8	−4.1	−2.7	−4.4	−1.6
	北越	−1.7	−1.5	−1.5	−3.8	−1.3
	雲南	−2.0	—	−1.5	−3.4	—
下降區域	東北黃海韓國	5.0, 3.8	3.4	3.1	2.9, 3.2	2.1
	新疆	5.4	4.5	5.1	4.2	5.1
	北海道	1.5	2.3	—	2.7	—
	菲律賓東方海面	3.0	3.1	2.7	2.2	2.2
	廣西	2.0	2.3	1.0	1.1	—

表一　500 mb 上各上升和下降氣流中心，由四種不同的方程式所得到的垂直速度極大值或極小值（單位爲 10^{-6} bar/s）。

琉球臺灣一帶，雲層很厚，此處應有旺盛的上升氣流。用其他三種程式所求得的垂直速度充分反映出這個事實。我們可以發現，用準地轉和線性平衡系的 ω 方程式得到的垂直速度在鋒面區域只有其他三種方法的 $^1/_5$。這點和 Danard (1964) 所得到的結果相似，即若不考慮潛熱的釋出，在 600mb 以下各層由準地轉 ω 方程式所得到的垂直速度只有運動學法所得到的 $^1/_4$。由表一我們可以進一步看出，在其他各主要的上升區域或下降區域中，由準地轉和線性平衡系的 ω 方程式所得的垂直速度和其他三種方法求得的相近。由於在梅雨鋒面處降雨很多，潛熱釋出的物理過程變得非常重要，假如不考慮這一點，無法得到正確的垂直速度值。本研究所使用的準地轉和線性平衡模式並未考慮到潛熱的釋出，因此在降水豐富的梅雨鋒面處所得的垂直

速度未能反映出實際的天氣情況。可是在求中緯度天氣系統的垂直速度時，本研究的結果顯示，若不考慮潛熱的釋出只用絕熱的準地轉 ω 方程式，仍能得到令人滿意的結果，至少在本研究所使用的個案中是如此。由圖 11, 12, 13, 14 中顯示，用準地轉 ω 方程式所得到的垂直速度要在 300mb 以上各層在梅雨鋒面帶才會和其他三種方法求得的垂直速度相當。其他三種方法，即第一種變分程式，第二種變分程式和運動學法所得到的垂直速度值非常相近，其上升運動或下降運動的分佈也非常相似。

由 700mb 處的垂直速度圖（圖 8a, 8b, 8c, 8d, 8e）中顯示，第一種變分程式，第二種變分程式和運動學法所得的垂直速度大致互相符合。準地轉和線性平衡系的 ω 方程式所得的垂直速度在梅雨槽線前方過於微弱，而且中緯度槽線前方（即在中國大陸綏遠省）的上升氣流區域過於偏北。第一種變分程式所得的長江中游處的上升氣流過於旺盛，而且垂直速度梯度過大，這是因爲數值計算的誤差，沒有經過修勻所致。

400mb 的垂直速度圖中（圖 10a, 10b, 10c, 10d, 10e），由準地轉和線性平衡系的 ω 方程式得到的垂直速度，在梅雨鋒面上仍很微弱。其他三種方法得到的垂直速度仍互相符合。300mb 的垂直速度圖中（圖 11a, 11b, 11c, 11d, 11e），由準地轉 ω 方程式所得的垂直速度，在梅雨鋒面上，已達 $-3.3\mu b/s$，與其他方法計算得到的數值相去不遠，但位置稍爲偏北，位置在日本本土，而非在琉球群島上。第一種變分程式所得的垂直速度在臺灣東部海面其梯度很大，這是和運動學法的結果不同。250mb 以上（圖 12 至圖 14），由第一種變分程式所得的垂直速度梯度在臺灣東部海面仍然很大，與運動學法得出的結果不同，第二種變分程式所得的結果並無此情形。

在梅雨鋒面近地面處之暖鋒前方，即日本南方海面，其處應屬局部的上升氣流，況且暖鋒前的上升氣流無法到達較高層，故在第一種變分程式所得的結果中，700mb 的日本以北處仍有上升氣流又一直出現至 300mb，此與實際天氣並不一致。

在非律賓東方的太平洋海面上，700mb 與 500mb 均有一高溫中心，如圖3, 4，由衛星照片中（圖 6）可見，此區域仍有上升氣流，故此處之上升氣流一直發展

至 300mb 而漸減弱，此乃這一種變分程式較運動學法所得的結果爲合理。

綜上所述，兩種變分程式所得的結果與天氣系統、衛星圖片符合，也與運動學法所得的結果一致。而準地轉與線性平衡系的 ω 方程式所得的垂直速度在梅雨鋒面帶上相當微弱，只有其他三種求得的$^1/_5$，可是在中緯度天氣系統的垂直速度計算時，用絕熱的準地轉和線性平衡系的 ω 方程式仍能得到合理的結果。本研究所使用的兩種變分垂直速度計算程式在估計大氣大幅度垂直運動結果與天氣系統和衛星圖片尙能符合。

伍、結　　語

本研究利用變分最佳化的原理，設計一種新的垂直速度計算法，校正水平風的觀測值，使其滿足連續方程式和熱力學方程式，以維持計算得到的垂直速度與其他氣象變數之間的一致。這種變分程式採取運動學法和絕熱法的優點，充分利用水平風和溫度的觀測資訊。本研究利用1975年 6 日10日的梅雨資料來探討這種方法（本文中簡稱第二種變分程式）的適用性，研究結果顯示，第二種變分程式所求得的垂直速度與天氣系統、衛星圖片符合，也與運動學法所得的結果一致。

此外本研究比較五種方法，卽第一種和第二種變分程式，準地轉和線性平衡系的 ω 方程式以及運動學法，所得到的垂直速度。研究結果顯示，準地轉和線性平衡系的 ω 方程式所求得的垂直速度在梅雨鋒面處相當微弱，僅及其他三種方法的$^1/_5$，可是在求中緯度天氣系統的垂直速度時，用絕熱他準地轉和線性平衡系的 ω 方程式仍能得到合理的結果。第一種、第二種變分程式所得的結果和連續方程式的結果也相吻。

因此除了傳統的三種垂直速度計算法外，本研究所使用的兩種變分程式，在估計大氣大幅度的垂直速度時，仍屬可行。

致　　謝

本研究是在國家科學委員會 NSC-67M-0202-02(01)「大氣垂直速度計算之研究」專題計劃補助下完成的。本所研究助理陳文達和臺大學生許晃雄協助程式上機工作，本所研究助理劉振榮協助繪圖工作。此外承臺大大氣科學系陳泰然博士提供若干資料。對上述的機關和個人著者深表謝意。

參 考 文 獻

Chen, T. -J. G., and C. Y. Tsay, 1977: A detailed analysis of a case of Mei-Yu system in the vicinity of Taiwan. *Tech. Rept No. Mei-Yu-001, Dept. of Atmospheric Sciences, National Taiwan University*, Taipei, Taiwan, 249pp.

Danard, M. B., 1964: On the influence of released latent heat on cyclone development. *J. Appl. Meteor.*, **3**, 27-37.

Haltiner, G. J., 1971: *Numerical Weather Prediction.* Wiley, New York, 317pp.

Lateef, M. A., 1968: Vertical motion at 100 mb in the tropics. *Mon. Wea. Rev.*, **96**, 286-290.

Liang, W. J., 1976: The variational optimization of wind field for the estimation of vertical velocity. *Ann. Rept. Inst. Phys., Acad. Sin.*, **6**, 179-198, Taipei, Taiwan.

Liang, W. J., 1977: Comparison of McGinley's and O'Brien's variational optimization formulation for the computation of vertical velocity. *Atmospheric Sciences*, **4**, 73-76. The Meteorological Society of the Republic of China, Taipei, Taiwan.

McFarland, M. J., 1975: Variational optimization analysis of temperature and moisture advection in a severe storm environment. Ph. D. Dissertation, University of Oklahoma, Norman, 86pp.

McGinley, J. H., 1973: Environmental energy fields associated with severe storms. M. S. Thesis, University of Oklahoma, Norman, 129pp.

O'Brien, J. J., 1970: Alternative solution to the classical vertical velocity problem. *J. Appl. Meteor.* **9**, 197-203.

Sasaki, Y., 1958: An objective analysis based on the variational method. *J. Meteor. Soc. Japan*, **36**, 77-88.

Sundqvist, H. and G. Veronis, 1970: A simple finite difference grid with non-constant intervals. *Tellus*, **22**, 26-31.

曾忠一，1976：東亞地區天氣資料變分客觀分析之研究。中央研究院物理研究所集刊，**6**，161—178。

曾忠一，1977：利用原始方程式進行變分客觀分析之研究。中央研究院物理研究所集刊，**7**，77—92。

Vincent, D. G., K. E. Bossingham and H. J. Edmon, 1976: Comparison of large scale vertical motions computed by the kinematic method and quasi-geostrophic omega equation. Preprints of Papers, *Six Conference on Weather Forecasting and Analysis*, Albany, N.Y., 357-364.

Wilson, G. S., 1976: Large-scale vertical motion calculations in the AVE IV experiment. *Geophys. Res. Letters*, **3**, 735-738.

圖 表 說 明

本文中各圖均爲1975年 6 月10日 0000Z 的資料。圖 6 引用自梅雨報告 (Chen and Tsay, 1977)。圖 7, 8e, 9e 10e, 11e, 12d, 13e, 14d, 15b 的原始資料是臺大大氣科學系陳泰然教授提供的。

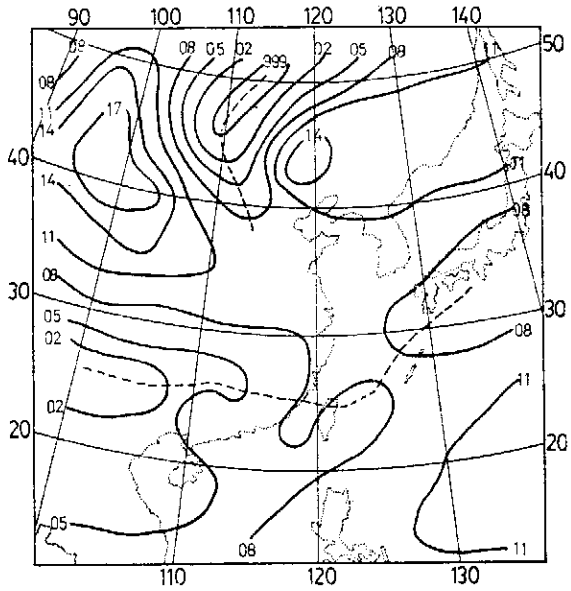

圖 1. 海平面氣壓（實線），單位爲 mb 與鋒（虛線）

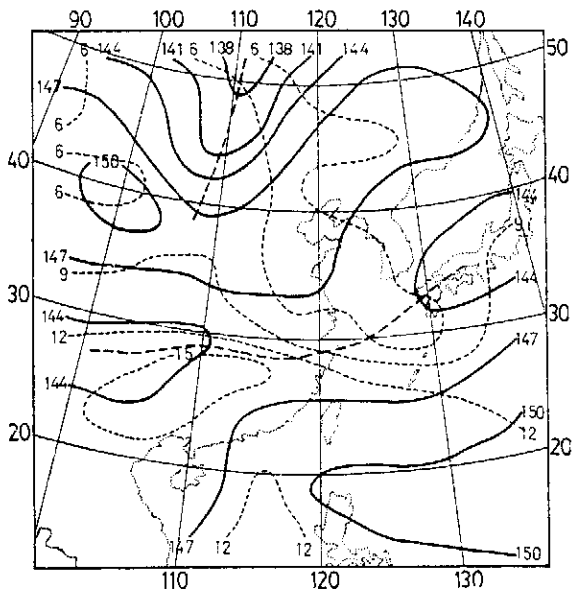

圖 2. 850mb 高度場，等高線間隔 30m（實線），混合比（虛線）單位爲 g/kg 以及槽線（黑虛線）

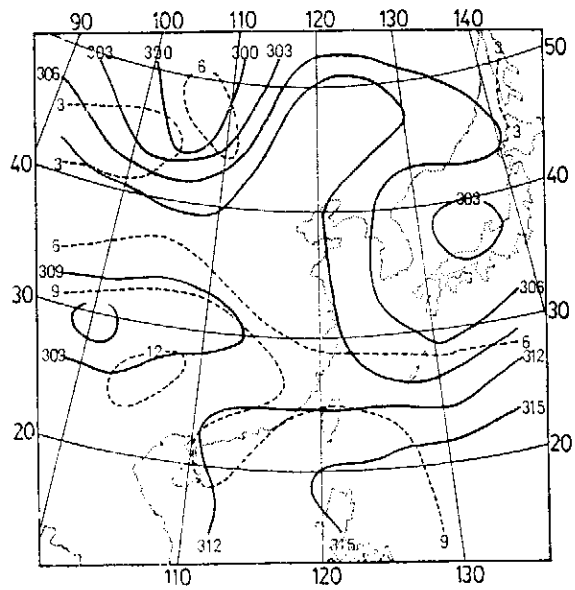

圖 3. 同圖2，但爲 700mb

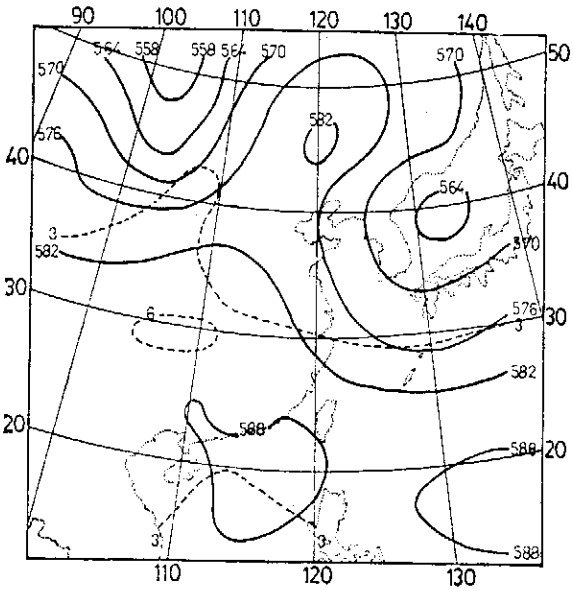

圖 4. 同圖2，但爲 500mb，等高線間隔 60m

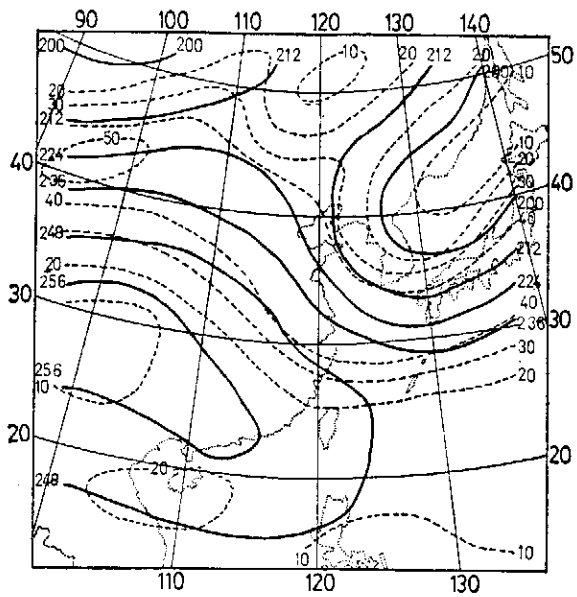

圖 5. 200mb 高度場，等高線間隔 120m（實線）以及風速，單位 m/sec（虛線）

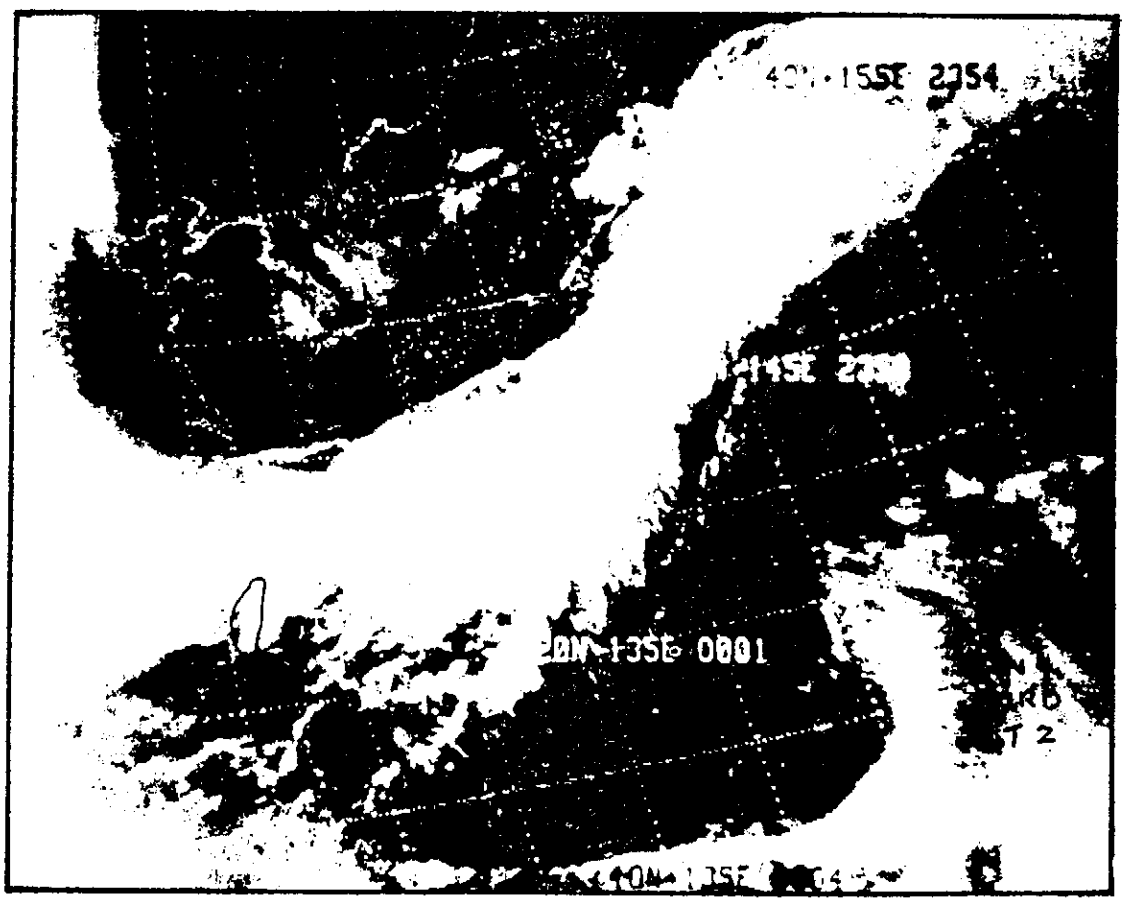

圖 6. NOAA-4 紅外光衛星照片，白色虛線表示經緯度以及海岸線，臺灣的位置用實線表示

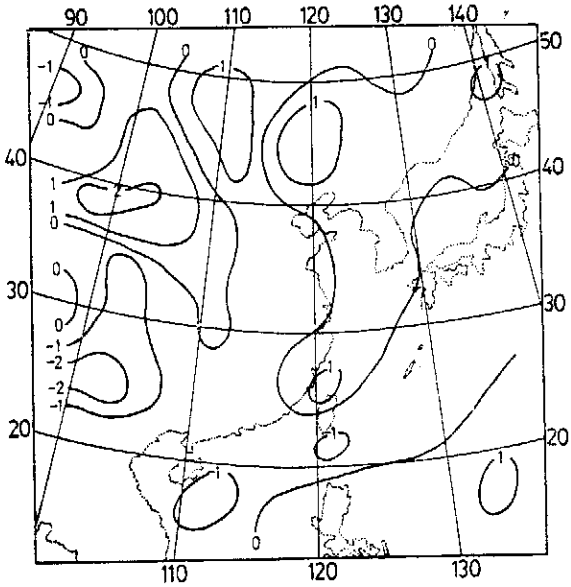

圖 7. 850mb 垂直速度場（實線），單位爲 10^{-3} mb/sec

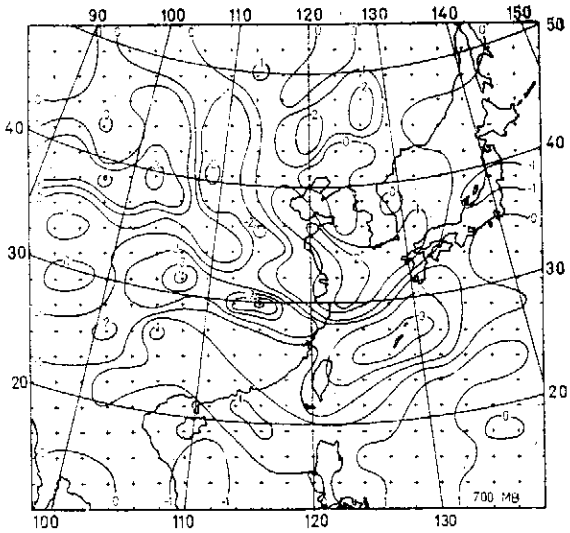

圖 8a. 用第一種變分程式得到的 700mb 垂直速度場，單位爲 10^{-3}mb/sec

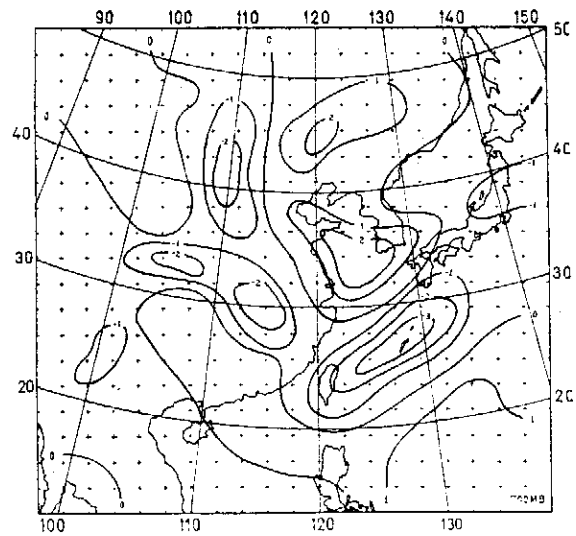

圖 8b. 用第二種變分程式得到的 700mb 垂直速度場，單位爲 10^{-3} mb/sec

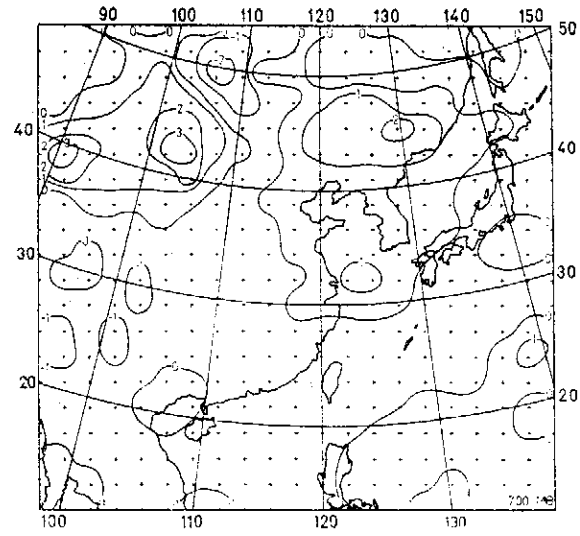

圖 8c. 用準地轉垂直速度方程式得到的 700mb 垂直速度，單位爲 10^{-3} mb/sec

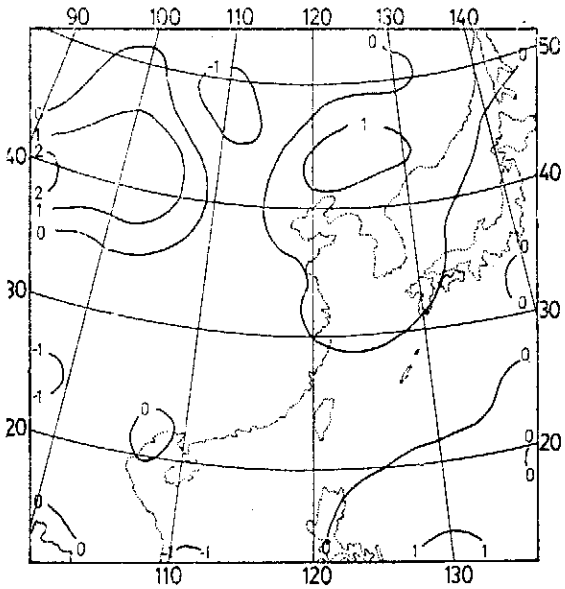

圖 8d. 用線性平衡系垂直速度方程式得到的 700mb 垂直速度，單位爲 10^{-3} mb/sec

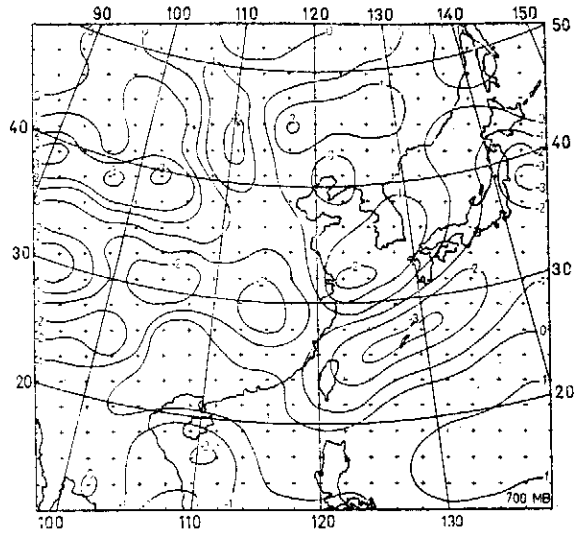

圖 8e. 用運動學法得到的 700mb 垂直速度，單位爲 10^{-3} mb/sec

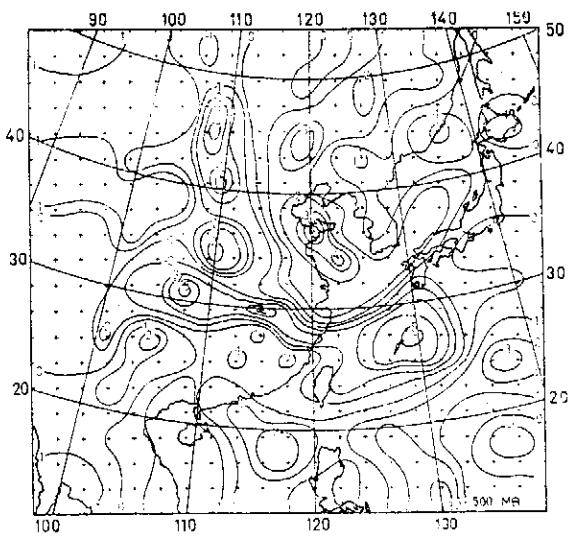

圖 9a. 同圖 8a，但爲 500mb

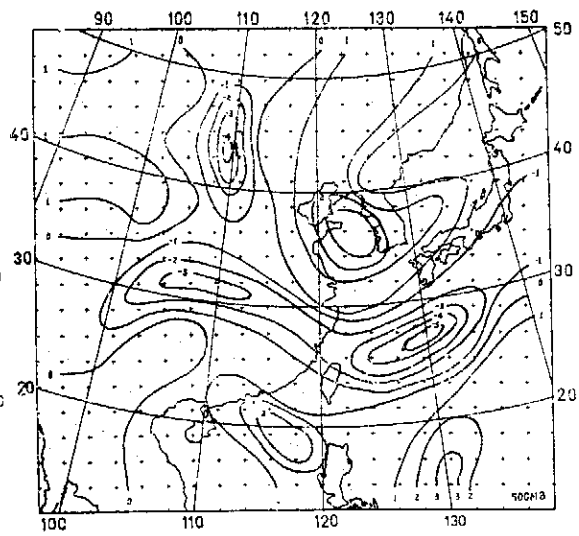

圖 9b. 同圖 8b，但爲 500mb

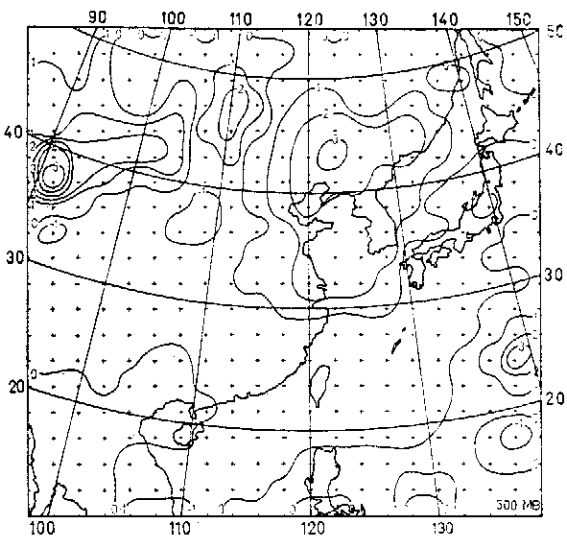

圖 9c. 同圖 8c，但爲 500mb

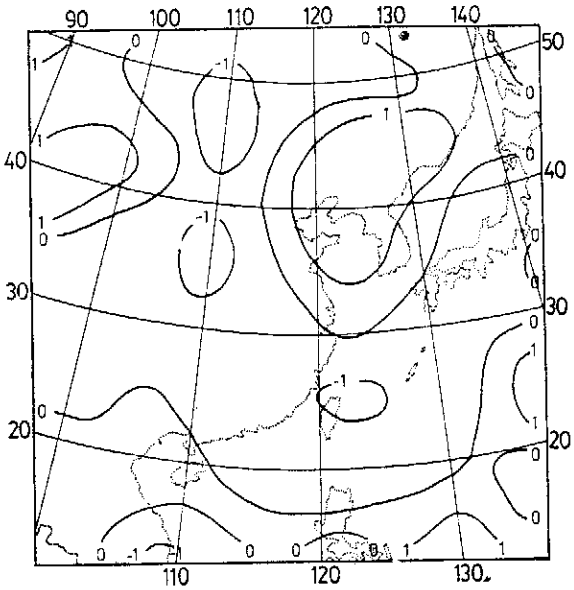

圖 9d. 同圖 8d，但爲 500mb

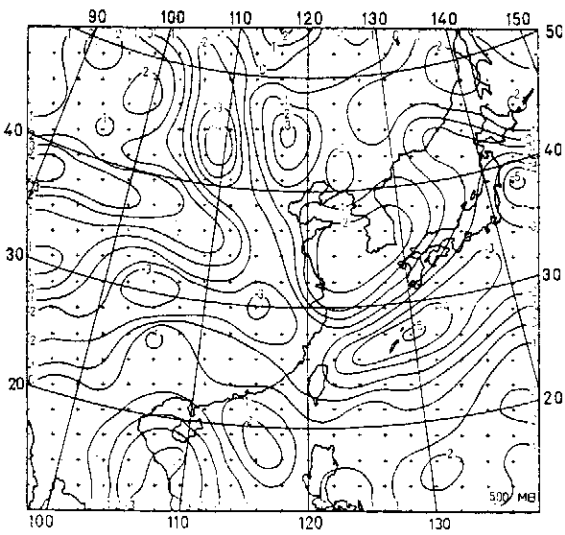

圖 9e. 同圖 8e，但爲 500mb

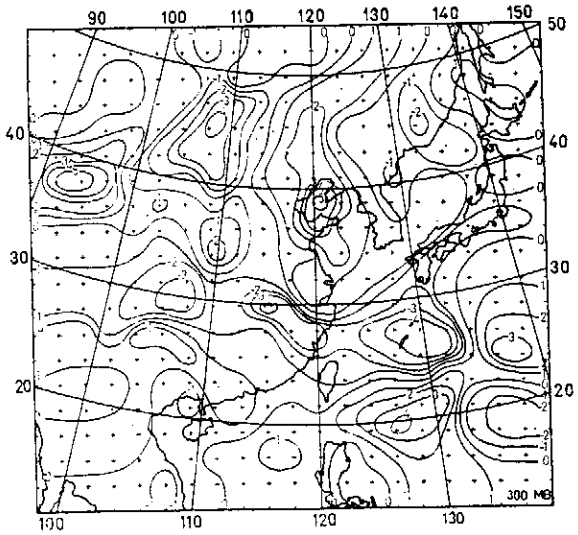

圖 10a. 同圖 8a，但爲 400mb

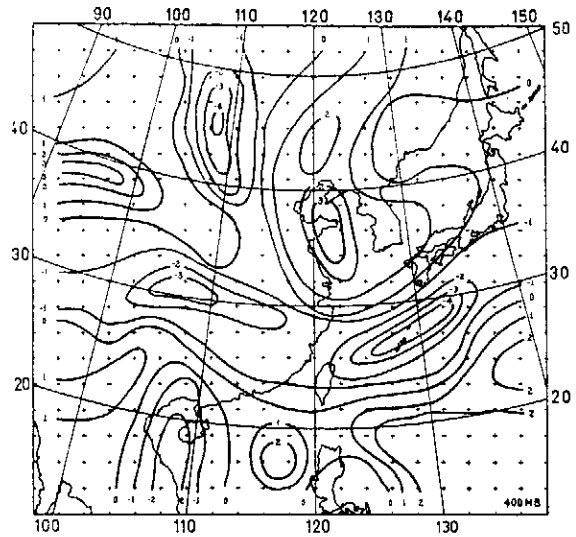

圖 10b. 同圖 8b，但爲 400mb

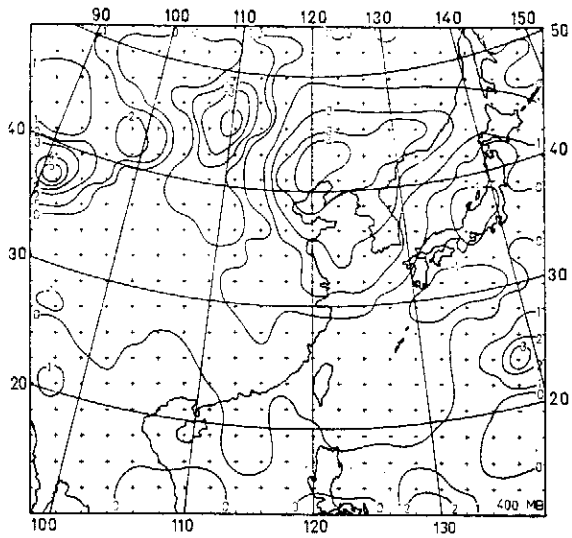

圖 10c. 同圖 8c，但爲 400mb

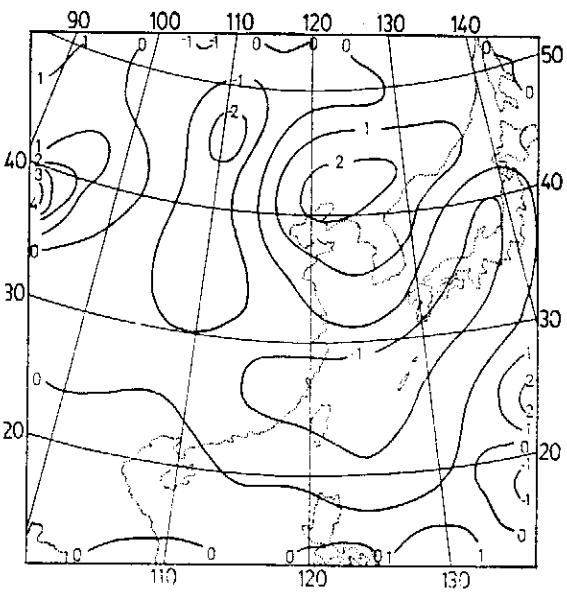

圖 10d. 同圖 8d，但爲 400mb

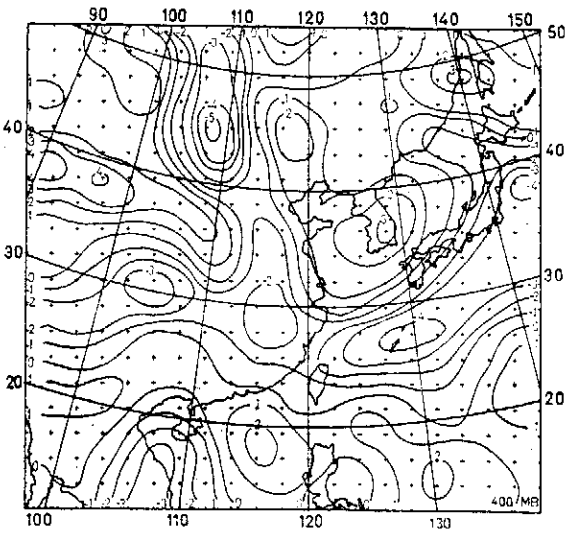

圖 10e. 用運動學法得到的 400mb 垂直速度

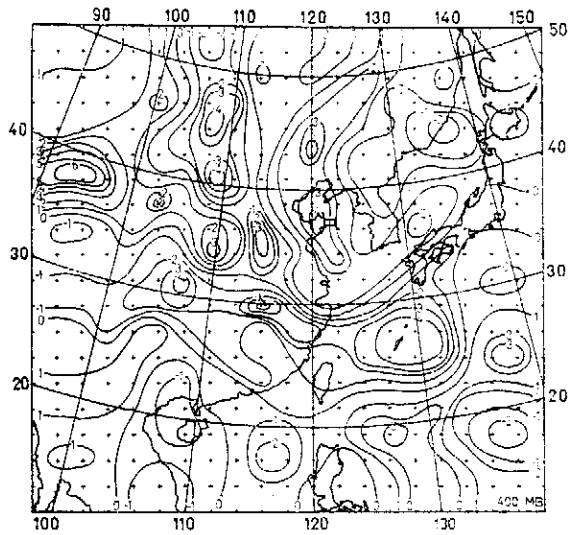

圖 11a. 同圖 8a，但爲 300mb

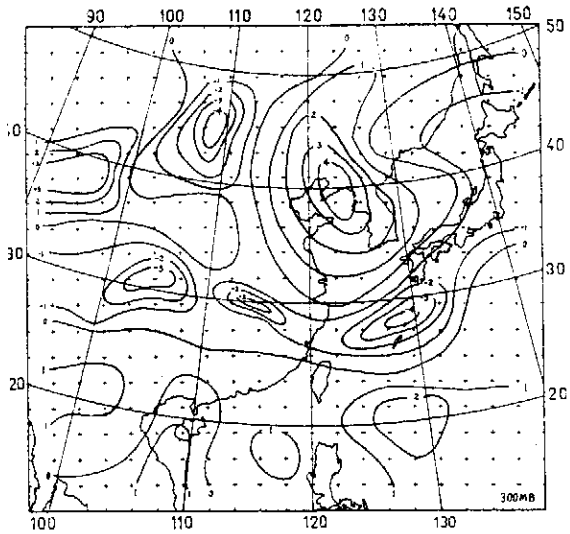

圖 11b. 同圖 8b，但爲 300mb

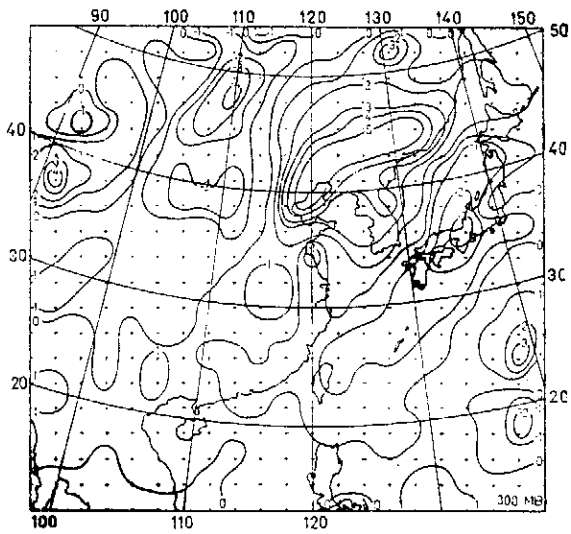

圖 11c. 同圖 8c，但爲 300mb

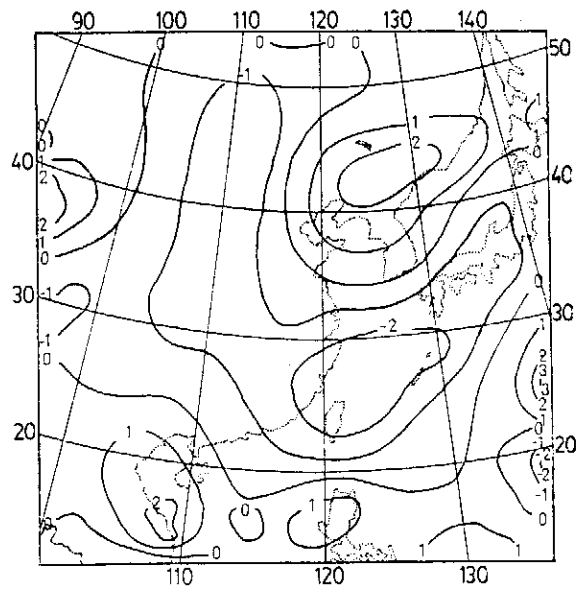

圖 11d. 同圖 8d，但爲 300mb

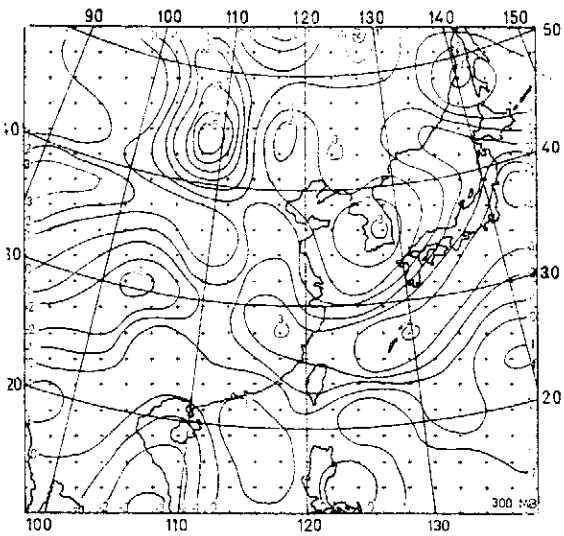

圖 11e. 同圖 10e，但爲 300mb

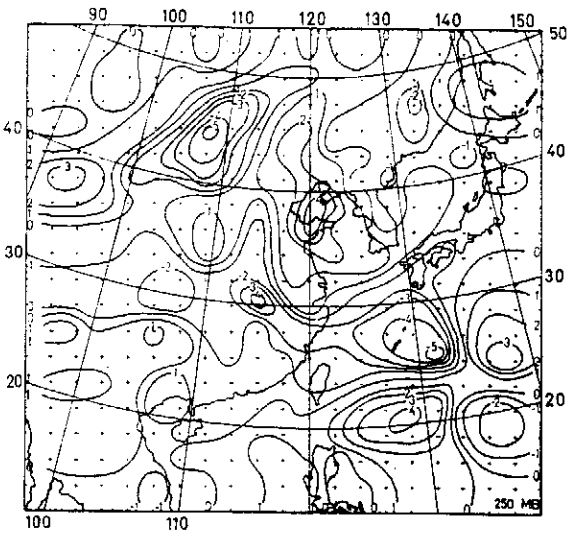

圖 12a. 同圖 8a，但爲 250mb

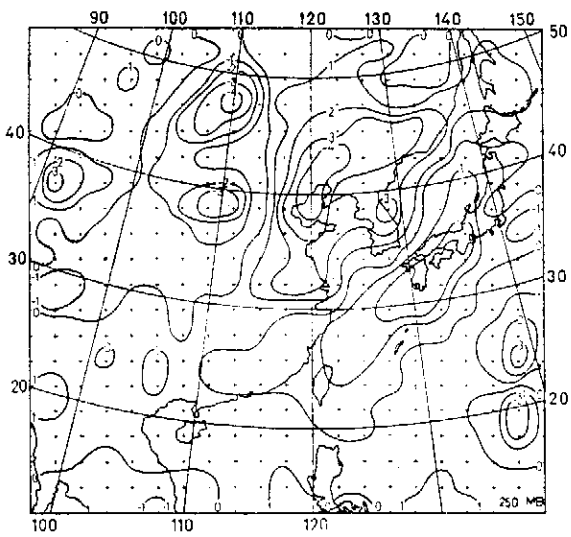

圖 12b. 同圖 8c，但爲 250mb

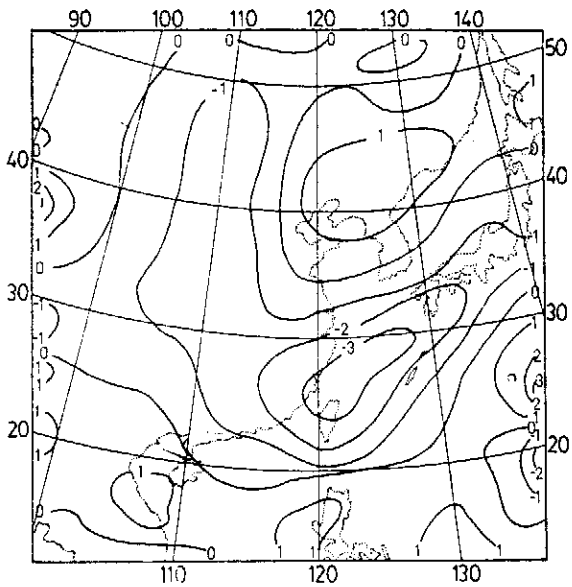

圖 12c. 同圖 8d，但爲 250mb

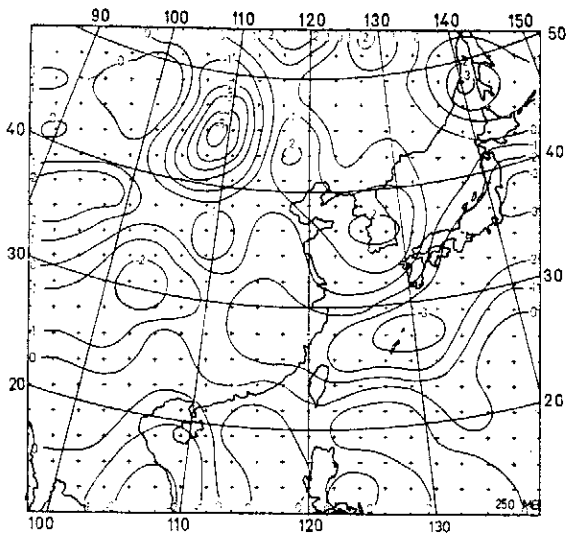

圖 12d. 同圖 8e，但爲 250mb

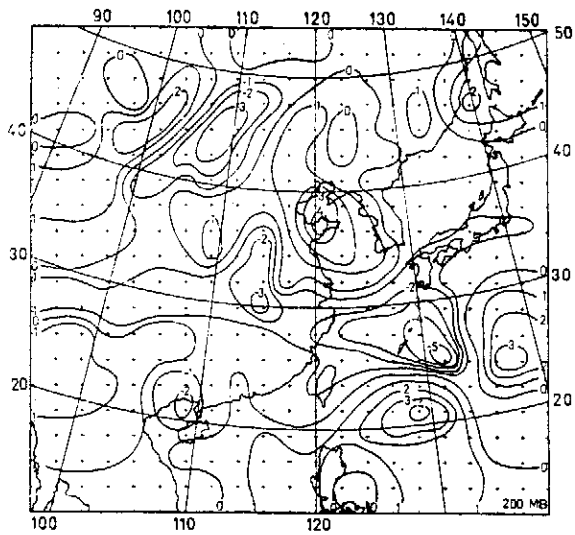

圖 13a. 同圖 8a，但爲 200mb

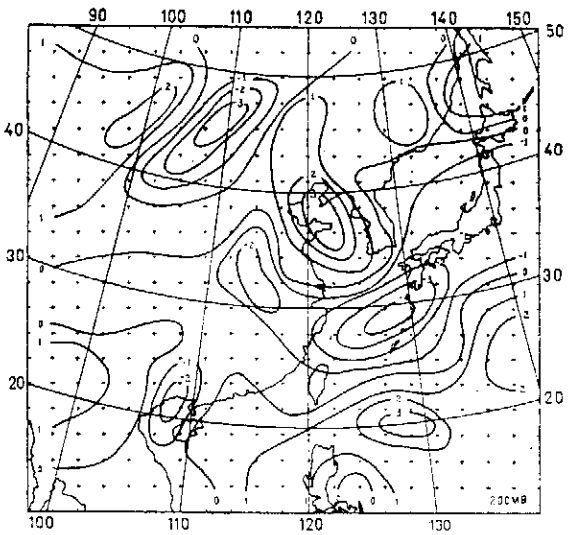

圖 13b. 同圖 8b，但爲 200mb

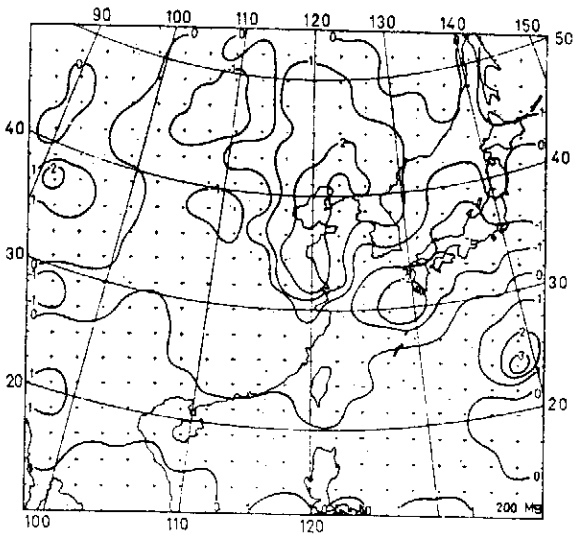

圖 13c. 同圖 8c，但爲 200mb

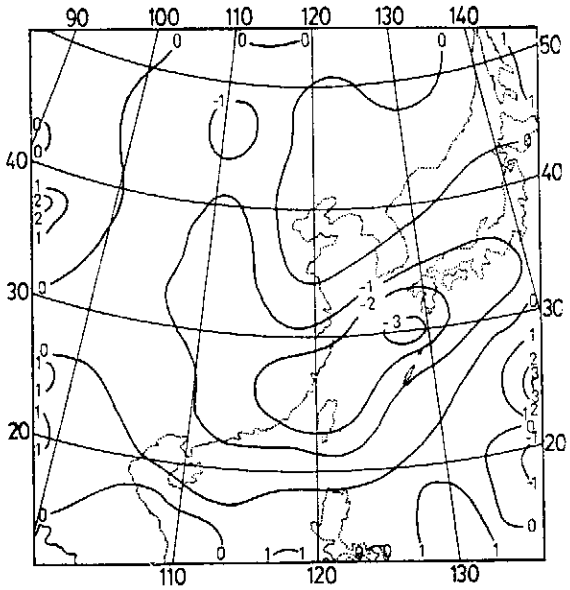

圖 13d. 同圖 8d，但爲 200mb

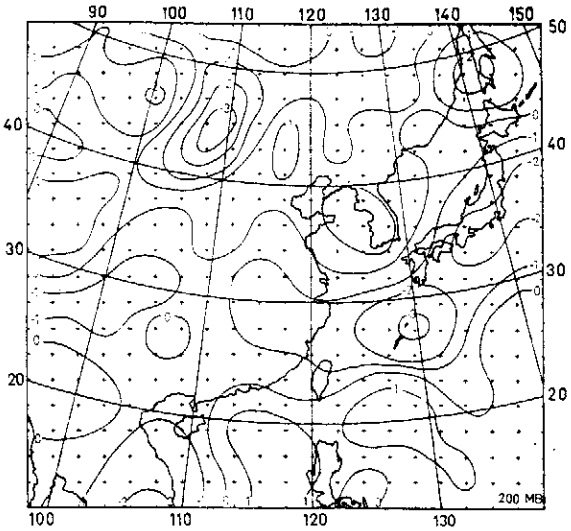

圖 13e. 同圖 8e，但爲 200mb

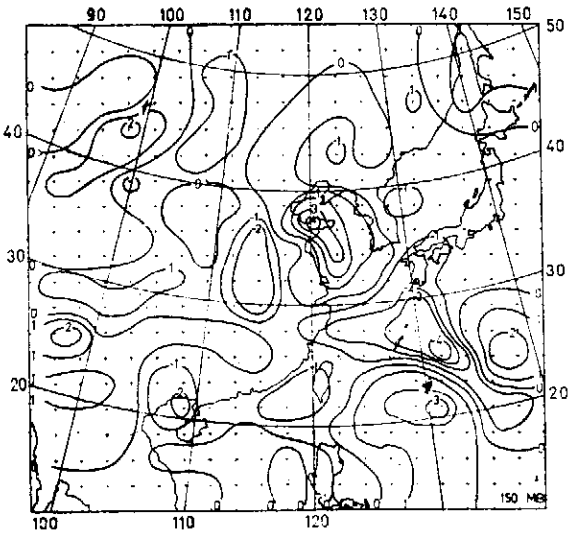

圖 14a. 同圖 8a，但爲 150mb

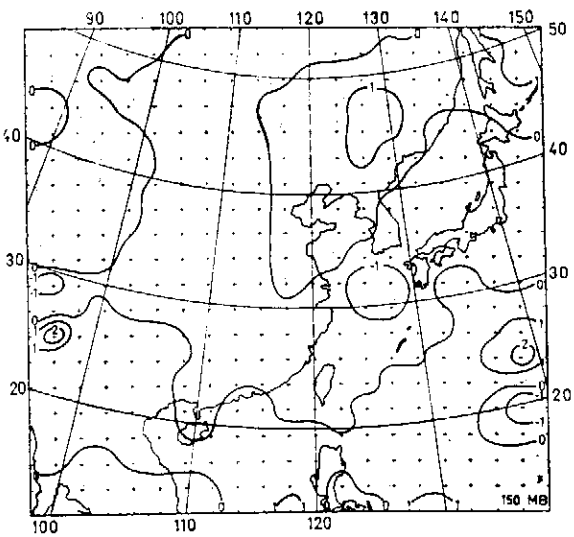

圖 14b. 同圖 8c，但爲 150mb

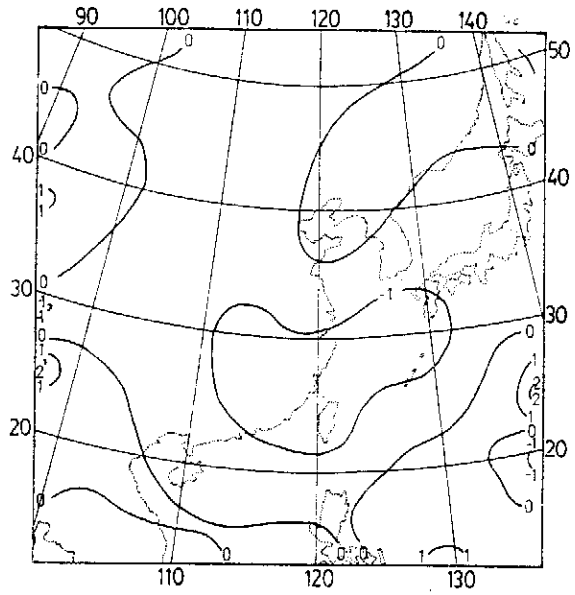

圖 14c. 同圖 8d，但爲 150mb

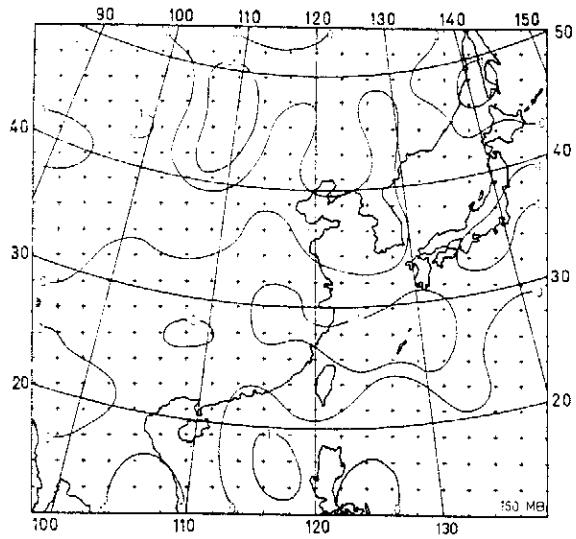

圖 14d. 同圖 8e，但爲 150mb

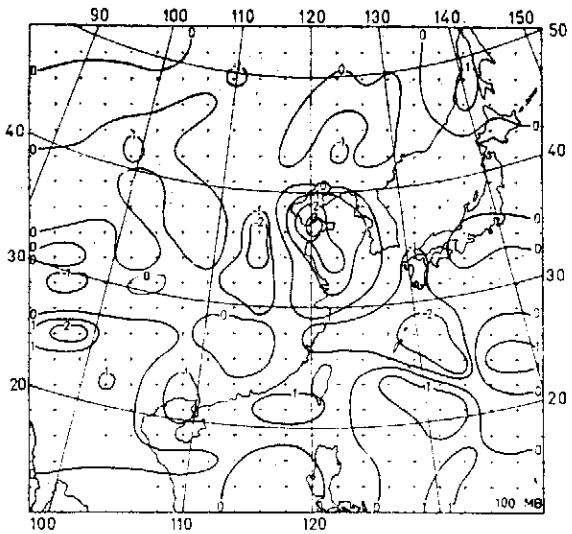

圖 15a. 100mb 的垂直速度場，單位爲 10^{-3} mb，由第一種變分程式求得

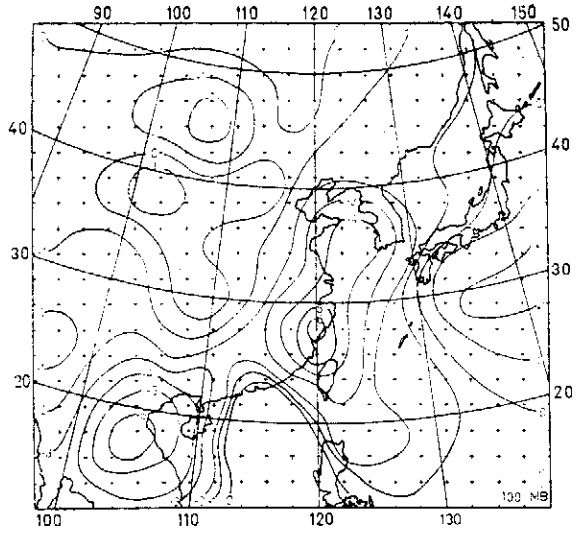

圖 15b. 100mb 的垂直速度場，單位爲 10^{-3} mb，由絕熱法求得

Abstract

A COMPARATIVE STUDY OF VERTICAL MOTION COMPUTATIONS

CHUNG YI TSENG

Institute of Physics, Academia Sinica
and
Department of Atmospheric Sciences, Natonial Taiwan University

Large scale vertical velocity is important in diagnostic and prognostic studies of atmospheric motions and in the parameterization of the physical processes in the atmosphere. Due to its smallness in magnitude, it is commonly computed from the horizontal wind velocity, the pressure or temperature distributions. The methods commonly used have been called the kinematic method, adiabatic method and dynamic method. In recent years various variational optimization schemes have been developed for the correction of vertical velocity using kinematic method. In this study a new variational optimizational approach to the vertical motion computations has been developed to adjust the observed wind subject to the dynamic constraints of continuity equation and thermodynamic equation. A comparison is made between the two variational methods, omega equation methods and the kinematic method for a case study in the East Asia area during the Mei-Yu season. Results of the present study indicate that omega equation methods are inferior to the other three methods in computing large scale vertical motions. The results of the two variational methods and the kinematic method show that the magnitudes and the general patterns of vertical velocity field are in good agreement with the synoptic weather system and the NOAA satellite picture.

三種客觀分析程式之比較研究

A comparative study of three objective analysis schemes

曾　忠　一

中央研究院物理研究所與國立臺灣大學大氣科學系

摘　　要

本研究進行三種客觀分析程式的試驗，並與主觀分析互相比較。研究結果顯示，客觀分析能準確定出高低壓中心，以及冷區和暖區。當然其中仍存在若干缺點，尤其是東南亞和西太平洋等地區資料缺乏，嚴重影響客觀分析的正確性。此外各種客觀分析程式的驗證工作，亦尚待進一步研究。

壹、導　　言

用客觀的數值方法來從事氣象變數的分析是近年氣象學最常用的方法。客觀分析就是把分佈不規則的測站上所測得的氣象變數值內插到規則的網格點上，以作爲例行數值天氣預報的初值或作爲分析大氣現象之用。客觀分析的任務除了內插之外，必須能使氣象場保持內部一致，例如高度場和溫度場之間的靜水平衡以及高度場和風場之間的準地轉平衡。此外一個完善的客觀分析程式必須具有除錯和修勻的能力。

Bergthorsson 與 Doos (1955) 建立了客觀分析法的基本概念。他們先把網格點周圍測站上的氣象變數值做加權平均以求得該變數在網格點上之值。在客觀分析程式中使用初次估計值減少了許多資料缺乏地區的分析問題。同樣的利用觀測風以地轉風的關係式求得高度的傾斜率，對分析高度也有很大的助益。Bushby 與 Huckle (1957) 進一步把預報值當作初次估計值。Shuman (1957) 使用濾波器減少了分析場上的短波。Cressman (1959) 設計一種權重，已被美國氣象中心使用於例行的天氣分析 (McDonell 1962)。Inman (1970) 修改 Cressman 的權重，考慮到測站上因觀測風不同而引起的權重的不同。Barnes (1973) 利用指數的權重來分析中幅

度的大氣現象，並且指出這種指數權重的優點。McFarland (1975) 合併了Inman 權重和 Barnes 權重的優點，設計一種非均質非等向性的權重來分析暴風環境。

我國氣象單位爲了要將數值天氣預報納入預報作業內，近年來也積極研究客觀分析法，現在已能從事例行的天氣圖客觀分析。胡氏 (1975) 利用客觀分析值作爲正壓模式天氣預報的初值。曾氏 (1976，1977) 利用客觀分析所得的高度場、溫度場和風場做爲輸入值，以進行變分最佳分析。胡氏 (1977) 從事高空天氣圖客觀分析的研究，此項分析法係由電子計算機一貫作業，業經中央氣象局採用，並納入電子計算機例行作業。

本研究對 Cressman, Inman 和 Barnes 三種權重繼續進行數值試驗，以期了解這三種權重的特性，以便改進現有的分析程式。

貳、研 究 方 法

測站上的天氣資料，諸如高度、溫和風等，經過各種檢定處理，改正錯誤並且補充漏失的資料以後，就可以進行客觀分析工作，將測站上的天氣資料內插到網格點上。本研究所使用逐次校正法，其內容如下：

㈠ **基本分析法**　假設 $D_k^{\mu-1}$ 是測站 k 上觀測值與第 $\mu-1$ 次分析值之差，即

$$D_k^{\mu-1}=Z_k-Z_s^{\mu-1}$$

其中 Z_k 是測站 k 上的觀測值，$Z_s^{\mu-1}$ 是測站 k 上第 $\mu-1$ 次分析。某一網格點的校正值可由影響半徑內的 $D_k^{\mu-1}$ 值加權平均值得到，

$$C_{ij}^{\mu}=\frac{\sum_{k=1}^{N} W_k\, D_k^{\mu-1}}{\sum_{k=1}^{N} W_k}$$

其中 W_k 是測站 k 的權重函數，N 是測站的數目。因此網格點的新分析值爲

$$Z_{ij}^{\mu}=Z_{ij}^{\mu-1}+C_{ij}^{\mu}$$

得到新的分析值以後可以照上面所敍述的方法重覆掃描三四次，就可以得到分析結果。

在進行下一次掃描之前，測站上的分析值必須先加估計，在網格範圍內測站上的分析值可用下列線性內插法（圖1）求得

$$Z_s = Z_1 + (Z_4 - Z_1)\frac{\Delta x}{\Delta} + (Z_2 - Z_1)\frac{\Delta y}{\Delta}$$
$$- (Z_2 - Z_3 + Z_4 - Z_1)\frac{\Delta x \Delta y}{\Delta^2}$$

其中 Δ 是網格長度。觀測值的誤差可以比較測站上的觀測值與分析值而檢查出來。假如其差的絕對值大於某一最大容許值，我們就可判斷這測站上的觀測有錯，也就是說當

$$|D_k^{\mu}| > \varepsilon$$

時，觀測值有錯。分析高度時，ε 可定爲 30m。在進行下一次掃描時，觀測值錯誤的測站資料就不再使用。事實上進行主觀分析時也經常使用這種方法除錯。

㈡ **權重函數**　Cressman (1959) 使用的權重比較簡單，與測站到某一網格點的距離有關，即

$$W_k = \frac{R^2 - d_k^2}{R^2 + d_k^2} \qquad d_k < R$$
$$= 0 \qquad d_k > R$$

其中 R 是影響半徑，d_k 是某一網格點到測站 k 的距離（圖 2）

Inman (1970) 修改 Cressman 的權重，加重網格點上風處和下風處測站的權重，因此他的權重是

$$W_k^* = \frac{R^{*2} - d_k^2}{R^{*2} + d_k^2}$$

其中

$$R^{*2} = R^2(1 + \beta \cos^2 \theta)$$

θ 是風向與網格點和測站方向角間之夾角（圖 2）。β 可以控制權重的影響，其值可由下式推定

$$\beta = \frac{bC}{C^*}$$

其中 C 是風速，C* 是一種最大風速，b 是常數，通常定爲 1。由此看來在網格點上下風處測站的權重較大。

㈢ **初次估計值**　即 $Z_{i_1}^{(0)}$ 與 $Z_s^{(0)}$。初次估計值可以用氣候值，十二小時前的分析，或者預報值。McDonell (1967) 曾比較各種客觀分析程式的初次估計值。本研究爲方便起見，溫度和高度的初次估計值均爲零，風的初次估計值爲地轉風。初次估計值在資料缺乏地區的分析甚爲重要，若不選定適當的初次估計值，分析場

不一定會收斂。曾氏 (1976) 的研究結果指出，風場的初次估計值用零，所得到的分析非常不良，甚至不能收斂。後來改用地轉風才得到較佳的分析。

㈣ **網格範圍外測站的資料**　本研究曾利用到網格範圍外測站的資料，以便在邊界附近能得到較佳的分析。網格範圍外測站的分析值用下列式子估計

$$Z_s=\frac{\sum_{i=1}^{N}W_iZ_i}{\sum_{i=1}^{N}W_i}$$

其中

$$W_i=\frac{R^2-d_i^2}{R^2+d_i^2} \qquad d < R$$

$$=0 \qquad d_i > R$$

㈤ **高度場分析程式**　除了高度場分析之外，其他變數的分析都用上述的方法。觀測風可以改進高度場的分析，由於大幅度大氣運動均保持準地轉平衡，因此觀測風代表高度場的傾斜率。假如測站爲等距離，這些測站所能測得的最短波長爲兩倍於測站的間距，根據抽樣定理 (Stephens 1971)，假如在測站上也測得某一變數的梯度，則這些測站能測得的最短波長減小了，也就是說可定義幅度減小，因此更能代表實際的天氣資料。雖然氣象測站分佈不均勻，用抽樣定理來討論比較困難，但其原理仍是一樣。同時使用高度與風，會使其資料更具代表性，尤其在資料缺乏地區爲然。因此我們根據上述原理，在分析高度的時候，假如測站兼有高度與風的觀測值，則

$$D_k=Z_k+(\frac{\partial Z}{\partial x}\Delta x+\frac{\partial Z}{\partial y}\Delta y)_k-Z_{ij}$$

假如測站上只有高度觀測值，則

$$D_k=Z_k-Z_s$$

其中 Z_k, Z_s 分別是測站上的觀測值和分析值，Z_{ij} 是網格點上的分析值。高度的梯度可用地轉風的關係式得到，即

$$\frac{\partial Z}{\partial x}=\frac{1.08f}{mg}v$$

$$\frac{\partial Z}{\partial y}=-\frac{1.08f}{mg}u$$

其中常數 1.08 是地轉風對觀測風的平均比例，u 與 v 分別爲測站上 x 方向與 y 方

向的風速分量，m是地圖投影放大因子，f 爲科氏參數。

用以上敘述的方法可以得到網格點上的分析值，掃描的次數大致三四次，每次都把影響半徑R縮小，以便較短波能重現在分析場上。

(六) 指數權重函數

Barnes (1973) 使用指數形式的權重，即

$$W_k = \frac{1}{4\pi K} \exp\left(-\frac{d_k^2}{4K}\right)$$

其中K是濾波參數，d_k 是測站 k 至網格點的距離。

Barnes 指出指數權重具有下列優點

1. 因爲濾波參數 4K 可以事先決定，因此反應函數亦可事先知道。
2. 由於指數權重函數隨着測站至網格點間距離的增加而漸近於零，因此測站上的資料可以影響到各處的網格點。
3. 這種指數權重本身可以濾去雜波，而不需再使用濾波器。
4. 用指數權重只要掃描一次即可，可以節省許多計算時間。

叁、研 究 結 果

本研究使用民國 64 年 9 月 21 日格林尼治標準時間零時的九個定壓層 (850mb, 700mb, 500mb, 400mb, 300mb, 250mb, 200mb, 150mb, 與 100mb) 的高空天氣資料。當時中度颱風貝蒂在北緯 21.8 度，東經129.5度，即在臺北市東南東方海面 930 公里處向西北西進行，時速22公里，最大風速33m/s，暴風半徑250公里。此外在庫頁島西方有一低壓中心，冷鋒由該處向西南延伸經過日本海到達黃海。本研究考察範圍包括整個東亞地區。本研究使用21×21個網格點，網格間隔在一千五百萬分之一的地圖上爲2公分，也就是說在北緯30度處的網格間距爲300公里。進行客觀分析時，在西太平洋和東南亞等處測站稀少地區，遭遇許多問題，只有增加影響半徑R來進行分析，方能得到較佳結果。

主觀分析的高度場分別在圖 3a(850mb), 圖 4a(700mb), 圖 5a(500mb), 圖 6a(300mb), 圖 7a(200mb), 圖 8a(100mb). Cressman 權重客觀分析高度場分別在 圖 3b(850mb), 圖 4b(700mb), 圖 5b(500mb), 圖 6b(300mb), 圖 7b(200mb), 圖 8b(100mb). Inman 權重客觀分析的高度場分別在 圖 3c(850mb), 圖 4c(700mb),

圖 5c(500mb), 圖 6c(300mb), 圖 7c(200mb), 圖 8c(100mb). 指數權重客觀分析的高度場分別在 圖 3d(850mb), 圖 4d(700mb), 圖 5d(500mb), 圖 6d(300mb), 圖 7d(200mb), 圖 8d(100mb). 比較這些圖我們可以發現：

1. 主觀分析與客觀分析所得的低壓中心和高壓中心位置相符合，但客觀分析場高低壓的強度較小。後者是因爲使用濾波器加以修勻之故。客觀分析若不使用濾波器，則其高低壓強度與主觀分析場相當，但客觀分析場中會出現許多短波。

2. 三種客觀分析所得的結果非常相似，相互之間的差異大致在30公尺以內。客觀分析和主觀分析間之差異有時大於60公尺，尤其在資料缺乏地區，諸如在颱風中心附近。

3. 850mb (圖 3a) 主觀分析場中由中緯度低壓中心延伸出去有兩條槽線，客觀分析場中 (圖3b, 3c, 3d.) 只有一條比較顯著，這是因爲在千島羣島以東太平洋海面資料缺乏之故。

4. 300mb 的主觀分析 (圖 6a) 與客觀分析 (圖 6b, 6c, 6d) 高度場在颱風中心附近相差很大，這也是因爲菲律賓東方海面資料缺乏之故。

5. 至於三種客觀分析中何種分析場較佳，不易由天氣圖中看出。理論上應當 Inman 權重較佳，指數函數次之，Cressman 權重較差。若以計算時間而言，則指數函數所用計算時間較少，其次爲 Cressman 權重和 Inman 權重。

主觀分析的溫度場分別在 圖 9a(850mb), 圖 10a(700mb), 圖 11a(500mb), 圖 12a(300mb), 圖 13a(200mb), 圖 14a(100mb). Gressman 權重客觀分析溫度場分別在 圖 9b(850mb), 圖 10b(700mb), 圖 11b(500mb), 圖 12b(300mb), 圖 13b(200mb), 圖 14b(100mb). Inman 權重的客觀分析的溫度場分別在 圖 9c(850 mb), 圖 10c(700mb), 圖 11c(500mb), 圖 12c(300mb), 圖 13c(200mb), 圖 14c (100mb). 指數權重的客觀分析溫度場分別在 圖 9d(850mb), 圖 10d(700mb), 圖 11d(500mb), 圖 12d(300mb), 圖 13d(200mb), 圖 14d(100mb). 由這些圖中我們可以看出：

6. 主觀分析與客觀分析的溫度場大致相符。兩者最大的差異是客觀分析場等溫線較爲平滑，這也是因爲客觀分析場使用濾波器加以修勻之故。

7. 三種客觀分析溫度場之間差異甚小，相差只在1度以內。

8. 200mb 的主觀分析 (圖 13a) 和客觀分析 (13b, 13c, 13d), 兩者等溫線

差異較大，這是因爲在 200mb 溫度梯度較小，較不易分析。

除了以上各點之外，主觀分析與三種客觀分析大致能互相符合。

肆、結　　語

本研究進行三種客觀分析程式的試驗，並與主觀分析互相比較。研究結果顯示，客觀分析能準確定出高低中心，以及冷區和暖區。當然其中仍存在若干缺點，尤其是東南亞和西太平洋等地區資料缺乏，嚴重影響客觀分析的正確性。此外各種客觀分析程式的驗證工作，亦尚待進一步研究。

致　　謝

本研究在行政院國家科學委員會 NSC-66M-0204-08(01)「亞洲地區氣象資料之蒐集檢定與分析及程式處理系統之研究」專案計畫支援下完成，殊深感激，本計畫在執行階段，由於中央氣象局鼎力協助，使研究工作得以順利完成。其中尤以研究助理劉振榮，臺大學生許晃雄貢獻良多，特此致謝。

參　考　文　獻

Barnes, S. L., 1973: Mesoscale objective map analysis using weighted time series observations. *NOAA Tech. Memo. ERL NSSL-62*, 60 pp.

Bergthorsson, P. and B. R. Doos, 1955: Numerical weather map analysis. *Tellus*, **7**, 329-340.

Bushby, F. H. and V. M. Huckle, 1957: Objective analysis in numerical forecasting. *Quart. J. Roy. Meteor. Soc.*, **83**, 232-247.

Cressman, G. P. 1959: An operational objective analysis scheme. *Mon. Wea. Rev.*, **87**, 367-374.

胡仲英，1975：正壓大氣數值模式及其應用，大氣科學，第二期，1-7。

胡仲英，1977：高空天氣圖客觀分析之研究，大氣科學，第四期，1-10。

Inman, R. L., 1970: Papers on operational objective analysis schemes at NSSFC. *NOAA Tech. Memo. ERL NSSL-51*, 91 pp.

McDonell, J. E., 1962: On the objective analysis system used at the National Meteorological Center. *NMC TM* No. 23, National Meteorological Center, Washington, D. C., 32 pp.

McDonell, J. E., 1967: A summary of the first guess fields used for operational analysis. *ESSA TM WBTM NMC-38*, 17 pp.

McFarland, M. J., 1975: Variational optimization analysis of temperature and moisture advection in a severe storm environment. *WEAT Report No. 16*, University of Oklahoma, Norman, Oklahoma, 86 pp.

Shuman, F. G. 1957: Numerical method in weather prediction: II. Smoothing and filtering. *Mon. Wea. Rev.*, **85,** 357-361.

Stephens, J. J., 1971: On the definable scale reduction by simultaneous observations. *J. Appl. Meteor.*, **10,** 23-25.

Tseng, C. Y., 1976a: A variational analysis scheme suitable for operational use. *Ann. Rept. Inst. Phys., Acad. Sin.*, **6,** 153-159.

曾忠一，1976b：東亞地區天氣資料變分客觀分析之研究。中央研究院物理研究所集刊，第六卷 161-178。

曾忠一，1977：利用原始方程式進行變分客觀分析之研究。中央研究院物理研究所集刊，第七卷 77-92。

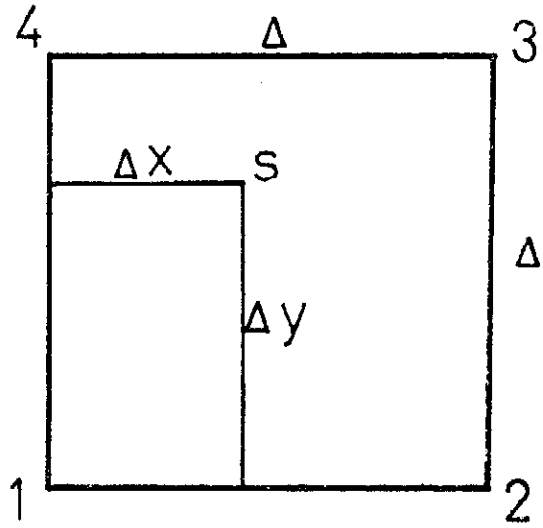

圖 1. 本圖說明測站上分析值的求法

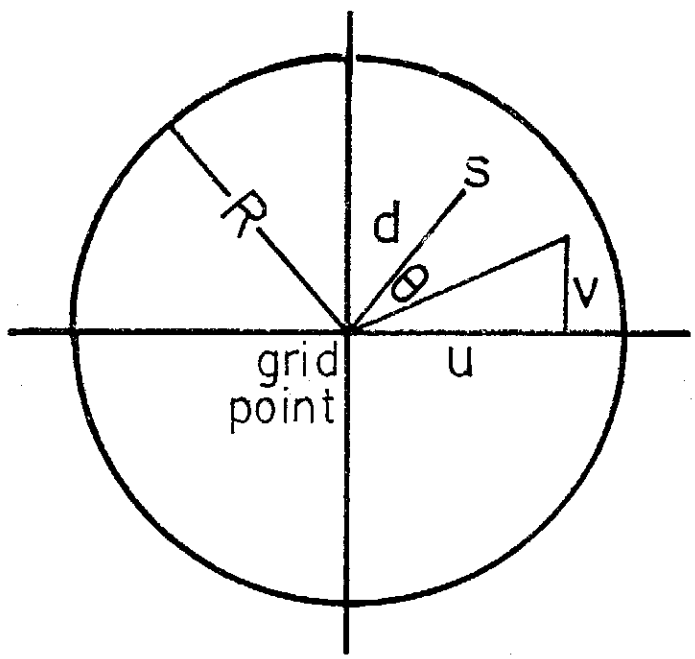

圖 2. 本圖說明各符號的定義

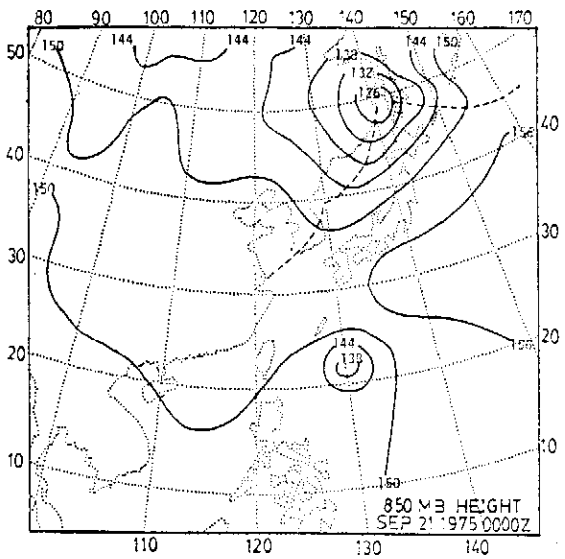

圖 3a. 850mb主觀分析高度場

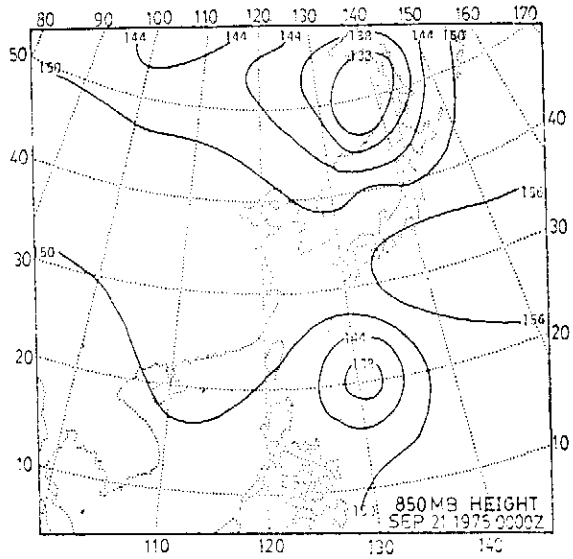

圖 3b. 850mb Cresman 權重客觀分析高度場

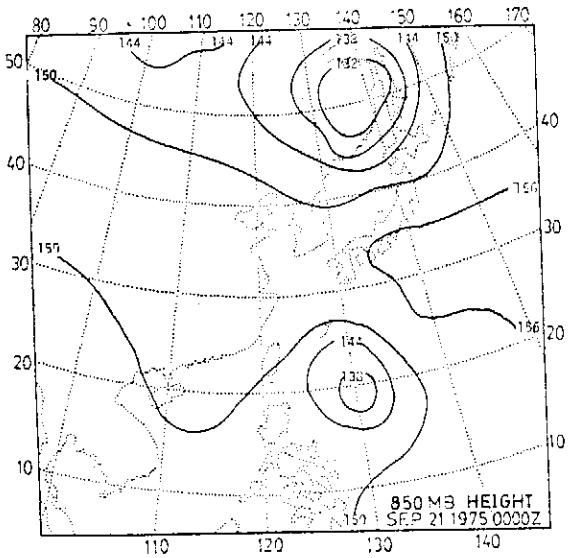

圖 3c. 850mb Inman 權重客觀分析高度場

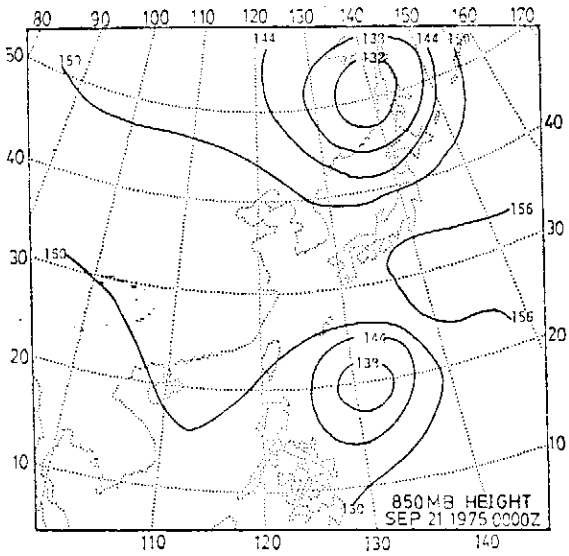

圖 3d. 850mb 指數權重客觀分析高度場

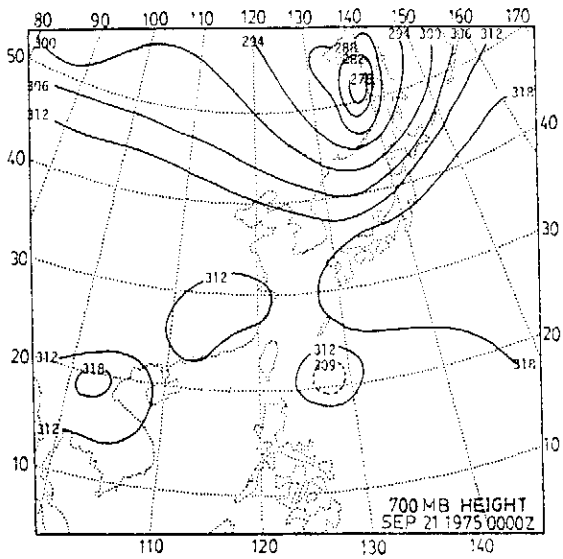

圖 4a. 同圖 3a 但爲 700mb

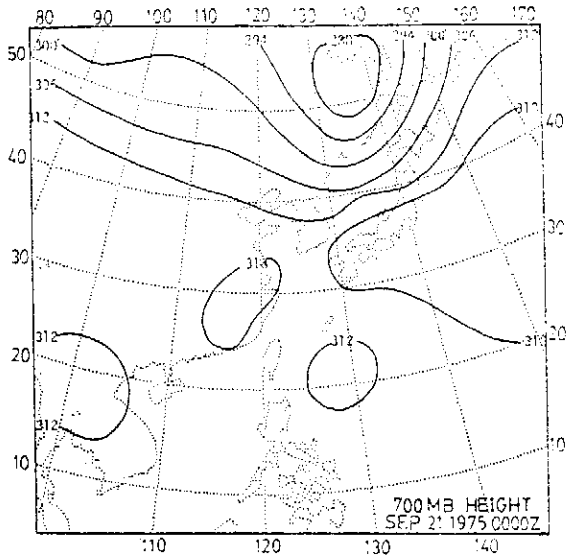

圖 4b. 同圖 3b 但爲 700mb

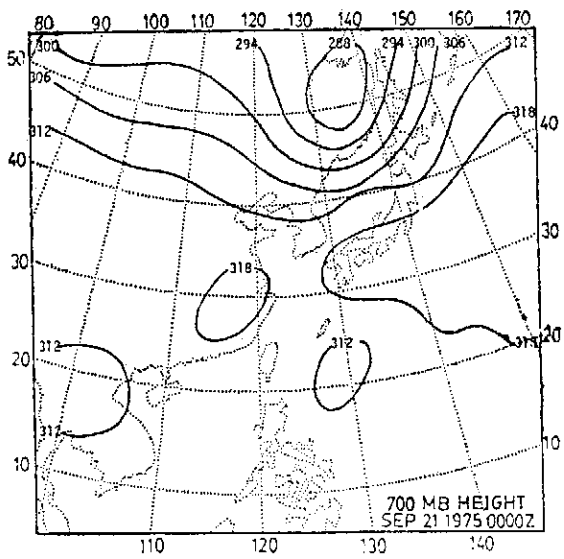

圖 4c. 同圖 3c 但爲 700mb

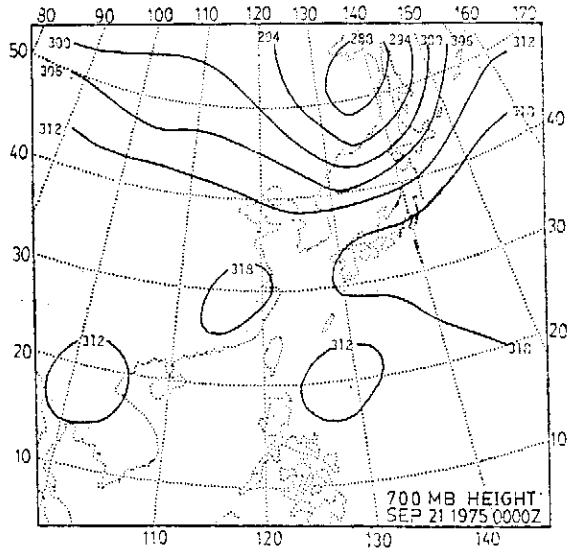

圖 4d. 同圖 3d 但爲 700mb

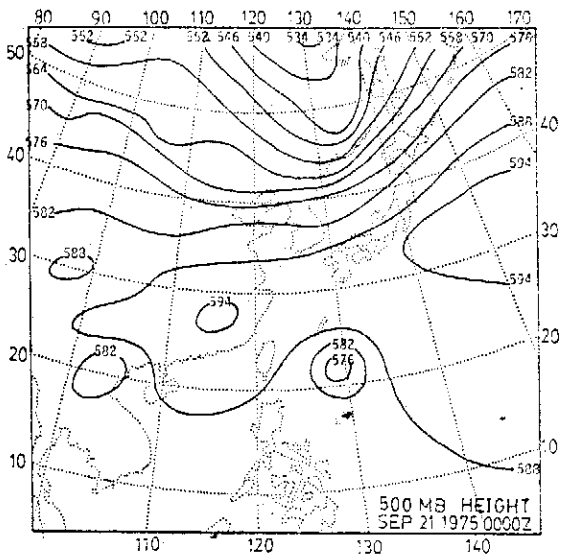

圖 5a. 同圖 3a 但爲 500mb

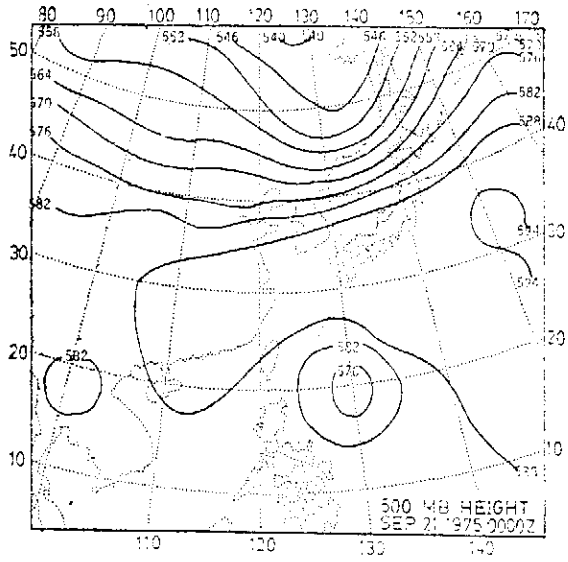

圖 5b. 同圖 3b 但爲 500mb

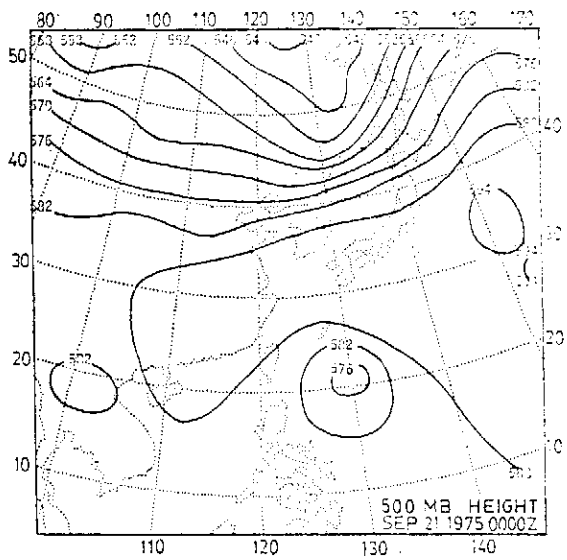

圖 5c. 同圖 3c 但爲 500mb

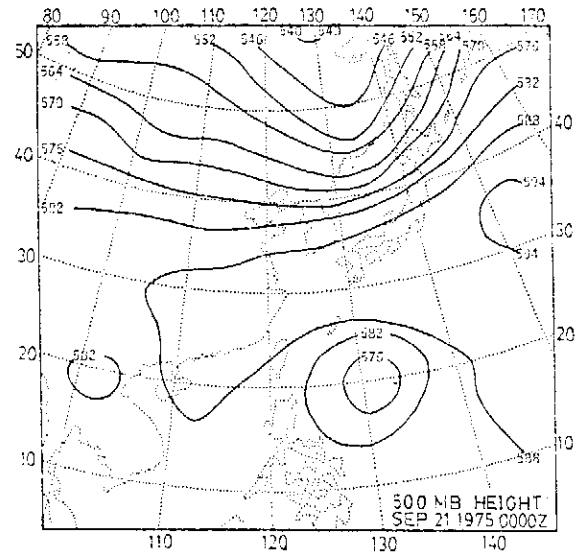

圖 5d. 同圖 3d 但爲 500mb

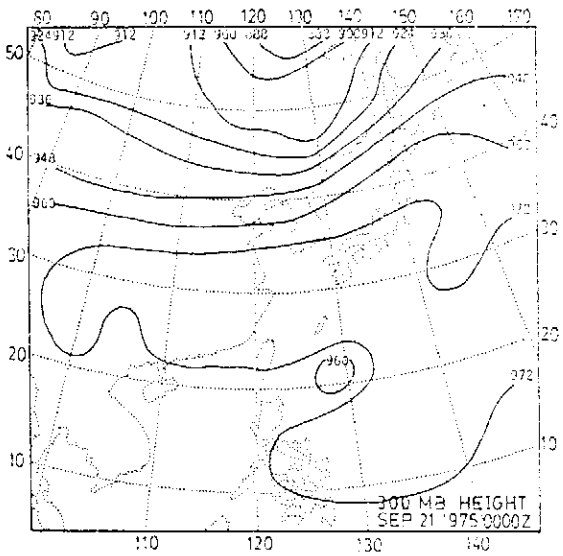

圖 6a. 同圖 3a 但爲 300mb

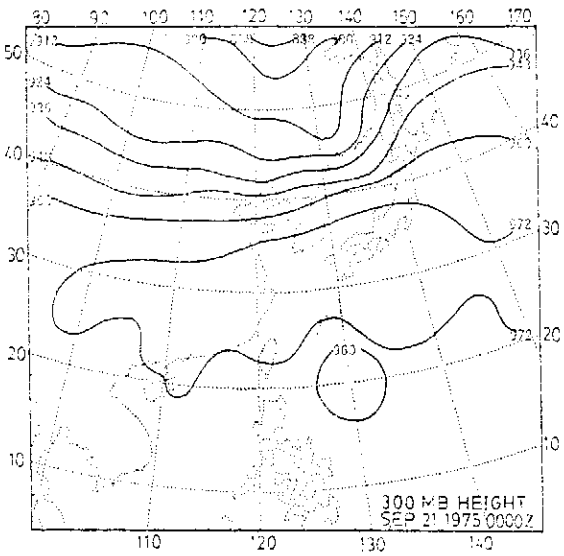

圖 6b. 同圖 3b 但爲 300mb

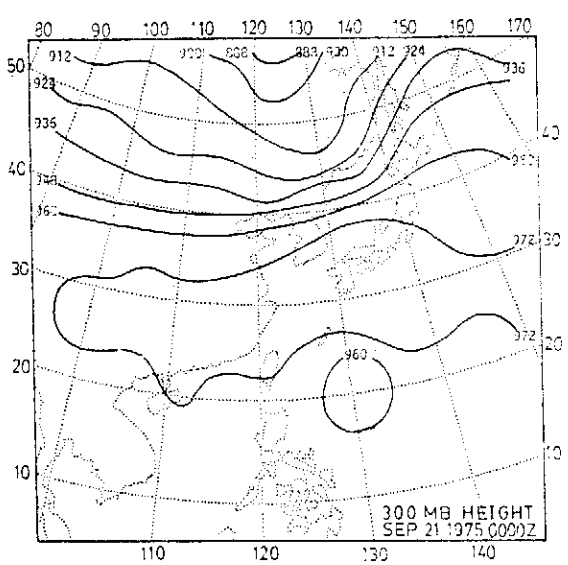

圖 6c. 同圖 3c 但爲 300mb

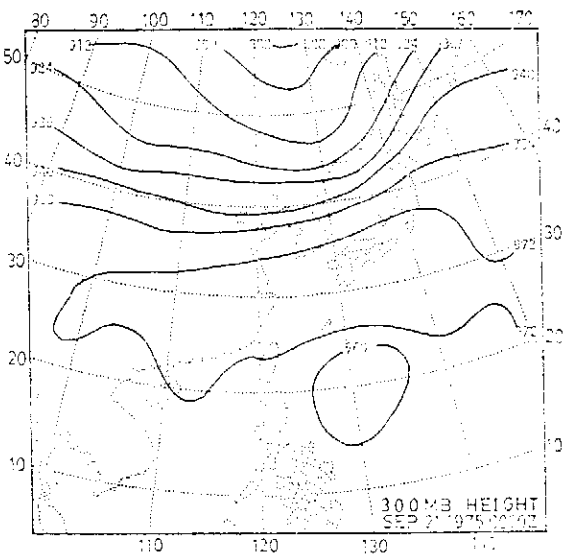

圖 6d. 同圖 3d 但爲 300mb

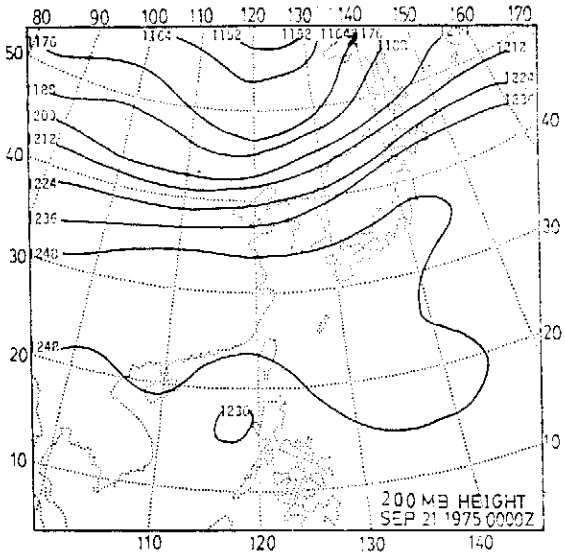

圖 7a. 同圖 3a 但爲 200mb

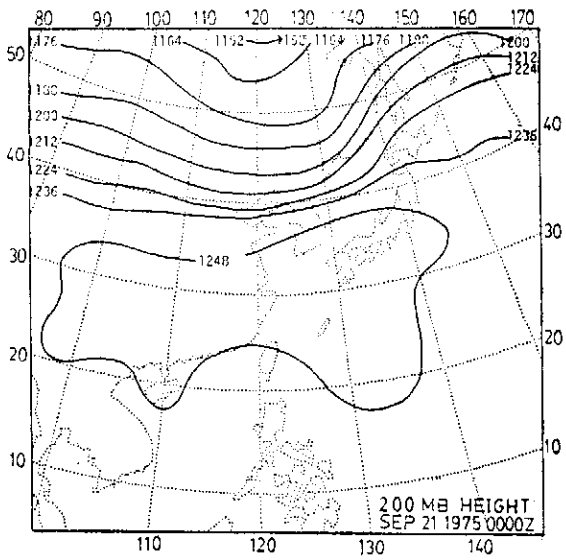

圖 7b. 同圖 3b 但爲 200mb

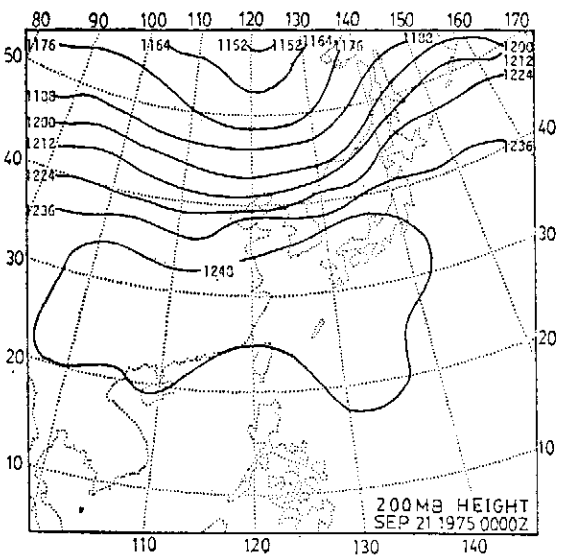

圖 7c. 同圖 3c 但爲 200mb

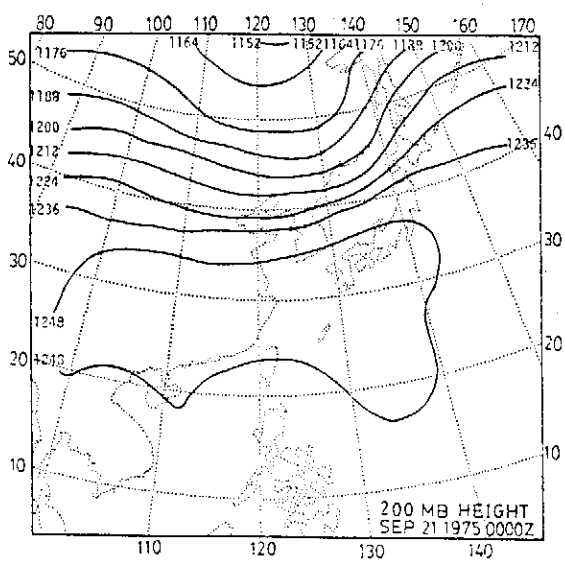

圖 7d. 同圖 3d 但爲 200mb

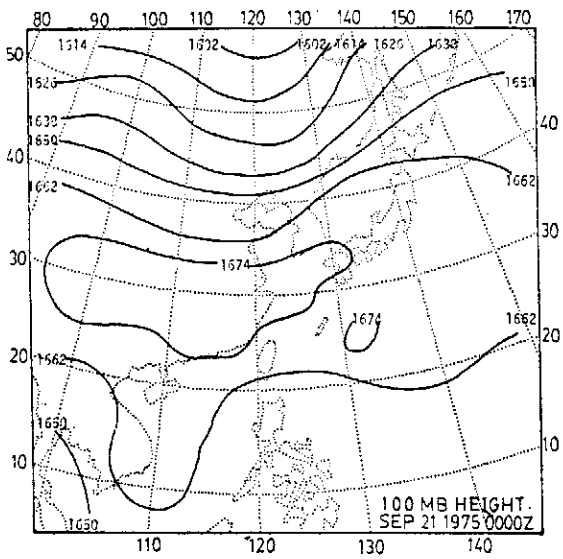

圖 8a. 同圖 3a 但爲 100mb

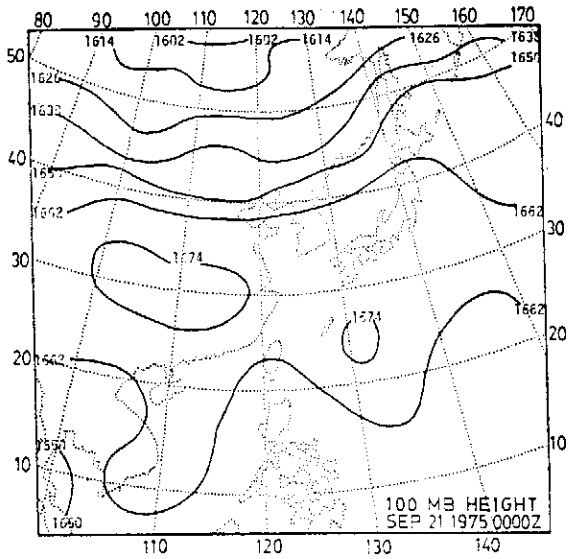

圖 8b. 同圖 3b 但爲 100mb

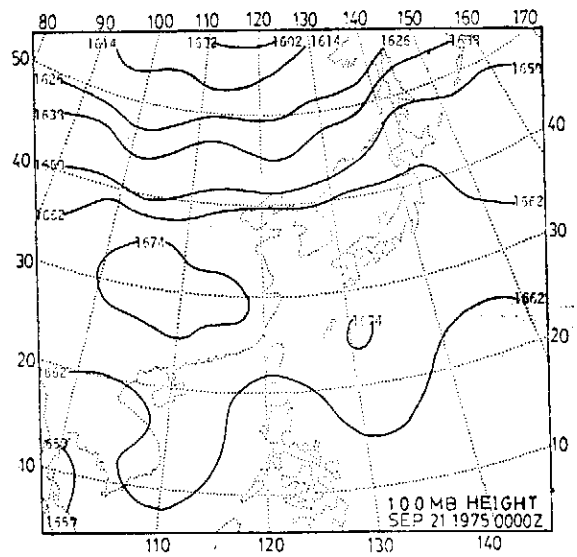

圖 8c. 同圖 3c 但爲 100mb

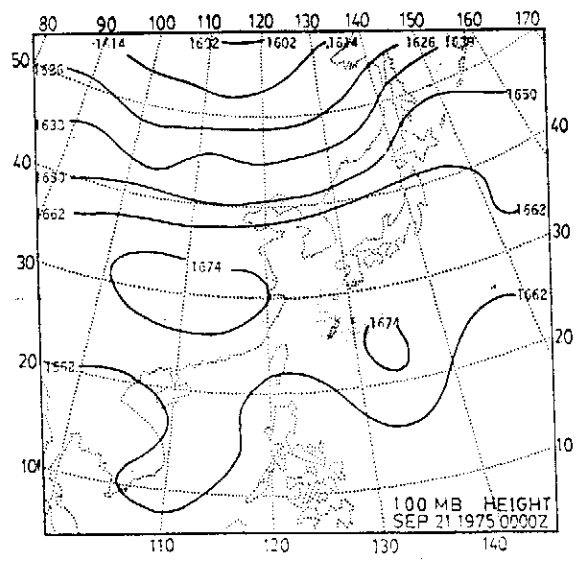

圖 8d. 同圖 3d 但爲 100mb

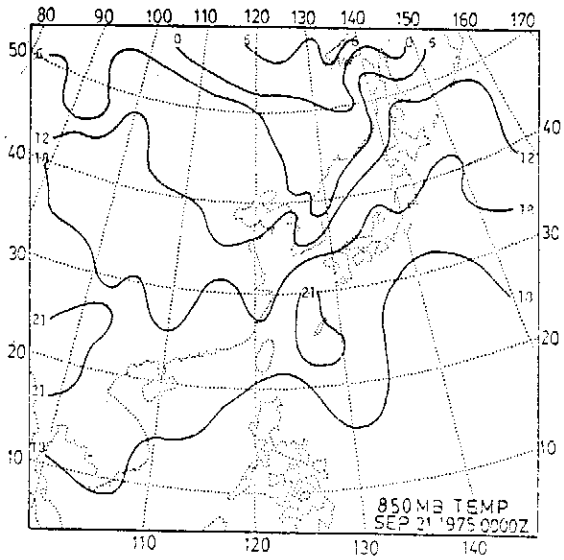

圖 9a. 850mb 主觀分溫度場

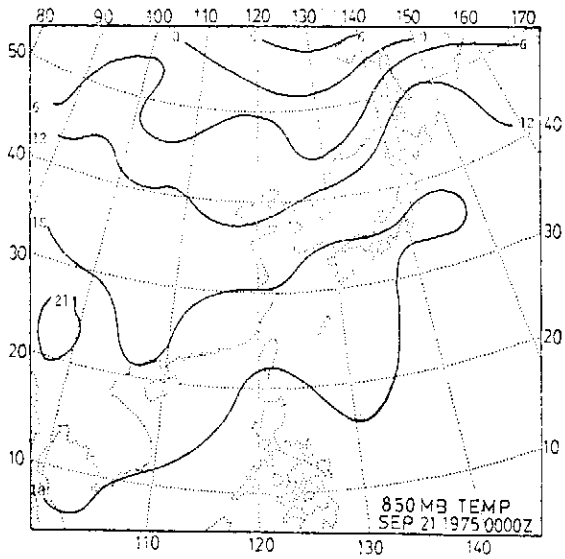

圖 9b. 850mb Cressman 權重客觀分析溫度場

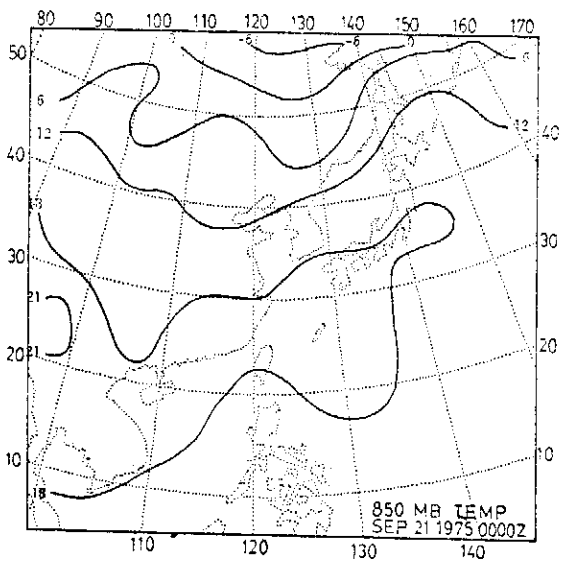

圖 9c. 850mb Inman 權重客觀分析溫度場

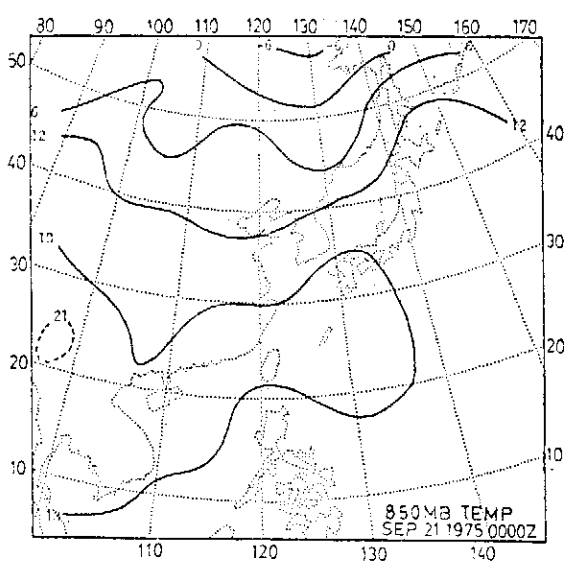

圖 9d. 850mb 析指數權重客觀分析溫度場

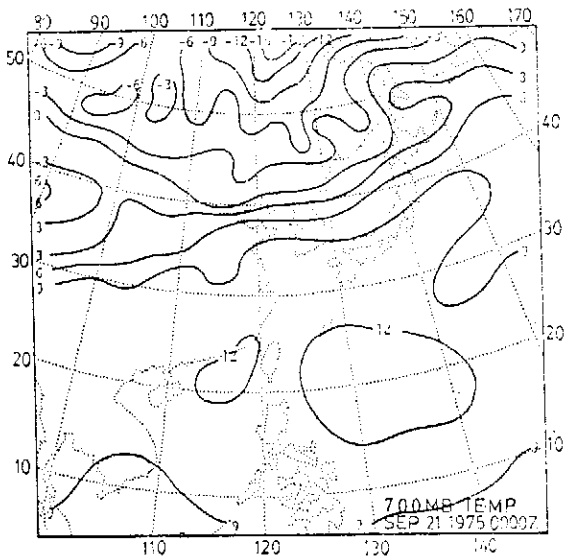

圖 10a. 同圖 9a 但爲 700mb

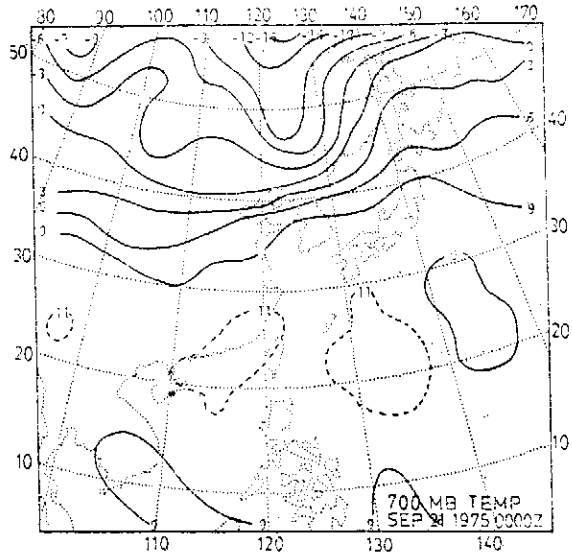

圖 10b. 同圖 9b 但爲 700mb

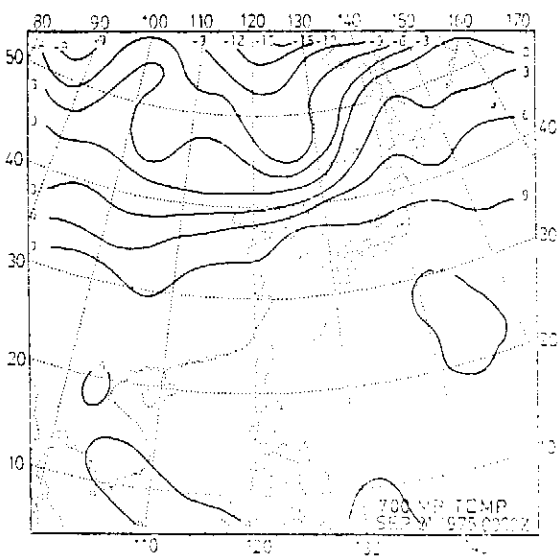

圖 10c. 同圖 9c 但爲 700mb

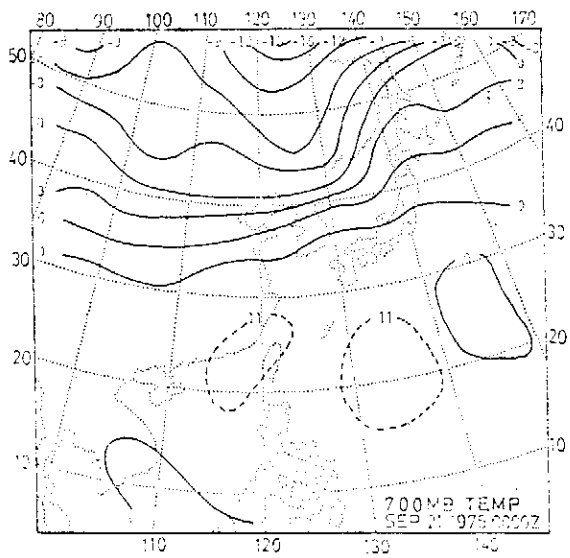

圖 10d. 同圖 9d 但爲 700mb

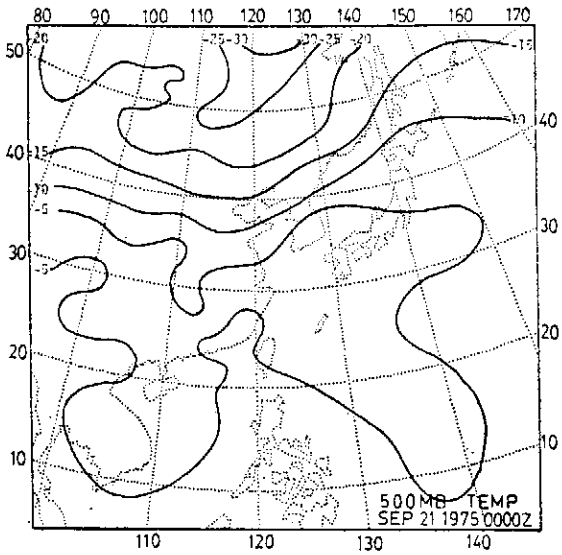

圖 11a. 同圖 9a 但爲 500mb

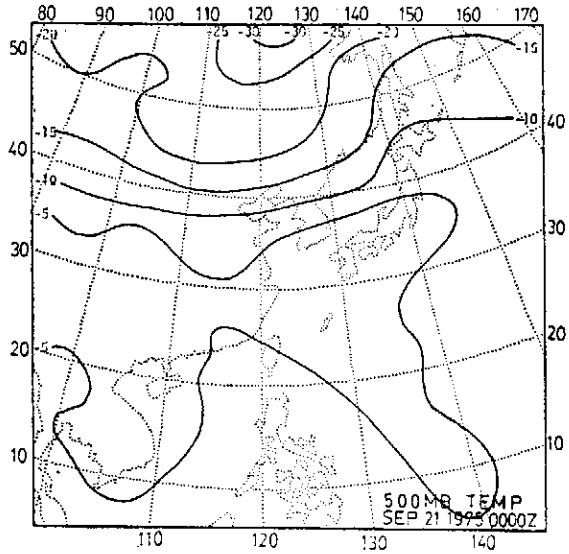

圖 11b. 同圖 9b 但爲 500mb

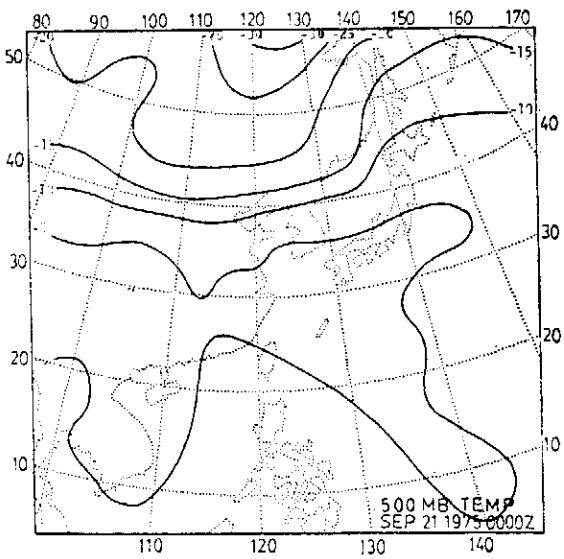

圖 11c. 同圖 9c 但爲 500mb

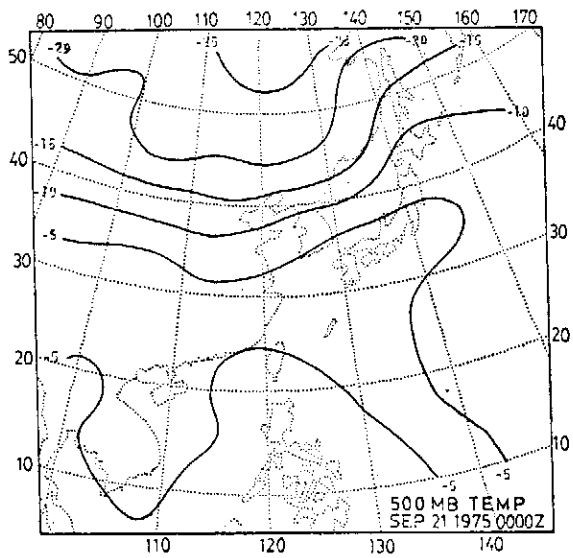

圖 11d. 同圖 9d 但爲 500mb

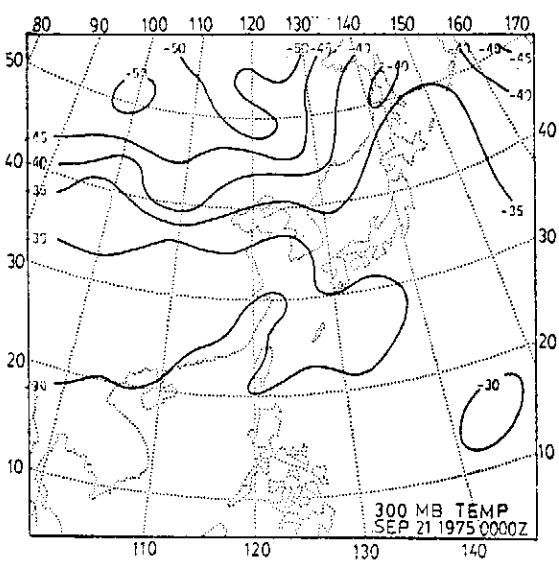

圖 12a. 同圖 9a 但爲 300mb

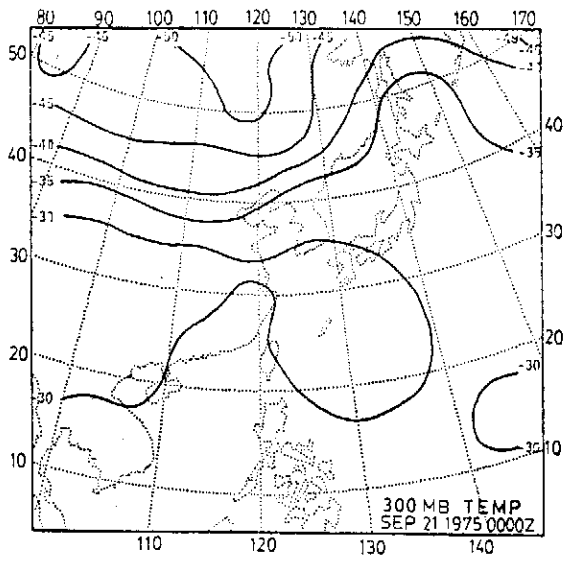

圖 12b. 同圖 9b 但爲 300mb

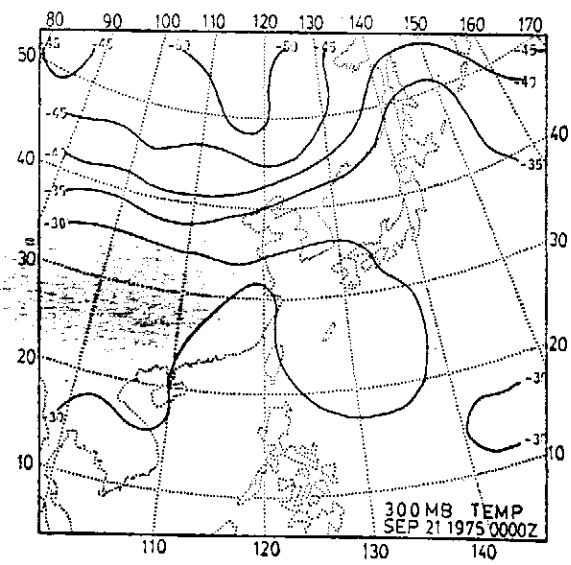

圖 12c. 同圖 9c 但爲 300mb

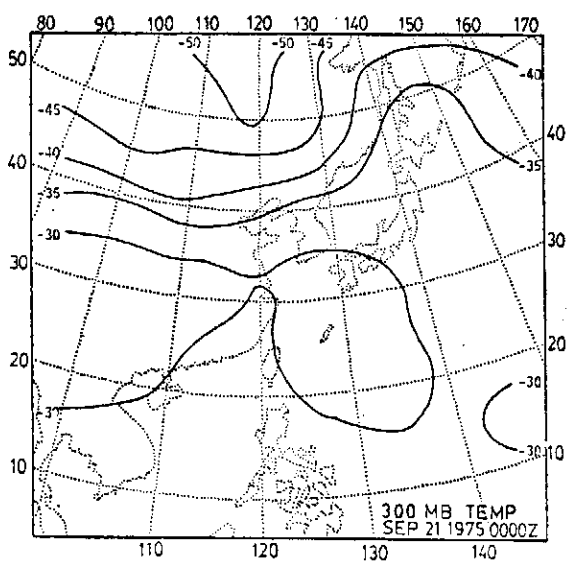

圖 12d. 同圖 9d 但爲 300mb

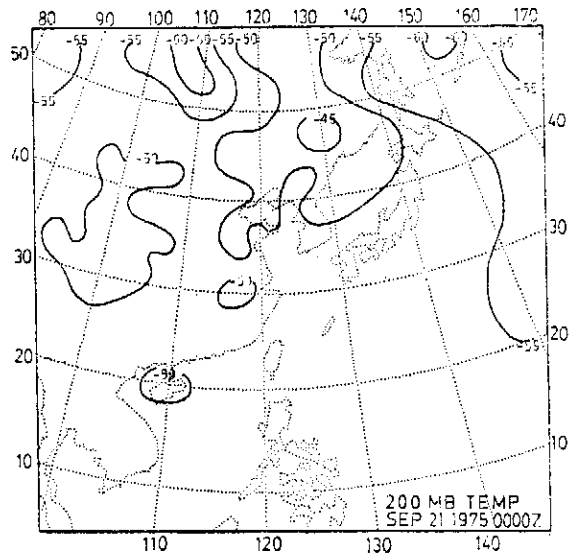

圖 13a. 同圖 9a 但爲 200mb

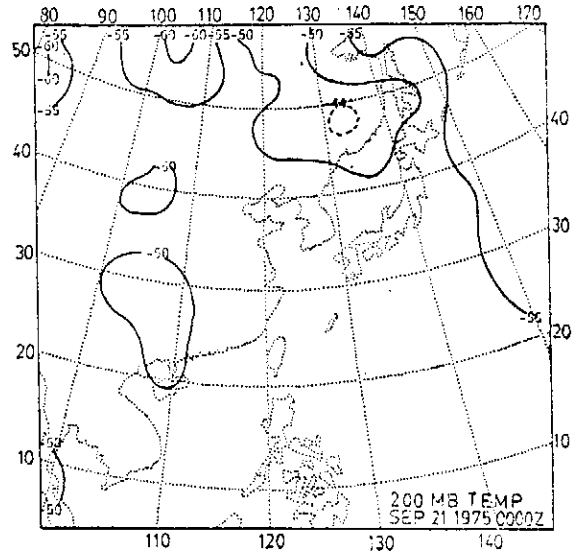

圖 13b. 同圖 9b 但爲 200mb

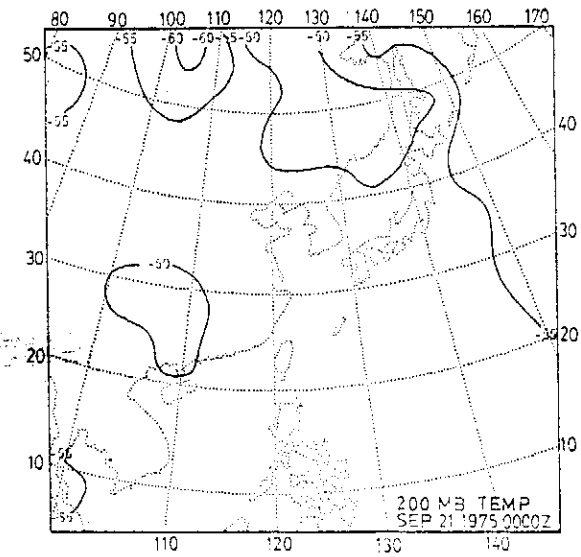

圖 13c. 同圖 9c 但爲 200mb

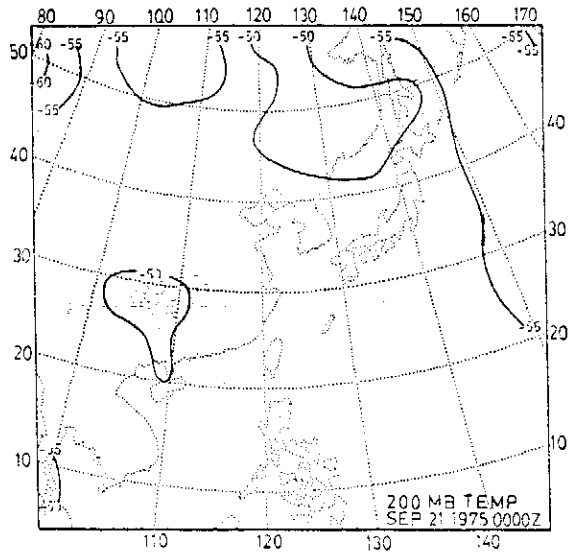

圖 13d. 同圖 9d 但爲 200mb

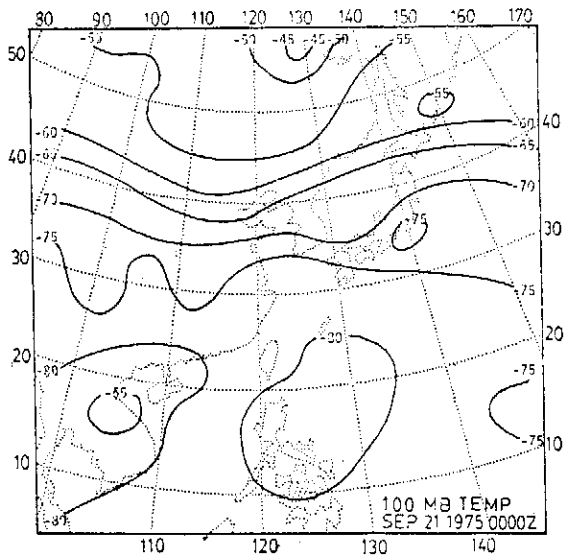

圖 14a. 同圖 9a 但爲 100mb

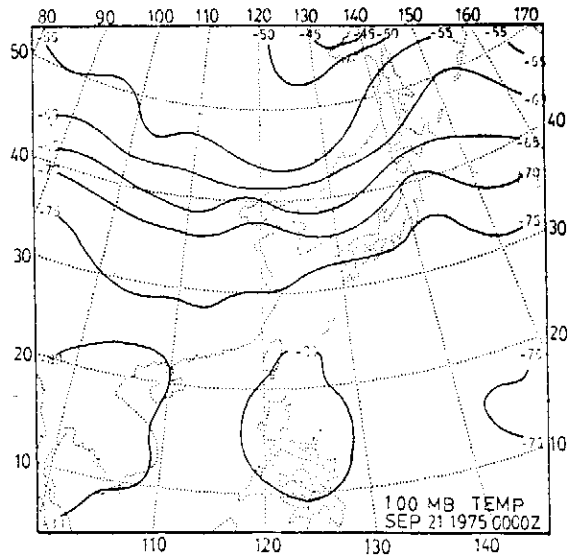

圖 14b. 同圖 9b 但爲 100mb

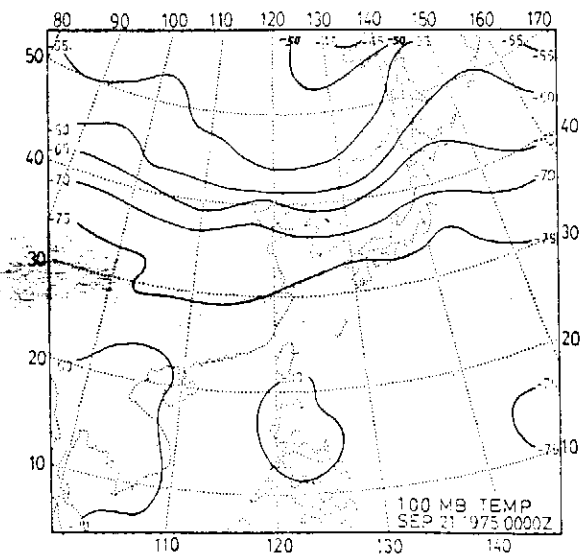

圖 14c. 同圖 9c 但爲 100mb

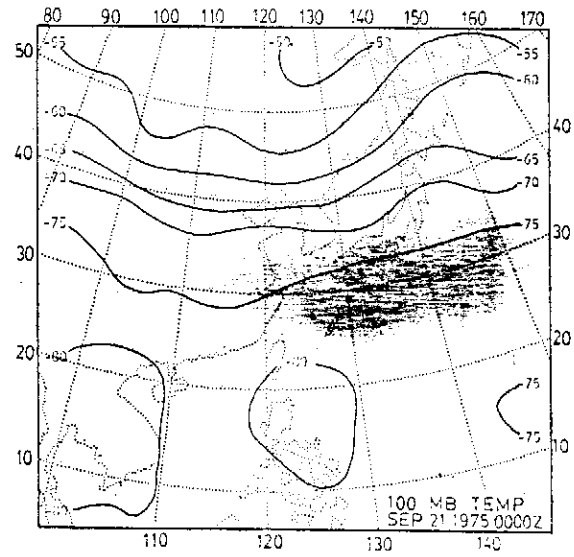

圖 14d. 同圖 9d 但爲 100mb

THE GENERALIZATION OF KUO'S PARAMETERIZATION OF CUMULUS CONVECTION
Part II. The Closed Theory

WEN-JEY LIANG (梁文傑)

Institute of Physics, Academia Sinica and
Dept. of Mech. Eng., National Taiwan University

Abstract

In this study, a closed theory of the generalization of Kuo's parameterization of cumulus convection is developed by combining a one-dimensional cloud ensemble model. The theory is the extension of Kuo's (1965 and 1974) and Liang's (1977) parameterization schemes. It includes the transport of the dry static energy which is closely corrclated to che baroclinity of the weather systems, and is able to apply to the middle latitudes as well as in the tropics. The theory is diagnosticated using the Marshall Islands data set, waich is used in the budgets study by Yanai *et al* (1973). The results show that the estimations on the latent heat released, the cloud depth, the net entrainment rate and the cloud bulk properties are satisfactorily explained by the observations, and the physical phenommena revealed are consistent to the real situations.

I. INTRODUCTION

In Liang (1977), a new parameterization of cumulus convection had been developed based on the moisture conservation equation of the largescale motion. The scheme is considered as a generalization of Kuo's parameterization concepts, and Kuo's (1965 and 1974) schemes are reduced from it as two special cases. It is also shown that Kuo's two schemes are essentially the same.

According to the large scale moisture equation, the total moisture supply from the large-scale and the subgrid scale motions is utilized to increase the local moisture content of the mean fllow, $\bar{q}$, and to produce the net precipitation. In generalized scheme, the local increasing of the moisture of the environmental air is regarded from two processes. One is the mixing process of the cloud mass and the environmental air, and the other is the transport process directly from the large-scale motion. In other words, the latter reflects the efficiency of the moisten effect of the total moisture supply bypass the cumulus mixing process, and the generalized scheme is closed if this term is specified. In Liang (1977), this term is assumed to be proportional to the total moisture supply and the proportional constant is called the effect coefficient. The plausibility of the scheme was diagnosticated utilizing the combination of the parameterization formula and the large-scale heat and moisture budgets. Compared with the observations, although the generalized scheme

gives better estimations on the latent heat released and the pressure of the cloud top, it is still unsatisfactory. The results show that the pressure of the cloud top is about 180 mb lower and the precipitation rate is about 17% smaller than those of the observational values. Also, the maximum excess temperature at 700 mb is too high. The shortcomings are considered from the rough parameterization of the effect coefficient term. For increasing the applicability of the scheme, further studies are required.

In this study, a closed theory of the generalization shceme is developed by the combination of a one-dimensional cloud ensemble model, and the effect coefficient term is reformulated from this cloud model. The theory is investigated diagnostically using the Marshall Islands data, which are used in the study by Yanai *et al* (1973), and the results are compared with those obtained in Yanai *et al.*

II. FORMULATION FOR THE CLOSED THEORY

For convenience, the dry static energy s and moist static energy h are defined as

$$s \equiv C_p\ T + gz,$$

and

$$h \equiv C_p\ T + gz + Lq,$$

where T is temperature, z the height, q the mixing ratio, C_p the specific heat of dry air, L the latent heat of condensation, and g the acceleration of gravity. It is obvious that the static energy is the sum of enthalpy and potential energy and the moist static energy is the sum of the static energy and latent energy. For the clarification of the essential points of the parameterization problem, the large-scale variables are represented as the average values over a hypothesized area, and the actual values are the sum of the average values and the departures. The hypothesized area is taken to be large enough such that a great deal of cumulus clouds may be surrounded, and to be small enough thus the large-scale motion may be described by the area mean values of its variables. This quasi-homogeneous assumption is based on the fact that the physical properties of the largescale syetem may approximately be homogeneous over a suitablly chosen area. For prediction of the synoptic scale motion, for example, the grid area may reasonablly be taken as the hypothesized area. Furthermore, based on the assumption of the feasibility of the parameterization of cumulus convection, the location and time of the convection occurrence are random distributed and the distribution may be estimated in term of the large-scale variables.

For the description of the large-scale motion, the equations of heat and moisture continuity are averaged over the hypothesized area:

$$\frac{\partial \bar{s}}{\partial t} + \nabla \cdot \bar{s}\bar{V} + \frac{\partial \bar{s}\bar{\omega}}{\partial p} = Q_R + Q_c, \tag{1}$$

$$\frac{\partial \bar{q}}{\partial t} + \nabla \cdot \bar{q}\bar{V} + \frac{\partial \bar{q}\bar{\omega}}{\partial q} = -\frac{Q_c}{L} \tag{2}$$

$$Q_c = L\,(c+e) \tag{3}$$

where $\bar{V}$ is the wind velocity, ω the vertical p- velocity, Q_R the radiation heating, Q_c the latent heat released by net condensation, c the condentsation rate, and e the re-evaporation. The equations are expressed in (x, y, p, t) coordinates, and the area averages are denoted by ( ). As the variables are represented by the area mean values and the departure, (1) and (2) become

$$Q_1 \equiv \frac{\partial \bar{s}}{\partial t} + \overline{\nabla \cdot s\vec{V}} + \frac{\partial \bar{s}\bar{\omega}}{\partial p} = Q_R + Q_c - \frac{\partial}{\partial p}\overline{s'\omega'} \tag{4}$$

$$-Q_2 = \frac{\partial \bar{q}}{\partial t} + \overline{\nabla \cdot q\vec{V}} + \frac{\partial \bar{q}\bar{\omega}}{\partial p} = \frac{Q_c}{L} - \frac{\partial}{\partial p}\overline{q'\omega'} \tag{5}$$

where $(\,)'$ denotes the departures. In the above, Q_1 is the called the apparent heat source of the large-scale system and Q_2 is called the apparent moisture sink. According to Kuo (1974), the average of the vertical eddy transport of any variable χ can be expressed as:

$$\overline{\omega'\chi'} = \frac{\sigma}{1-\sigma}(\omega_c - \bar{\omega})(\chi_c - \bar{\chi}),$$

where σ is the fractional area covered by the active clouds, and the subscript c denotes the flow variables in σ. Since ω_c is much larger than $\bar{\omega}$ and σ is much smaller than unity, (5) can be approximated by

$$\overline{\omega'\chi'} = -M_c(\chi_c - \bar{\chi}), \tag{6}$$

where

$$M_c = -\sigma\omega_c. \tag{7}$$

The substitution of (6) into (4) and (5) leads to

$$\frac{\partial \bar{s}}{\partial t} + \overline{\nabla \cdot s\vec{V}} + \frac{\partial \bar{s}\bar{\omega}}{\partial p} = Q_R + Q_c + \frac{\partial}{\partial p}[M_c(s_c - \bar{s})], \tag{8}$$

$$\frac{\partial \bar{q}}{\partial t} + \nabla \cdot \bar{q}\bar{V} + \frac{\partial \bar{q}\bar{\omega}}{\partial p} = -\frac{Q_c}{L} + \frac{\partial}{\partial p}[M_c(q_c - \bar{q})], \tag{9}$$

where $\overline{\nabla \cdot s\vec{V}}$ and $\overline{\nabla \cdot q\vec{V}}$ can be separated as

$$\overline{\nabla \cdot s\vec{V}} = \nabla \cdot (\bar{s}\,\bar{\vec{V}}) + \overline{\nabla \cdot s'\vec{V}'},$$

and

$$\overline{\nabla \cdot q\vec{V}} = \nabla \cdot (\bar{q}\,\bar{\vec{V}}) + \overline{\nabla \cdot q'\vec{V}'},$$

The horizontal diffusion terms $\overline{\nabla \cdot s'\vec{V}'}$ and $\overline{\nabla \cdot q'\vec{V}'}$ may be parameterized in term of large-scale variables by the use of nonlinear horizontal diffusion coefficients similar to those used by Smagorinsky *et al.* (1965) and Manabe *et al.* (1965). Therefore, the apparent heat source Q_1 and the apparent moisture sink Q_2 can be determined from the large- scale observations. However, from the forecast point of view, the local changes of the temperature, the geopotential height, and the mixing ratio should be computed from the past and the present fields through the governing equations, e.g., (8), (9) and the hydrostatic equation. Therefore, Q_1 and Q_2 are unknowns. The determinations of Q_1 and Q_2 require the estimations of Q_R, Q_c, M_c, s_c and q_c. In most situations Q_R is ressonablly approximated by the climatological value, and the forecast depends on the computations of Q_c, M_c, s_c and q_c. The purpose of the parameteiization is to estimate these values in terms of the observable large-scale variables. It is worth to mention that even the cloud properties M_c, s_c and q_c are not involved in the parameterization of the latent heat released, the parameterization of these cloud properties are required in the numerical weather prediction.

The parameterizations of the cloud properties and the latent heat released require to consider a cloud ensemble model. The governing equations of a cloud model can be derived from the budgets of the static energy and the moisture for an individual cloud as:

$$\frac{\partial}{\partial t}(\sigma_i s_i) = \frac{\partial}{\partial p}(m_i s_i) + LC_i + E_i \bar{s} - D_i s_i,$$

$$\frac{\partial}{\partial t}(\sigma_i q_i) = \frac{\partial}{\partial p}(m_i q_i) - C_i + E_i \bar{q} - D_i q_i$$

where σ_i, m_i, C_i, E_i, and D_i are the cloud coverage, the vertical mass flux, the condensation rate, the entrainment rate, and the detrainment rate in the ith cloud, respectively. These two equations can be approximated as

$$\frac{\sigma}{\tau}(s_c - s) = \frac{\partial}{\partial p}(M_c s_c) + LC + Es - \sum_i D_i s_i, \qquad (10)$$

$$\frac{\sigma}{\tau}(q_c - q) = \frac{\partial}{\partial p}(M_c q_c) - C + Eq - \sum_i D_i q_i, \qquad (11)$$

or,

$$\frac{\sigma}{\tau}(h_c-\bar{h})=\frac{\partial}{\partial p}(M_c\ h_c)+(E\bar{h}-\sum_i D_i\ h_i)\ , \tag{12}$$

where

$$M_c=\sum_i m_i=\sum_i(-\sigma\omega_i)$$

and σ, C and E are defined similarly, and

$$s_c=\sum_i m_i\ s_i/\sum_i m_i\ ,$$

and q_c and h_c are defined similarly. The combination of (3), (10) and (12) leads to

$$Q_c=\frac{\sigma}{\tau}(s_c-\bar{s})-\frac{\partial}{\partial p}(M_c\ s_c)-A\ , \tag{13}$$

$$\frac{\sigma}{\tau}=[\frac{\partial}{\partial p}(M_c\ h_c)+B]/(h_c-h)\ , \tag{14}$$

$$A=E\bar{s}-\sum_i D_i\ s_i+Le\ , \tag{15}$$

$$B=E\bar{h}-\sum_i D_i\ h_i\ , \tag{16}$$

where e is the rate of re-evaporation.

From (13), it is obvious that the estimation of the latent heat released depends on the determinations of the entrainment, the detrainment and the re-evaporation rate. However, the processes associated with these quantities are complicate. Since their net effects on the latent heat released are only concerned, A and B in (13) and (14) can be parameterized in terms of known variables. Here, we assume that

$$A=s_r\ \beta\ , \tag{17}$$

$$B=h_r\ \beta\ , \tag{18}$$

where β is the net entrainment rate, and s_r and h_r are the reference dry and moist static energy. In this study, s_r and h_r are approximated as $\bar{s}$ and h*, respectively, and the net entrainment rate is assumed to be proportional to the cloud mass produciton rate defined as:

$$\beta=K\frac{\alpha}{(p_s-p_c)(h_c-h)} \tag{19}$$

where

$$\alpha=-\int_{p_t}^{p_s}\nabla\cdot(h\ \bar{\vec{V}})\ dp+Hs\ ,$$

Hs is the moist static energy flux from the surface, and K is the proportional constant.

In order to determine Q_c, the estimation of M_c, s_c, h_c and K are required. The consideration of mass conservation in the clouds gives

$$\frac{\sigma}{\tau} = \frac{\partial}{\partial p} M_c + \beta \tag{20}$$

The combination of (14) and (20) leads to

$$\bar{h}\frac{\partial}{\partial p} M_c + M_c \frac{\partial h_c}{\partial p} = (h_c - \bar{h}^* - \bar{h})\beta .$$

Since β and $\partial M_c/\partial p$ are the same order of magnitude, the right hand side of the above equation can be approximated as $(-\bar{h}\beta)$, and the equation becomes

$$\frac{\partial M_c}{\partial p} = -\frac{M_c}{\bar{h}} \frac{\partial h_c}{\partial p} - \beta , \tag{21}$$

$$\doteq -\frac{M_c}{h} \frac{\partial \bar{h}^*}{\partial p} - \beta . \tag{22}$$

From the scale analysis, the order of magnitude of the first term in the right of (21) is much smaller than that of the other two terms. Therefore the value of K can be approximately estimated by the integration of (21) neglection the first term of the right, that is

$$K = -(M_c)_b / \left[\frac{\alpha}{p_s - p_t} \int_{p_t}^{p_b} \frac{dp}{h_c - h}\right] \tag{23}$$

where subscript b denotes the values at the cloud base.

Kuo (1965) suggested that the temperature inside the cloud, T_c, can be taken as the temperature of the moist adiabat through the condensation level of the representative surface air. This approximation implies that h_c keeps constant through the whole depth of the cloud, and the entrainment and the detrainment are neglected. It is somewhat overestimated. In Kuo (1974), he assumed that the rate of entrainment increases with ω such that the influence of entrainment on T_c can be taken as proportional to the integral of certain power of $(p_b - p)$ multiplied by $\bar{T}$. For simplicity, he took $T_c - \bar{T}$ as given by

$$T_c - \bar{T} = T_s - \left[1 + \alpha\left(1 - \frac{p}{p_b}\right)^{\gamma}\right] \bar{T} ,$$

where T_s is the temperature of the moist adiabat through the condensation level of the representative surface air. Since h_c is between $\bar{h}^*$ and h_c at cloud base, $(h_c)_b$ it may be taken as a weighted average value of $\bar{h}^*$ and $(h_c)_b$ i.e.,

$$h_c = \bar{h}^* + \delta[(h_c)_b - \bar{h}^*], \quad 0 \leq \delta \leq 1, \tag{24}$$

where δ is the weighted coefficient. It is obvious that h_c is equal to $(h_c)_b$ and δ is equal to zero. In other words, δ equal to unity implies the process without entrainment, and δ equal to zero implies the complete mixing. In this study, δ is assumed to be 0.5, and s_c and q_c are computed according to Arakawa (1969) as

$$s_c = s + \frac{1}{1+\gamma}(h_c - \bar{h}^*) \tag{25}$$

$$q_c = \bar{q}^* + \frac{\gamma}{(1+\gamma)L}(h_c - \bar{h}^*), \tag{26}$$

where

$$\gamma \equiv \frac{L}{C_p}\left(\frac{\partial \bar{q}^*}{\partial T}\right)_p$$

The combination of (13), (17)-(18), (20), and (22)-(26) forms a closed theory of the parameterization of the latent heat released of cumulus convection. There are nine equations for the nine unknowns: Q_c, σ/τ, A, β, K, M_c, h_c, s_c and q_c. Where Q_c, M_c, s_c and q_c are determined from the parameterization theory, the numerical weather prediction can be in progress.

III. SOME SPECIAL CASES

a. The relationship to the generalized scheme

According to Liang (1977), the formula for the cloud mass production rate is

$$\frac{(h_c - \bar{h})}{L}\frac{\sigma}{\tau} = \dot{q}_T - b^*$$

where

$$\dot{q}_T \equiv -[\nabla \cdot q\vec{V} + \frac{\partial}{\partial p}(\bar{\omega}\bar{q})] + \frac{\partial}{\partial p}[M_c(q_c - \bar{q})] \tag{27}$$

$$b^* = \frac{\partial \bar{q}}{\partial t} - \frac{\sigma}{\tau}(q_c - \bar{q}).$$

In the formula, b* represents the transport processes other than the mixing of the cloud mass and the environmental air. There are two important pracesses involved in b*. One is the adiabatic subsidence of the environmental atmosphere, and the other is the transport of the dry static energy. Indeed, from (8) and (9), we have

$$\frac{\partial \bar{h}}{\partial t} = \dot{h}_L + \frac{\partial}{\partial p}[M_c(h_c - \bar{h})] \equiv \dot{h}_T \tag{28}$$

$$\dot{h}_L = -[\nabla \cdot h\bar{\vec{V}} + \frac{\partial}{\partial p}(\bar{h}\bar{\omega})],$$

$$\doteq -\nabla \cdot (\bar{h}\bar{\vec{V}}) - \frac{\partial}{\partial p}(\bar{h}\bar{\omega}).$$

If we generalized (27) to include the dry static energy, we have

$$\frac{\partial \bar{h}}{\partial t} = b_0 + \frac{\sigma}{\tau}(h_c - \bar{h}), \tag{29}$$

where b_0 represents the transport processes other than the mixing of the moist static energy between the cloud mass and the environmental air. The combination of (28) and (29) leads to

$$(h_c - \bar{h})\frac{\sigma}{\tau} = \dot{h}_T - b_0. \tag{30}$$

If we assume that the main transport process in b_0 is the subsidence of the environmental atmosphere and the arising idside the cloud, then

$$\frac{\partial \bar{h}}{\partial t} = \frac{\sigma}{\tau}(h_c - \bar{h}) + M_c\frac{\partial h_c}{\partial p} + \tilde{M}^*\frac{\partial \bar{h}}{\partial p},$$

where $\tilde{M}^*$ is the partial subsidence of the environmental atmosphere due to M_c. Since $\tilde{M}^*$ can be expressed as $(-M_c)$, the above equation becomes

$$\frac{\partial \bar{h}}{\partial t} = \frac{\sigma}{\tau}(h_c - \bar{h}) + M_c[\frac{\partial}{\partial p}(h_c - \bar{h})]. \tag{31}$$

From (29) and (31), we have

$$b_0 = M_c[\frac{\partial}{\partial p}(h_c - \bar{h})]. \tag{32}$$

The substitution of (32) into (30) gives

$$\frac{\sigma}{\tau} = \frac{\partial M_c}{\partial p} + \frac{\dot{h}_L}{(h_c - h)} \tag{33}$$

Because there are considerable errors from the observations introduced to the value of $\dot{h}_L$ in each level, σ/τ can be modified by assuming that $\dot{h}_L$ is proportional to its average value. In other words, the effect of $\dot{h}_L$ is assumed to be replaced by its mean value. Then, (33) can be approximated as

$$\frac{\sigma}{\tau} = \frac{\partial M_c}{\partial p} + \beta$$

where β is defined as (19), and the scheme is reduced to the closed theory described in section 2. Therefore, the closed theory can be regarded as a special extension from the generalized parameterization scheme developed in Liang (1977).

b. Kuo's parameterization schemes

If the variation of the vertical mass flux inside the cloud is assumed to be neglected, (20) and (29) give

$$\frac{\sigma}{\tau}(h_c-\bar{h}) = \frac{K}{p_s-p_t}\{-\int_{p_t}^{p_s}\nabla\cdot(\bar{h}\bar{\vec{V}})\,dp+H_s\}, \tag{34}$$

and

$$\frac{\partial\bar{h}}{\partial t} = \frac{\sigma}{\tau}(h_c-\bar{h}) \tag{35}$$

After the substitution of (35) into (34), the integration of the resultant equation implies that K is equal to unity. Furthermore, if the transport of the dry static energy is approximately negligible because of the barotropy in the tropics, and if σ/τ is assumed to be a constant through the whole depth of the cloud, the integration of (34) leads to

$$\frac{\sigma}{\tau} = \frac{M_t}{\bar{M}_t}, \tag{36}$$

and

$$M_t = \frac{1}{g}\{-\int_{p_t}^{p_s}\nabla\cdot(\bar{q}\bar{\vec{V}})\,dp + E_s\},$$

$$M_t = \frac{1}{gL}\int_{p_t}^{p_b}[C_p(T_c-\bar{T}) + L(q_c-\bar{q})]\,dp,$$

where E_s is the evaporation rate from the surface, and h_c is equal to $\bar{h}$ below the cloud base. It is obvious that (36) is just the formula for the cloud mass production rate derived in Kuo (1965), and is a special case of the formulation in the generalized closed theory.

On the other hand, if we separte the moist static energy into two parts, the dry static energy and the mixing ratio, (35) may give

$$\frac{\partial\bar{q}}{\partial t} = \frac{\sigma}{\tau}(q_c-\bar{q})$$

and (34) becomes

$$\frac{\sigma}{\tau}(s_c-\bar{s}) = g\,M_t\left[1-\frac{\partial\bar{q}/\partial t}{\bar{M}_t}\right], \tag{37}$$

where the transport of the dry static energy in the right of (34) is assumed to be negligible. While we assume that σ/τ is independent of p, the integration of (37) leads to

$$\frac{\sigma}{\tau} = (1-b)\frac{M_t}{M_t^*}, \tag{38}$$

where

$$b = \frac{1}{g\bar{M}_t}\int_{p_t}^{p_s}\frac{\partial q}{\partial t}\,dp,$$

and

$$M_t^* = \frac{1}{g\bar{L}}\int_{p_t}^{p_s} C_p\,(T_c-\bar{T})\,dp.$$

Equation (38) is exact the formula derived in Kuo's (1974) parameterization scheme of cumulus convection.

IV. THE PROCEDURE FOR DIAGNOSTICATING THE THEORY OF THE CUMULUS PARAMETERIZATION

Here, a procedure is proposed to evaluate and to clarify the applicability and the mechanisms involved in a parameterization scheme. The procedure is enssentially similar to that performed in Liang (1977) and will be described briefly in the following.

From the diagnostic study point of view, Q_1 and Q_2 are specified, and there are three unknowns in (8) and (9) if Q_c is expressed in thrms of known variables. They are M_c, s_c and q_c and the combination of (8), (9), (25) and (26) gives four equations for four unknowns, M_c, s_c, q_c and h_c. They can be solved provided that the observed large-scale heat and moisture budgets over the area considered are known. The associated boundary conditions are

$$\frac{\Delta p}{g}(Q_1-Q_R) = S_s - \frac{M_{cb}}{g}(s_{cb}-\bar{s}_b),$$

$$-\frac{\Delta p}{g}Q_2 = LE_s - \frac{M_{cb}}{g}L\,(q_{cb}-\bar{q}_b),$$

$$S_s/LE_s = C_p\,(\bar{T}s-\bar{T}_0)/[L\,(\bar{q}_s-\bar{q}_0)]$$

where the subscript b denotes values at cloud base, S_s and E_s are, respectively, the supply of sensible heat and the rate of evaporation from surface, and $\Delta p = p_s - p_b$. Defining Y as $-\overline{\omega' h'}$, adding (8) and (9) and integrating the resultant equation, we get

$$Y(p) = \int_{p_t}^{p} (Q_1 - Q_2 - Q_p)dp, \\ = M_c(h_c - \bar{h}) + Y(p_{ct}), \text{ if } p \leq p_b \tag{39}$$

where p_{ct} is the pressure at the top of clouds, and $Y(p_t)$ and $M_c(p_{ct})$ are assumed to be be zero. Utilizing (39), the boundary conditions are explicitly expressed as

$$M_{cb} = \frac{a_1 - (1+\gamma_b)a_2}{\bar{h}_b^* - \bar{h}_b}, \tag{40}$$

$$h_{cb} = \bar{h}_b + \frac{a_1}{M_{cb}} \tag{41}$$

where

$$a_1 = g(S_s - LE_s) - \Delta P(Q_1 - Q_R - Q_2), \\ a_2 = gs - \Delta p(Q_1 - Q_R),$$

and

$$S_s + LE_s = Y(P_s).$$

During the diagnosticating procehure, the cloud base is assumed to be at the lifted condensation level representative of the surface laayer, and the top of of cloud is assumed to be at a level where the temperature of the clouds is equal to that of the environment or at a level where M_c is zero.

According to (13), Q_c is specified as

$$Q_c = \sigma\tau(s_c - \bar{s}) - \frac{\partial}{\partial p}(M_c s_c) - \overline{s}\beta,$$

where β and σ/τ are specified in (19) and (20). After elimination of s_c, q_c and h_c from (8), (9), (25) and (25), an ordinary nonlinear differential equation is obtained:

$$(F_0 + F_1 U)\frac{dM_c}{dp} = M_c(G_0 + G_1 M_c) \tag{42}$$

where

$$F_0 = \frac{Y - Y(P_{ct})}{1+\gamma},$$

$$F_1 = -\left(\frac{h}{1+\gamma} + \bar{s}\right),$$

$$G_0 = Q_1 - \frac{\beta_0}{1+\gamma},$$

$$G_1 = \frac{\beta_0 \Delta h}{(1+\gamma)[Y - Y(P_{ct})]},$$

$$\Delta h = \bar{h}^* - \bar{h},$$

and

$$\beta_0 = \frac{K\alpha L}{p_s - p_t}$$

Since the pressure at cloud top is unknown before the solution is obtained, (32) should be solved utilizing the Rung-Kutta method and iterative procedure. While the solution is determined, h_c, s_c, q_c and Q_c can be computer according to (39), (25), (26) and (13), respectively.

V. RESULTS OF THE DIAGNOSTIC STUDY OF THE CLOSED THEORY

a. Data

The data utilized in this study are 1956 Marshall Islands data. This special data set was collected in the Marshall Islands area during the period from 15 April to 22 July, 1956. In their diagnostic study, Yanai *et al.* (1973) used this data set to compute the bulk properties of tropical cloud clusters from a combination of the observed large-scale heat and moisture budgets over an area covering the cloud cluster, and a model of a cumulus ensemble which exchanges mass, heat, water vapor ahd liquid water with the environment through entrainment and detrainment. The model utilized in their study is more complicate than that we used. In the data set, five stations, which form a pentagonal region of about 62×10^4 km^2, were selected. The geometrical consideration and the vertical distributions of the large-scale mass, heat and moisture budgets were presented and detailed in that paper. The profiles of the large-scale motion include the mean values of the horizontal divergence, the vertical velocity, the dry static energy, the moist static energy, the saturation moist static energy, the apparent heat source and moist sink, and the derived vertical eddy heat flux. As mentioned before, all of these should be used in our diagnostication for the determinations of the latent heat released and the cloud properties. Since the input data are the same, our diagnostic results are comparable to those obtained in Yanai *et al.*

b. Cloud mass flux

In Fig. 1., the vertical profile of the mass flux inside the clouds computed from our diagnostic procedure (solid curve) is shown. It is decreasing upward monotonically and vanishes at the cloud top. The most significant part of the cloud mass flux is below 200 mb and also reveals the existence of a lot of shallow clouds. Through the whole cloudy layer, the mass fiux inside the cloud is larger than the meanmass fiux $\bar{M}$. This means that the upward mass flux supplied from the large-scale horizontal convergence. Since the mass flux in

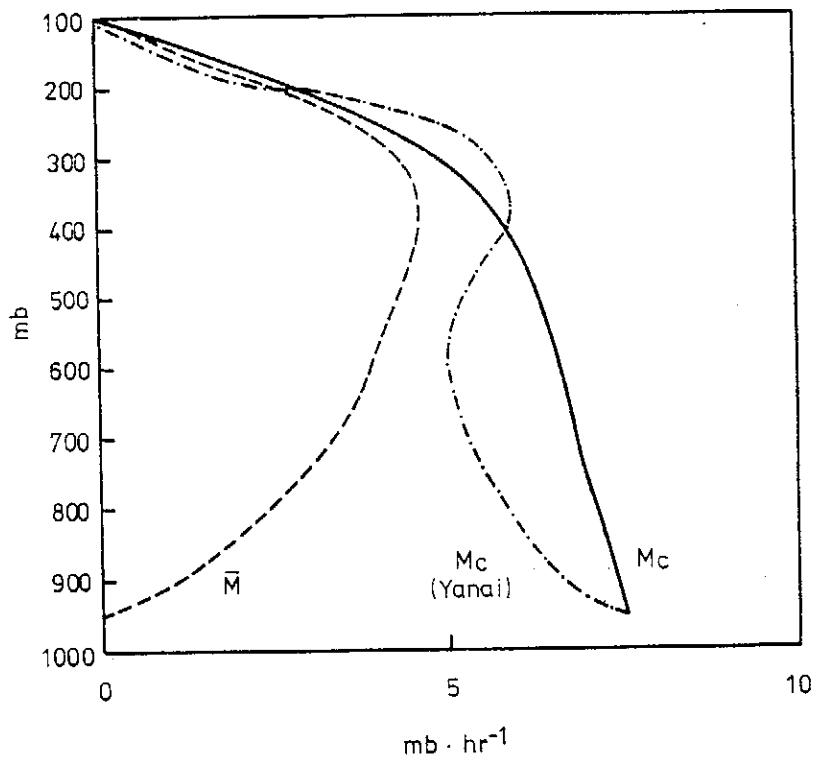

FIG. 1. The cloud mass flux M_c (Solid), M_c (Yanai) from Yanai *et al* (1973, dash-dot), and the large-scale mass flux $\bar{M}$ (dashed).

the environment $\tilde{M}$ is $(\bar{M}-M_c)$, it is downward and, therefore, warms and dries the environment by adiabatic compression.

c. Latent heat released

In Fig. 2., the vertical distribution of the latent heat released Q_c computed from our diagnostic study (solid curve) is shown. There are two maximum exist. One appears at 900 mb level, and the other is near 300 mb. Because the level of the maximum latent heat released for a individual cloud is about 100 to 200 mb below the cloud top, the exist of two maximum in Q_c curve implies that there are two main kinds of clouds with their top at 700 mb and 200 mb levels. This fact is also shown in the profile of the excess mixing ratio in Fig. 3., and is consistent with the observations in tropics.

In order to obtain a better comparison between the observations and the results computed form the diagnosticating procedures, the required precipitation is determined from the large-scale heat and moisture budgets. Assuming the vertical eddy heat fiux and the vertical eddy moisture flux to be zero at the cloud tops, i.e.,

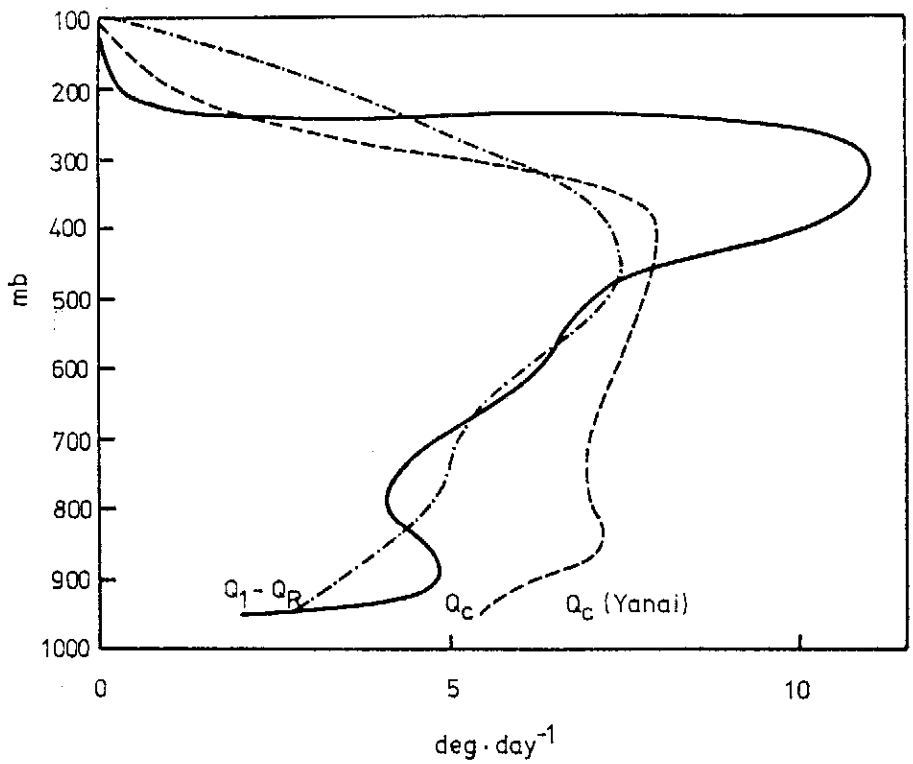

FIG. 2. The latent heat released Q_c (Solid), R_c (Yanai) from Yanai *et al* (1973, dashed), and the observed heat source Q_1-Q_R (dash-dot).

$$M_c (s_c - \bar{s})_{p=p_t} = 0 ,$$
$$M_c (q_c - \bar{q})_{p=p_t} = 0 ,$$

and integrating (8), we have

$$\frac{1}{g}\int_{p_t}^{p_s} (Q_1 - Q_R)\, dp = LP_0 + S_s ,$$

where P_0 is the total precipitation inside the clouds, and S_s is the rate of transport of sensible heat from the surface. Since the time-average Bowen ratio for the considered area was small (about 0.076), the required precipitation can be estimated approximately by

$$P_0 = \frac{1}{Lg}\int_{p_t}^{p_s} (Q_1 - Q_R)\, dp.$$

The total precipitation can be computed form the latent heat released as

$$P_0 = \frac{1}{gL}\int_{p_t}^{p_s} Q_c\, dp.$$

The required precipitation computed by Yanai *et al.* is about 1086 cal cm^{-2} day^{-1}, or 1.82 cm day^{-1}. The profile of the latent heat released from our

diagnostic study gives 1184 cal cm^{-2} day^{-1}, or 1.98 cm day^{-1}. It is very close to the required precipitation.

Compared to the latent heat released obtained in Yanai *et al.*, the pattern and the magnitude of our reault are fairy reasonable and the accuracy of the computed precipitation are about the same.

d. Cloud temperature and mixing ratio

In Fig. 3., the profiles of the excess temperature and the excess mixing ratio are shown. The excess temperature slowly increases from the cloud base (about 0.1 °C) to 0.3 °C near 700 mb, and then rapidly increases to the maximum value of 2.7 °C near 300 mb. The excess mixing ratio slightly decreases up to 900 mb, and then increases to the maximum value of 3.8 $g \cdot kg^{-1}$ near 700 mb. Above 700 mb, it decreases rapidly and vanishes at 100 mb. The occurence of the maximum of the excess mixing ratio accompanied the small excess temperature near 700 mb implies that there exist a lot of shallow clouds with the cloud top at 700 mb. These shallow clouds mainly pump the moisture from the subcloud layer upward to the cloud top layer near 700 mb and have small effect on the heat transfer. The heat transport mainly depends on the deep

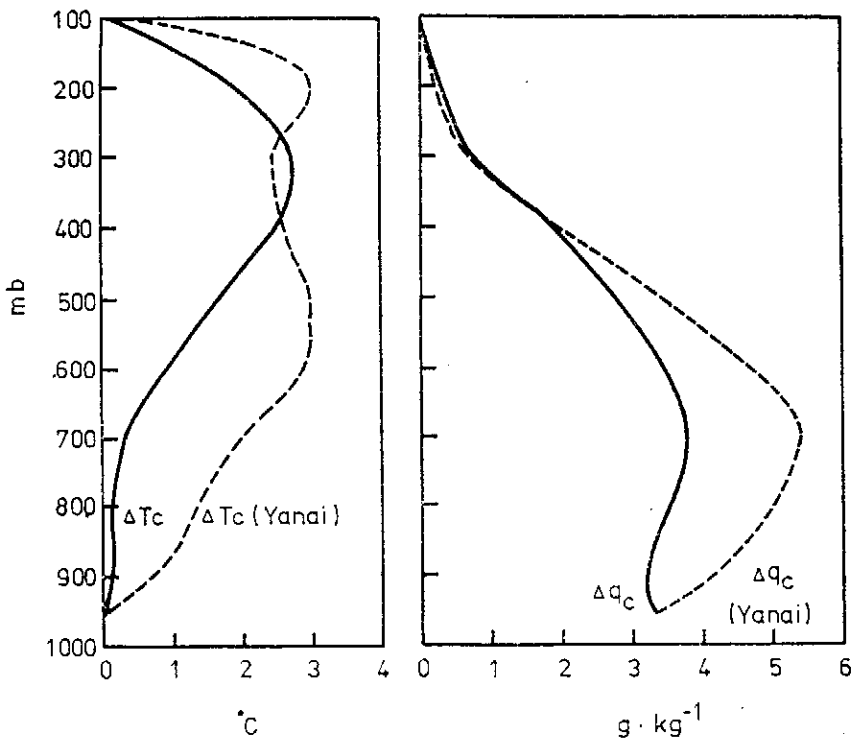

FIG. 3. Left: The excess temperature $\triangle T_c$ (Solid), and $\triangle T_c$ (Yanai) from Yanai *et al* (1973, dashed). Right: The excess mixing ratio $\triangle q_c$ (Yanai) from Yanai *et al* (1973, dashed).

cumuli, which penetrate to the higher level, and the maxima of the excess temperature and the latent heat released near 300 mb conform this fact. In other words, two main kinds of clouds are obtained from our diagnostic study, the shallow cloud and the deep penetrative cloud. The former pumps the moisture from the subcloud layer to the cloud top near 700 mb, and the latter transports the heat from the lower layer up-ward to the higher levels.

e. Moist static energy of clouds

In Fig. 4., the vertical profile of the moist static energy of the cloud ensemble, h_c, is shown together with h and $\bar{h}^*$. Near the tropopause, h_c is about equal to its value at the cloud base. This indicates that the most clouds are deep clouds penetrated through the whole troposphere. At the cloud base, h_c is about equal to $\bar{h}^*$. This is consistent with the observations (Malkus, 1958, and Simpson and Wiggert, 1971). Below 700 mb level, $(h_c - \bar{h}^*)$ is very small and h_c rapidly decreases thereupon. The smallness of $(h_c - h^*)$ implies the smallness of the excess temperature. Therefore, the growth and maintain of the deep clouds mainly depends on the dynamical effects of the triggering

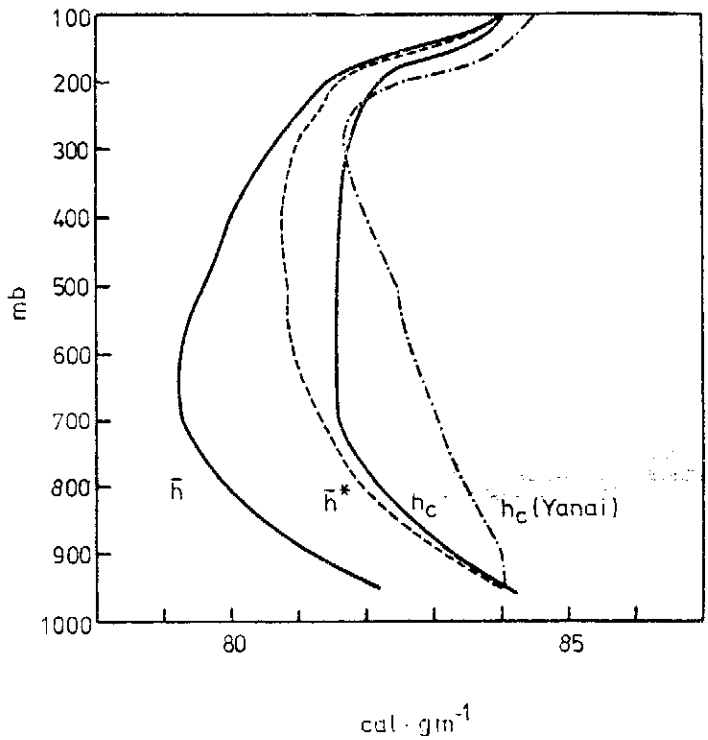

FIG. 4. The moist static energy of the cloud ensemble h_c (Solid), h_c (Yanai) from Yanai *et sal* (1973, dash-dot), the moist staic energy $\bar{h}$ (Sloid) and the saturation moist static energy h^* (dashed) of the environment.

mechanisms instead of the buoyancy force. Between 300 mb and 700 mb, h_c is nearly unchanged. This undilute phenomena tends to conform the existence of the hot towers (Riehl and Malkus, 1958) in the tropics.

In Fig. 5., the excess static energy, $h_c - h$, is shown. It reaches the maximum of 2.3 cal gm^{-1} near 700 mb and decreases to zero at 100 mb level.

f. Net entrainment and cloud mass production rate

In Fig. 6., the profiles of the net entrainment β, the vertical cloud mass convergence dM_c/dp and the cloud mass production rate σ/τ are shown.

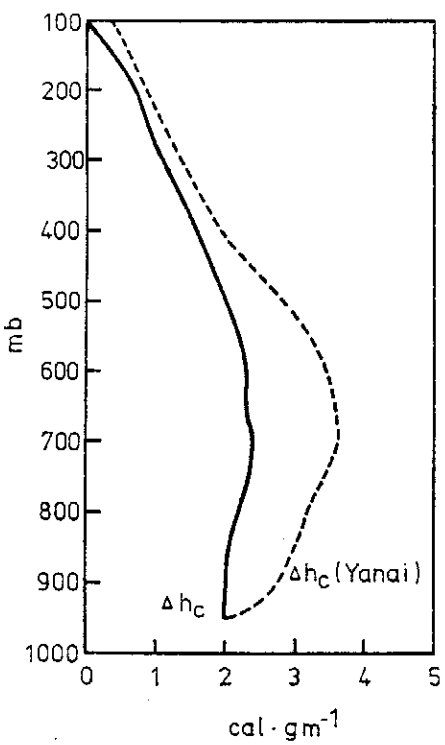

FIG. 5. The excess moist static energy of the cloud $\triangle h_c$ (Solid), and $\triangle h_c$ (Yanai) from Yanai *et al* (1973, dashed).

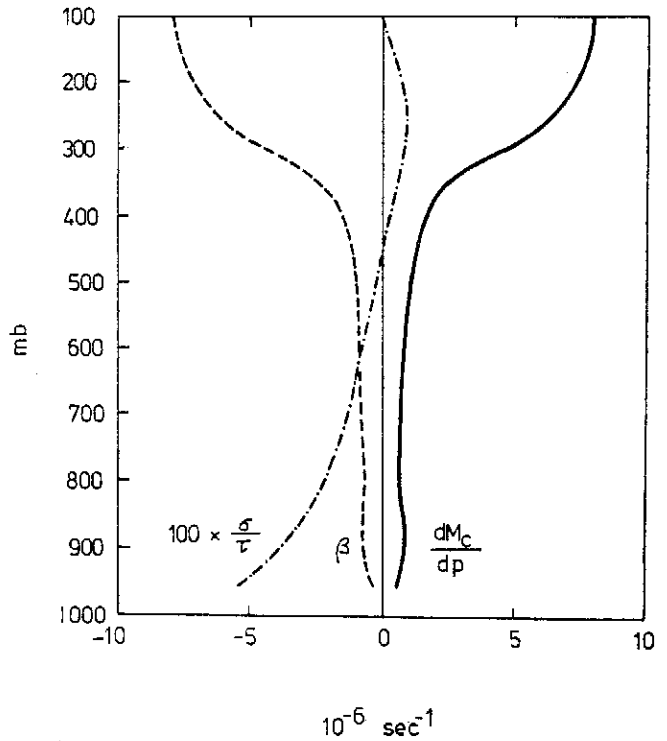

FIG. 6. The net entrainment β (Solid), the vetical cloud mass convergence dM_c/dp (dashed), and the cloud mass production rate [$\sigma/\tau \times 100$] (dash-dot).

Although the profiles of the excess mixing ratio and the latent heat released indicate the existence of the shallow clouds with the cloud top at 700 mb, the vertical distribution of the net entrainment does not show any special features corresponding to this fact. The reason may be that the strong entroinment is accompanied the strong detrainment near the top of the shallow clouds, or the fraction of the cloud mass transported by the shallow clouds is small. However, the occurence of the large net entrainment near the tropopause does conform, once more, the existence of the undilute hot towers in the tropics.

The dotted curve in Fig. 6, is the profile of the cloud mass production rate. Its value is two order of magnitude smaller than those of β and dM_c/dp. Therefore, the profile of dM_c/dp is nearly balanced by that of β. The smallness of the cloud mass production rate indicates that the latent heat released due to the mixing process between the net cloud mass and the environmental air is negligible. This fact is also revealed in Fig. 7., and will be discussed in the following.

g. Components of latent heat released

In Fig. 7., the vertical distributions of the total (dash-dot curve) and three components of the latent heat released are shown. The profiles indicate that the value of the mixing term $\sigma/\tau(s_c-\bar{s})$ and the total latent that released are five and one order of magnitude smaller than those of the other components, respectively. Therefore, these components are nearly balanced. The smallness of the mixing terms shown in the latent heat released and the cloud mass transport conforms the quasiequilibrium assumption of the cloud ensemble. The accuracy of the estimation of latent heat released primarily depends on the accurate estimation of the net entrainment rate and the cloud mass flux.

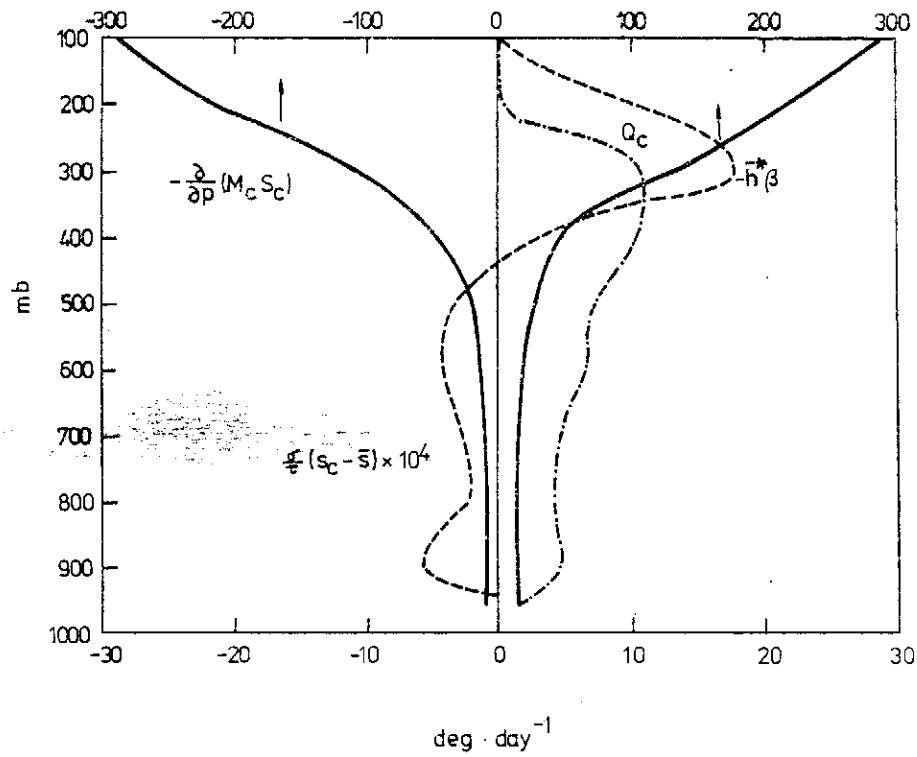

FIG. 7. The latent heat released Q_c (dash-dot), and its three components $-h^*$ (solid), $-\partial/\partial p(M_c S_c)$ (solid), and $[\sigma/\tau(s_c-s)\times 10^4]$ (dashed).

VI. CONCLUSIONS AND RECOMMENDATIONS

In this study, the closed theory of the generalized scheme of Kuo's parameterization of cumulus convection is developed by introducing a one-dimensional cloud ensemble model. The theory is the extension of Kuo's (1965 and 1974) and Liang's (1977) schemes, and the relationships between these schemes are clarified rigorously. The theory is diagnostic studied using the Marshall Islands data, which are used in the study by Yanai *et al.* (1973), and the results are compared with the observations and those obtained in Yanai et al.

The results show that the theory is closely consistent with the observations and the physical phenomena. The profiles and the magnitudes of the latent heat released, the entrainment rate, the cloud mass production rate and the cloud properties are all satisfactory and physical explainable.

The profiles of the excess temperature and the excess mixing ratio reveal the existence of the shallow clouds with the cloud topt at 700 mb in the tropics. These shallow clouds pump the moisture from low levels to the cloud top but have no any significant influence on the transport of heat and mass. The distributions of the latent heat released and the cloud moist static energy indicate that the undilute penetrative deep cumulus is the primary kind of clouds which transport the mass and the heat upward to the higher levels. This fact conforms the assumption of the existence of the hot towers in the tropical regions.

There are several further studies in progress. One is the numerical experiments of the parrmeterization schemes in numerical weather prediction models. These experiments can reveal that which scheme can be applicable to which kind of weather systems and regions. The other study is the estimations of the distribution of the total precipitation from the combination of the prrameterization schemes and the observations of the large-scale variables. The results will indicate that which scheme is able to objectively predict the precipitation. Since the generalized scoeme includes the transport of the dry static energy, which is closely correlated to the baroclinity of the weather systems, the scheme should be able to apply to the middle latitudes as well as in the tropics. The study of this applicability is investigating using the Mei-Yü data collected over the East Asia, and the results will be published somewhere else.

For the parameterization point of view, a good scheme should be accurate in estimation and simple in computation. Therefore, how to simplify the generalized scheme will be one of significant work in the future.

REFERENCES

1. Arakwa, A., 1969: Paramerization of cumulus convection. *Proc. WMO/IUGG Symp. Numerical Prediction,* Tokyo, IV 8, 1-6.
2. Kuo, H. L., 1965: On the formation and intensification of tropical cyclones through latent heat release by cumulus convection. *J. Atmos. Sci.,* 22, 40-63.
3. _____, 1974: Further studies of the parameterization of the influence of cumulus convection flow. *J. Atmos. Sci.,* 31, 1232-1240.
4. Liang, W. J., 1977: The generalization of Kuo's parameterization of cumulus convection. Part I. Diagnostic studies. *Annual Report of the Institute of Physics, Academia Sinica,* 7, 99-122.
5. Malkus, J. S., 1958: On the structure of the trade wind moist layer. *Papers Phys. Oceanoger. Meteor.,* 13, No. 2.
6. Manabe, S., J. Smagorinsky, and R. F. Strickler, 1965: Simulated climatology of a general circulation model with a hydrologic cycle. *Mon. Wea. Rev.,* 93, No. 12, 769-798.
7. Riehl, H., and J. S. Malkus, 1953: On the heat balance in the equatorial trough zone. *Geophysica,* 6, 503-538.
8. Simpson, J., and V. Wiggert, 1971: 1968 Florida cumulus seeding experiment: Numerical model result. *Mon. Wea. Rev.,* 99, 87-118.
9. Smagorinsky, J., S. Manabe, and J. L. Holloway, 1965: Numerical results from a nine-level general circulation model of the atmosphere. *Mon. Wea. Rev.,* 93, 727-768.
10. Yanai, M., S. Eskensen and J. Chu, 1973: Determination of bulk properties of tropical cloud clusters from large-scale heat moisture budgets. *J. Atmos Sci.,* 30, 611-627.

A NEW TIME INTEGRATION SCHEME FOR QUASI-GEOSTRAPHIC MODEL OVER THE EAST ASIA AREA*

LAI-CHEN CHIEN (簡來成) and CHUN-TSUNG WANG (汪群從)

Institute of Physics Academia Sinica
Taiwan, Republic of China

Abstract

An efficient computational process, hopscotch method, has been applied to four-level baroclinic quasi-geostrophic diabatic model for 24-hour forecasting in Mei-Yu season over East Asia. The method, equivalent to Peacemen-Rachford proceduce with the coeffcient matrix split in a novel way, is unconditionally stable and allowing an arbitrarily large time step, and is 3 to 4 time faster per computational step. This algorithm is very efficient with regard to storage requirement and ease of programming. The results show that the 24-hour predicted Z-field obtained by the method with triple or quadruple time increment agrees excellently with that of explicit method.

INTRODUCTION

Recently, the development of effiicient integration schemes for numerical weather prediction has occupied an important postion among the objectives of numerical meteorologists. The most widely used among the schemes is the explicit method (Smagorinsky, Manabe and Holloway, 1965; Bushby and Timpson 1967; Kashara and Washington, 1967; Schuman and Hovermale, 1968). Lilly (1965) and Kurihara (1967) studited the properties a number of time integration techniques to reduce the number of integration algorithms considered by atmospheric scientistists.

In order to enlarge the time increment in numerical weather predition, implicit method is developed. Krihara (1965), Holton (1967), Robert (1969), Rober, Henderson, and Turnbull (1972) applied the implicit method to study atmospheric problems. Because it takes more computation time for implicit scheme, more efficient method, semi-implicit time integration scheme is developed (Kwizak and Robert, 1971; Burridg, 1975; Gadd, 1978).

In this study, a newly developed numerical integration scheme, hopscotch method, is adopted to integrate the equations in numerical weather prediction. The model used is four-level quasi-geostraphic model includ diabatic heating and drag. Twenty-four-hour integration from real data with time steps of 60 and 30 min. shows no difference for 3 significant figures.

* Work supported by National Science Council, Republic of China, Grant NSC-67M-0202-02(07). Presented at American Meteorological Society Twelfth Technical Conference on Hurricanes and Tropical Meteorology, at New Orleans, Louisiana, April 24-27, 1979.

DESCRIPTION OF THE MODEL

The model resolves the atmosphere into four levels. The information levels for meteorological elements are shown in Figure 1. The predicting heighs and temperature are 300mb, 500mb, 700mb and 900mb. The vertical p-velocities are given at 400mb. 600mb and 800mb.

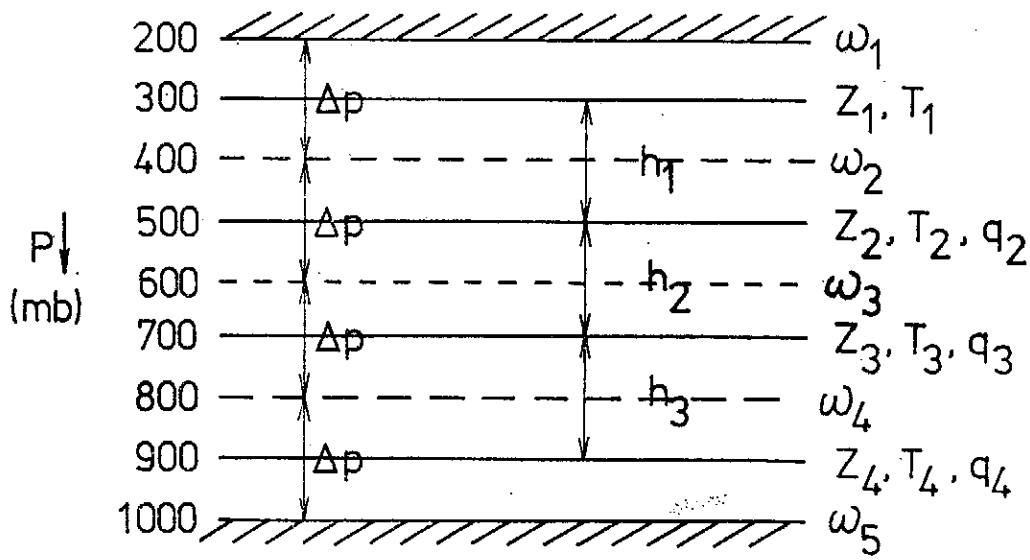

FIG. 1. Vertical grid stricture in 4-level model.

The governing equation in (x, y, p) coordinate may be wirtten as following:

(1) Equation of motion.

$$\frac{d\vec{V}}{dt} + \vec{K} \times f\vec{V} + g\nabla Z = -g\frac{\partial \vec{\tau}}{\partial p}, \qquad (1)$$

where $\vec{V}$ is horizontal velocity; $\vec{k}$, vertical unit vector; g, gravity acceleration; Z, isobaric heigh, τ, friction drag; f, coriolis parameter.

(2) Hydrostatic equation.

$$\frac{\partial Z}{\partial p} = -\frac{1}{\rho g}, \qquad (2)$$

where ρ is the density.

(3) Equation of continuity

$$\nabla \cdot \vec{V} + \frac{\partial \omega}{\partial p} = 0, \qquad (3)$$

where $\omega = dp/dt$ is the vertical p-velocity.

(4) Equation of state $p=\rho RT$, (4)

where R is the gas constant, T, the temperature.

(5) First law of thermodynamics,

$$\frac{dQ}{dt} = C_p \frac{dT}{dt} - \frac{RT}{p}\omega \tag{5}$$

where dQ/dt is the heating rate; C_p, specific heat at constant pressure.

(6) Specific humidity equation.

$$\frac{dq}{dt} = C \tag{6}$$

where q is the specific huminity; C the condensation or evaporating rate.

By geostraphic assumption, $\vec{V} = \vec{k} \times \frac{g}{f} \nabla Z$ (7)

Eq. (1) and Eq. (2) can be reduced to vorticity equation

$$\frac{\partial \zeta}{\partial t} + \vec{V} \cdot \nabla (\zeta + f) - \bar{f} \frac{\partial \omega}{\partial p} + g \bar{k} \cdot \nabla \times \frac{\partial \vec{\tau}}{\partial p} = 0 \tag{8}$$

where $\bar{f}$ is the averaged coriolis parameter over the domain of interest; $\zeta \equiv \vec{k} \cdot \nabla \vec{V}$, the relative vorticity. By Eq. (7), the relative voriticity is

$$\zeta = \frac{g}{f} \nabla^2 Z \tag{9}$$

and the voriticity equation (8) can be rewritten as

$$\frac{\partial}{\partial t} \nabla^2 Z = - J(\eta, Z) + \frac{\bar{f}^2}{g} \frac{\partial \omega}{\partial p} - \bar{f} \vec{k} \cdot \nabla \times \frac{\partial \vec{\tau}}{\partial p} \tag{10}$$

where $\eta = \zeta + f$ is absolute vorticity. By the definition of virtual temperature, and Equations (2), (5), (7), we have the thickness tendency equation.

$$\frac{\partial}{\partial t}\left(\frac{\partial Z}{\partial p}\right) = \frac{g}{f} J\left(\frac{\partial Z}{\partial p}, Z\right) - \sigma\omega - \frac{R}{C_p g p}\left[\frac{dQ}{dt} - \frac{d\bar{Q}}{dt}\right] \tag{11}$$

where $\frac{dQ}{dt}$ is the spatial constant ratiational cooling (Staffmember, 1966), σ static stability parameter, and defined as

$$\sigma \equiv \frac{\partial Z}{\partial p} \frac{\partial \ln \theta}{\partial p} \tag{12}$$

Combining equation (10) and (11) by eliminatng $(\partial Z/\partial t)$, it gives omega equation,

$$\nabla^2\sigma\omega + \frac{\bar{f}^2}{g}\frac{\partial\omega}{\partial p} = \frac{g}{f}\nabla^2[J(\frac{\partial Z}{\partial p}, Z)] - \frac{\partial}{\partial p}[J(\eta, Z)] + \frac{R}{C_p g p}\nabla^2\frac{dQ}{dt} + \bar{f}\ k\cdot\nabla\times\frac{\partial^2\vec{\tau}}{\partial p^2} \tag{13}$$

Using the quasigeostraphic approximation (7), the energy energy equation and humidity eqnation can be rewritten as

$$\frac{\partial T}{\partial t} = \frac{g}{f}J(T, Z) - \omega\frac{\partial T}{\partial p} + \frac{RT}{C_p p}\omega + \frac{1}{C_p}\frac{dQ}{dt} \tag{14}$$

$$\frac{\partial q}{\partial t} = \frac{g}{f}J(q, Z) - \omega\frac{\partial q}{\partial p} + C \tag{15}$$

The omega-equation (13) is diagnostic equation, while the vorticity equation (10), thickness tendency equation (11), energy equation(14) and humidity equation (15) are forecasting equations. If the initial conditions of height, temperature, humidity field, and proper boundary conditions, are given, we can predict height field, temperature field and humidity field.

FRICTION

It is assumed that the surface stress due to friction has a value at 1000mb but it is zero at all other levels in the model. Cressman (1960), Benwell and Bushby (1970) assumed that

$$\vec{\tau}_{1,000} = \rho_{1,000}\ C_D|\vec{V}_{1,000}|\vec{V}_{1,000} \tag{15}$$

where $\rho_{1,000}$ and $\vec{V}_{1,000}$ are the density and horizontal velocity at 1000mb. C_D, the drag coefficient over sea and land, has been studied by many investigators and recently reviewed by Garrett (1977).

Cressman (1960) used the formula derived by Sawyer (1959) to calculate C_D over the Northern Hemisphere. We have taken the values of drags coefficient from his work. The computation results are inferior to that of Millers (1969)

$$C_D = (1.0 + 0.07|\vec{V}_{1,000}|)\times 10^{-3} \tag{16}$$

where $V_{1,000}$ is assumed equal to 0.7 V_{900} (Staff member, 1965).

DIABATIC HEATING

Considering the effects of non-adiabatic heating, we examine the transport of sensible heat from the ocean into the atmosphere and the latent heat due to the condensation as well as cumulus convection, we have

$$\frac{dQ}{dt} = \frac{dQ_s}{dt} + \frac{dQ_L}{dt} + \frac{dQ_C}{dt} \tag{17}$$

where dQ_L/dt is the non-adiabatic rate of heating per unit time and unit mass due to condensation, and dQ_C/dt, heating rate per unit mass due to cumulus convection. dQ_s/dt denotes the sensible heating rate owing to ocean transportation.

The rate of heating due to the transport of sensible heat been studied by Gambo (1963), Miller (1969) and Haltiner (1971). In this study, we use the formula (Miller, 1969)

$$\begin{aligned} \frac{dQ_s}{dt} &= g\,|\vec{V}_{1,000}|\,(T_{sea}-T_{1,000})\;C_D C_p \eta/300 && \text{below 900mb} \\ &= 0 && \text{above 900mb} \end{aligned} \tag{18}$$

where T_{sea} is the sea surface water temperature; T_{1000}, the 1000mb surface air temperature. And

$$\begin{aligned} \eta &= 1.0 && \text{when } T_{sea} > T_{1000} \\ &= 0.1 && \text{when } T_{sea} < T_{1000} \\ &= 0 && \text{over the land.} \end{aligned}$$

When the atmosphere is stable, the contribution to heating rate is from the large-scale released latent heat

$$\begin{aligned} \frac{dQ_L}{dt} &= -\,LF^*\;\omega\Delta S && \text{when } \omega < 0,\ \Gamma < \Gamma_m \\ &= 0 && \text{when } \omega \geq 0, \text{ or } p \leq 500\text{mb} \end{aligned} \tag{19}$$

where L is heat of condensation per unit mass, ΔS represent the fraction of the atmosphere which is saturated, and is defined by

$$\begin{aligned} \Delta S &= 1 - \frac{T-T_d}{\Delta T} && \text{for } T-T_d < \Delta T \\ &= 0 && \text{other wise} \end{aligned} \tag{20}$$

where T_d is the dew point temperature, the ΔT is an empirical value. $\Gamma = -\partial T/\partial p$, is the temperature lapse rate. Γ_m is the moist temperature lapse rate, is given by

$$\Gamma_m = \frac{RT}{pC_p}\left[\frac{1+L\ q^*/RT}{1+0.622\ L^2\ q^*\ RT^2}\right] \tag{21}$$

$$q^* = 0.622\ e/(p-0.378e)\text{, saturated mixing ratio} \tag{22}$$

$$e = 6.11\ (273/T)^{5.31}\ \exp[25.22\ (1-273/T)$$

satuated vapor pressure (23)

F* is function of pressure and temperature (Kuo, 1965), the detail form is

$$F^* = \left[\left(\frac{\partial q^*}{\partial p}\right)_T + \frac{RT}{C_p p}\left(\frac{\partial q^*}{\partial T}\right)_p\right] \Big/ \left[1+\frac{L}{C_p}\left(\frac{\partial q^*}{\partial T}\right)_p\right] \tag{24}$$

when the atmosphere is unstable, $\Gamma > \Gamma_m$, the latent heat of condensation released by comulus convection is considered. It has been investigated by Kuo (1965), Gambo (1968), Krishnamurti and Moxim (1971), Liao, et. al. (1978), Liang (1977).

Liao et. al. (1978) estimated the amount of heat released by cumulus convection,

$$\frac{dQ_c}{dt} = -\ L\ a\ \omega_c\ F^*\delta(x, y, p) \quad \text{for } \Gamma > \Gamma_m,\ q \geqslant 0.85q^* \text{ and } p > 500\text{mb} \tag{25}$$

$$= 0 \qquad \text{otherwise}$$

where δ (x, y, p) is atmosphere relative humidity q/q^*. And ω_c is the vertical P-velocity of cumulus convective motion and is given by Liao et. al. (1978),

$$\omega_c = -\frac{pg}{RT}\left[(1-a)\frac{pg^2h^2}{12RT^2}(\Gamma-\Gamma_m)\right]^{1/2} \tag{26}$$

where a is the percentage of area covered by cumulus; h, the thickness of the layer considered.

The latent heat released by large scale atmospheric motion, dQ_L/dt, is proportial to the vertical p-velocity. It can be combined with the first term of omega equation. Equation (12) can be rewritten as

$$\nabla^2\sigma^*\omega + \frac{f^2}{g}\frac{\partial^2\omega}{\partial p^2} = \frac{g}{f}\nabla^2\left[J\left(\frac{\partial Z}{\partial p}, Z\right)\right] - \frac{\partial}{\partial p}\left[J\ (\eta, Z)\right]$$

$$- \frac{R}{C_p g p}\nabla^2\left[\frac{dQ_s}{dt} + \frac{dQ_c}{dt}\right] + \bar{f}\,\vec{K}\cdot\nabla\times\frac{\partial^2\vec{\tau}}{\partial p^2} \tag{27}$$

where

$$\sigma^* = \sigma - RLF^*\Delta S/C_p g p \geqslant 0.2\sigma \quad \text{for } \omega < 0 \text{ and } p > 500\text{mb}$$

$$= \sigma \qquad \text{otherwise}$$

HOPSCOTCH METHOD OF THE FORECASTING

Vorticity equation, thickness tendency equation, energy equation and humidity equation are partial differential equations of parabolic type. Ames (1969) described several numerical methods to solve the parabolic equation. They are explicit, and semi-implicit method.

Explicit method has been widely used in the study of numerical weather forecasting (Shuman and Hovermale, 1968; Staff member, 1972; Shao and Wang, 1976; Liao and Jiang, 1978; Brown and Campana, 1978). The main disadvantage is that the time increment must be small enough to keep ability. Implicit method, has been used by Holton (1967), Robert, Henderson and Turnbull (1972) to study the atmospheric problems. The disadvantage is the simultaneous solution of a large number of algebraic equation for the new step. Semi-implicit method is currently the most popular scheme for atmospheric study (Staniforth and Mitchell, 1977; Gadd, 1978). It keeps the advantage of the full implicit method, unconditionally stable.

Although the method, mentioned above have their own merits, another approach, hopscotch method, is proposed. It combines the advantages of implicit and explicit method. Gourly (1970) has shown that this method is unconditionally stable and that it is three to four times as fast as semi-implicit method for each computational step. We try to incorporate this method in numerical weather prediction.

Hopscotch method computes each time step in two sweeps of the mesh. In the first and subsequent odd-number time steps, the points with $(i+j+k)$ equal to odd are calculated based on the current values of neighboring points. For vorticity equation (10), thickness tendency equation (11), energy equation (14) and humidity equation (15), the new values of vorticity ζ_{ijk}^{m+1}, thickness h_{ijk}^{m+1}, temperature T_{ijk}^{m+1}, and humidity q_{ijk}^{m+1}, are given by

$$\zeta_{ij2}^{m+1}=\zeta_{ij2}^{m}+\frac{g}{\bar{f}}\,J\,(\zeta^{m}+f,Z)_{ij2}+\bar{f}\,\frac{\omega_{ij3}^{m}-\omega_{ij2}^{m}}{\Delta p}\Delta t \quad \text{for } i+j=\text{odd} \tag{28a}$$

$$h_{ijk}^{m+1}=h_{ij}^{m}+\{\frac{g}{f}\,J\,(h^{m},Z^{m})_{ijk}-\tau\omega_{ijk}^{m}-\frac{R}{C_{p}gp}[(\frac{dQ}{dt})_{ijk}-(\frac{\overline{dQ}}{dt})_{k}]\}\Delta t\Delta p \quad \text{for } i+j+k=\text{odd} \tag{29a}$$

$$T_{ijk}^{m+1}=T_{ijk}^{m}+[\frac{1}{4}\frac{g}{\bar{f}}\frac{m^{2}}{d^{2}}\bar{J}\,(T^{m},Z^{m})_{ijk}-\frac{\omega_{ijk}^{m}+\omega_{ijk+1}^{m}}{2}(\frac{T_{ijk+1}^{m}-T_{ijk-1}^{m}}{2\Delta p}-\frac{RT_{ijk}^{m}}{C_{p}p_{k}})+\frac{1}{C_{p}}(\frac{dQ}{dt})_{ijk}]\Delta t \quad \text{for } i+j+k=\text{odd} \tag{30a}$$

$$q_{ijk}^{m+1} = q_{ijk}^{m} + \left[\frac{1}{4}\frac{g}{f}\frac{m^2}{d^2}\bar{J}(q^m, Z^m)_{ijk} - \frac{\omega_{ijk}^m + \omega_{ijk+1}^m}{2}\frac{q_{ijk+1}^m - q_{ijk-1}^m}{2\Delta p} - \frac{1}{L}\left(\frac{dQ}{dt}\right)_{ijk}\right]\Delta t \quad \text{for } i+j+k=\text{odd} \tag{31a}$$

The second sweep at the same time level, the points $(i+j+k)$ equal to even are calculated using the new values of the neighboring points obtained in the first sweep.

$$\zeta_{ij2}^{m+1} = \zeta_{ij2}^{m} + \left[\frac{g}{f}J(\zeta^{m+1}+f, Z)_{ij2} + \bar{f}\frac{\omega_{ij3}^m - \omega_{ij3}^m}{\Delta p}\right]\Delta t \quad \text{for } i+j=\text{even} \tag{28b}$$

$$h_{ijk}^{m+1} = h_{ijk}^{m} + \left\{\frac{g}{f}J(h^{m+1}, Z^{m+1})_{ijk} - \tau\omega_{ijk}^m - \frac{R}{C_p g p}\left[\left(\frac{dQ}{dt}\right) - \left(\overline{\frac{dQ}{dt}}\right)_k\right]\right\}\Delta t\Delta p \quad \text{for } i+j+k=\text{even} \tag{29b}$$

$$T_{ijk}^{m+1} = T_{ijk}^{m} + \left[\frac{1}{4}\frac{g}{f}\frac{m^2}{d^2}\bar{J}(T^{m+1}, Z^{m+1})_{ijk} - \frac{\omega_{ijk}^m + \omega_{ijk+1}^m}{2}\left(\frac{T_{ijk+1}^{m+1} + T_{ijk-1}^{m+1}}{2\Delta p} - \frac{RT_{ijk}^{m+1}}{C_p p_k}\right) + \frac{1}{C_p}\left(\frac{dQ}{dt}\right)_{ijk}\right]\Delta t \quad \text{for } i+j+k=\text{even} \tag{30b}$$

$$q_{ijk}^{m+1} = q_{ijk}^{m} + \left[\frac{1}{4}\frac{g}{f}\frac{m^2}{d^2}J(q^{m+1}, Z^{m+1})_{ijk} - \frac{\omega_{ijk}^m + \omega_{ijk+1}^m}{2}\frac{q_{ijk+1}^{m+1} - q_{ijk-1}^{m+1}}{2\Delta p} - \frac{1}{L}\left(\frac{dQ}{dt}\right)_{ijk}\right]\Delta t \quad \text{for } i+j+k=\text{even} \tag{31b}$$

The first sweep consists of forward-time-central-space differencing for $(i+j+k)$ odd, whilst the second sweep is fully implicit in the sense that the new values are required at the neighboring points but this implicitness involving no simultaneous algebraic solutions.

The new values of the Z-field at 500mb are computed for all grid points by using finite-difference approximation of the Poisson equation, the boundary conditions of Z=fixed, and the new values of vorticity ζ_{ij2}^{m+1}. The Poisson equation for the Z-field, $\frac{g}{f}\nabla^2 Z = \zeta$, is a partial differential equation of elliptic type. We use the direct method developed by Ogura (1969) for more accuracy.

NUMERICAL EXPERIMENT

The synoptic situation at 0000GTM 10 June, 1975 analysed by Chen and Tsay (1977) is used as initial data for numerical experiment. The counters and isotherms of the synoptic situation for June 10 to 15, 1975 are shown in the report of Chen and Tsay. The investigation showed a cut-off low at Japan

Sea moved very slowly southward. Figure 2 through Figure 5 showed a trough line extended from the low center southwestward passing throngh the area of the north of Taiwan into Southwestern China. This trough moved Southeastward to the northwert of Taiwan. There was another low at Mangolia. The trough line extended southward to Central China and moved southeastward about 200 Km in 24 hours.

A twenty-four hour forecast was produced using explicit integration scheme with time increment 15 min. Figure 6, through Figure 9 show the predicted fields for 300mb, 500mb, 700mb and 900mb respectively. Figures 6, 7 and 8 shows the low at Japan sea and the trough line extended southwestward to the Southwestern China. The trough line predicted by computation moved southward slower than that analysis by Chen and Tsay. The low at Mangolia weakened and moved southeastward. The temperature fied forecasted almost agreed with that computed by Shiau (1977) using primitive equation model. We compared the result with that analysed by Chen and Tsay at 0000 GTM, June 11, 1975. The forecasted temperature field almost coincided with analysed field except at the low center and high center.

We adopted the hopscotch numerical integration with the same initial conditions and boundary condition. At first, our computation is excuted with the same time increment. The 24-hr forecasted Z-field, exactly the same as those obtained explicit method. Further, we enlarge the time increment with $\Delta t = 30$ min. and 60 min. The print out shows no difference for 3 significant figures. The CPU on CDC CYBER 74-18 for $\Delta t = 15$, 30 and 60 minutes are 163, 96 and 56 seconds respectively.

CONCLUSION

The newly developed numerical integration scheme, hopscotch method, is applied to four-level quasi-geostraphic model. As described in above section, the main advantages for the operational forecasting of the hopscotch scheme are a substantial economy in computation and a modest improvement in the accuracy of the forecasts. Another advantages of the scheme are its uncondutionally stable and its simplicity, involving no simultaneous algebraic solution. Comparisons with the other integration schemes, it is recommended to be applied to a variety of forecasting models.

REFERENCES

Ames, W. F. (1969). Numerical Methods for Partial Differential Equations, Barnes and Noble, Inc., New York.

Benwell, G.R.R. and Bushby, F. H. (1970). A case study of Frontal Behaviour Using a 10-level Primitive Equation Model. *Quart. J. R. Met. Soc.* 96, 287-296.

Burredge, D. M. (1975). A Split Semi-implicit Reformulation of the Bushby-Timpson 10-level Model, *Quart, J. R. Met. Soc.* 101, 777-792.

Bushby, F. H. and Timpson, M. S. (1967). A 10-level Atmospheric Model and Frontal Rain, *Quart. J. R. Met. Soc.* 93, 1-17.

Chen, T. J. G. and Tsay, C. Y. (1977). A detailed Analysis of a Case of Mei-Yu System in the Vicinity of Taiwan, *Tech. Rept. No. Mei-Yu-001, Dept. Atmos. Sci., National Taiwan Univ. ROC.*

Cressman, G. P. (1960). Improved Terrain Effects in Barotropic Forecasts, *Mon. Wea. Rev.* 88, 327-342.

Gambo, K. (1963). The Role of Sensible Heat and Latent Heat in the Baroclinic Atmosphere, *J. Met. Soc. Japan*, 41, 233.

Gambo, K. and Machida, E. (1968). The Characteristic Feature of Thermal Convection in the Atmosphere (II) *J. Met. Soc. Japan*, 46, 466-482.

Gadd, A. J. (1978). A Split Explicit Integration Scheme for Numerical Weather Prediction, *Quart. J. R. Met. Soc.* 104, 569-582.

Garratt, J. R. (1977). Review of Drag Coefficients over Oceans and Continents, *Mon. Wea. Rev.* 105, 915-929.

Gordan, P. (1965). Nonsymmetric Difference Equations, *Journ. Soc. Ind. Appl. Math.* 13, 667-673.

Gourlay, A. R. (1970). Hopscotch: A Fast Second-order Partial Differential Equation Solver, *Journ. Inst. Math. Applics.*, 6, 375-390.

Haltiner, G. J. (1971). Numerical Weather Prediction, John Wiley and Sons, Inc., New York.

Holton, J. A. (1967). A Stable Finite Difference Scheme for the Linearized Vorticity and Divergence Equation System, *J. Appl. Met.* 6, 519-522.

Kasahara, A. and Washington, W. M. (1967). NCAR Global General Circulation Model of the Atmosphere, *Mon. Wea. Rev.* 95, 389-402.

Kuo, H. L. (1965). On Formation and Intensification of Tropical Cyclone. Through Latent Heat Release by Cumulus Convection, *J. Atm. Sci.* 22, 40-63.

Krishnamurti, T. N. and Moxim, W. (1971). On Parameterization of Convective and Non-convective Latent Heat Release, *J. Appl. Met.* 10, 3-13.

Kurihara, Y. (1965). On the Use of Implicit and Iterative Methods for the Time Integration of the Wave Equation, Mon. Wea. Rev., 93, 33-46.

Kwizak, M. and Robert, A. J. (1971). A Semi-implicit Scheme for Grid Point Atmospheric Model of the Primitive Equations, *Mon. Wea. Rev.* 99, 32-36.

Liang, W. J. (1977). Generalization of Kuo's Parameterization of Cumulus Convection, Part I. Diagnostic Studies, *Ann. Rept. Inst. Phys. Acad. Sin.* 1977. 99-122.

Liao, S. Y., Jiang, H. M. and Lee, C. Y. (1978). The Dynamic Interaction of the Latent Heat Release of Cumulus-Convection to the Development of an Ex-

tratropical Cyclone, *National Science Council Monthly*, 6, 50-75.

Liao, S. Y. and Jiang, M. M. (1978). Numerical Simulation of the Frontal Numerical Simulation of the Frontal Motion in the Moist Atmosphere, Research Report, NSC-67M-0202-06(01). National Science Council, ROC.

Lilly, D. K. (1965). On the Computational Stability of numerical Solution of Time-dependent Non-linear Geophysical Fluid Dynamics Problems, *Mon. Wea. Rev.* 93, 11-26.

Ogura, M. (1969). A Direct Solution of Poisson's Equation by Dimension Reduction Method, *J. Met. Soc. Japan*, 47, 319-323.

Robert, A., Handson, J. and Turnbull, C. (1972). An Implicit Time Integration Scheme for Baroclinic Models of the Atmosphere, *Mon. Wea. Rev.*, 100, 329-335.

Sawyer, J. S. (1959). The Introduction of the effects of topography into Methods of Numerical Forecasting. *Quart. J. Roy. Meteor. Soc.* 85, 31-43.

Smagorinsky, J., Manabe, S. and Holloway, J. L. (1965). Numerical Results from a Nine-Level General Circulation Model of the Atmosphere, *Mon. Wea. Rev.*, 93, 727-768.

Shiau, C. J. and Wang, C. T. (1976). On the Preliminary Study of Limited-area Primitive Equation Model, *Ann. Rept. Inst. Phys. Acad. Sin.* 1976, 231-262.

Shiau, C. J. (1977). Study on Primitive Equation Model, *Rept. Inst. Phys. Acad. Sin.* 1977, 171-186.

Staff Member (1972). Simulation Model for Atmospheric Motion (IV). Heat and Drag, *Ann. Rept. Inst. Phys, Acad. Sin.* 1971, 177-198.

Staff Members of Electronic Computation Center (1965). 72-hr Baroclinic Forecast by Diabatic Quasi-geostraphic Model. *Jour. Met. Soc. Japan.* 41, 242-246.

Staniforth, A. and Mitchell, H. L. (1977). A Semi-Implicit Finite-Element Barotropic Model, *Mon. Wea. Rev.*, 105, 154-169.

Richtymer, R. D. and Morton (1967). *Difference Methods for Initial-Value Problems*, Interscience Publisher, New York.

Shuman, F. G. and Hovermale, J. B. (1968). An Operational 6-layer Primitive Equation Model, *J. Appl. Met.* 7, 525-547.

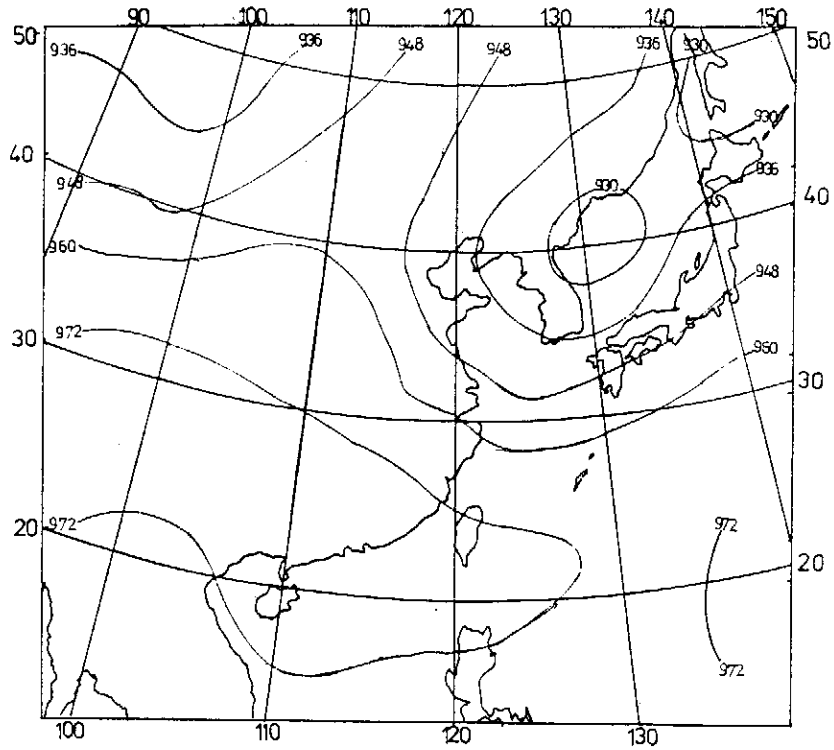

FIG. 2. Geopotential height on 300mb at 0000Z, June 10, 1975.

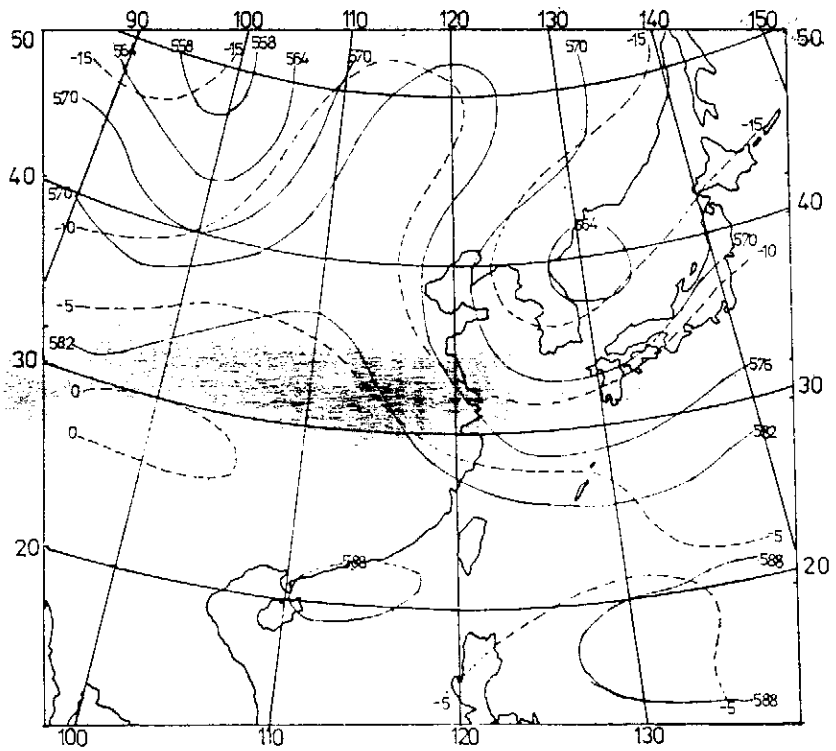

FIG. 3. Geopotential height (solid line) and temperature (dash line) on 500mb at 0000Z, June 10, 1975.

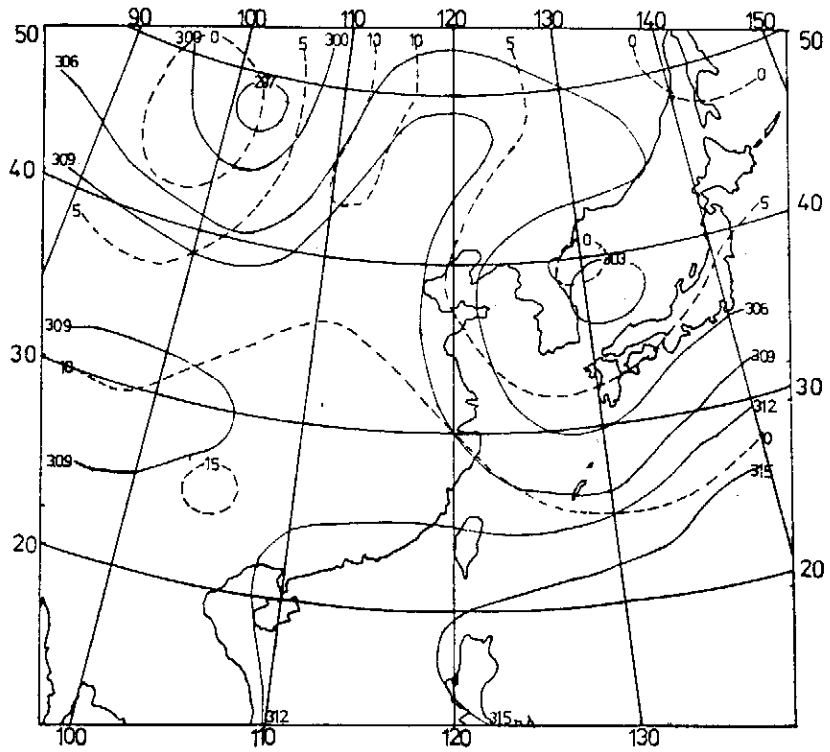

Fig. 4. Geopotential heiget (solid line) and temperature (dash line) on 700mb at 0000Z, June 10, 1975.

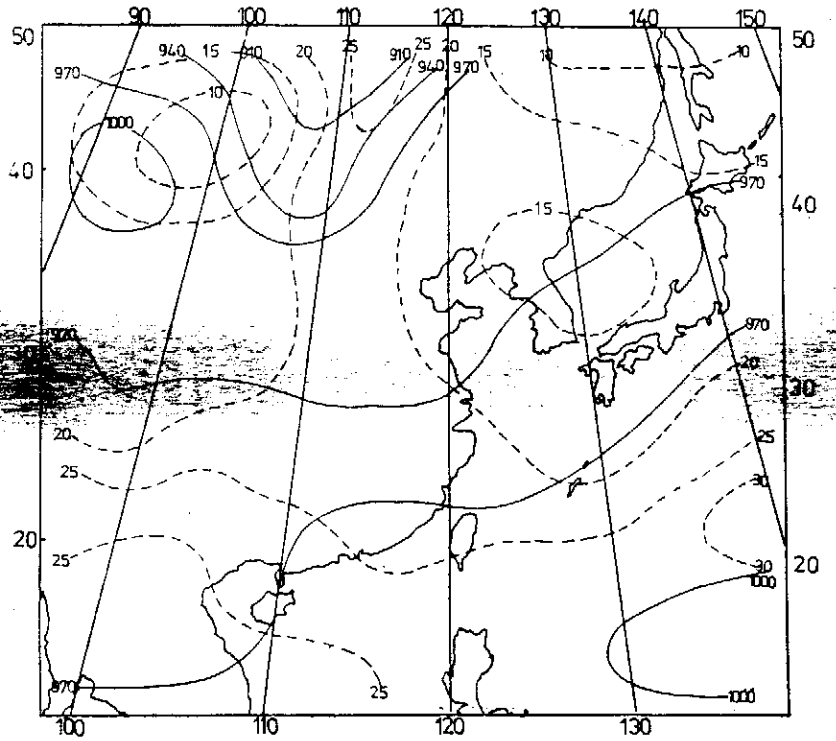

FIG. 5. Geopotentional height (solid line) and temperature (dash line) on 900mb at 0000Z, June 10, 1975

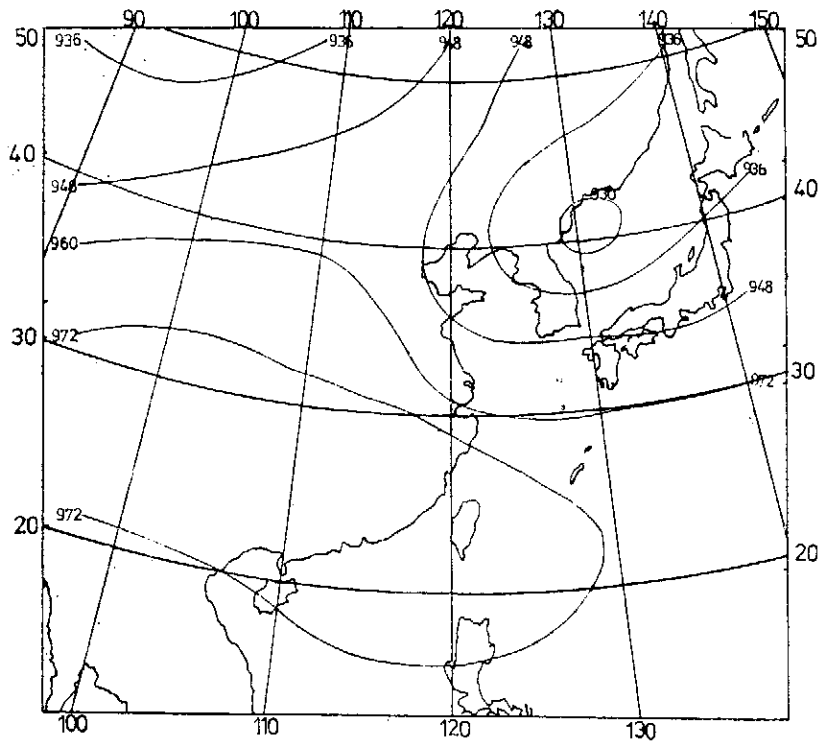

FIG. 6. 24-hour forecasted geopotential height on 300mb.

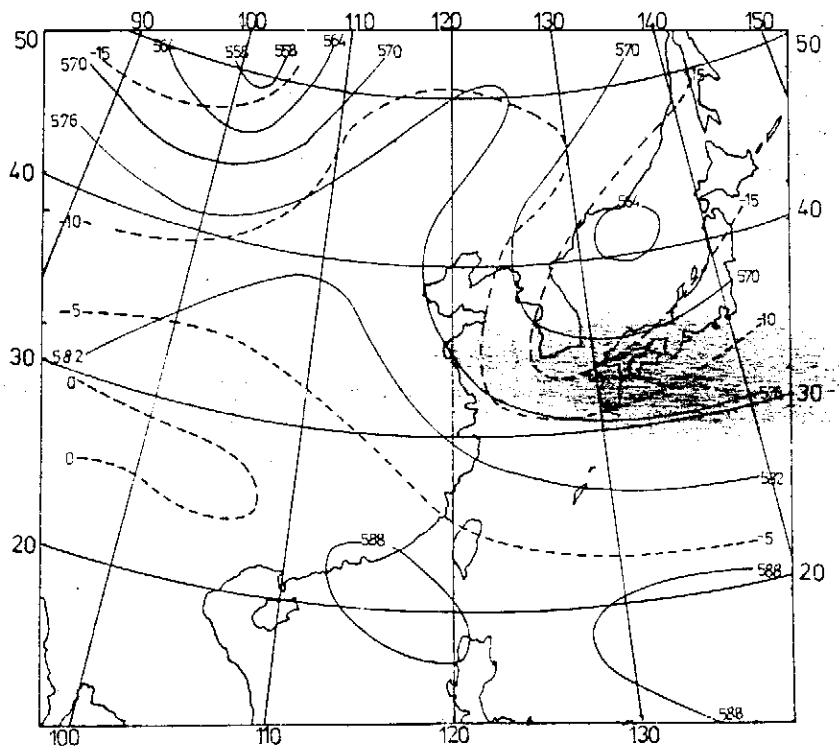

FIG. 7. 24-hour forecasted geopotential height (solid line) and temperature (dash line) on 500mb.

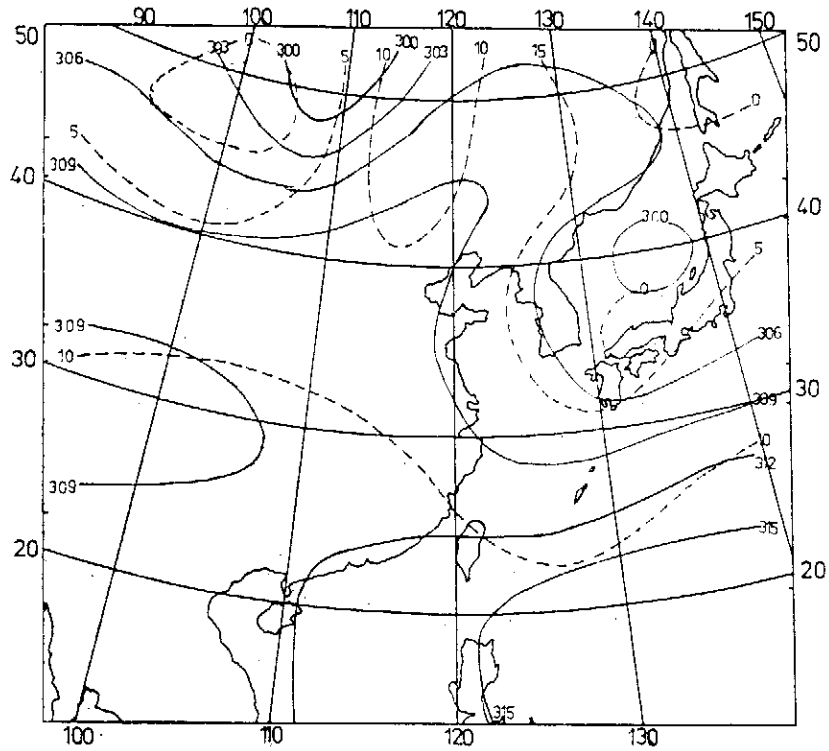

FIG. 8. 24-hous forecasted geopotential height (solid line) and temperature (dash line) on 700mb.

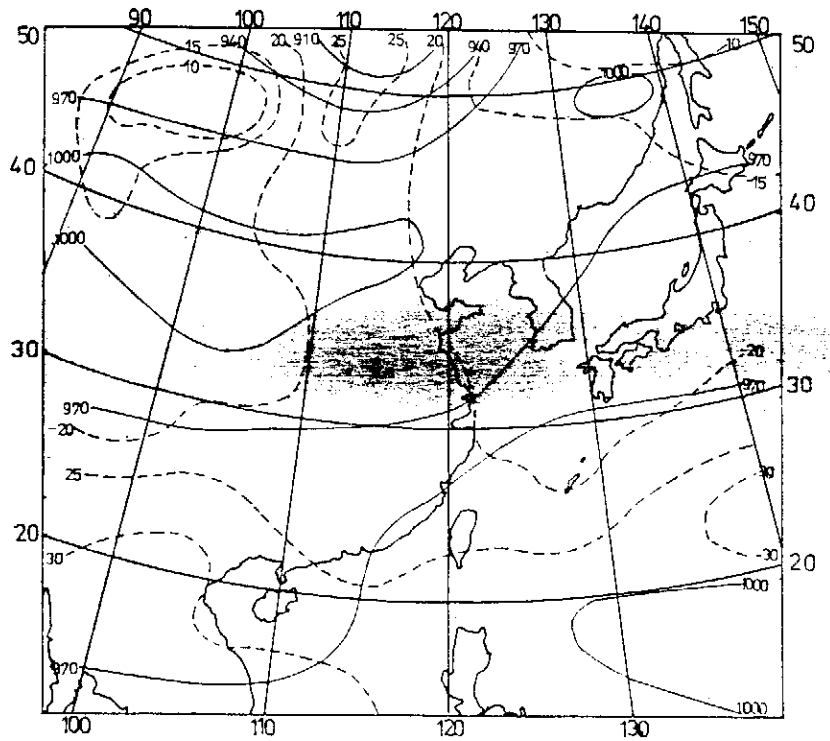

FIG. 9. 24-hour forecasted geopotential height (solid line) on 900mb.

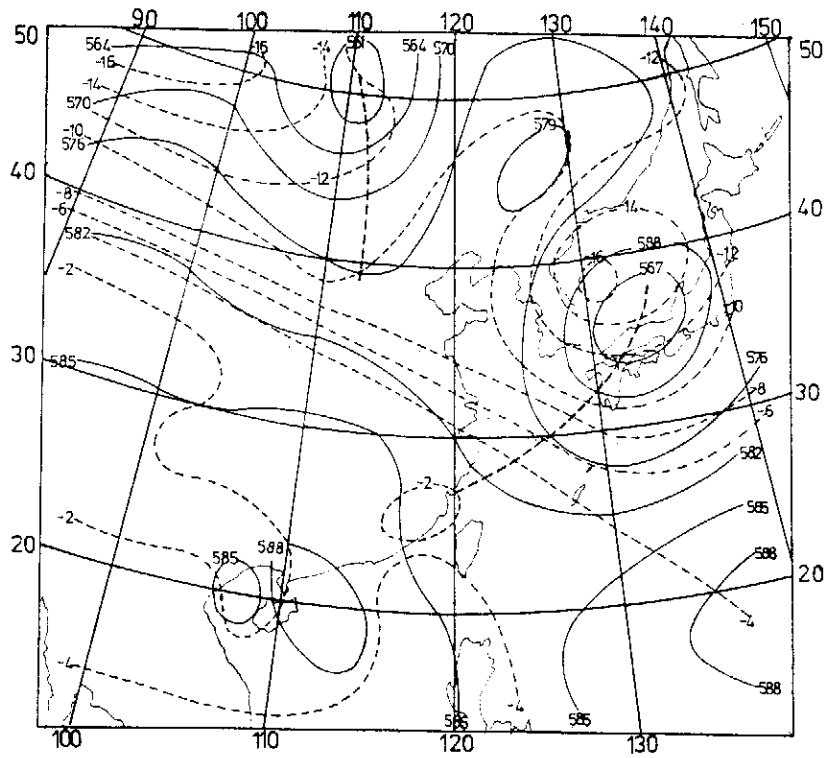

FIG. 10. Geopotential height (solid line) and temperature (dash line) (sold line) and temperature (dash line) on 500mb at 0000Z, June 11,1975.

組合模式數值天氣預報之研究

梁文傑　蕭錫璋
中央研究院物理研究所

胡仲英　陳熙揚　徐月娟
中央氣象局

摘　　要*

本文係對原始方程式預報模式作業化的可行性作初步的探討。一文面以北半球準地轉模式從事粗網格網上的預報，一方面以此結果作爲邊界值從事有限區域內細網格網上原始方程式模式的預報。結果顯示對於大規模天氣系統的分布與運動狀態，此種組合模式的預報確能大大改進預報的精確度，唯每小時更新一次邊界值似應縮短以增强有限區域邊界處的播散效果。

壹、引　　言

由於電子計算機及各種數值模擬方法之發展，許多國家數值天氣預報已被廣泛採用爲日常作業，而我國正值經濟高度發展，工業突飛猛進，天氣預報對各行業亦愈加重要。爲應國計民生之需，數值天氣預報之作業化，實爲當務之急。

數值天氣預報始於英人 L. F. Richardson，可惜由於觀測資料之不足，以及由聲波與重力波所引起之數值不穩定問題，使得 Richardson 的嘗試終歸失敗，也使得爾後許多年中數值預報不再爲人所試。直至一九四八年，J. G. Charney 證明大氣運動之動力方程式可藉由流體靜力(hydrostatic) 及地轉 (geostrophic) 假設，濾去聲波及重力波而簡化之，此卽爲準地轉模型 (quasi-geostrophic model) 之基石。在許多試驗中顯示出此模型在中緯度地區約可得 10～20% 以內的準確度。近年來

由於準確度之要求日益增高，準地轉模型已數不應用。更有進者，若欲使用此模型於低緯度地區，由於地轉假設不佳，流線函數需從頗爲複雜之平衡方程式 (balance equation) 求得，使得求解過程耗時耗力，就所耗之時間，所遭遇之困擾，與所得之準確度相較，顯得頗不經濟。近年來，由於數值模擬方法之發展，短波之壓制及時間積分之穩定問題已可初步解決，原始方程式模式 (primitive equation model) 之數值預報乃應運而生。

在原始方程式模式中，大氣運動仍假設合乎流體靜力近似 (hydrostatic approximation)，因此等壓坐標仍然可用，此坐標擁有以下數優點：(1) 一般氣象資料皆爲等壓坐標，(2) 連續方程式之形態極爲簡單，(3) 大氣密度不顯然出現，(4) 聲波完全被濾去。然而，由於原始方程式模式含有重力波，與濾過性模式 (Filtered Models, 諸如準地轉模式等) 相較，更易受擾動的影響，當預報地區爲有限區域時，由於邊界條件無法眞切的模擬，此種誤差的影響在原始方程式模式的預報過程中會很快的由邊界傳播到整個預報地區。此問題的根本解決辦法當然是採用全球預報模式 (global model)，但是由於原始方程式模式所包含的變數甚多，當垂直層數與水面網格數目足以產生滿意的精確度時，計算機的容量與所耗的時間皆非我們現階段所能承受，因此乃有「組合模式」構想的產生。

所謂組合模式係將北半球準地轉模式與有限區域原始方程式模式聯合使用，一方面使用北半球準地轉模式作預報，並將每一個時間間格點的預報值存於磁帶中，另一方面以原始方程式模式在有限區域作預報，預報過程中的有限區域邊界值則取自磁帶中的半球模式預報值，如此，則一方面可減少計算機的容量負荷，另一方面又可合理的模擬有限區域的邊界狀況。當然，利用組合模式處理有限區域邊界值的方法很多，但本研究僅就其中一種作數值實驗，亦即每一小時以北半球準地轉模式的預報值更新有限區域的邊界值，而此後一小時內的邊界值則保維不變。此種方法誠然簡單，却更能顯示出邊界值處理與否的效果。

爲便於瞭解組合模式的功效，本研究同時討論北半球準地轉模式，固定邊界值之原始方程式模式與組合模式（更新邊界值之原始方程式模式）三種模式，十二小時與二十四小時的預報結果，且與實際天氣狀況作詳細的印證。

貳、北半球準地轉模式

模式使用於 (x, y, p, t) 坐標上，主要的控制方程式包括運動方程式、連續方程式、熱力方程式、流體靜力方程式、狀態方程式：

$$\frac{\partial u}{\partial t}=-u\frac{\partial u}{\partial x}-v\frac{\partial u}{\partial y}-\omega\frac{\partial u}{\partial p}+fv-\frac{\partial \phi}{\partial x}-g\frac{\partial \tau}{\partial x} \tag{2-1}$$

$$\frac{\partial v}{\partial t}=-u\frac{\partial v}{\partial x}-v\frac{\partial v}{\partial y}-\omega\frac{\partial u}{\partial p}-fu-\frac{\partial \phi}{\partial y}-g\frac{\partial \tau}{\partial y} \tag{2-2}$$

$$\frac{\partial u}{\partial x}+\frac{\partial v}{\partial y}+\frac{\partial \omega}{\partial p}=0 \tag{2-3}$$

$$\frac{d\theta}{dt}=\frac{1}{C_p}\left(\frac{p_0}{p}\right)^{R/C_p}\frac{dQ}{dt} \tag{2-4}$$

$$\frac{\partial \phi}{\partial p}=-\frac{RT}{p} \tag{2-5}$$

$$p=\rho RT \tag{2-6}$$

其中 u, v 表示 x, y 方向的水平風場單位爲 ms^{-1}，$\omega=\frac{dp}{dt}$ 單位爲 mbs^{-1}，f 爲科氏力，ϕ 爲重力位高度場，g 爲垂直加速度，τ 爲摩擦力，T 爲氣溫，θ 爲位溫，$\theta\equiv T\left(\frac{1000}{p}\right)^{R/C_p}$，單位爲 °K, C_p 爲等壓比熱，$p_0=1000mb$

$\frac{dQ}{dt}$ 爲單位時間，單位質量的空氣的加熱率。

在準地轉假設下（輻合項除外）由 (2-1)，(2-2) 可得渦漩度 (ζ_g) 方程式：

$$\frac{\partial}{\partial t}\nabla^2 Z=-J(Z,\ \zeta+f)+\frac{\bar{f}^2}{g}\frac{\partial \omega}{\partial p}-\bar{f}\vec{k}\cdot\nabla\times\frac{\partial \tau}{\partial p}=F^1(Z,\ \omega) \tag{2-7}$$

由 (2-4)，(2-5)，(2-6) 諸式可將熱力方程式化爲：

$$\frac{\partial}{\partial t}\left(\frac{\partial Z}{\partial p}\right)=-\frac{g}{f}J\left(Z,\frac{\partial Z}{\partial p}\right)-\sigma\omega-\frac{R}{C_p gp}\left[\frac{dQ}{dt}-\frac{d\bar{Q}}{dt}\right]=F^2(Z,\omega) \tag{2-8}$$

由 (2-7) (2-8) 式可得準地轉 ω 方程式：

$$\sigma\nabla^2\omega+\frac{\bar{f}^2}{g}\frac{\partial^2\omega}{\partial p^2}=\frac{g}{f}\nabla^2\left[J\left(\frac{\partial Z}{\partial p},\ Z\right)\right]-\frac{\partial}{\partial p}\left[J\left(\frac{g}{f}\nabla^2 Z+f,\ Z\right)\right]$$
$$-\frac{R}{C_p gp}\nabla^2\frac{dQ}{dt}+\bar{f}\vec{k}\cdot\nabla\times\frac{\partial^2\tau}{\partial p^2} \tag{2-9}$$

式中 $\sigma=-\frac{\alpha}{\theta}\frac{\partial\theta}{\partial p}$ 爲靜力穩定度，$\frac{d\bar{Q}}{dt}$ 爲對空間平均的輻射冷却率，而加熱率

$\frac{dQ}{dt}$ 則包括可感熱 $\frac{dQ_s}{dt}$ 及潛熱 $\frac{dQ_L}{dt}$。根據 Gambo (1963) 可感熱可假設爲：

$$\frac{dQ_s}{dt}=A|V_{10000}|(T_{sea}-T_{1000})\left(\frac{p}{1000}\right)^2, \tag{2-10}$$

$A=0.001$, 當 $T_{sea}>T_{1000}$,

$=0.0001$, 當 $T_{sea}<T_{1000}$,

$|V_{1000}|=0.7|V_{900}|$,

而潛熱釋放（在此僅考慮大規模運動可產生之穩定加熱）可設爲 (Gambo, 1963; Danard, 1966, Miller et. al., 1972)

$$\frac{dQ_L}{dt}=-LF^*\,\omega\Delta s, \qquad \omega<0 \quad p\geq 700mb, \tag{2-11}$$

$=0$, 其他情況

式中 F^* 爲 (Kuo 1965; Haltiner & Martin 1957):

$$F^*=\left[\left(\frac{\partial q^*}{\partial p}\right)_T+\frac{RT}{C_pP}\left(\frac{\partial q^*}{\partial T}\right)_p\right]\cdot\left[1+\frac{L}{C_p}\left(\frac{\partial q^*}{\partial T}\right)_p\right]^{-1} \tag{2-12}$$

$$q^*=0.622\,e\,[p-0.378e]^{-1},$$

$$e=0.611\left[\frac{273}{T}\right]^{5.31}\exp\left[25.22\left(1-\frac{273}{T}\right)\right] \quad \text{爲飽和水汽壓}$$

式中 q^* 與 e 分別爲飽和混合比與飽和水汽壓，Δs 爲大氣團中飽和部分率：

$$1\geq\Delta s=1-\frac{T-T_d}{\Delta T}\geq 0,$$

ΔT 爲一經驗值設爲 2.5°K

將 (2-11) 代入 (2-9) 式，則 ω-eq. 可寫爲

$$\nabla^2\sigma^*\omega+\frac{\bar{f}^2}{g}\frac{\partial^2\omega}{\partial p^2}=\frac{g}{\bar{f}}\nabla^2\left[J\left(\frac{\partial Z}{\partial p},Z\right)\right]-\frac{\partial}{\partial p}\left[J\left(\frac{g}{\bar{f}}\nabla^2Z+f,Z\right)\right]-\frac{R}{C_pgp}\nabla^2\frac{dQ_s}{dt}$$
$$+\bar{f}\vec{k}\cdot\nabla\times\frac{\partial^2\tau}{\partial p^2}=F^3(Z) \tag{2-13}$$

式中

$$\sigma^*=\sigma-\frac{RLF^*}{C_pgp}\nabla s\geq 0.2\bar{\sigma}, \qquad \text{當 } \omega<0 \text{ 且 } p>500mb \tag{2-14}$$

$=\sigma$ 其他情況。

關於摩擦阻力 τ，本文不考慮高聳山嶺之影響，並假設渦流黏滯所引起之側面混

合所造成的阻力不大，可予以忽略，則大氣與地球表面摩擦阻力可粗估爲 (Cressman, 1960) 在1000mb 處

$$\tau=\rho\ C_D|V_{1000}|V_{1000} \tag{2-15}$$

其餘各層 τ 爲零，式中 C_D 爲阻力係數，假設爲 (Staff members, 1965; Miller, 1969)

$$\begin{aligned} C_D&=[1.0+0.07|V_{1000}|]\times 10^{-3}, && \text{在海面上}\\ &=0.003 && \text{在陸地上}\end{aligned} \tag{2—16}$$

至於溫度露點差 $(T-T_d)$ 的預報係參考 Danard (1966) 提出的方法：

$$\frac{\partial}{\partial t}(T-T_d)=-\vec{V}_g\cdot\nabla(T-T_d)+K\nabla^2(T-T_d),\quad \text{當 } T=T_d \text{ 且 } \omega<0,$$

$$=-\vec{V}_g\cdot\nabla(T-T_d)+\omega\left\{\frac{d}{dp}(T-T_d)\right\}_\theta+K\nabla^2(T-T_d),\quad \text{其他情況，}$$

式中K爲水平紊流擴散係數 (取爲 $2\times10^{-10}cm^2\ sec^{-1}$)。此式可預報某一定層溫度露點差之時間增量，因而求得下一個時間溫度露點差之值。其他各層則可聯合熱力學第一定律與 Clausius-claypeyron 方程式：

$$\left[\frac{d}{dp}(T-T_d)\right]_\theta=\frac{\alpha}{C_p}\frac{R\ T_d^2}{0.622\ L_v\ p},$$

與已預報之值外插而得。

北半球準地轉模式，係以北半球爲計算範圍，利用 Polar stereoprojection 投影於投影面上，由於水平面之側向邊界恰在赤道附近，故可以固定邊條件模擬之。在垂直方面則假設大氣層頂與底的垂直速度皆爲零。

叁、有限區域原始方程式模式

在此模式中不考慮地形及摩擦阻力，在 (x, y, p, t) 坐標上的控制方程式爲運動方程式、熱力方程式、連續方程式、流體靜力方程式 (Shiau, 1976)：

$$\frac{\partial u}{\partial t}=-u\frac{\partial u}{\partial x}-v\frac{\partial u}{\partial y}-\omega\frac{\partial u}{\partial p}+fv-\frac{\partial\phi}{\partial x} \tag{2-16}$$

$$\frac{\partial v}{\partial t}=-u\frac{\partial v}{\partial x}-v\frac{\partial v}{\partial y}-\omega\frac{\partial v}{\partial p}-fu-\frac{\partial\phi}{\partial y} \tag{2-17}$$

$$\frac{\partial\theta}{\partial t}=-u\frac{\partial\theta}{\partial x}-v\frac{\partial\theta}{\partial y}-\omega\frac{\partial\theta}{\partial p}+\frac{\theta}{C_pT}\frac{d\ (Q-\bar{Q})}{dt} \tag{2-18}$$

$$\frac{\partial u}{\partial x}+\frac{\partial u}{\partial y}+\frac{\partial \omega}{\partial p}=0 \tag{-19}$$

$$\frac{\partial \phi}{\partial p}=-\frac{RT}{p} \tag{2-20}$$

其中 u, v, θ, ω, ϕ 爲未知數，$\frac{dQ}{dt}$ 爲加熱率，表示方法與前同，由 (2-17) ，對 x 微分，(2-16) 對 x 微分二式相減，經幅度分析可得平衡方程式

$$\nabla^2\phi=f\left(\frac{\partial v}{\partial x}-\frac{\partial u}{\partial y}\right)-u\frac{\partial f}{\partial y}+2J(u,\ v) \tag{2-21}$$

大氣中大幅度的運動是準平衡狀態的，要達到完全的平衡並不可能，事實上也不存在，尤其是在摩擦阻力大和熱效應大的地方。此外，觀測資料的誤差及雜波的存在，使模式在計算過程中產生慣性重力波的擾動而使計算失敗。所以在計算之前必須校正原始資料，使壓力場與風場儘可能接近平衡狀態，此即初值化 (Initialization) 之手續 。 本文利用平衡方程式，ω- 方程式，流體靜力方程式和連續方程式來處理初值化的問題 (Hawkins, 1972) ，其步驟如下：

(1)以高度場經平衡方程式，求得流線函數 (Stream function)，即得風的旋轉部份 (rotational part)：

$$f\nabla^2\psi-u\frac{\partial f}{\partial y}+2(\psi_{xx}\ \psi_{yy}-\psi_{xy})=\nabla^2\phi, \tag{2-22}$$

足碼 x, y 表示對 x 或 y 微分。

(2)溫度場由厚度經流體靜力方程式計算而得：

$$T=-\frac{p}{R}\frac{\partial\phi}{\partial p},\qquad \theta=T\left(\frac{1000}{p}\right)^{R/C_p} \tag{2-23}$$

(3)風的發散部份 (divergent part), χ 由連續方程式求得：

$$\nabla^2\chi=-\frac{\partial\omega}{\partial p} \tag{2-24}$$

求解時，假設 ω 之初值爲零，ω 及 χ 的邊界值爲零，反覆求至 n+1 次，使

$$|\chi^{n+1}-\chi^n|\leqslant\epsilon$$

本文中 ϵ 取爲 10^{-2} sec^{-1}。由所求得之 ψ 與 χ 可得風場爲

$$u=-\frac{\partial\psi}{\partial y}+\frac{\partial\chi}{\partial x} \tag{2-25}$$

$$v=-\frac{\partial\psi}{\partial x}+\frac{\partial\chi}{\partial y} \tag{2-26}$$

(4)垂直速度由 ω－方程式求得：

$$\nabla^2\sigma^*\,\omega+f^2\frac{\partial^2\omega}{\partial p^2}=-\nabla^2\left[J\left(\psi,\frac{\partial\phi}{\partial p}\right)+\nabla\chi\cdot\nabla\frac{\partial\phi}{\partial p}+\frac{R}{C_p\,p}\cdot\frac{dQ}{dt}\right.$$
$$\left.+\frac{\partial}{\partial p}\left[\frac{\partial}{\partial t}\nabla f\cdot\nabla\psi+f\,J\left(\psi,\eta\right)+f\,\nabla\chi\cdot\nabla f\right]\right] \tag{2-27}$$

其中 η 爲絕對渦旋度 (absolute vorticity)，而

$$\sigma^*=\sigma-0.06\,\Delta s\cdot\frac{R}{p}\geqslant 0.2\bar{\sigma}, \qquad \text{當 } \omega<0 \text{ 或 } p>500\text{mb},$$
$$=\sigma\geqslant 0.2\,\bar{\sigma}, \qquad \text{當 } \omega\geqslant 0 \text{ 或 } p\leqslant 500\text{mb}, \tag{2-28}$$

σ 爲靜力穩定度 (static stability)。

(2-26) 式中假設 ω 的邊界值爲零。反覆求至 $n+1$ 次使 $|\omega^{n+1}-\omega^n|\leqslant 10^{-6}$ mb/sec.

(5)重覆(1)至(4)的步驟，直到符合所有條件爲止。如此可得一組近乎平衡的初始 u, v, θ, ϕ, 及 ω 值。

肆、模式之組合與比較

爲了使有限區域原始方程模式在預報區域的邊界上能够更適當的模擬實際天氣狀況，本文將北半球準地轉模式與有限區域原始方程式模式合併使用，也就是以北半球地轉模式所預報者作爲有限區域原始方程式模式之邊界值。由於兩種模式之時間間格與空間間格不同，北半球準地轉模式在網格點上之起始值與預報值需經內插至有限區域原始方程式模式的網格點上，因北半球準地轉模式之時間間格爲一小時，所以本文將半球模式內插至有限區域網格點上的初始值（包括海水溫度，600,800 mb 的溫度露點差場，300, 500, 700, 900mb 上的高度場及溫度場）及每小時預測的高度場，溫度場在有限區域邊界上的網格值寫在磁帶上，當有限區域原始方程式模式進行預報時，有限區域之邊界值以半球模式之預報值每一小時更新一次，而在此一小時的時間間格內此值則固定不變。

爲便於瞭解組合模式之預報能力，本文將北半球準地轉模式與有限區域原始方

程式模式（固定邊界值）12小時與24小時之預報場與組合模式預報場相比較，並且與實際天氣情況相印證。由於有限區域原始方程式模式與組合模式之相異僅在於邊界值之有否更新，故預報效果之良否當可顯示出邊界值更新之實際效應，而北半球準地轉模式之預報效果則可顯示出用以更新之邊界值是否具實際代表性。

伍、數值方法與分析

北半球準地轉模式，以北半球爲計算範圍，在此範圍內共分（24×26）個網格點。各網格點間的距離爲 762 公里。有限區域原始方程式模式運算範圍在東亞地區，以北緯30度，東經 120 度爲參考點。共（19×20）個網格點，各網格點間的距離爲 240 公里（參見第一圖）。

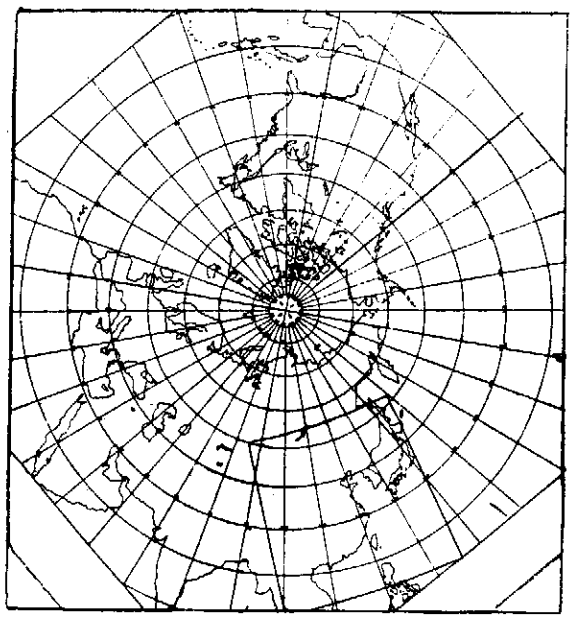

圖一　運算範圍。

A. 北半球準地轉模式

將大氣垂直分作四層，以 200 mb 爲此模式之頂，以 1000 mb 爲底，其分層的方式及各變數所在層次請參見第二圖 (a)。

在水平網格坐標中，起始點在左下角。網格間距離相等，以 d 表示。900 mb 的高處場由下式求取：

$$z=a+b\ell_n p+c(\ell_n p)^2 \qquad (3\text{-}1)$$

北半球準地轉模式之預報步驟如下：

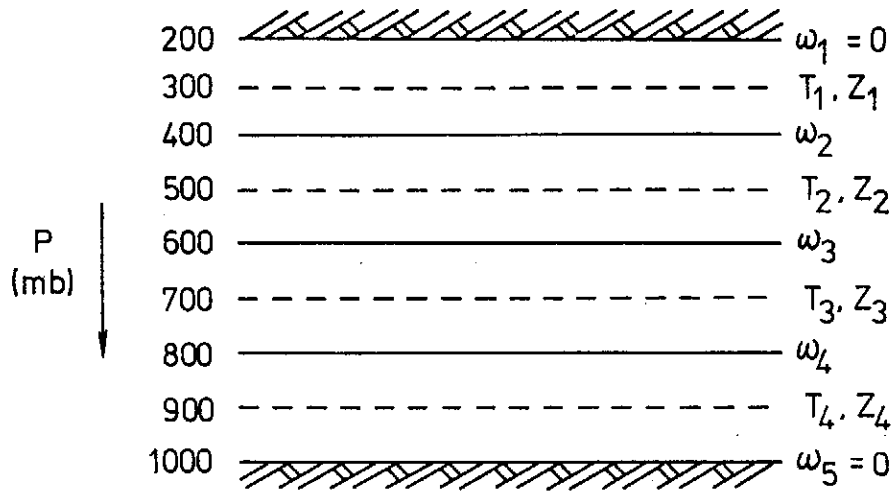

(a)

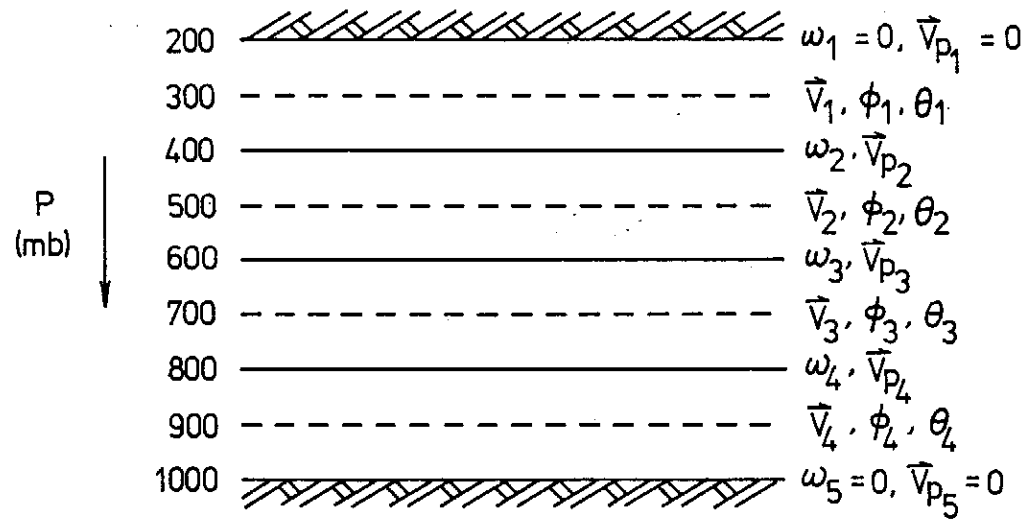

(b_1)

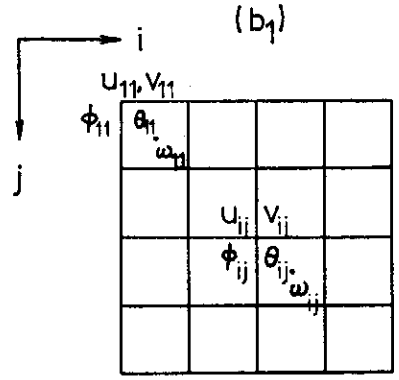

(b_2)

圖二　垂直分層結構（a）北半球準地轉模式（b1）有限區域原始方程式模式。(b2) 有限區域原始方程式模式水平網格系統。

(1)由 (2-12) 式化爲定差式可寫爲：

$$\omega^{n+1}_{i,j,k}=[\sigma^{*}_{i+1,j,k}\,\omega_{i+1,j,k}+\sigma^{*}_{i-1,j,k}\,\omega_{i-1,j,k}+\sigma^{*}_{i,j+1,k}\,\omega_{i,j+1,k}+\sigma^{*}_{i,j-1,k}\,\omega_{i,j-1,k}$$
$$+\frac{\bar{f}^2d^2}{gm^2\,\Delta p^2}(\omega_{i,j,k+1}+\omega_{i,j,k-1})-\frac{F^3_{ijk}\,d^2}{m^2}]^n\Big/[4\sigma^{*}_{i,j,k}+\frac{2\bar{f}^2}{gm^2}\frac{d^2}{\Delta p^2}]^n \qquad (3\text{-}2)$$

式中 n 及 n+1 爲 iteration 過程中二連續步驟，m爲 polar stereo-projection factor。

在適當的邊界條件下，(3-2) 式重複運用至

$$\max|\omega^{n+10}_{ijk}-\omega^{n}_{ijk}|\leqslant\epsilon \qquad (3\text{-}3)$$
$$\epsilon=10^{-6}$$

由此可求得 ω 場

Δt 爲時間增量，爲使計算穩定，必須符合 von Neumann 必要條件：

$$\Delta t\leqslant\min\left(\frac{d}{|u|+|v|+|\omega|}\right) \qquad (3\text{-}4)$$

u, v 爲水平方向風速，以地轉風近似取代，ω 爲垂直速度 ($\omega=\frac{dz}{dt}$)。

故上式亦可寫爲：

$$\Delta t\leqslant\min\frac{d}{\frac{g}{f}\left(\left|\frac{\partial z}{\partial x}\right|+\left|\frac{\partial z}{\partial y}\right|\right)+\left|\omega\frac{\partial z}{\partial p}\frac{d}{d_{\Delta p}}\right|}$$

(3-5) 式中 $d_{\Delta p}$ 爲 Δp 之厚度。

(2)同理，渦旋度方程式，(2-7) 式，寫成定差式爲：

$$\frac{\partial z^{n+1}}{\partial t_{ijk}}=0.25\left[\frac{\partial z}{\partial t_{i+1,j,k}}+\frac{\partial z}{\partial t_{i-1,j,k}}+\frac{\partial z}{\partial t_{i,j+1,k}}+\frac{\partial z}{\partial t_{i,j-1,k}}-\frac{d^2}{m^2}F^1_{ijk}\right]^n \qquad (3\text{-}6)$$

此式重複運用以解 500 mb 的高度趨勢$\frac{\partial z}{\partial t}$場，直至

$$\max\left|\frac{\partial z^{n+10}}{\partial t_{ijk}}-\frac{\partial z^{n}}{\partial t_{ijk}}\right|\leqslant\epsilon$$

因此可得 500 mb 在下一時刻的預報高度場。

(3)再由厚度方程式 (2-8) 式，可得下一時刻 300～500, 500～700, 700～900mb 間的厚度場，進而可得 300, 700, 900 mb 一時刻的預報高度場。

上述 (1) 至 (3) 步驟重複運用，直到所須預報的時刻 (24小時) 爲止。

以上諸式之 F^1 F^2 F^3 除 Jacolian 項以 Arakawa (1971) 方式表示外，

其餘皆採用 centered-difference。

本模式之邊界條件，在 200 與 1000 mb 層上令 ω 爲零。

在水平面上，由於探討的是北半球短時間模擬問題，假設在預報時間範圍（24 小時）內，邊界上的高度場不變外，並假設固定的邊界條件即：

$$\frac{\partial z}{\partial t}=0, \quad \text{在側邊界上。} \tag{3-7}$$

若不考慮邊界及其以外之熱源，則 (2-8) 式可得

$$\omega_{\text{邊界}}=-\frac{g}{\bar{\sigma}\,f}J\left(z,\frac{\partial z}{\partial p}\right) \tag{3-8}$$

此外，本模式之時間間隔 $\Delta t=1$ 小時，當時間開始時 ($t=0$) 採用 forward difference method 以後，$t>0$, 採用 centered difference method 外延以求取下一時刻的預報值。

B. 有限區域原始方程式模式

此模式在垂直方向上亦分爲四層，以 200 mb 爲模式頂，1000 mb 爲底其垂直分層及各變數所在層次請參見第二圖 (b1)。

在此模式中運算範圍在水平面爲 (NX−1), (NY−1) 的有限區域網格，NX=19, NY=20, 各網格點間之距離爲 240 公里，假設 $\omega, \frac{\partial u}{\partial p}, \frac{\partial v}{\partial p}$ 值在模式頂及底部爲零。利用定差數值分析可得 (2-15) 式至 (2-19) 式的聯立方程。其水平網格系統如第二圖 (b2)，起始點在左上角 (2-15) 式至 (2-20) 式的差定方程式可寫爲：(Miller, 1969; Shuman, 1957)：

$$\bar{u}_t^{xy}=-\overline{\bar{m}^{xy}\left[\bar{u}^{xy}\bar{u}_x^{-y}+\bar{v}^{xy}\bar{u}_y^{-x}+\bar{\phi}_x^{-y}\right]-\omega\,\bar{u}_p^{-xyp}+f\,\bar{v}^{-xy}}^{xy} \tag{3-9}$$

$$\bar{v}_t^{xy}=-\overline{\bar{m}^{xy}\left[\bar{u}^{xy}\bar{v}_x^{-y}+\bar{v}^{xy}\bar{v}_y^{-x}+\bar{\phi}_y^{-x}\right]-\omega\,\bar{v}_p^{-xyp}-f\,\bar{u}^{-xy}}^{xy} \tag{3-10}$$

$$\bar{\theta}_t^{xy}=-\overline{\bar{m}^{xy}\left[\bar{u}^{xy}\bar{\theta}_x^{-y}+\bar{v}^{xy}\bar{\theta}_y^{-x}\right]-\omega\,\bar{\theta}_p^{-xyp}}^{xy}+\overline{\frac{1}{C_p}\left(\frac{1000}{p}\right)^{R/C_p}\left(\frac{dQ}{dt}-\frac{d\bar{Q}}{dt}\right)}^{xxyy} \tag{3-11}$$

$$\overline{\bar{m}^{xy}\left(\bar{u}_{xp}^{-y}+\bar{v}_{yp}^{-x}\right)}^{xy}=-\bar{\omega}_{pp}^{-xy} \tag{3-12}$$

$$\bar{\phi}_p^{xxyy}=-\frac{R}{p}\left(\frac{p}{1000}\right)^{R/C_p}\bar{\theta}^{xxyy} \tag{3-13}$$

$$\overline{\frac{m^2}{d^2}}^{xxyy}\nabla^2\phi=\overline{f}^{xy}(\overline{v}^{y}_{x}-\overline{u}^{x}_{y})-\overline{f}^{x}_{y}\overline{u}^{xy}+\frac{2}{4}\overline{\frac{m^2}{d^2}}^{xxyy}J(u,v) \tag{3-14}$$

其中 $$\overline{A}^{yyxx}=\frac{1}{16}(A_{j+1,j+1}+A_{i+1,j-1}+A_{i-1,j+1}+A_{i-1,j-1})+\frac{1}{8}(A_{i+1,j}+$$

$$A_{i-1,j}+A_{i,j+1}+A_{i,j-1})+\frac{1}{4}A_{i,j} \tag{3-15}$$

$$\overline{A}_{x}^{xyy}=\frac{1}{8\Delta x}(A_{i+1,j+1}+A_{i+1,j-1}-A_{i-1,j+1}-A_{i-1,j-1})$$

$$+\frac{1}{4\Delta x}(A_{i+1,j}-A_{i-1,j}) \tag{1-16}$$

$$\overline{A}_{y}^{xxy}=\frac{1}{8\Delta y}(A_{i+1,j+1}+A_{i-1,j+1}-A_{i+1,j-1}-A_{i-1,j-1})$$

$$+\frac{1}{4\Delta y}(A_{i,j+1}-A_{i,j-1}) \tag{3-17}$$

$$\overline{\omega}^{xy}=\frac{1}{4}(\omega_{i,j}+\omega_{i+1,j}+\omega_{i,j-1}+\omega_{i-1,j-1}) \tag{3-18}$$

$$u_{p_k}=\frac{1}{2\Delta p}(u_{k+1}-u_{k-1}),\ v_{p_k}=\frac{1}{2\Delta p}(v_{k+1}-v_{k-1}),\ \theta_{p_k}=\frac{1}{\Delta p}(\theta_k-\theta_{k-1}) \tag{3-19}$$

$$\omega_{pp}=\frac{1}{(\Delta p)^2}(\omega_{k+1}+\omega_{k-1}-2\omega_k) \tag{3-20}$$

足碼 t, x, y, p 分別表示對時間及空間水平，垂直方向之偏微分，$\bar{A}$ 表示平均值。J 表示 Jacobian operater，採用 Arakawa 的方法，使渦旋度平方 (the square vorticity) 及動能守恆 (Arakawa, 1971)。

在此模式中採用自由滑動邊界條件，(Free-slip B. C.)。

其計算步驟爲：

(1)由 (3-9)，(3-10)，(3-11) 式分別可計算 $\overline{u}^{t}_{t}$, $\overline{v}^{t}_{t}$, $\overline{\theta}^{t}_{t}$, 再對時間積分可得下一時刻的風場 u, v 及相當位溫場 θ。

(2)將步驟 (1) 中求得的風場代入 (3-14) 式可得下一時刻的重力位高度場 ϕ。

(3)步驟 (1) 中求得的風場代入 (3-12) 式可求得下一刻的 ω 場重複上述步驟，至所需預報的時刻爲止。

此外，爲抑制擾動之發展，模式中時間外插採用 Euler-backward time advancement。

陸、數值預報之結果與討論

本文所採用的資料爲 NOAA 北半球網格點上的資料，時間爲民國六十五年八月七日 00Z, ，此組資料原爲在八角形網格點上，原網格距爲 381 公里。

共有 47×51 點，爲適應計算機容量的要求，今每隔一點取一值，共取 24×26 個網格點值，網格距爲762公里，輸入資料包括高度場（300，500，700，900 mb）溫度場（300，500，700，900 mb）平均相對濕度（中層、低層分別換算爲 600，800 mb 的溫度露點差值），以及月平均海面溫度場。

爲便於分析與比較，茲將初始場及12小時與24小時之預報場分別敍述如下。

A. 初 始 場

900 mb 上初始高度場的型態爲，在副熱帶，菲律賓東方海面有一颱風，而在西經 115 度及北緯 20 度，東經 20 度爲氣壓較低區。另外，整個中國大陸、印度半島、中東的連緜低壓區內有巴基斯坦（北緯 30 度，東經 60 至 70 度），及西藏高原（北緯 30 度，東經 80 至 90 度）兩個熱低壓。除此之外，整個北半球副熱帶均爲高壓所籠罩；而中緯度（北緯 30 至 60 度）除了西經 115 度及東經20度附近仍爲低壓外，日本附近有一短槽線，白令海有一低壓中心，而貝加爾湖西北方（東經 100 度，北緯60度）附近則有一未具封閉等壓線的低壓中心。此外，從中亞西亞迄蒙古則爲高壓區；至於高緯度，整個極渦均位於西半球。東半球除東經 30 度至 60 度爲低壓區外，其餘均爲高壓區。

至於高度場的垂直分佈及溫度場與濕度場的情形，由於吾人所選的個例爲夏天的資料，針對季節及吾人所處區域，在此僅討論對我們比較有興趣的系統。就颱風而言，其低層含水量豐富，此一暖心低壓隨高度的傾斜很小，其環流在 500 mb 面上，只剩一低壓中心畫不出封閉等高線。而至 300 mb 面則已無跡象可尋；至於太平洋的暖心高壓，則隨著高度的增加，高壓脊一直向西南伸展，只不過在 300 mb 面上，在東經 180 度附近被分裂爲二，但此時西邊分裂高壓的高壓脊已向西伸展至東經80度；而白令海的冷心低壓，水汽含量亦豐，隨著高度的增加，此低壓中心一直往西傾斜，亦卽渦管（vortex tube）的軸心向西傾斜，故此低壓似有增强的可能。另外，貝加爾湖西北的冷心低壓，亦含有豐富的水汽，隨著高度的增加，此低壓的强度漸增，但中心傾斜很少，且槽線沒有明顯的溫度槽，故此低壓未來移速應爲

緩慢，即使增强亦屬有限。至於巴基斯坦的低壓，向上伸展較高，在 500 mb 仍非常明顯，但西藏高原的暖心熱低壓，則隨高度迅速減弱，在 700 mb 面上已消失不見。值得一提的是，對流中層 (700 mb)，在海南島附近有一低壓中心，此一低壓中心可伸展至 500 mb，但在 900 mb 等高線圖上，又有顯著的氣旋型彎曲。

B. 十二小時的預測場

(1)北半球準地轉模式之預報結果：

颱風的位置，强度改變很少，但 700 mb 原有的封閉環流變爲不封閉，外圍等高線高度從 3,100公尺塡塞爲 3,130公尺；而太平洋高壓，一般而言，中心强度均增高，在 700 mb 與 500 mb 面上，不但範圍增廣，且高壓脊均向西伸展，伸展的强度在 700 mb 面上可達 20 度經度，在 500 mb 面上亦可達 10 度經度，至於 300 mb 面上的脊則後退 15 度經度。而東經 170 度的白令海低壓中心，高空各等壓面預測結果顯示强度均輕微塡塞，位置約向東北移動15度經度。至於貝加爾湖西北的低壓，預測位置無顯著改變，但强度均減弱，尤以 300 mb 爲甚， 由原來的 9,120公尺升爲 9,200 公尺。另外 700 mb 海南島附近低壓在預測圖上已消失。

(2)北半球準地轉模式的預測結果與實際情形的比較：

實際狀況，低層颱風中心强度，非但未見減弱，反而稍爲增强， 700 mb 颱風中心約向西北移動四個緯度，而太平洋高壓在 700 mb 與 500 mb，範圍沒有明顯的改變，只是脊向西伸展10個經度左右。而在 500 mb 則分裂爲二，至於 300 mb 脊後退13個經度左右，與預測的結果甚爲接近。而 700 mb 海南島附近低壓與預測情形一樣已消失了。另外貝加爾湖西北方的低壓位置及强度與預報結果甚爲吻合。白令海的低壓，預測速度較實際快10度經度左右。

(3)有限區域原始方程式模式十二小時的預測結果：

在此模式的預測範圍內，主要的系統爲颱風，太平洋高壓從華南向南伸展至海南島的低壓，北緯 40 度以北東經 100 度至 110 度間的低壓，太平洋高壓北邊，東經 130 度附近的脊線，由庫頁島向西南延伸的槽線及位於日本附近的槽線等。茲分兩種情形討論如下：

(a) 更新邊界值的預測結果：

颱風在 700 mb 向東南退 1 個緯度左右，在 500 mb 則向西北移動 1 個緯度左右，太平洋高壓在 700 mb 與 500 mb 分別東退 2 個與 3 個經度。在 500 mb 其中心由 5,910 公尺降爲 5,900 公尺，並向東南移 2 個經度左右，此高壓在 300 mb 東經 120 度附近向南移 2 個緯度。700 mb 海南島附近低壓範圍不變，但中心由 3,080公尺塡塞爲 3,090公尺。500 mb 北緯44度，東經 107 度的低壓則平淺，中心由 3,010 公尺塡爲 3,020 公尺。500 mb 與 300 mb 面上太平洋高壓以北的脊線槽線均平淺化。此種邊界條件有個特別現象，卽 900 mb 和 700 mb 西北東邊邊界附近均有明顯的高度增加現象，例如在 900 mb 從華南向東南延伸至南海的低壓區竟形成一封閉的低壓，而 700 mb 則同樣的在北緯 48 度，東經 130 至 140 度形成一封閉低壓中心。

(b) 固定邊界條件的預測結果：

颱風在 700 mb 向東南後退 1 個緯度，太平洋高壓在各層均東退；在 700 mb, 500 mb, 300 mb 分別東退 5 個，10 個，及 2 個經度左右。在 500 mb 上它的範圍顯著縮小，而中心則由 5,910公尺降爲 5,890公尺，並向東南移 2 個經度左右，從華南，延伸至海南島的低壓在 700 mb，範圍稍增廣，但中心由 3,080 公尺塡爲 3,090 公尺，且西移了一個度。500 mb 其範圍則向西南退 2 個緯度。至於太平洋高壓以北的槽脊線亦有平淺化的現象。日本附近的槽線更明顯的西退。

(4)有限區域原始方程式模式預測十二小時的結果與實際天氣情況的比較：

實際天氣，在 700 mb 與 500 mb，颱風中心分別向西北移動 1.8 個緯度及 1.2 個緯度。700 mb 颱風中心略爲增强。太平洋高壓脊在 700 mb 東退，在 500 mb 則西進 6 個經度；在 120 度經線附近向北移 2 個緯度，在 300 mb 其中心由 9,770 增高爲 9,780 公尺。至於東經 120 度的脊線在 700 mb 往東移 10 個經度，在 500 mb 則向北伸展。北緯 40 度以北，東經 100 至 110 度間的槽線在 700 及 500 mb 分別向東移動 10 個經度與 5 個經度。700 及 500 mb，日本附近的槽線位置沒有變化，但變淺。至於由庫頁島延伸至西伯利亞的槽線均向東移10個徑度。由上述情形，在不同的邊界條件下，有限區域原始方程式模式對各天氣系統十二小時的預測結果可歸納如下：

天氣系統	每小時更新邊界值	固定邊界值
颱風	可以預測其向西北移動。在 500 mb 其速度約慢 0.5 個經度左右，700 mb 則往東南退一個緯度。	700 mb 往東退 1 個經度，無法預測 700 mb 的增强及 500 mb 的移動
太平洋高壓	在 700 mb 可預測西東退， 500 mb 亦可預測其西進，但速度略慢，無法預測 300 mb 高壓中心的增强。	在 700 mb 可預測其東退，而 500 mb 則不西進，反而東退 10 個經度， 300 mb 非但不增强，反而東退，並降低20公尺。
日本附近的槽線	位置沒有變化與實際情況相符	位置西退
太平洋高壓以北其他槽脊線	不能預測其向東移動	不能預測其向東移動

C. 二十四小時的預測結果（與十二小時的預測圖比較）

(1)北半球準地轉模式的預測結果：

700 mb 面上仍無颱風中心，其外圍環流位置及强度均無任何改變。太平洋高壓在各層均繼續向西伸展，在 700 mb, 500 mb 及 300 mb 分別到達東經60，85及80度。此外，黃海的分裂高壓中心上升至具有封閉等高線的形態。700 mb 及 500 mb，前者由 3,190 公尺上升至 3,230 公尺，後者由 5,940 公尺上升至 5,990公尺，其中心原位於華中，高度場爲 9,800公尺，現移至山東半島，高度場升爲 9,860公尺。至於白令海的低壓仍然向東移動在700，500 及 300 mb 分別移至東經160，170，180 度附近；移動的速度在 700 mb 及 500 mb 均爲10個經度，但在 300 mb 可達15個經度左右，另外在貝加爾湖西北的低壓，位置沒有什麼變動，但各層强度均減，在 300 mb 無封閉等高線，而 700 mb 只剩强烈氣旋形彎曲等高線。至於巴基斯坦的低壓，在 700 mb 消失，在 500 mb 有一未具封閉等高線的低壓中心，而在 300 mb 則變爲高壓。此外，預測 700 mb 極渦向南移動，强度增强。300 mb 東經30度左右的槽線向東移五個經度。

(2)北半球準地轉模式24小時預測值與實際情況比較：

1976年8月8日 0000Z, 700 mb 颱風中心位於北緯 20 度，東經 130度，其環流已接近臺灣東南海面，此颱風環流垂直方向仍可達 500 mb；其中心位於北緯18度，東經 130 度，預測結果顯然不符，而 700 mb 面上，極渦向南移，

强度增加。在巴基斯坦（北緯30度，東經72度）及東京灣附近，分別有兩個封閉低壓中心。至於太平洋高壓脊則僅伸展至東經 137 度。500 mb 亦僅伸至東經 130 度，中心在北緯 27 度，東經 163 度附近，强度爲 5,930公尺，故預測的高壓脊西伸過甚，中心過份壓强。白令海的低壓中心在 700 mb 仍在東經 170 度附近滯處，並未向東移動，其在 500 mb 及 300 mb 的位移亦屬有限，至於貝加爾湖西北的低壓與預測情況類似，但 700 mb 仍有中心存在。此外，北緯30度附近的槽線亦與預測相近。

(3)有限區域原始方程式模式的預測結果與實際情形的比較：

在此模式的預報範圍內，實際天氣型態大致如下：700 mb 颱風中心位於北緯 20 度，東經 130 度附近，其在 500 mb 仍有封閉中心，到 300 mb 其環流業已消失。太平洋高壓脊在 700 mb 位於東經 137 度附近，隨著高度增加，其脊急劇向西伸展，在 500 mb 伸展主東經 107 度，而在 300 mb 則伸展至東經84度。另外，700 mb 在東經 110 度附近有一槽線，隨著高度的增加，此槽向西傾斜。以下分別討論兩種邊界條件的預報結果：

(a) 更新邊界值的預測結果

颱風的預測速度在 700 mb 較實際慢 3 個經度，500 mb 在北緯 16 度，東經 132 度附近仍保有一低壓中心。太平洋高壓的預測，在 700 mb 較實際爲强，位置與範圍均與實際情況相符。在此邊界條件，低層西、北、東邊界高度場仍有升高現象，故在 700 mb 面上，在北緯 48 度東經103及 106 度附近分別產生兩個低壓中心。

(b) 固定邊界值的預測結果：

颱風的預測在 700 mb 面上向西北移速較實際慢 5 個經度左右，500 mb 颱風環流已消失。太平洋高壓的型態與 (a) 顯著不同，在 700 mb 它外圍 3,130 的易高線向西伸展至東經 118 度，而在 500 mb 它的脊伸展程度不够，比實際少了 8 個經度，在 300 mb 預測的高壓竟然分裂爲二。

至於太平洋高壓脊以北的槽脊線三種情況均無法預測其向東的移動。可能是太接近北邊的邊界所致。

柒、結論與建議

由上述1976年 8 月 7 日個例模式的預測結果與實際情形比較，我們可以獲得如下結論：

(1)就颱風而言，由於半球準地轉模式網格點間的距離達 762 公里，而颱風又恰位於邊界附近，加上模式內未考慮積雲對流上升凝結所釋放的潛熱，所以無法很精確的處理颱風，而預測的結果颱風被填塞，與實際情況相反而預報的位移亦不準確。至於有限區域原始方程式的預報結果則較佳，此除了因爲網格點間距離較小（240 公里），鑑別率較佳外，物理過程的考慮較爲嚴密亦屬主因之一。有限區域原始方程式模式在兩種不同的邊界條件下，對颱風的預測結果以每小時更新邊界值的結果最好，但在 700 mb，24小時的預測速度仍然比實際速度落後三個經度之多，所幸數值預報的主要對象是大氣中的大幅度天氣現象，對於此種中幅度的天氣現象，數值模式的預測仍有待加强。

(2)就太平洋高壓而言，半球準地轉模式預測的高壓範圍不合理的擴大，中心也大幅度的升高。此種效應累積至24小時，已是非常嚴重，這是這個例子內，半球準地轉模式最嚴重的缺點，應該也是今後改進的重點所在。而有限區域原始方程式模式的預測却沒有這個問題。在兩種邊界條件中，更新邊界值的預測結果與實際情況相符，固定邊界值的預測結果則較差；在 700 mb 面上過份西伸，在 500 mb 面上則缺乏大幅度的伸展，至於 300 mb 面上的分裂，更與實際情況不符。

(3)有限區域原始方程式模式的兩種邊界條件中，從各種情況比較，更新邊界值的預報結果顯然較好。在低層邊界附近高度場有增高的現象，有待改進。此外兩種邊界條件均無法預測北端邊界附近，除日本附近的槽線外，槽脊線向東運動，此種缺點似可因半球準地轉模式之改進而改進。

(4)半球準地轉模式可預報白令海的低壓移動，但預報速度太快，填塞亦太快，對於貝加爾湖西北的低壓與北緯30度附近的槽線，半球準地轉模式的預報無明顯的移動，與實際情況吻合。總結來說，組合模式確能有效的改進有限區域原始方程式模式的預報能力，但其能力之加强，與半球之模式之預報能力息息相關。因此如何改進半球模式，當是此後的重要目標之一。此外，有限區域原始方

程式模式邊界值的更新，除本文所採用之方法外，尚有多種方法可以使用；不同的方法應該會有不同的效果，從各種預報實驗中挑選出最有效的方法亦應爲此後研究的重要論題。

參 考 文 獻

Arakawa, A., Design of the UCLA General Circulation Model, Dept. Met., UCLA, 1971.

Cressman, G. P., Improved Terrain Effects in Barotropic Forecasts, *MWR*, Sep.-Dec., 327, 1960.

Danard, M. B., A Quasi-Geostrophic Numerical Model Incorporating Effects of Release of Latent Heat, *J. Appl. Met.*, **5**, 85, 1966.

Gambo, K., The Role of Sensible and Latent Heats in the Baroclinic Atmosphere, *J. Met. Soc. Japan*, **41**, 233, 1963.

Haltiner, G. J., and F. L. Martin, *Dynamic and Physical Meteorology*, McGraw-Hill
Annual Report of the Institute of Physics, Academia Sinica, Vol. 8, 1978
Book Co., 1957.

Hawkins, H. F., Development of A Seven-level, Balanced, Diagnostic Model and Its Application to Three Disparate Tropical Disturbances. *NOAA Tech. Memo. ERL NHRL-98*, 207 PP., 1972.

Kuo, H. L., On the Formation and Intensification of Tropical Cyclones Through Latent Heat Release by Cumulus Convection., *J. Atm. Sci.*, **22**, 40, 1965.

Miller, B. I., Experiment in Forecasting Hurricane Development with Real Data, *ERLTA-NHRL 85, ESSA*, 1969.

Miller, B. I. et al., Numerical Prediction of Tropical Weather Systems, *MWR*, **100**, 825, 1972.

Shuman, F. G., and J. B. Hovermale, An Operational 6-layer Primitive Equation Model, *J. Appl. Met.*, **7**, 525, 1968.

Staff Members of Electronic Computation Center, 72-hr Baroclinic Forecast by the Diabatic Quasi-Geostrophic Model, *J. Met. Soc. Japan*, **43**, 246, 1965.

大氣物理組同仁，大氣及颱風運動模型 I. 邊界條件，中研院物理所集刊 2, 177, 1972。

_____，大氣及颱風運動模型 II. 運算範圍與網格大小，中研院物理所集刊 3, 191, 1973。

_____，大氣及颱風運動模型 III. 熱及摩擦阻力，中研院物理所集刊 3, 211, 1973。

蕭錫璋、汪群從，有限區域原始方程式模式之初步探討，中研院物理所集刊 6, 231, 1976。

Annual Report of the Institute of Physics, Academia Sinica, Vol. 8, 1978

ON THE STUDY OF THE NUMERICAL WEATHER PREDICTION UTILIZING COUPLING MODEL

WEN-JEY LIANG CHYI-JANG SHIAU

Institute of physics, Academia Sinica

CHUNG-YING HU SHI-YANG CHEN YUEH-JIUAN HSU

Central Weather Bureau

Abstract

In this study, the applicability of operationalization of primitive equation model is investigated. The numerical forecasting utilizing hemispherical quasi-geostrophical model is performed on coarse grid system and the results are assigned as the boundary values of primitive equation model in the limited fine mesh prediction. The results indicate that this coupling model significantly improves the forecasting for the patterns and the movements of synoptical weather systems. However, the time period for re-assigned the boundary values of primitive equation model should be shorten to increase the dispersion effects near the boundary of limited forecast area.

圖三　1976年8月7日0000Z北半球溫度露點差場。等值線以 5°C 爲間隔圖，中正、號負表示該處數值比周圍等值線高或低。(a) 中層（原爲 333 至 666 mb 的平均值，當作 600 mb 值）(b) 低層（原爲 666 至 1,000 mb 的平均值，當作 800 mb 值）

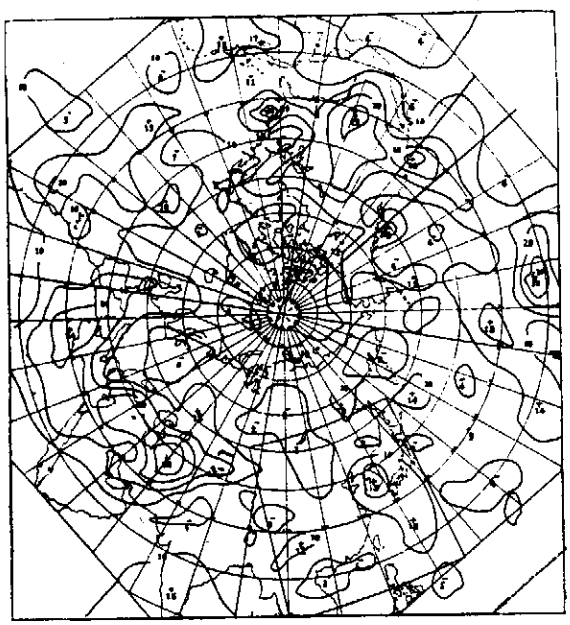

圖三 (a)

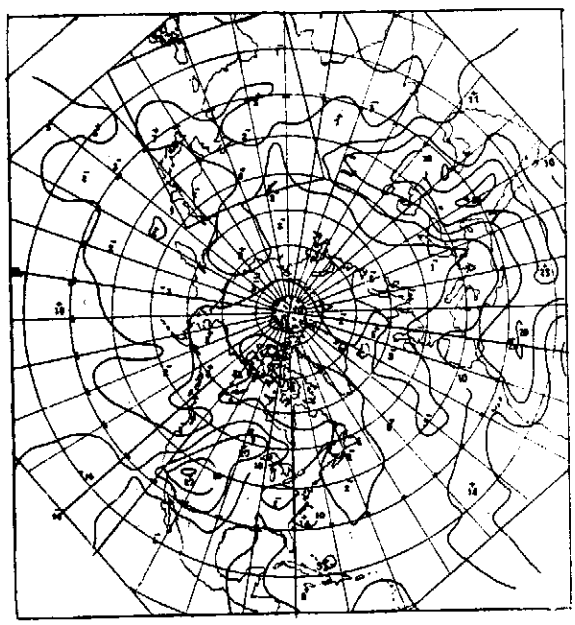

圖三 (b)

圖四　1976年8月7日0000Z北半球實際高度場，(a) 300 mb，等值線以120公尺隔，(b) 500 mb，等值線以 60 公尺爲間隔 (c) 700 mb，等價值以 30 公尺爲間隔 (d) 900 mb，等值線以 30 公尺爲間隔。

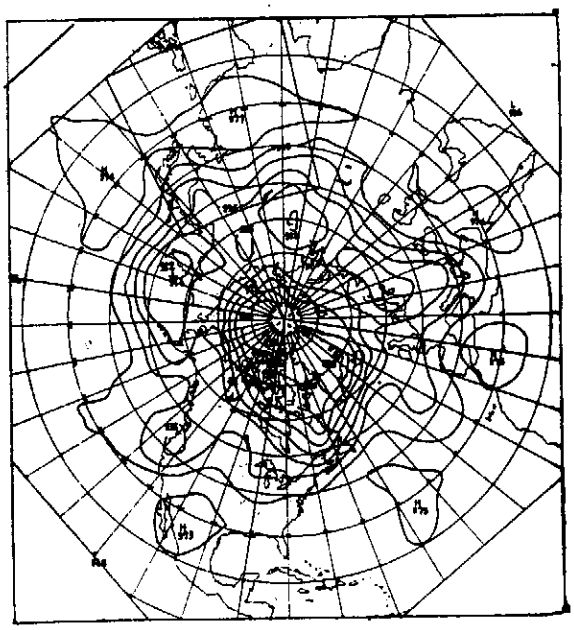

圖四 (a)

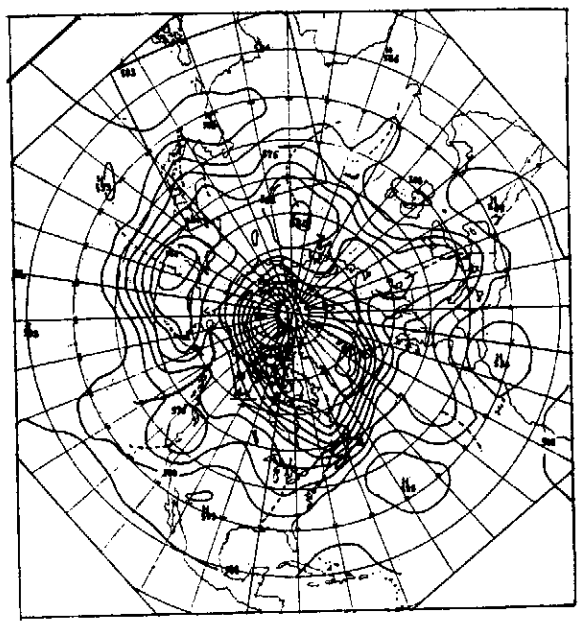

圖四 (b)

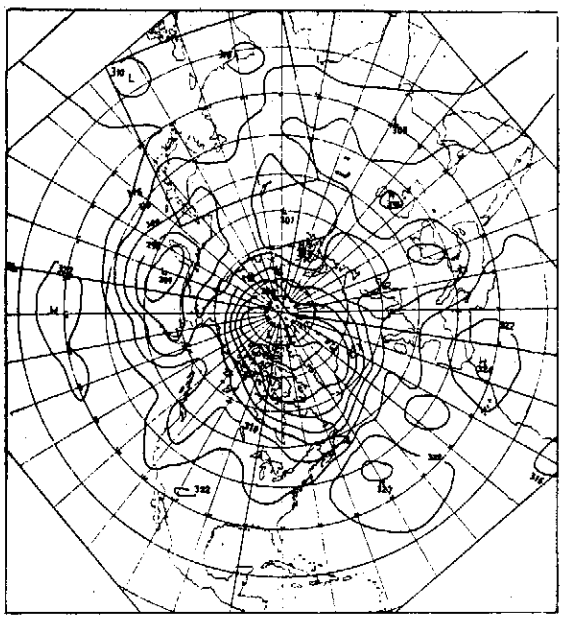

圖四 (c)

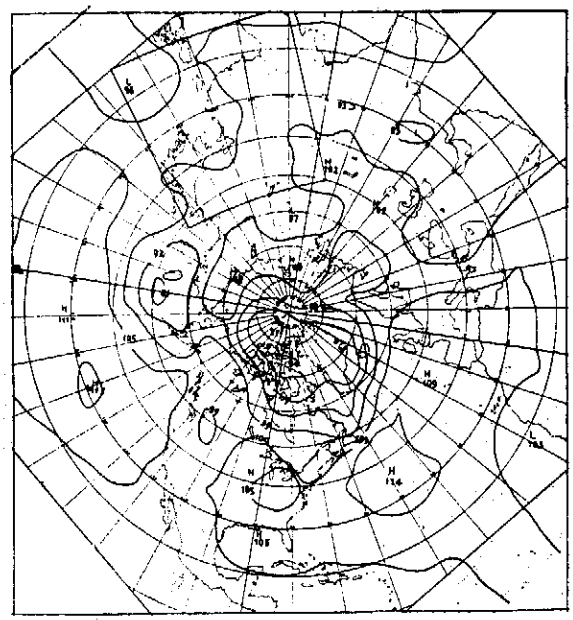

圖四 (d)

圖五　1976年 8 月 7 日 0000Z 北半球實際天氣溫度場，等值線以 5°C 爲間隔 (a) 300 mb, (b) 500 mb, (c) 700 mb, (d) 900 mb。

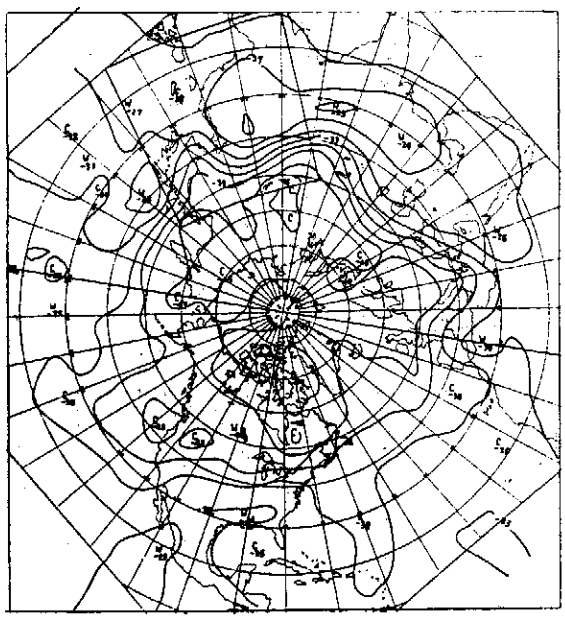

圖五 (a)

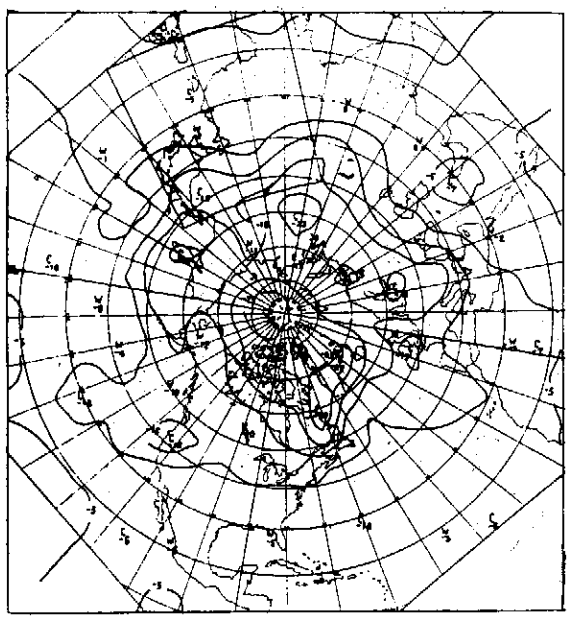

圖五 (b)

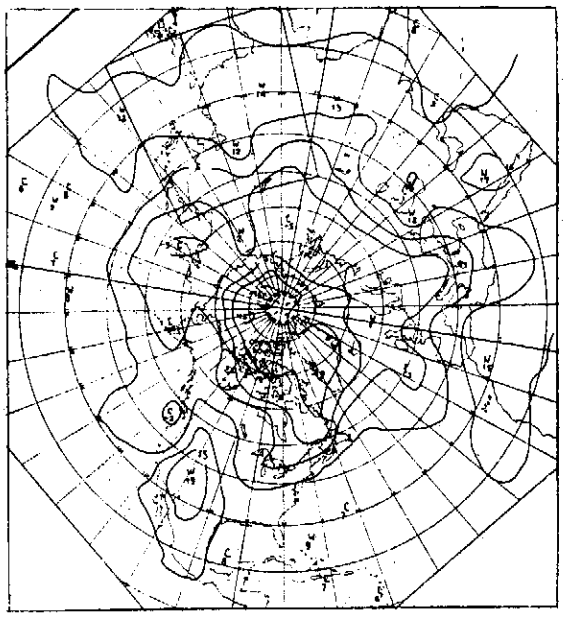

圖五 (c)

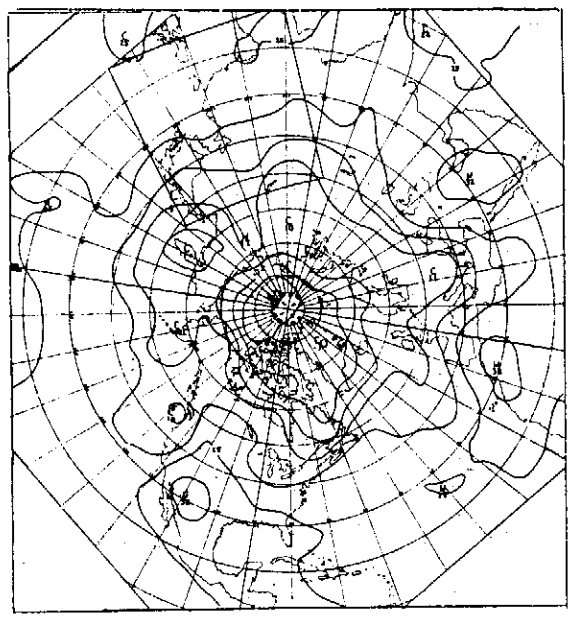

圖五 (d)

圖六　1976年8月7日 1200 Z 北半球溫度露點差場，等值線以 5°C 爲間隔，圖中正，負號表示該處數值比周圍等值線高或低，(a), (b) 中層 (原爲 333 至 666 mb 的平均值，當作 600 mb 值) (c), (d) 低層 (原爲 666 mb 至 1000 mb 的平均值當作 800 mb 值)，(a), (c) 爲準地轉模式計算結果，(b), (d) 爲實際天氣型態。

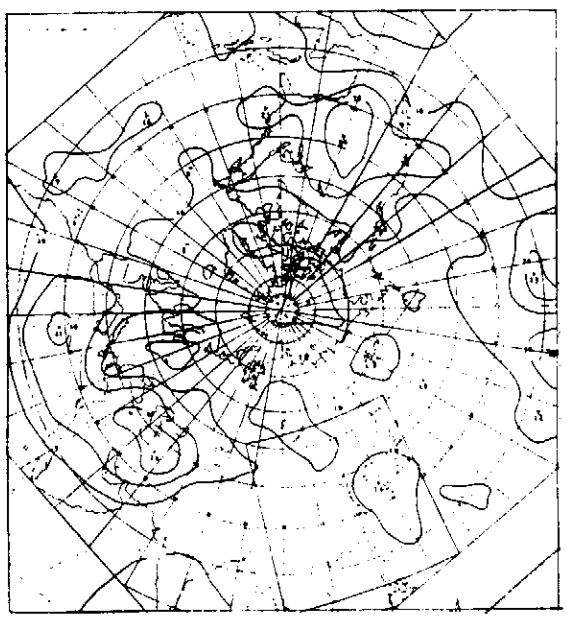

圖六 (a)

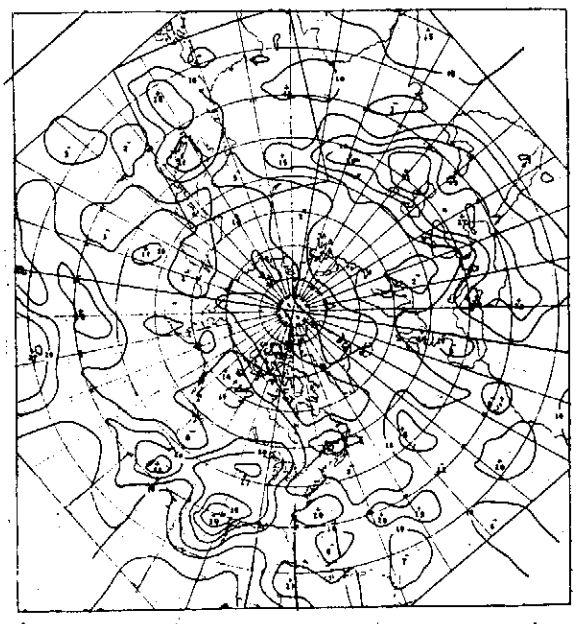

圖六 (b)

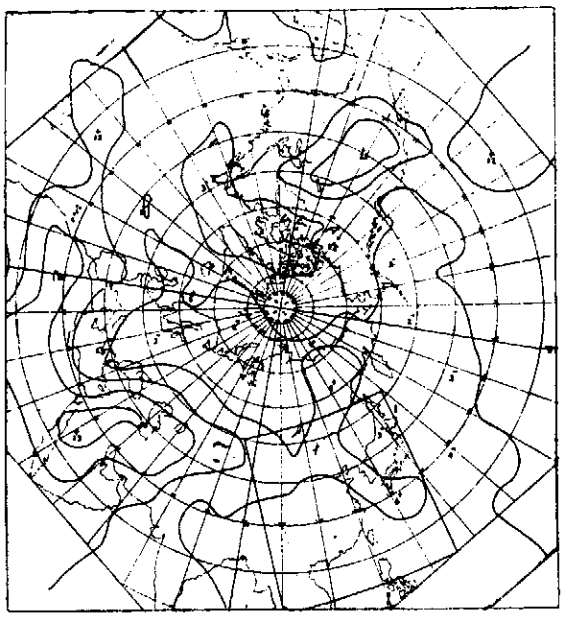

圖六 (c)

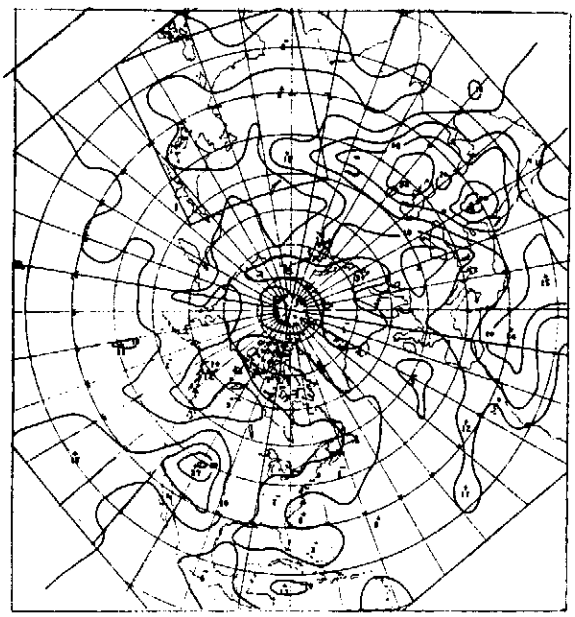

圖六 (d)

圖七　1976年 8 月 7 日 1200 Z 北半球高度場，(a1), (b1), (c1), (d1) 爲準地轉模式計算12小時的結果，(a2), (b2), (c2), (d2) 爲實際天氣型態 (a1), (a2) 300 mb，等值線以 120 公尺爲間隔 (b1), (b2) 500 mb 等值線以 60 公尺爲間隔 (c1), (c2) 700 mb 等值線以 38公尺爲間隔 (d1) (d2) 900 公尺，等值線以 30 公尺爲間隔。

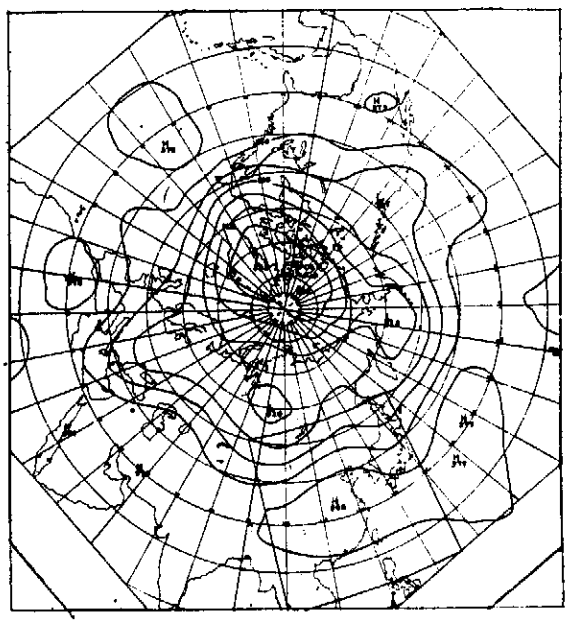

圖七 (a1)

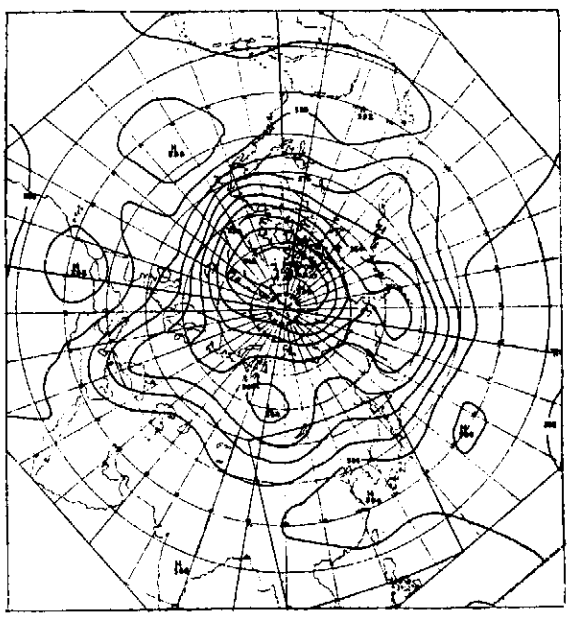

圖七 (b1)

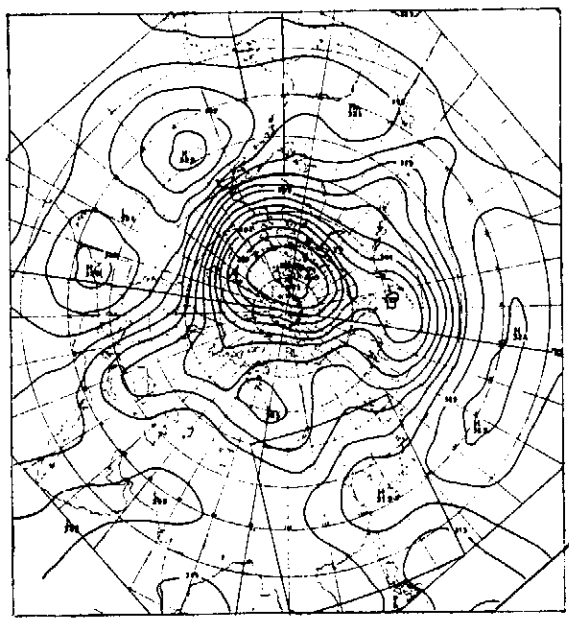

圖七 (c1)

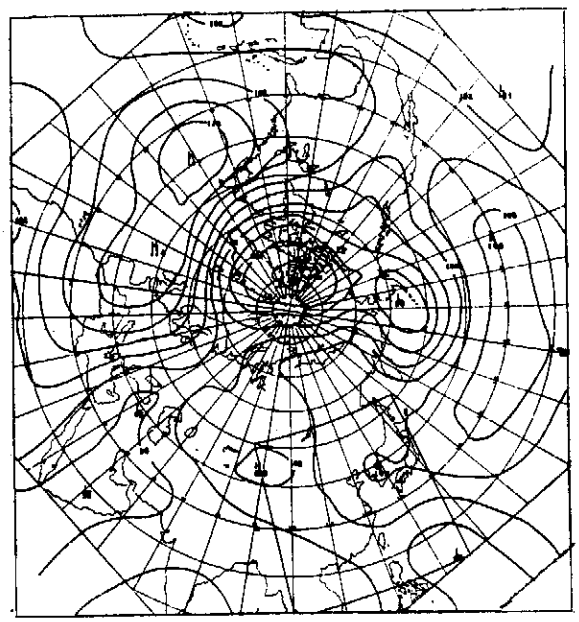

圖七 (d1)

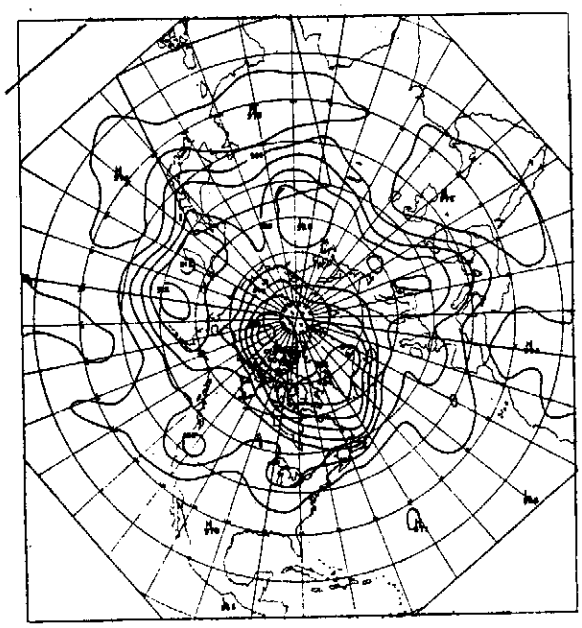

圖七 (a2)

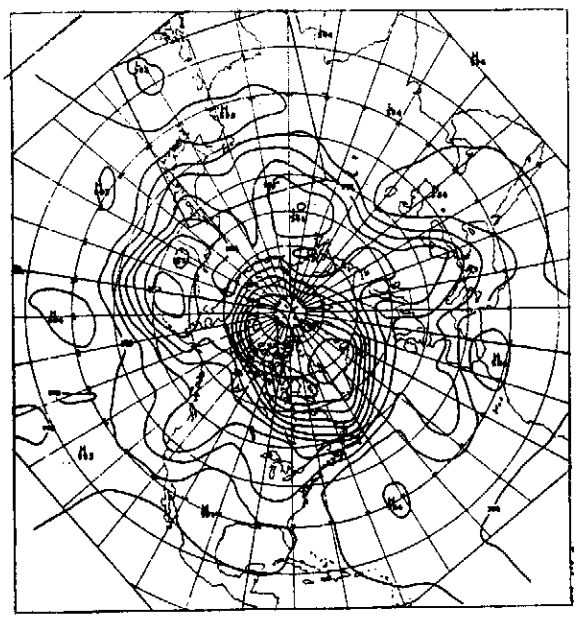

圖七 (b2)

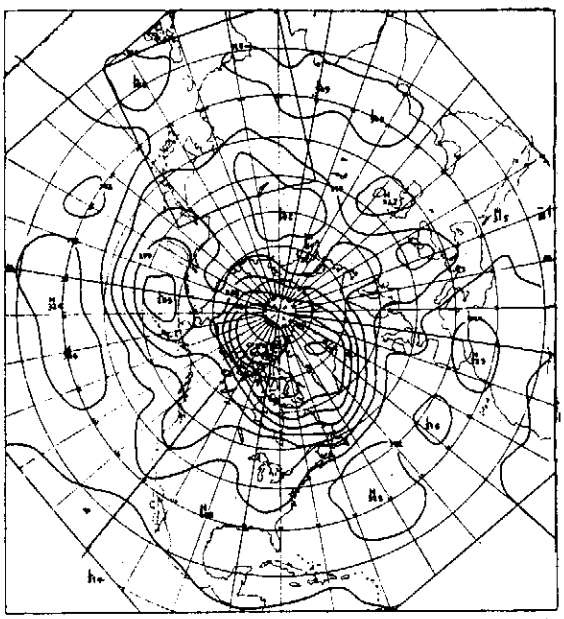

圖七 (c2)

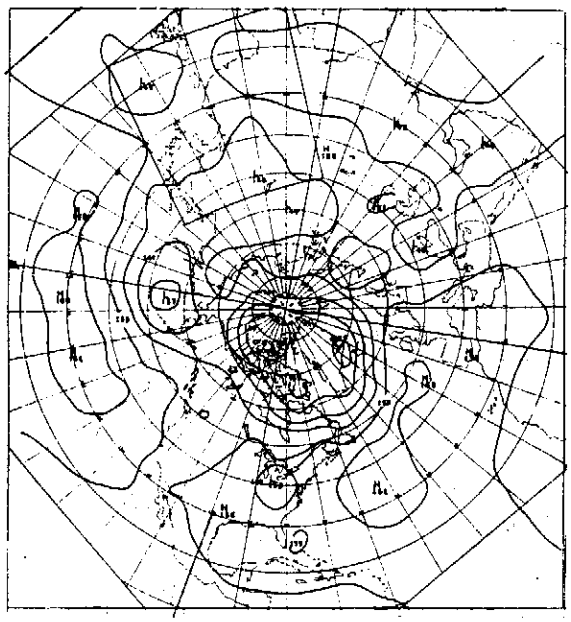

圖七 (d2)

圖八　1976年 8 月 7 日 1200 Z 北半球溫度場等值線以 5°C 爲間隔，(a1), (b1), (c1), (d1) 爲準地轉模式計算 12 小時後的結果，(a2), (b2), (c2), (d2) 爲實際天氣型態 (a1), (a2) 300 mb, (b1), (b2) 500 mb, (c1), (c2) 700 mb, (d1), (d2) 900 mb。

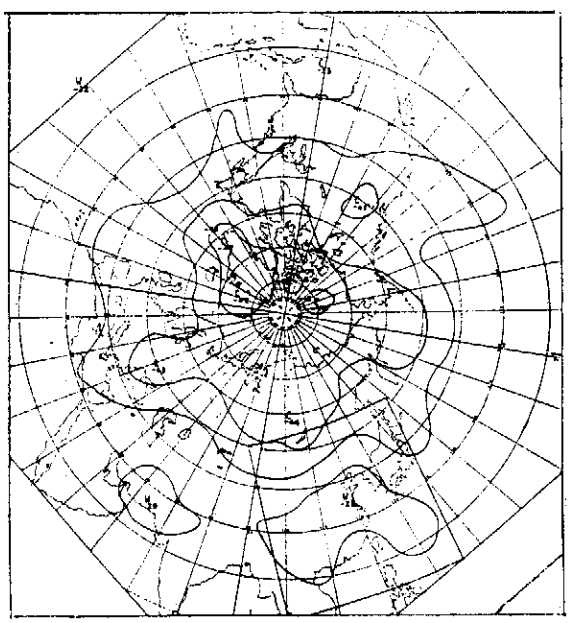

圖八 (a1)

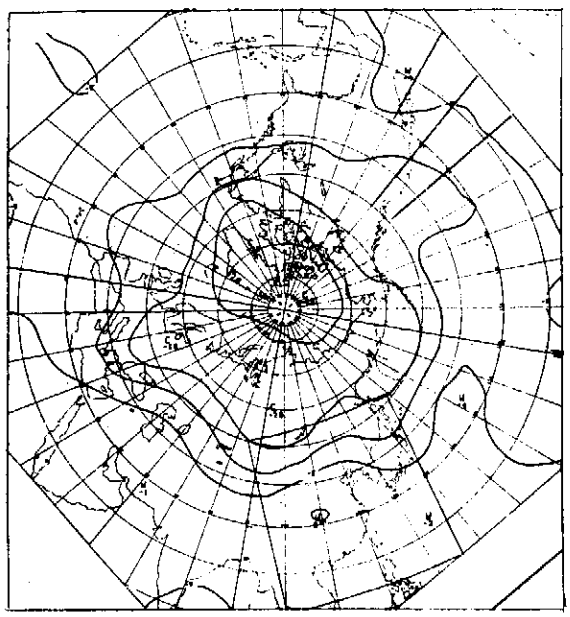

圖八 (b1)

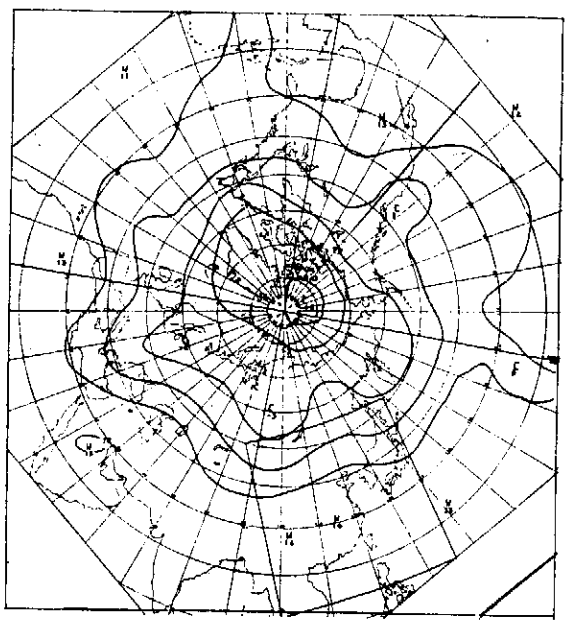

圖八 (c1)

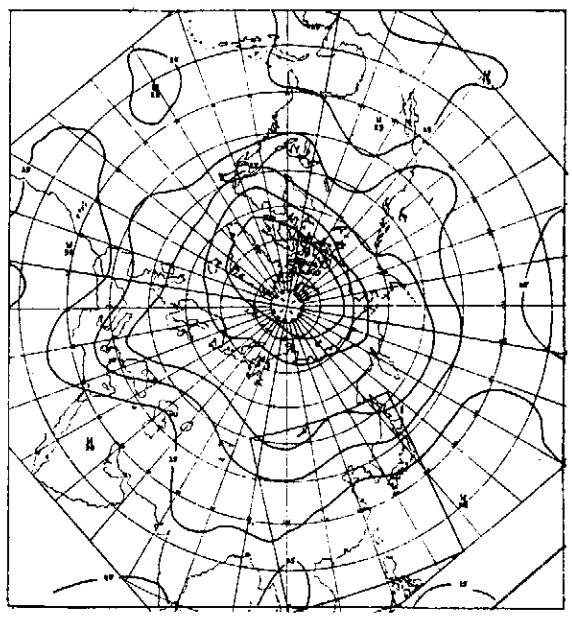

圖八 (d1)

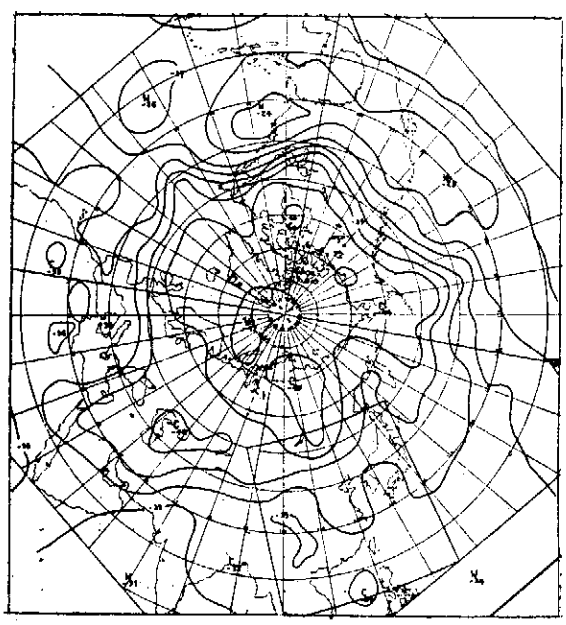

圖八 (a2)

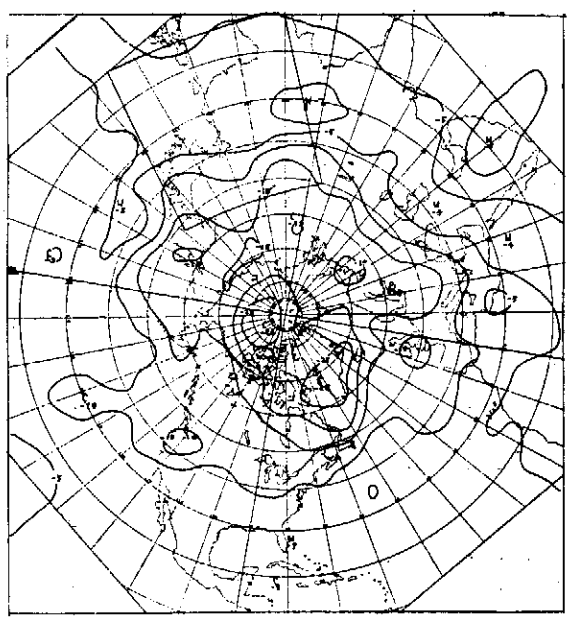

圖八 (b2)

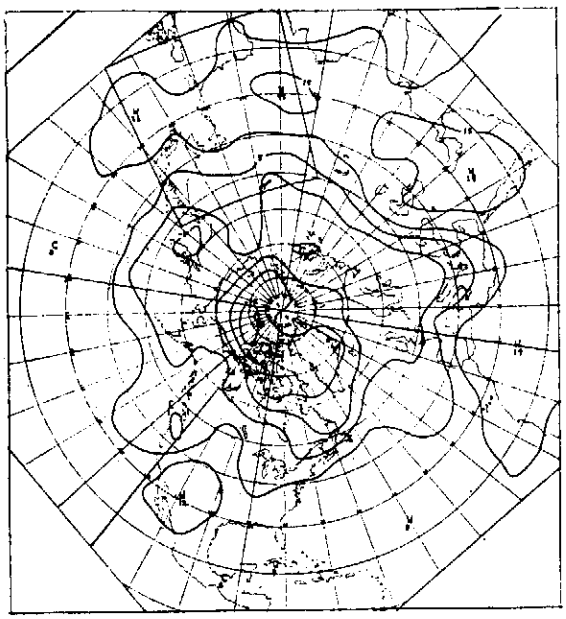

圖八 (c2)

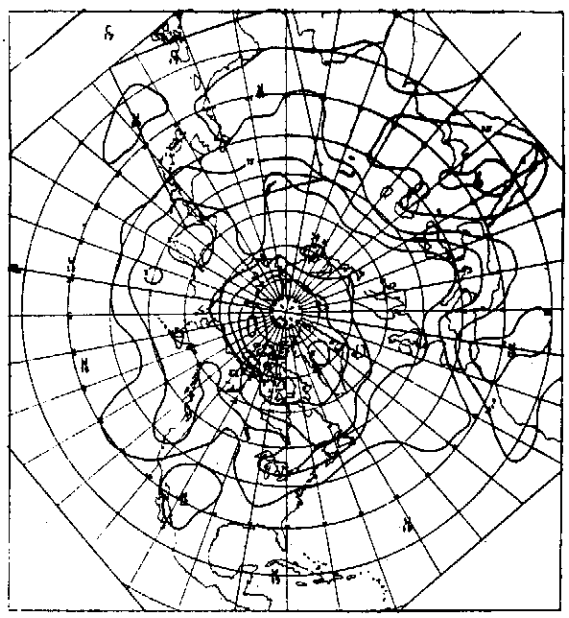

圖八 (d2)

圖九　有限區域原始方程式模式每小時更新邊界值，計算 12 小時的高度場，(a1), (a2) 300mb 等值線以 120 公尺爲間隔，(b1), (b2) 500 mb 等值線以 60 公尺爲間隔，(c1), (c2) 700 mb，等值線以 30 公尺爲間隔，(d1), (d2) 700 mb 等值線以 30 公尺爲間隔及溫度場，等值線以 5°C 爲間隔 (e1), (e2) 300 mb, (f1), (f2) 500 mb, (g1) (g2) 700 mb, (h1), (h2) 900 mb, (a1)～(h1) 爲計算的結果 (a2)～(h2) 爲實際天氣型態。

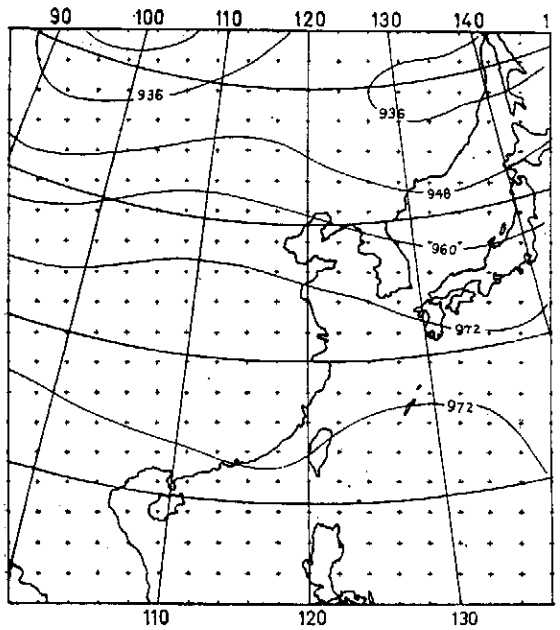

圖九 (a1)

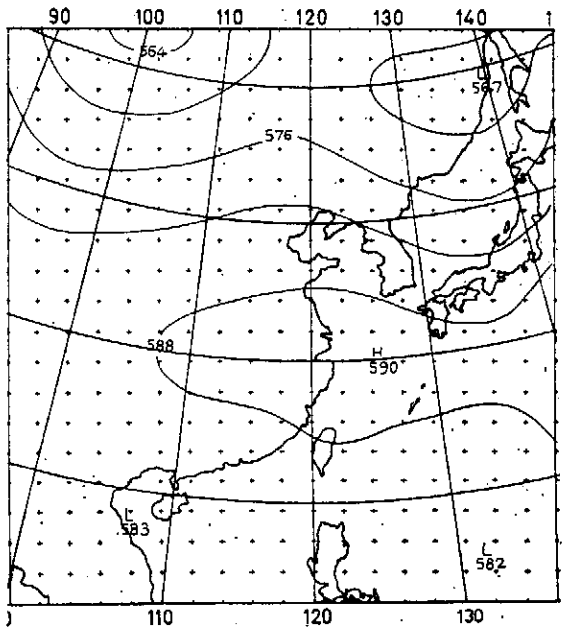

圖九 (b1)

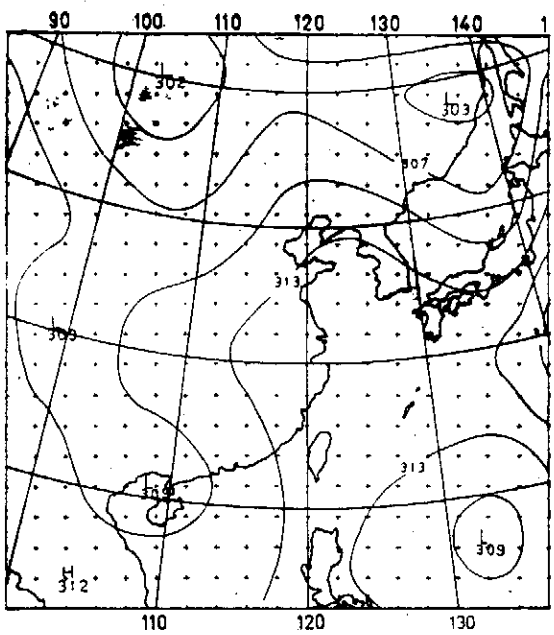

圖九 (c1)

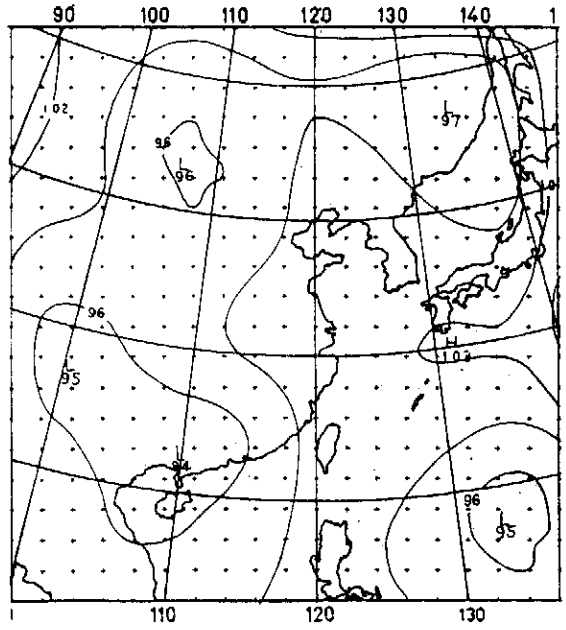

圖九 (d1)

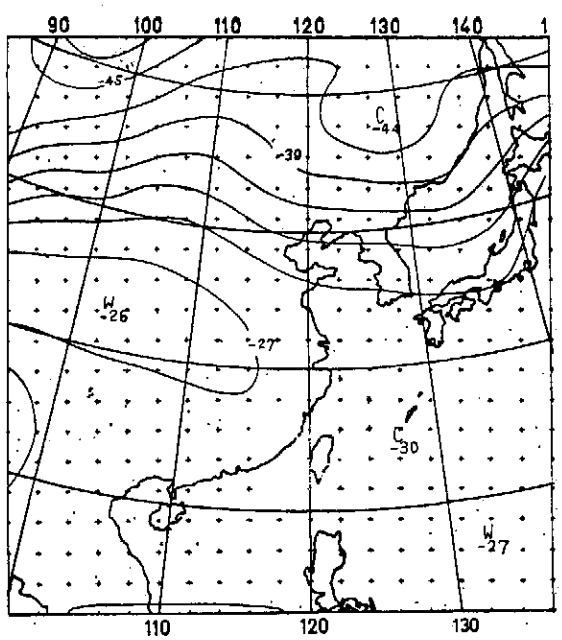

圖九 (e1)

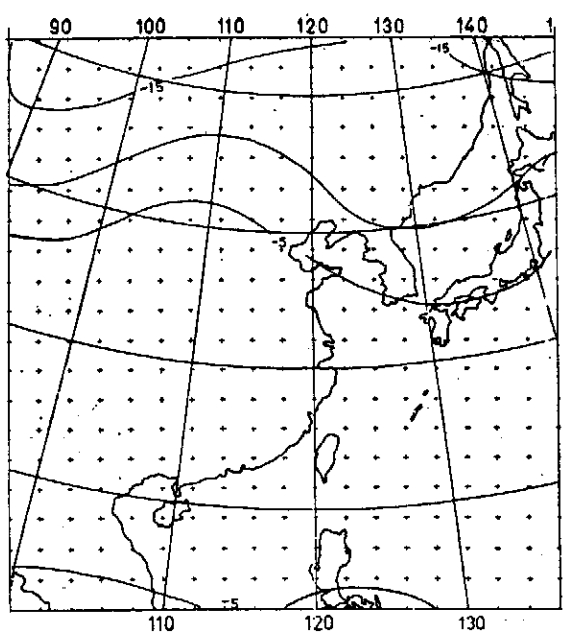

圖九 (f1)

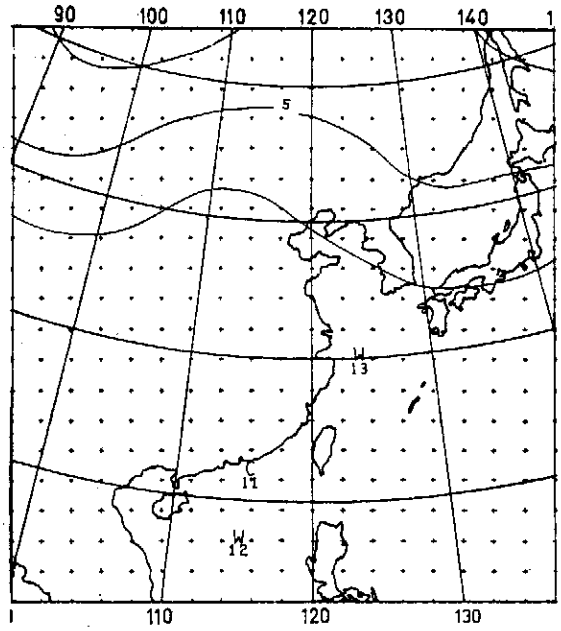

圖九 (g1)

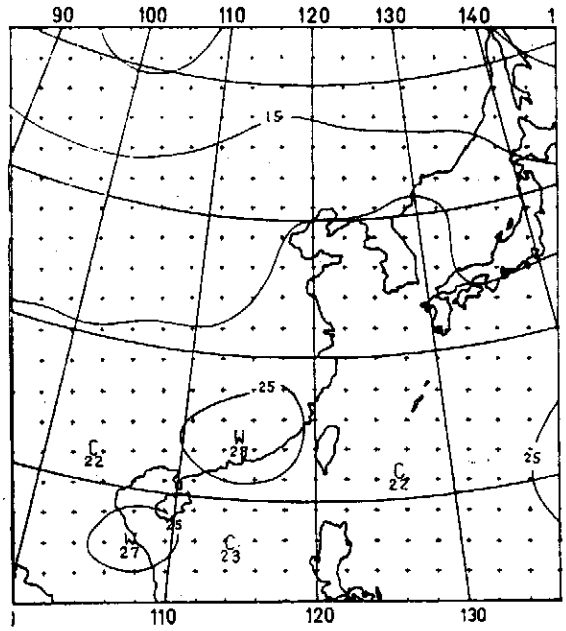

圖九 (h1)

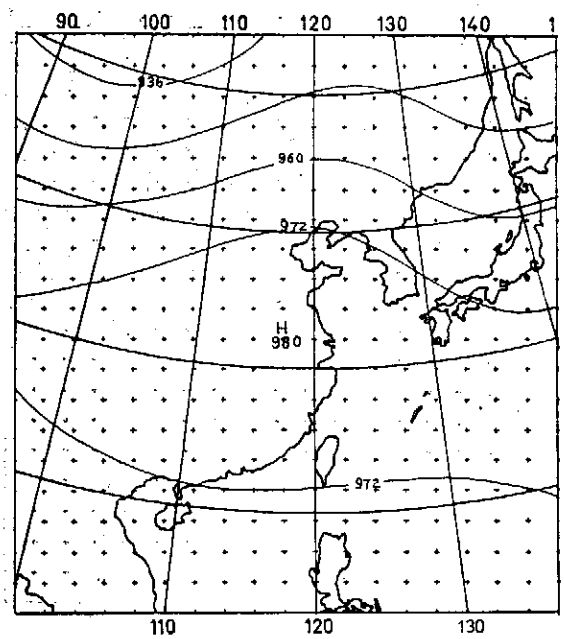

圖九 (a2)

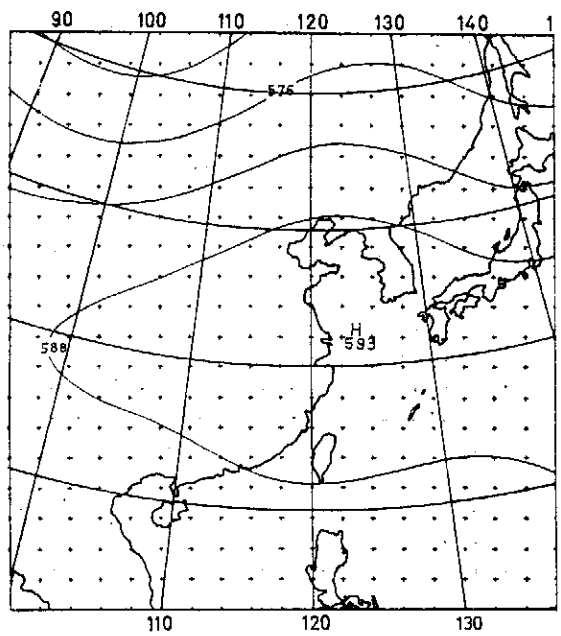

圖九 (b2)

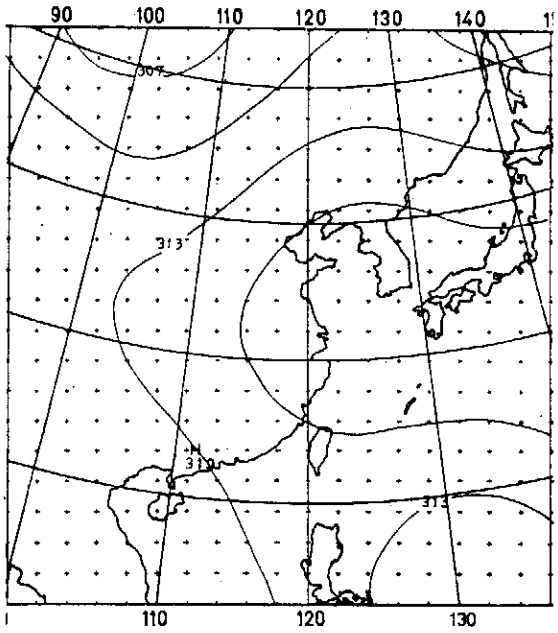

圖九（c2）

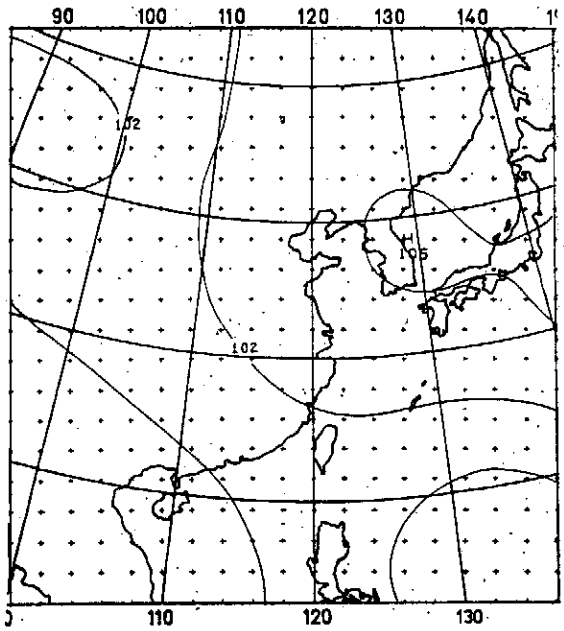

圖九（d2）

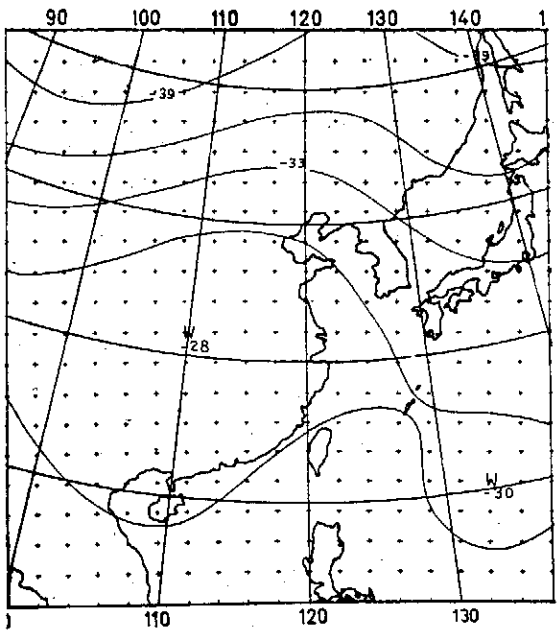

圖九（e2）

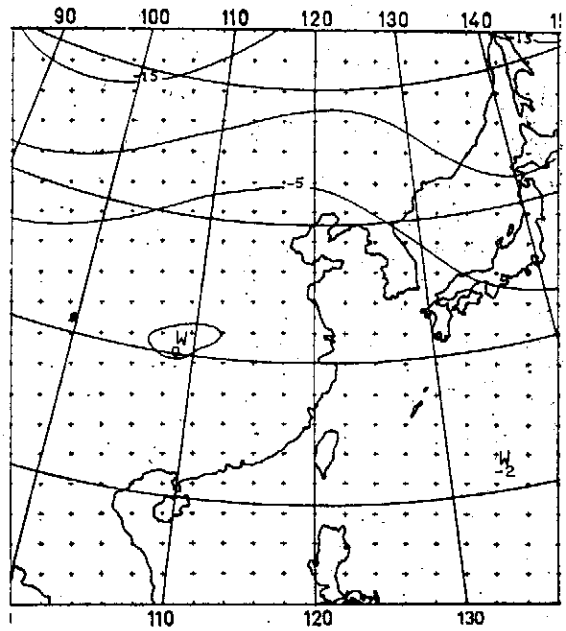

圖九（f2）

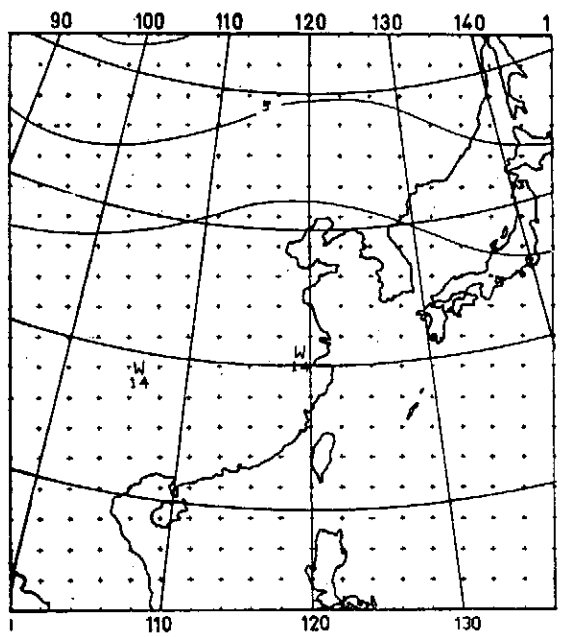

圖九 (g2)

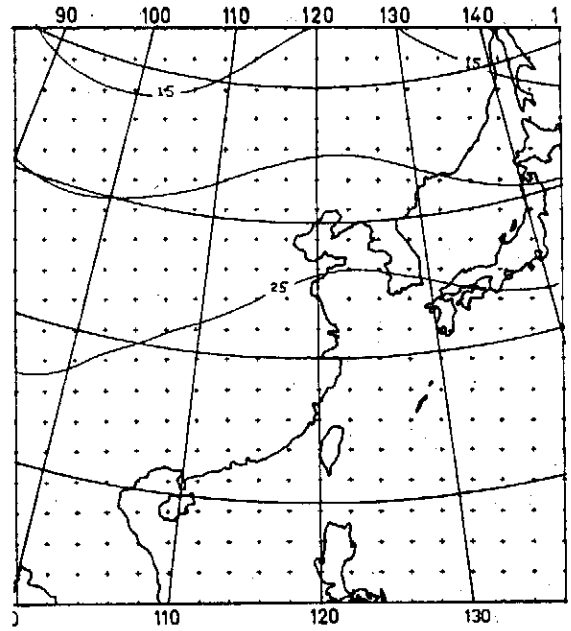

圖九 (h2)

圖十　有限區域原始方程式模式，邊界條件固定，計算 12 小時的高度場，(a) 300 mb，等值線以 120 公尺爲間隔，(b) 500 mb，等值線以 60 公尺爲間隔 (c) 700 mb，等值線有以30公尺爲間隔 (d) 900 mb，等值線以30公尺爲間隔。溫度場，等值線以 5°C 爲間隔 (e) 300 mb, (f) 500 mb, (g) 700 mb, (h) 900 mb。

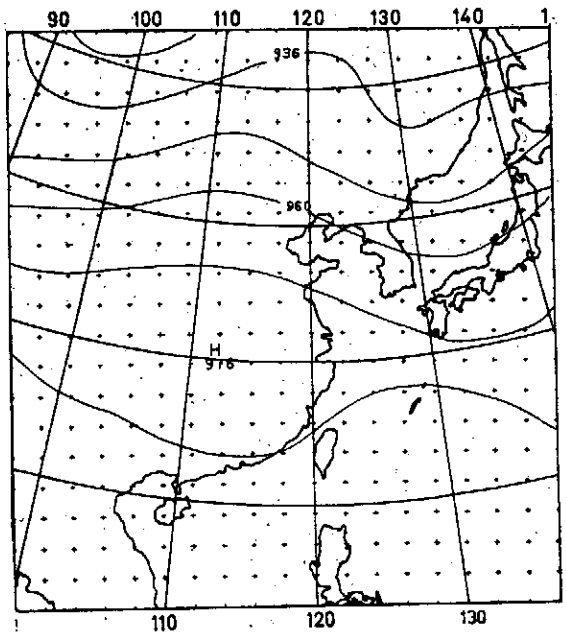

圖十 (a)

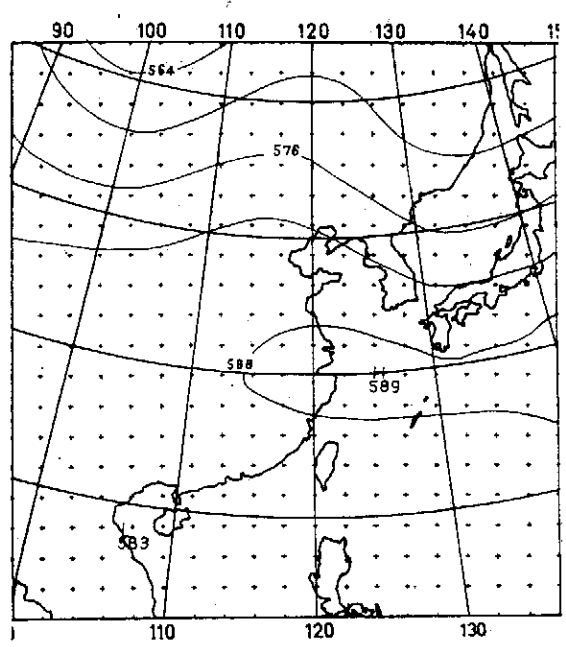

圖十 (b)

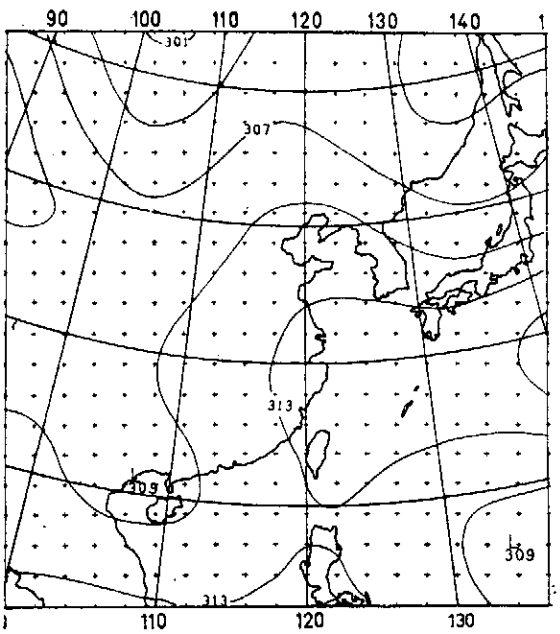

圖十 (c)

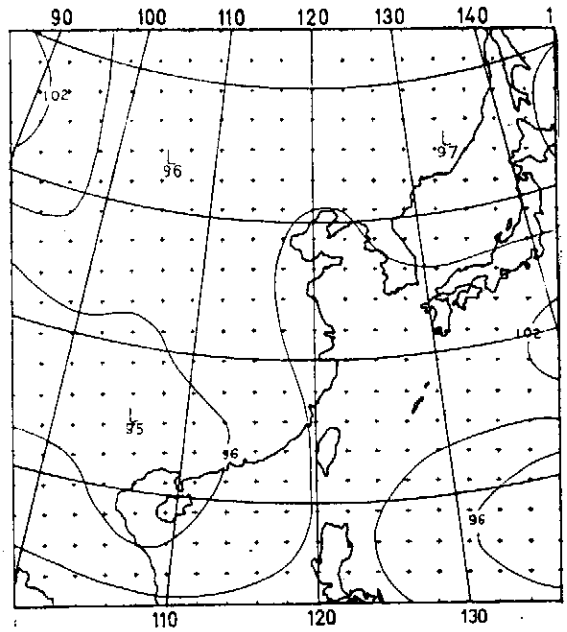

圖十 (d)

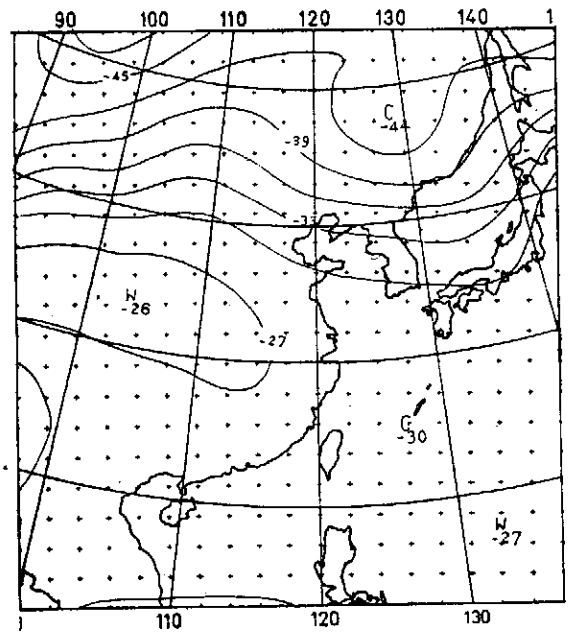

圖十 (e)

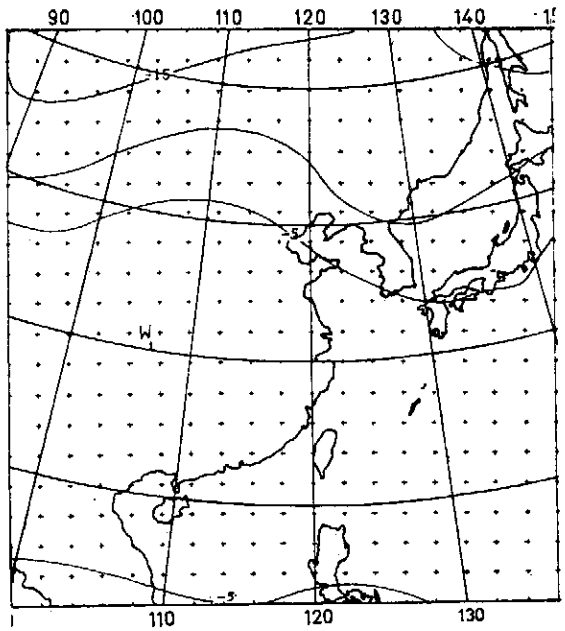

圖十 (f)

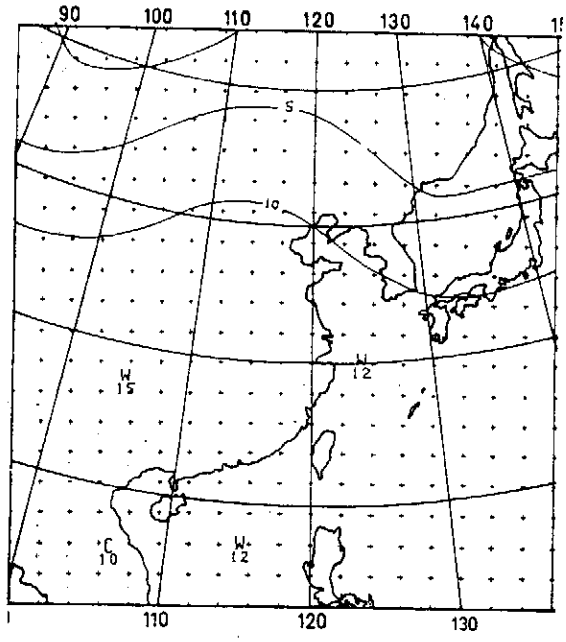

圖十 (g)

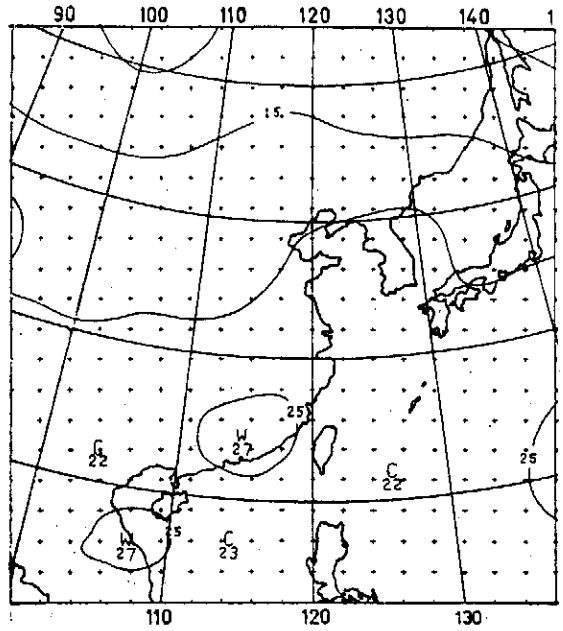

圖十 (h)

圖十一 1976年8月8日 0000 Z 北半球溫度露點差場，等值線球 5°C 爲間隔。圖中正，負號表示該處值比周圍與值線高或低。(a), (b) 中層 (原爲 333 至 666 mb 的平均值，當作600 mb 值) (c), (d) 低層 (原爲 666 至 1,000 mb 的平均值，當作 800 mb 值) ，(a), (c) 爲準地轉模式計算 24 小時的結果 (b), (d) 爲實際天氣型態。

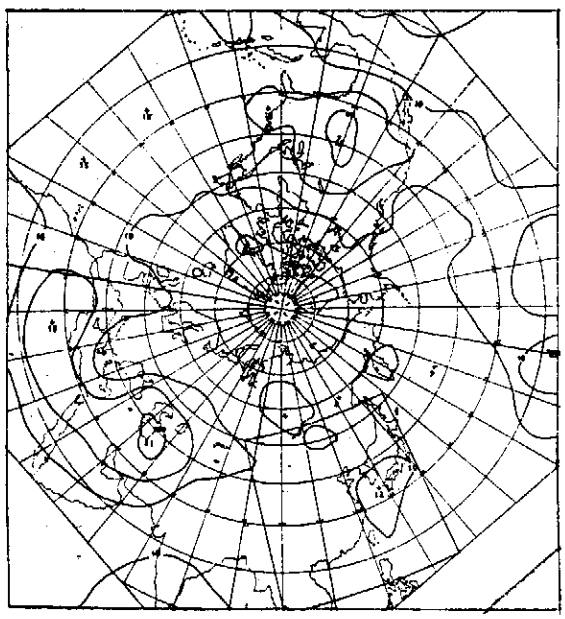

圖十一 (a)

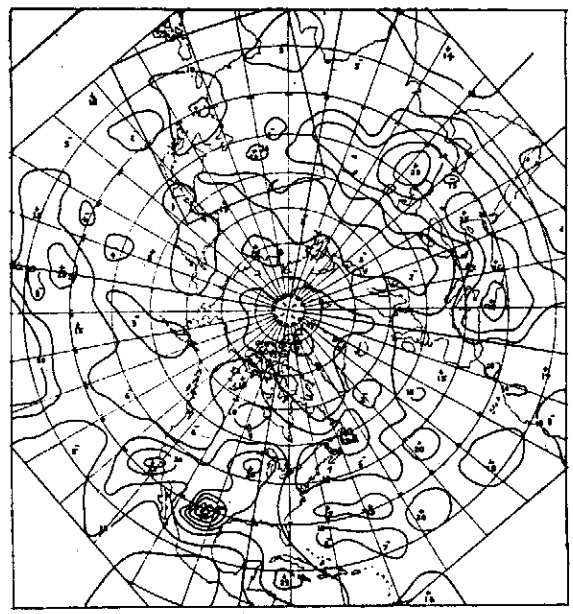

圖十一 (b)

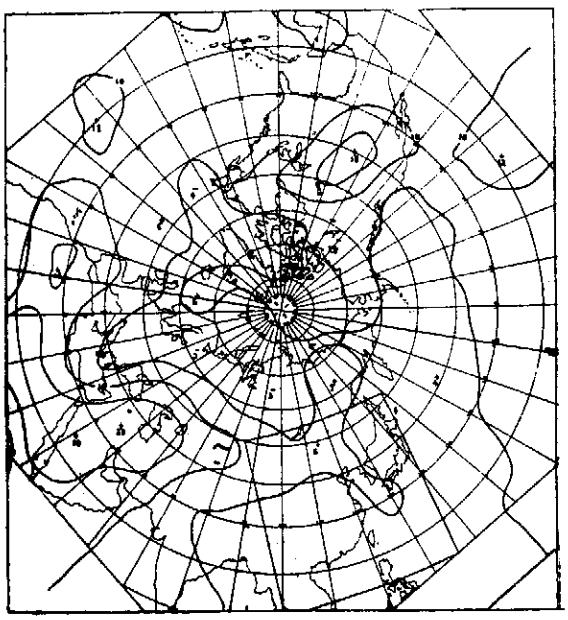

圖十一 (c)

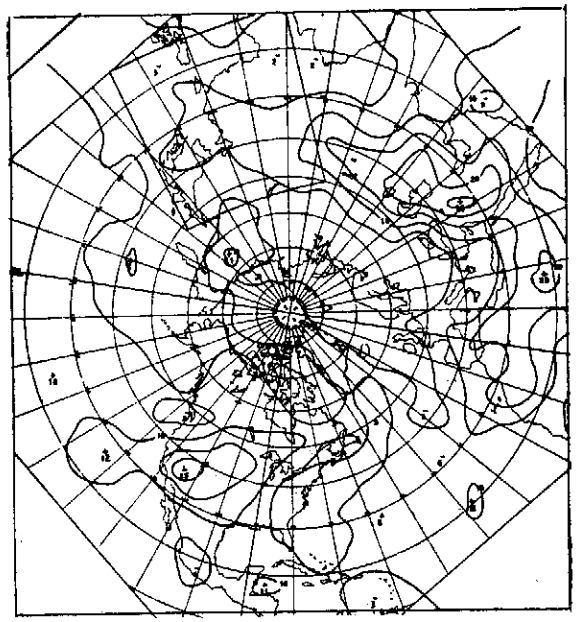

圖十一 (d)

圖十二　1976月 8 月 8 日 0000 Z 北半球高度場 (a1), (b1), (c1), (d1) 爲準地轉模式計算 24 小時的結果，(a2), (b2), (c2), (d2) 爲實際天氣型態 (a1), (a2) 300 mb ，等值線以120 公尺爲間隔，(b1), (b2) 500 mb，等值線以 60 公尺爲間隔，(c1), (c2) 700 mb，等值線以 30 公尺爲間隔，(d1), (d2) 900 mb，等值線以 30 公尺爲間隔。

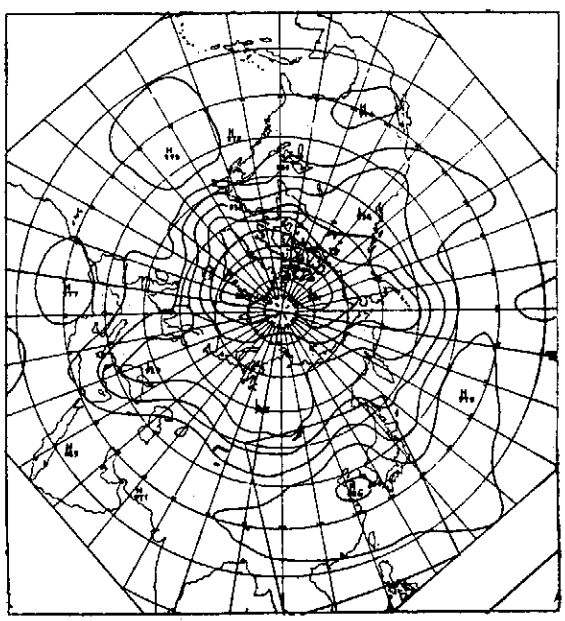

圖十二 (a1)

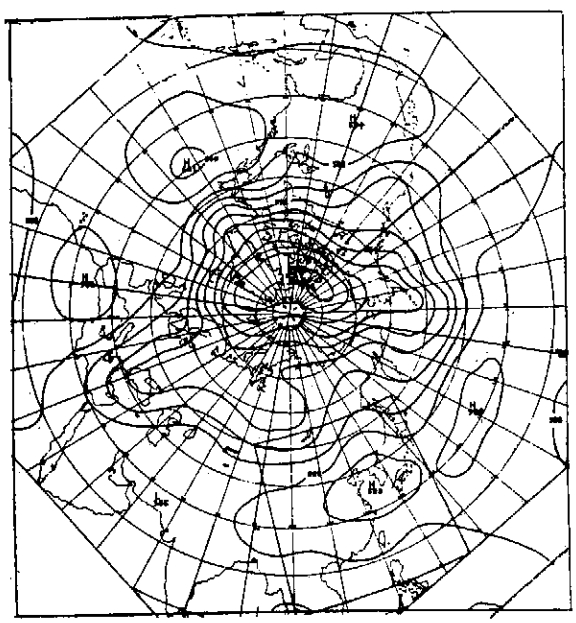

圖十二 (b1)

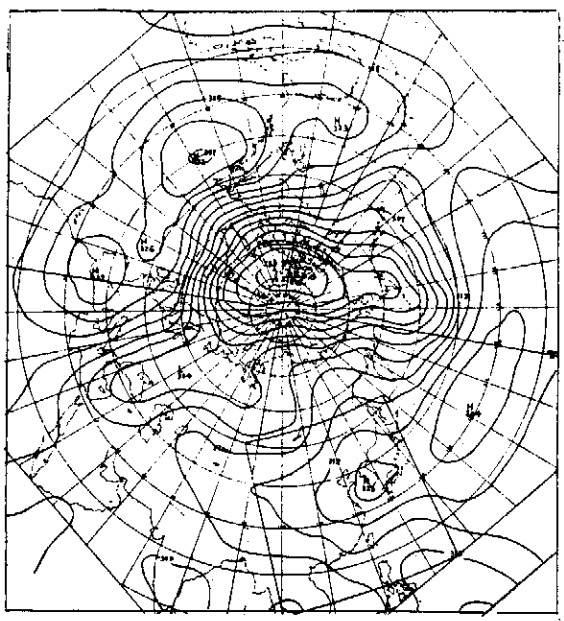

圖十二 (c1)

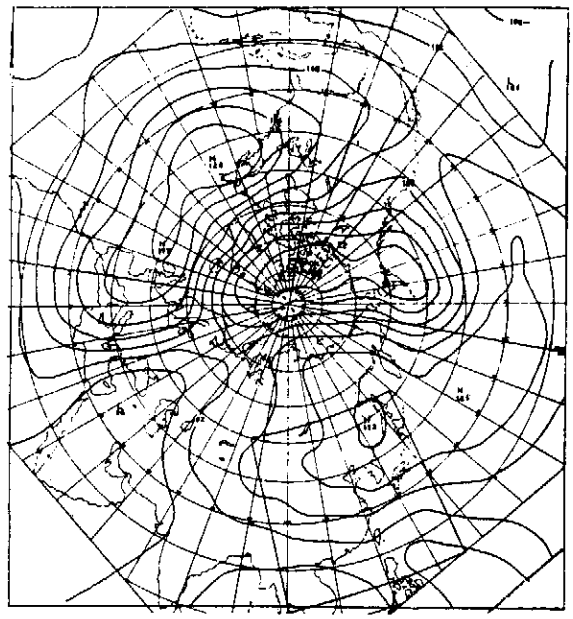

圖十二 (d1)

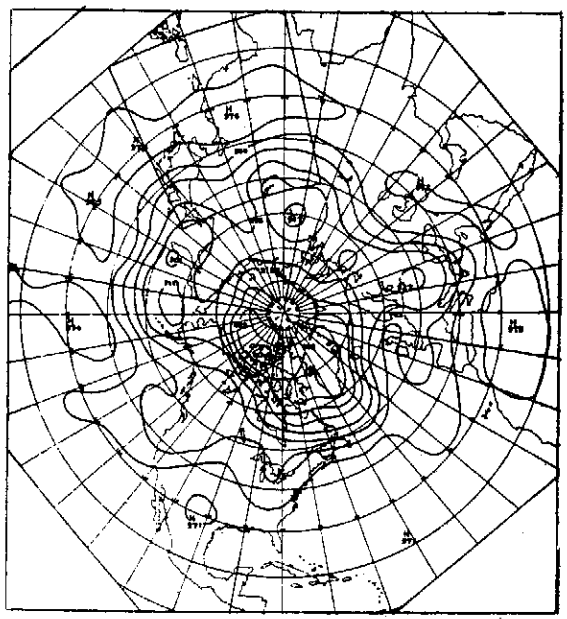

圖十二 (a2)

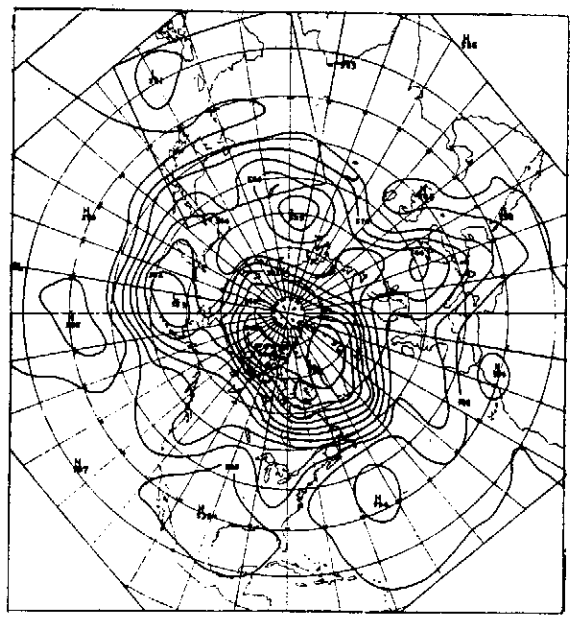

圖十二 (b2)

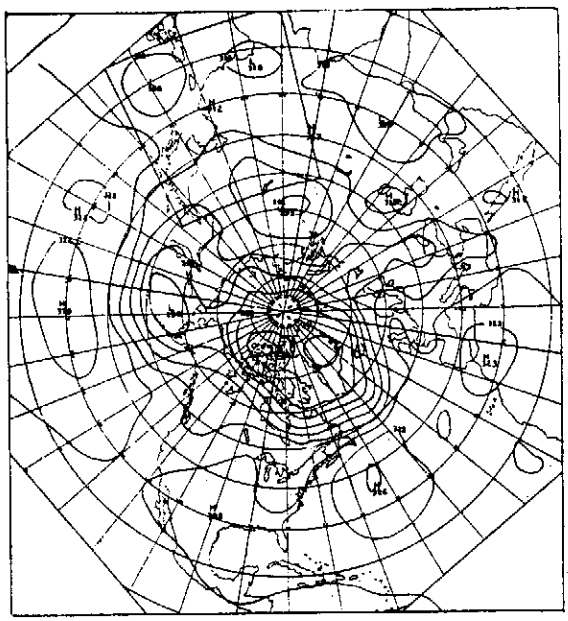

圖十二 (c2)

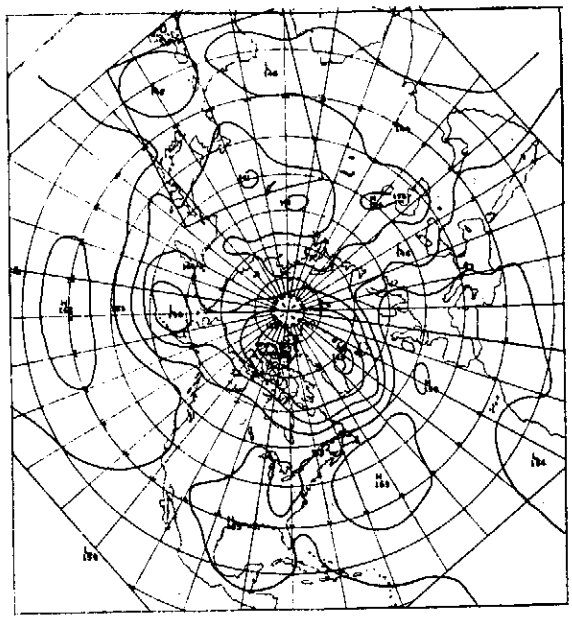

圖十二 (d2)

圖十三　1976年8月8日 0000 Z 北半球溫度場 (a1), (b1) (c1), (d1) 爲準地轉模式計算 24 小時的結果，(a2), (b2), (c2), (d2) 爲實際天氣型態。等值線以 5°C 爲間隔，(a1), (a2) 300 mb, (b1), (b2) 500 mb, (c1), (c2) 700 mb, (d1), (d2) 900 mb。

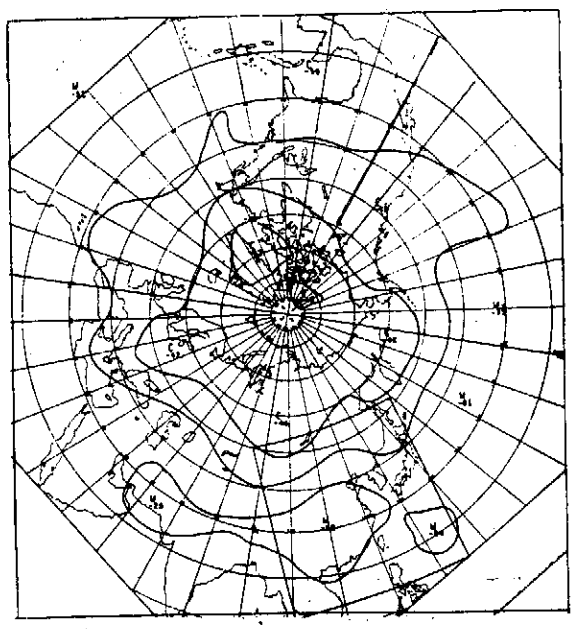

圖十三 (a1)

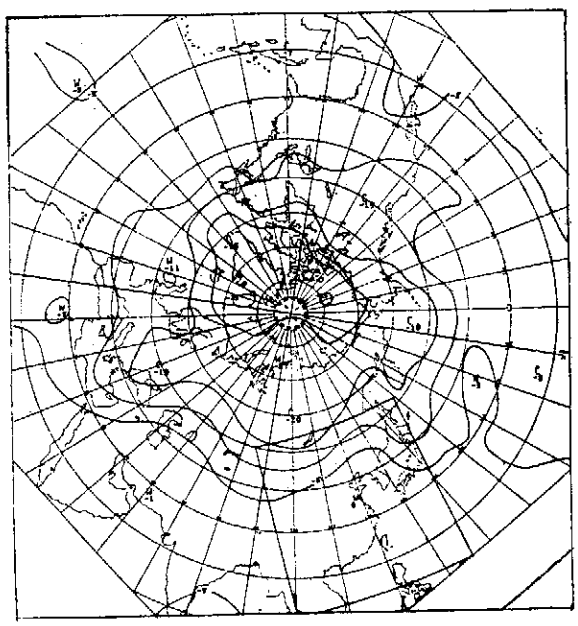

圖十三 (b1)

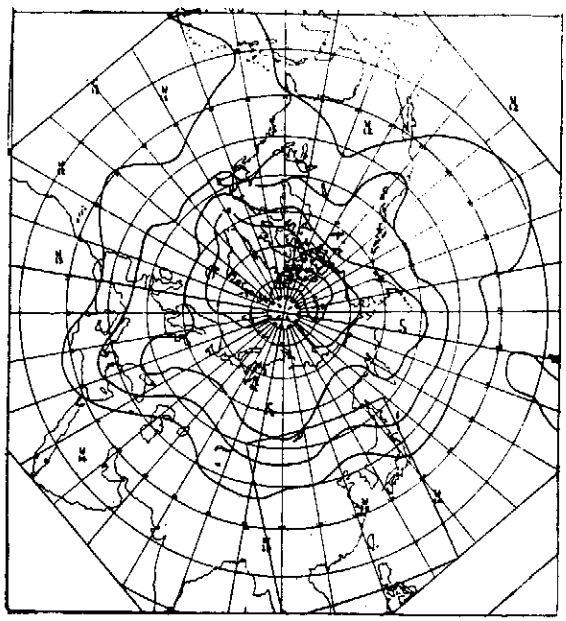

圖十三 (c1)

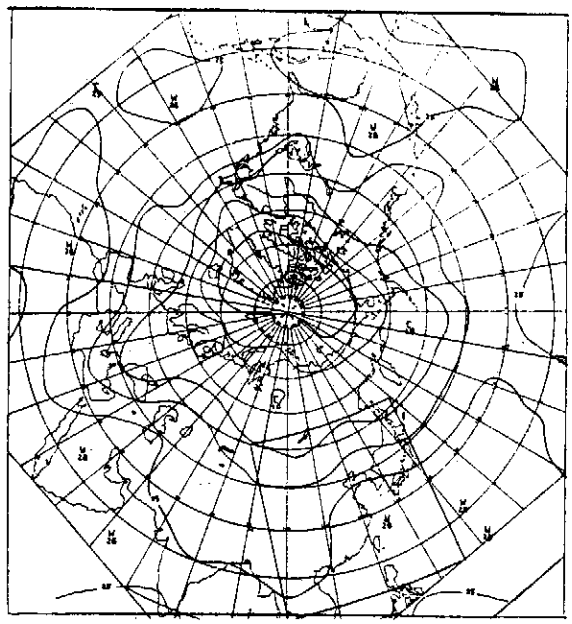

圖十三 (d1)

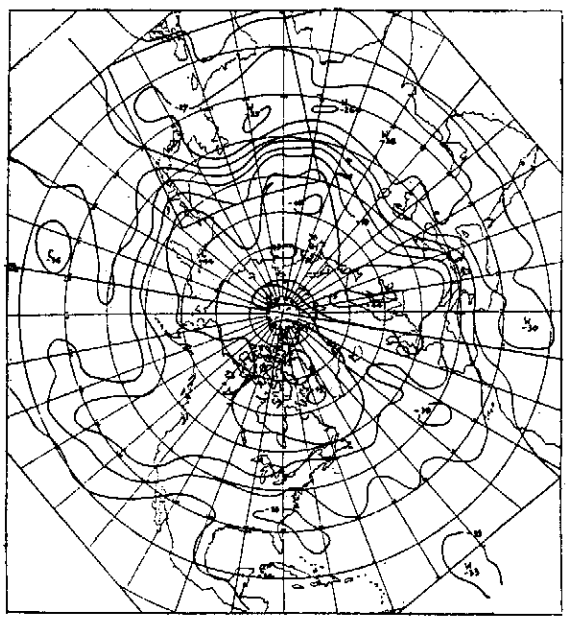

圖十三 (a1)

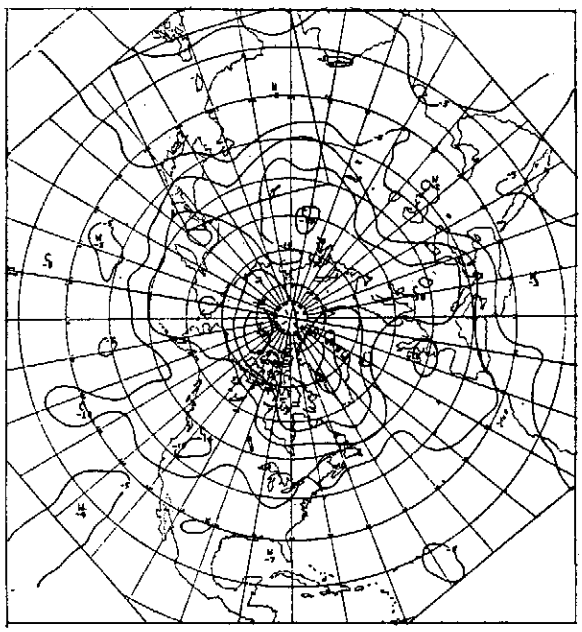

圖十三 (b2)

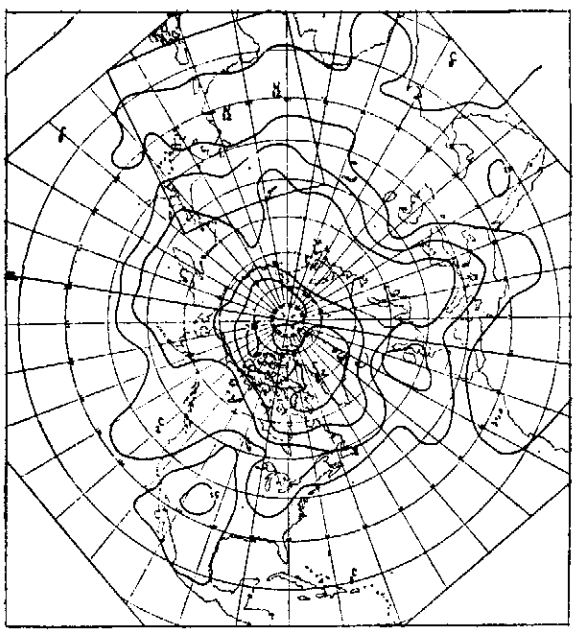

圖十三 (c2)

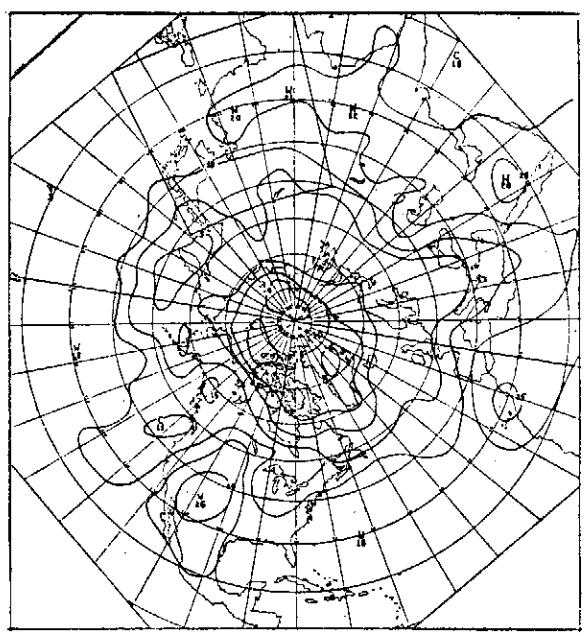

圖十三 (d2)

圖十四　有限區域原始方程式模式，每小時更新邊界值，計算 24 小時的高度場 (a1), (a2) 300 mb，等值線以 120 公尺爲間隔，(b1), (b2) 500 mb 等值線以 60 公尺爲間隔，(c1), (c2) 700 mb 等值線以 30 公尺爲間隔，(d1), (d2) 900 mb 等值線以 30 公尺爲間隔。溫度場，等值線以 5°C 爲間隔 (e1), (e2) 300 mb, (f1), (f2) 500 mb (g1), (g2) 700 mb, (h1), (h2) 900 mb, (a1)～(h1) 爲計算結果 (a2)～(h2) 爲實際天氣型態。

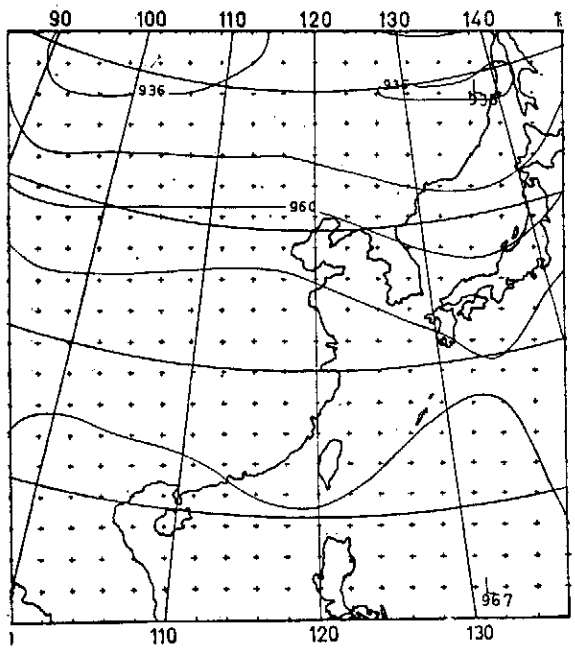

圖十四 (a1)

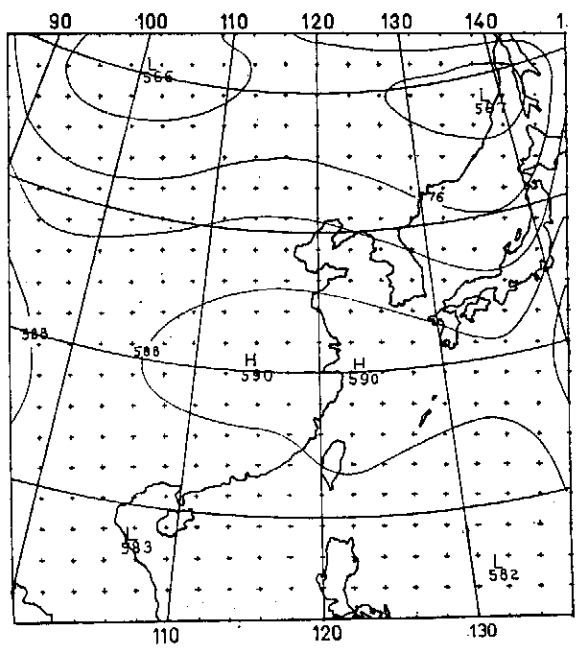

圖十四 (b1)

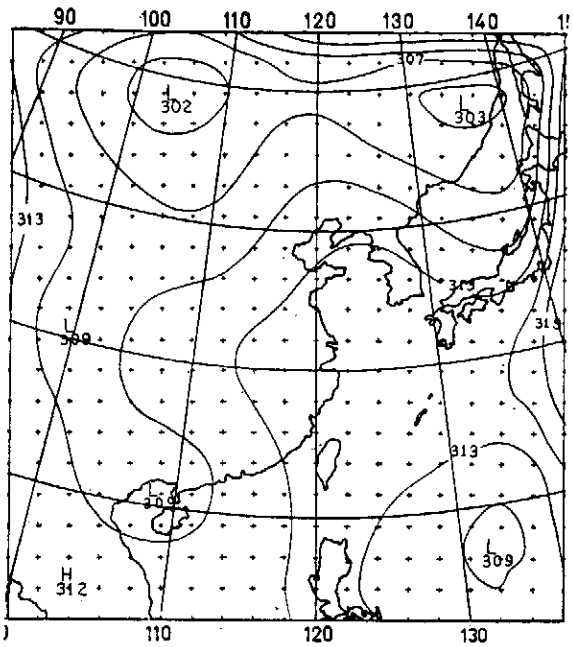

圖十四 (c1)

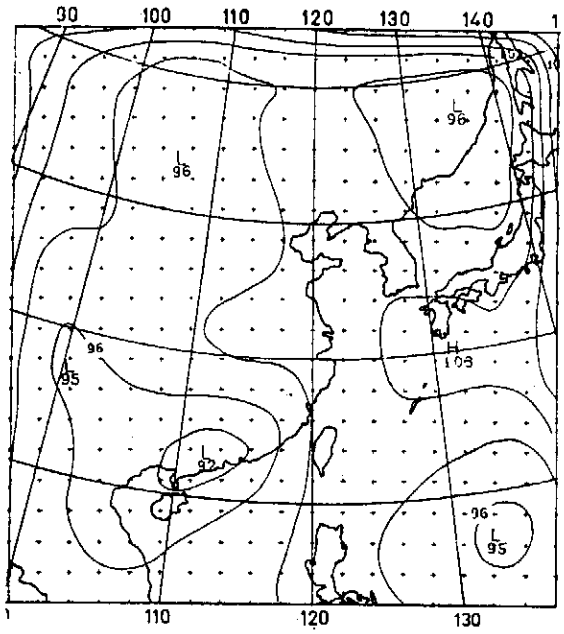

圖十四 (d1)

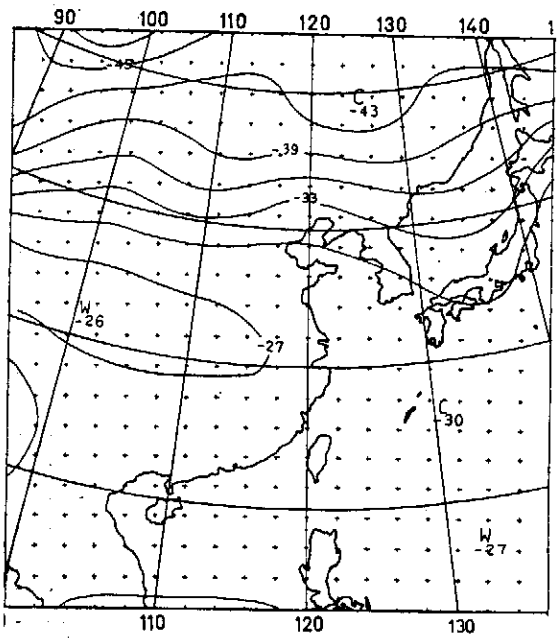

圖十四 (e1)

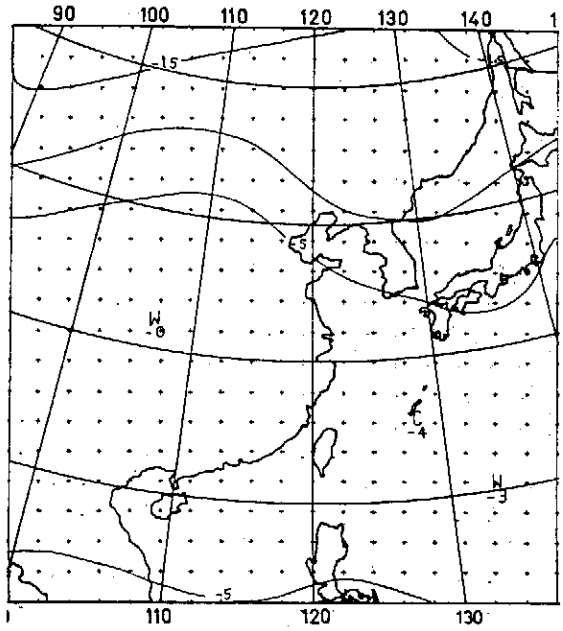

圖十四 (f1)

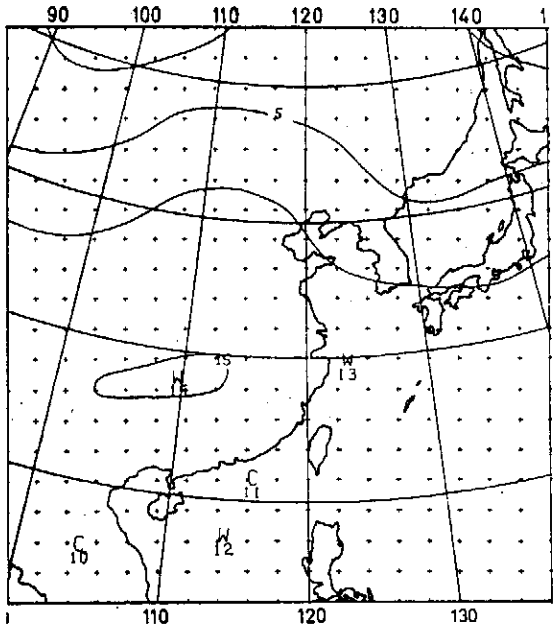

圖十四 (g1)

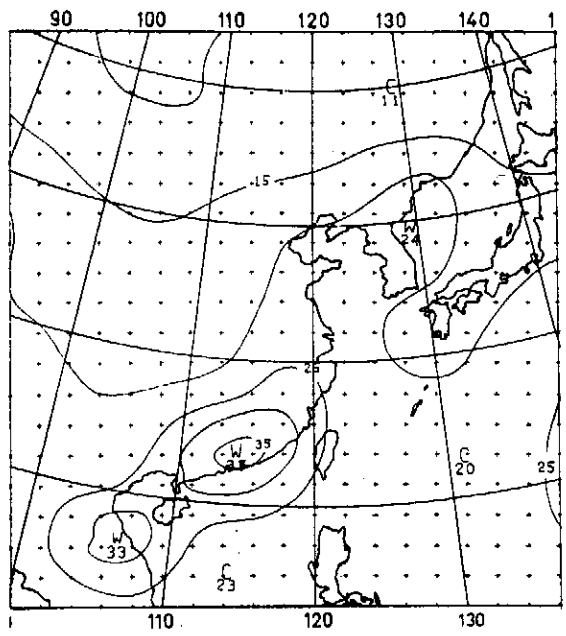

圖十四 (h1)

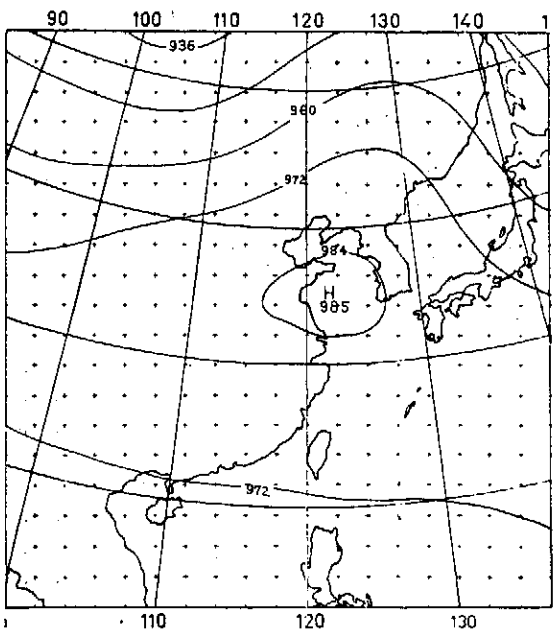

圖十四 (a2)

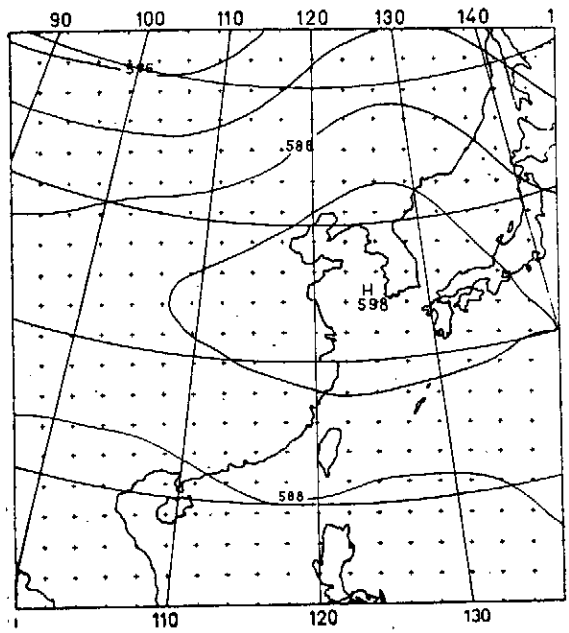

圖十四 (b2)

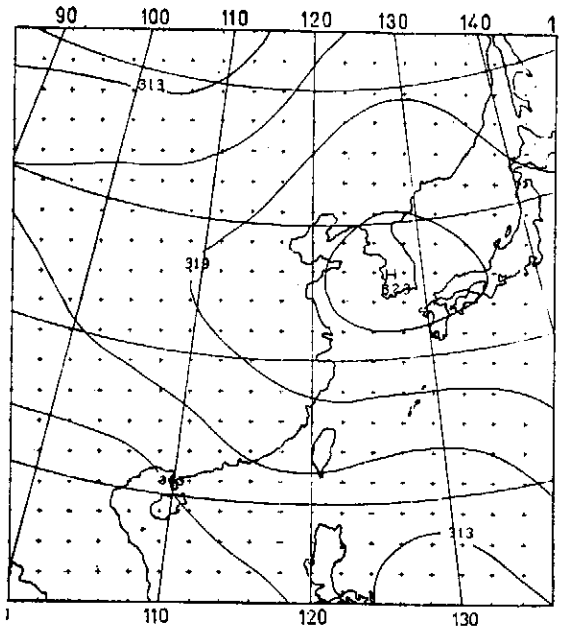

圖十四 (c2)

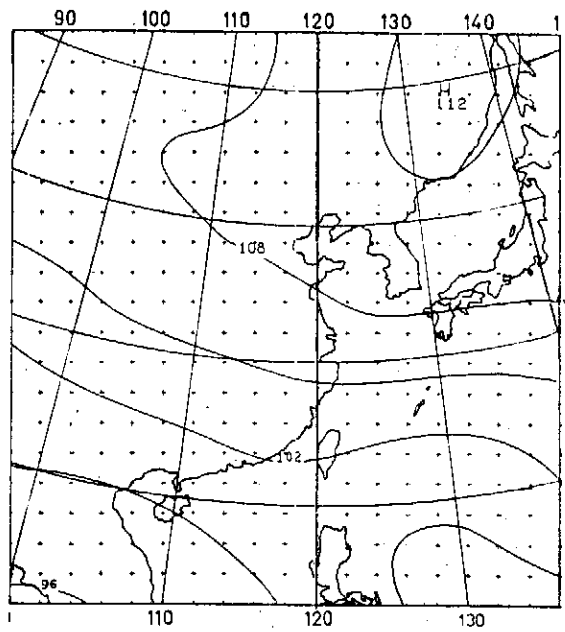

圖十四 (d2)

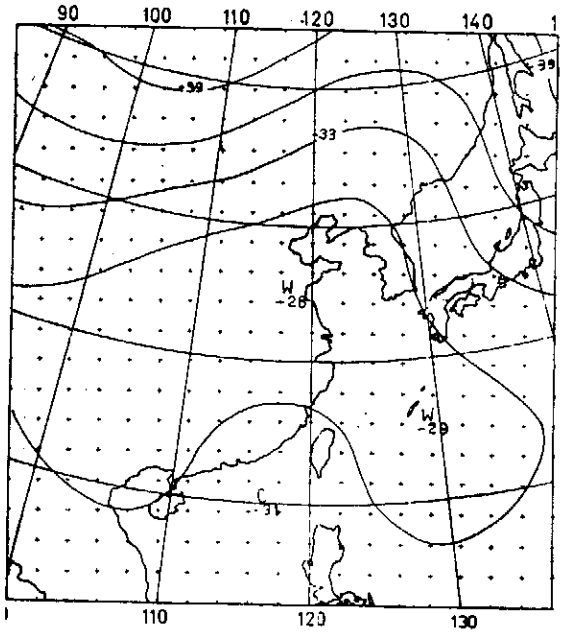

圖十四 (e2)

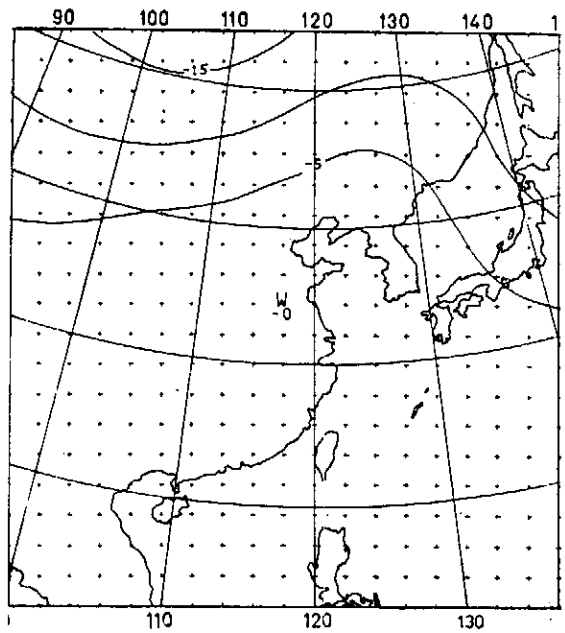

圖十四 (f2)

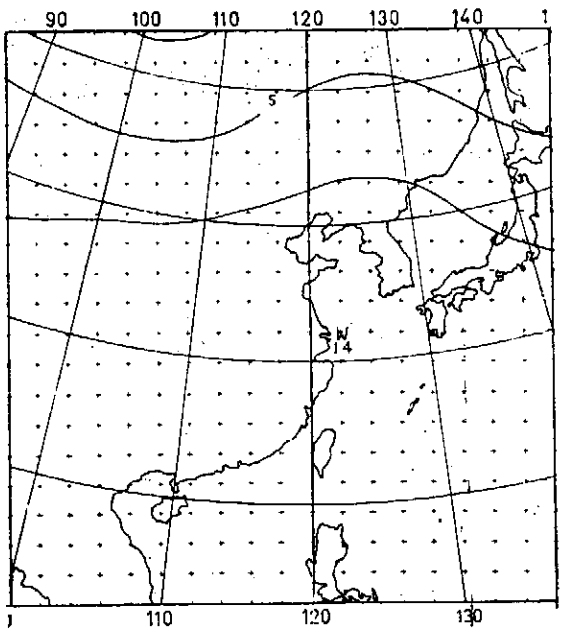

圖十四 (g2)

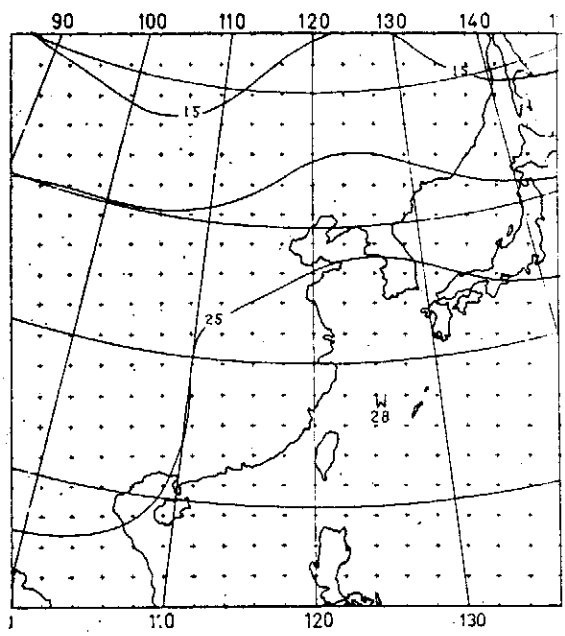

圖十四 (h2)

圖十五　有限區域原始方程式模式邊界條件固定，計算24小時的高度場 (a) 300 mb，等值線以120公尺爲間隔 (b) 500 mb，等值線以60公尺爲間隔，(c) 700 mb 等值線以300公尺爲間隔，(d) 900 mb 等值線以 30 公尺爲間隔。溫度場，等值線以 5°C 爲間隔，(e) 300 mb, (f) 500 mb, (g) 700 mb, (h) 900 mb。

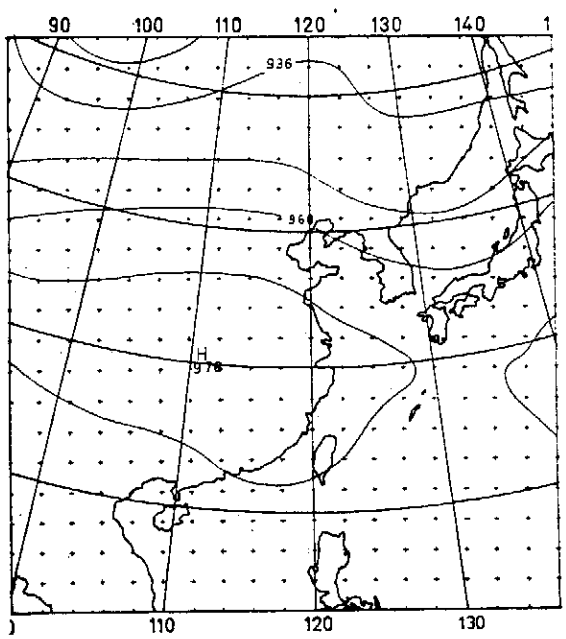

圖十五 (a)

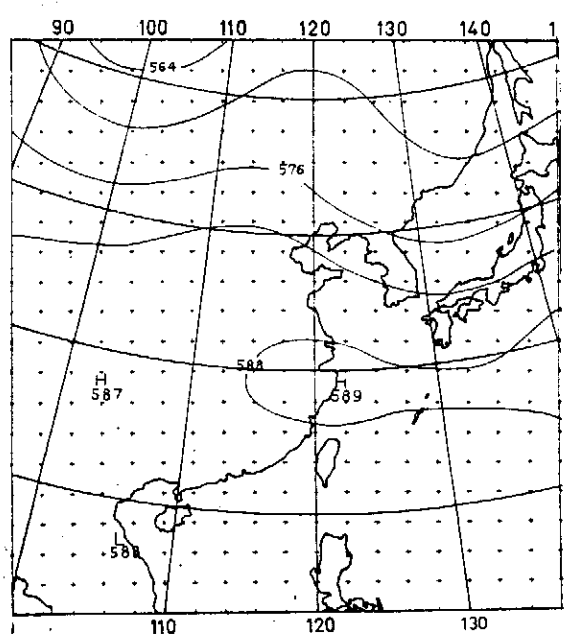

圖十五 (b)

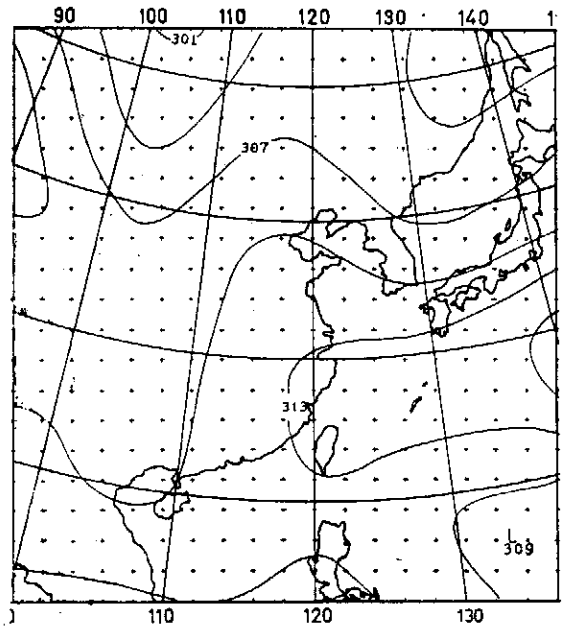

圖十五 (c)

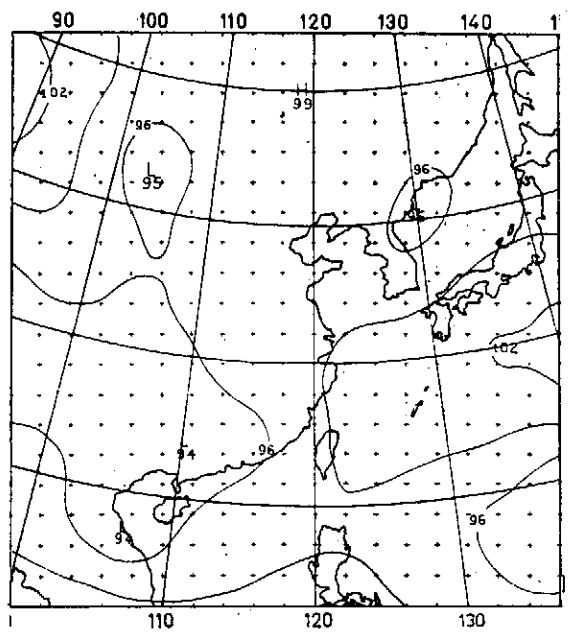

圖十五 (d)

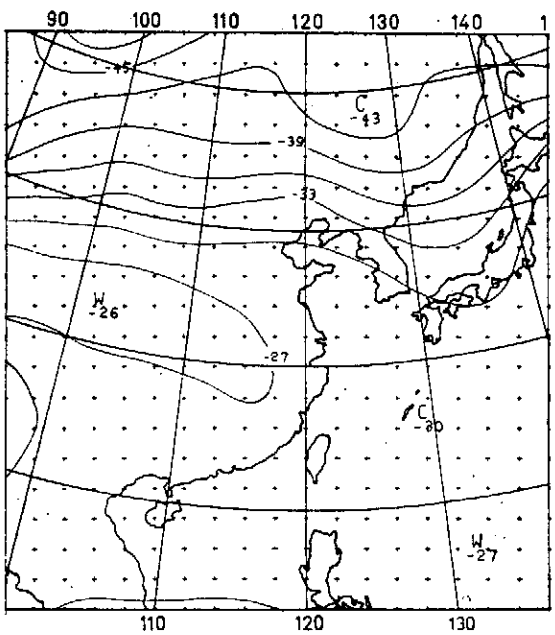

圖十五 (e)

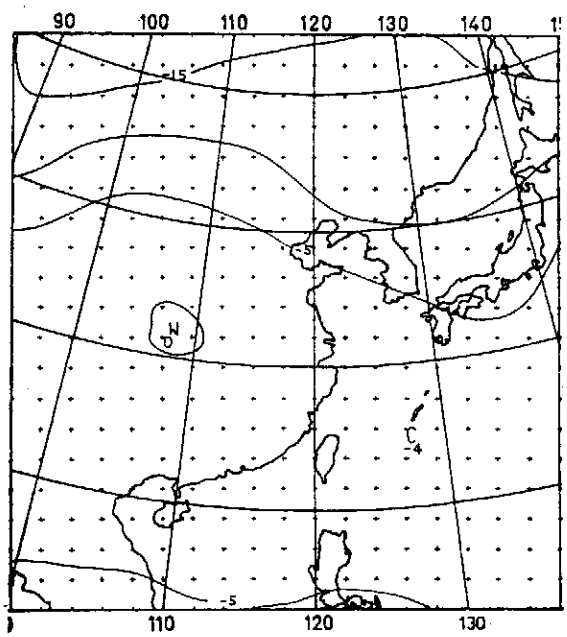

圖十五 (f)

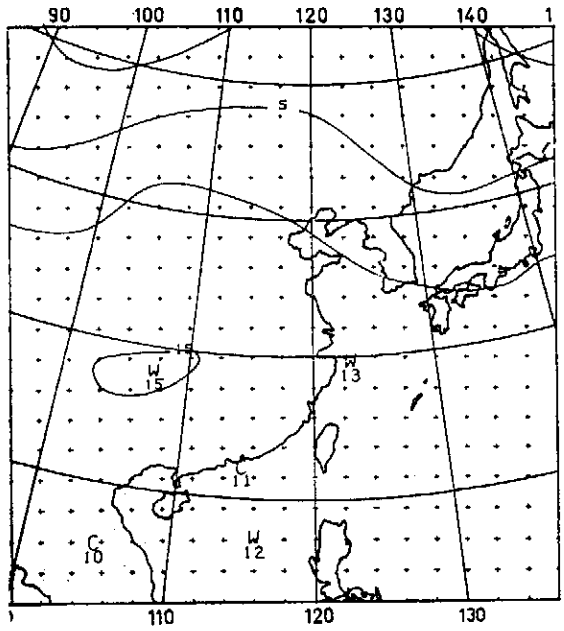
90
100
110
120
130
140
1
5
15
W
15
W
13
C
11
C
10
W
12
110
120
130

圖十五（g）

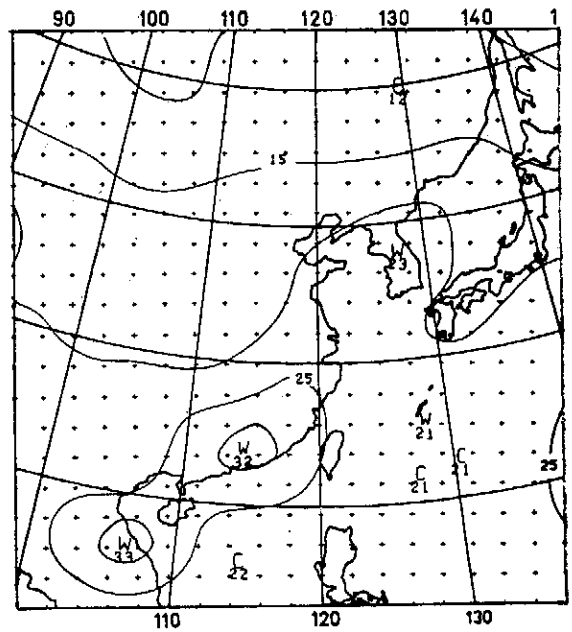
90
100
110
120
130
140
1
C
12
15
W
3
25
W
21
C
21
25
W
32
C
21
W
33
C
22
110
120
130

圖十五（h）

Annual Report of the Institute of Physics, Academia Sinica, Vol. 8, 1978

Energy Levels of ^{73}As from ^{72}Ge(p,γ) ^{73}As Reaction*

Y. C. LIU, (劉遠中), E. K. LIN, (林爾康), G. C. KIANG (江紀成) and W. S. HSU (徐雄武)
National Tsing Hua University and Academia Sinica, Hsinchu, Taiwan

Abstract

The ^{72}Ge(p,γ)^{73}As reaction has been investigated. High resolution measurements of the *de*-excitation γ-rays from this reaction have been made at E_p=2.213 MeV by using 42cm^3 Ge(Li) detector. 20 energy levels of ^{73}As up to 1947 keV excitation and γ-ray branching ratios were determined; one new level at 1399 keV excitation is proposed. The Q value of this reaction was also determind.

This paper has been published in Chinese Journal of physics Vol. 16, No. 2, 3, 1978.

A Study of the Quasi-free (α, 2α) Reaction Induced by 140 MeV Alpha Particles on ^{9}Be, ^{12}C, ^{16}O, and ^{20}Ne Targets

C. W. WANG (王建萬)
Institute of Physics Academia Sinica
Nankang, Taipei, Taiwan, R. O. C.
and
N. S. CHANT and P. G. ROOSS
Department of Physics, University of Maryland
College Park, Md. 20742 U. S. A.

Abstract

A coincidence technique was used to measure two outgoing alpha particles from the (α, 2α) reaction on ^{9}Be, ^{12}C, ^{16}O, and ^{20}Ne targets ot E_α = 140 MeV. Gas targets were used for ^{12}C(α, 2α)^{8}Be, ^{16}O(α, 2α)^{12}C, and ^{20}Ne(α, 2α)^{16}O measurements. A solid target was used for the ^{9}Be(α, 2α)^{5}He experiment. Data at twenty angle pairs were taken with special emphasis on the quasi-free angle pairs. The quasi-free knockout mechanism was found to dominate the (α, 2α) reaction at quasi-free angular sets for both alpha angles $\theta \geq 30°$ at 140 MeV for the targets under investigation.

The experimental data were analyzed with exact disorted wave impulse approximation (DWIA) calculations. The factorization of the quasi-free knockout cross section into the product of the kinematic factor and the two outgoing particles scattering cross section and the cluster distorted momentum distribution was found to be very good at the energy 140 MeV. The shapes of the experimental and calculated energy sharing spectra are in fairly satisfactory agreement with each other. The magnitudes of the distorted momentum distributions are found to be very sensitive to the cluster-core bound state radius parameter. A bound state radius parameter r_o = 2.52 fm was used for the analysis of the results for all the four target nuclei. The ground state absolute alpha spectroscopic factors extracted from the experimental data are 0.633 ± 0.120 for ^{9}Be target, 0.558 ± 0.107 for ^{12}C target, 0.244 ± 0.046 for ^{16}O target, and 0.202 ± 0.029 for ^{20}Ne target, quite consistent with the existing theoretical values. The (α, 2α) data from other groups at various energies were also analyzed with the same bound state and distorting parameters. The results are qualitatively consistent with our own results. Comparisons with other α knockout and α transfer reaction results were also made. Several possible explanations of the use of the rather large bound state radius parameter were also suggested.

Annual Report of the Institute of Physics, Academia Sinica, Vol. 8, 1978

Further Studies of the 12917 - and 12924 keV Levels in ^{28}Si*

G. C. KIANG (江記成), C. W. WANG (王建萬),
E. K. LIN (林爾康), D. WANG (王定)
and L. P. LIANG (梁靈平)

Institute of Physics, Academia Sinica and
National Tsing Hua University
Hsinchu, Taiwan

Abstract

The 12917- and 12924 keV levels in ^{28}Si have been populated by resonant proton capture at 1381- and 1388 keV in the ^{27}Al(p, γ) ^{28}Si reaction respectively. Measurements of the grmma-gamma directional correlation were carried out for the 12917 keV→1778 keV→0 and 12924 keV→1778 keV→0 cascades. The results suggest a spin-parity 2^+ assignment for the levels at 12917- and 12924 keV in ^{28}Si. The decayed gamma-rays emitted from these resonance states to the 1778 keV level of ^{28}Si were found to have admixture of E2 and M1 with the intensity mixing ratio 12% and 0.64% respectively.

* This paper has been published in Chinese Journal of physics Vol. 16, No. 1, 1978.

Is There Specific Alpha Clustering in Light Nuclei?*

N. S. CHANT, P. G. ROOS, and C. W. WANG (王建萬)

Department of Physics and Astronomy, University of Maryland, College Park, Maryland 20742

Institute of Physics, Academia Sinica, Nankang, Taipei, Taiwan

Abstract

The role of the α-core bound state wave function in direct reaction theories of α transfer and knockout reactions is discussed. It is pointed out that for $A \leq 16$, wave functions with excessive rms radii are needed in order to reproduce predicted $1p$ shell absolute spectroscopic factors. It is argued that this may indicate considerable specific α clustering in excess of $1p$ shell estimates.

* This paper has been published in Physical Review C, Vol. 17, No. 1, Jan. 1978.

Broadening of the Absorption Line of Aluminum Impurities in Silicon*

L. T. HO (何 倜 民)

Institute of Physics, Academia Sinica
Taipei, Taiwan

Abstract

The absorption spectrum of aluminm imputrities in silicon has been measured at various low temperatures for samples of various impurity concentrations. Experimental results indicate that the broadening of the absorption line can be attributed to five broadening contributions: internal strain, external strain, phonon, concentration and ionized impurity. The internal strain broadening due to dislocations, the external strain broadening due to sample mounting and the concentration broadening are all temperature independent. The temperature dependence of the phonon broadening is found in good agreement with the Barrie-Nishikawa theory. Experimental results also show that the ionized impurity broadening starts at ~55°K and depends on both temperature and concentration.

* This paper has been published in Chinese Journal of Physics Vol. 16, No. 2, 3; 87, 1978.

Drift Mobilities of Electrons and Holes in Intrinsic Semiconductors*

L. T. HO (何 倜 民) and J. S. TSAI

Institute of Physics, Academia Sinica

Abstract

The magnetoresistive effect on an intrinsic, high-resistivity semi-conductor is considered. From the relation between the resistivity and the drift mobilities of electrons and holes, the drift mabilities of both electrons and holes can be dêtermined simultaneously in a single measurement using a single sample of either conductivity type. Both p-type and n-type germanium single crystals were measured and the mobilities of electrons and holes were obtained and discussed.

* This paper has been published in "Studies and Essays in Commemoration of the Golden Jubilee of Academia Sinica" (June, 1978)

Annual Report of the Institute of Physics, Academia Sinica, Vol. 8, 1978

Determination of the Curie Temperature of Ferromagnetic Alloys Using the Deviation from Matthiessen's Rule*

YEONG DER YAO (姚 永 德)

Institute of Physics, Academia Sinica
Nankang, Taipei, Taiwan R. O. C.
and
SIGURDS ARAJS
Department of Physics
Clarkson College of Technology
Potsdam, N.Y. 13676 U. S. A.

Abstract

The Curie temperature (T_c) of a set of ferromagnetic binary alloys with different concentrations has been determined by means of the deviation from Matthiessen's rule (DMR) Specifically, from the electrical resistivity data of nickel-base nickel-titanium alloys and iron-base iron-vanadium alloys we find that the DMR exhibits an anomalous behavior at T_c from which T_c can be evaluated. The agreement with values obtained by other techniques is excellent.

* Accepted for publishing in Physica Status Solidi (b).

Magnetic Phase Transition in Nickel-Rich Nickel-Copper Alloys*+

YEONG DER YAO (姚 永 德) and J. H. TSAI**

Institute of Physics, Academia Sinica
Nankang, Taipei, Taiwan, The Republic of China

Abstract

The electrical resistivity, ρ, of a set of nickel-copper alloys has been sttudied between 300 °K and 700 °K. Our data show that each of the ρ vs. T curves exhibits a well-defined knee in the critical region of the magnetic phase transition, besides, the temperature dependent part of the electrical resistivity follows a $T^{1.74\pm0.05}$ variation in the ferromagnetic region and increases more slowly than T in the paramagnetic region. The concentration dependence of the Curie temperature of the Curie temperature of these Ni-Cu alloys has been determined from ($d\rho/dT$) vs. It is demonstrated that the $d\rho/dT$ method and the kink-point method give identical results.

* Work supported in part by the National Science Council, Republic of China.
** Institute of Physics, Fu Jen University, Taipei.
+ Accepted for publishing in Chinese Journal of Physics.

Determination of Curie Temperatures of Iron-Vanadium Alloys by the Deviation from Matthiessen's Rule

YEONG DER YAO (姚永德)

Institute of Physics, Academia Sinica

Abstract

A new concept is developed that is to determin Curie temperatures of iron-vanadium alloys by the deviation from Matthiessen's rule.

* Published in Studies & Essays in Commenoration of the Golden Jubilee of Academia Sinica (1978).

Fabrication of Interdigital Transducer and Surface Acoustic Wave Delay Lines Using Simple Mask Printers*

KUNG-YANG LIAO (廖寇仰), LAN-CHAN CHU (朱良蘸), CHY-PWU TZOU (鄒治璞), N. T. LIANG (梁乃崇), C. S. LAI (賴忠信), SHOU-YIH WANG (王守益), DAH-MIN HWANG (黃大民), and T. T. CHEN (陳 通)

Department of Physics, National Tsing Hua University
Hsinchu, Taiwan

(Received November 7, 1977)

Abstract

A simple, economic and efficient type of mask printer for micro-planar structure fabrications has been designed and made. Interdigital transducers and surface acoustic wave delay lines have been fabricated using this type of mask printers. Features of the delay line with two transducers each of 15 finger pairs were found excellent which include delay time 5.0 microseconds, frequency response bandwidth 4.5 MHz at center frequency 68 MHz, insertion loss 15 db and attenuation of surface acoustical wave 0.17 db/cm. The laser optical probing technique was used to measure the energy distribution profiles of surface acoustic waves.

* This paper has been published in Chinese Journal Physica, Vol. 15, No. 4, Winter, 1977, p. 273-278.

Annual Report of the Institute of Physics, Academia Sinica, Vol. 8, 1978

Artificial Upwelling Induced by Ocean Currents —Theory and Experiment*

NAI KUANG LIANG

Institute of Oceanography, National Taiwan Univesity, Taipei, Taiwan, Republic of China

and

N. T. LIANG (梁乃崇)

Institute of Physics, Academia Sinica, Nankang, Taipei, Taiwan, Republic of China

Abstract

A submerged apparatus, which consists of a buoy, several horizontal contraction and expansion tubes (Venturi-type tubes) and a long pipe, is expected to be used to pump the sub-surface sea-water (200-300 meter depth) containing abundant nutrients to surface layer (50-100 m) by the dynamic of ocean currents. i.e. an artificial upwelling without energy cost. A preliminary experiment and analysis are undertaken and shows that the capacity of pumping the nutrient-rich sea-water is worth to build a pilot prototype model.

* This paper has been published in Ocean Engry. Vol. 5, pp. 83-94. Pergamon Press 1978. Printed in Great Britain.

Percolation and Areal Electrical Conductance in an Ultra Thin Bismuth Film*

SHOU-YIH WANG (王守益) N. T. LIANG (梁乃崇)
and YUFH SHAN (單 越)

Department of Physics, National Tsing Hua University, Hsinchu, Taiwan

Abstract

Percolation models have been briefly discussed. The two dimensional continum percolation model was applied to the analysis of the areal electrical conductance as well as the bulky electrical conductivity of an ultra-thin bismuth film. The results of the normalized areal electrical conductance against the area fraction covered by islands on the substrate have been found to behave much smoother and reasonable in the slope and curvature than those based on the corresponding bulky conductivity, indicationg again that the system be a two-dimensional film.

* This paper has been published in Chinese Journal of Physics, Vol. 15, No. 4 winter, 1977, P. 243.—248.

Annual Report of the Institute of Physics, Academia Sinica, Vol. 8, 1978

海浪發電技術簡介*

梁 乃 崇

中央研究院物理研究所

摘 要

太陽能產生風，風又製造海浪，就其根源，海浪能除重力能（潮汐）外也是太陽能的另一種形式，據 Isaacs 和 Seymour (1973) 估計全世界海岸線的海浪能源有 2.5×10^{12} 瓦，此能源約等於預估公元 2000 年全球所需能源的十分之一。再者，當海浪的能量被吸收時，海浪自然減弱，此時風又會製造新的海浪以補充之，因爲海浪的效率原本很抵，海浪弱時，其效率相對提高之故，因此供採收的海浪能量可以增加很多，Isaac (1976) 認爲有增加一百倍的潛力，果如此，則全世界的能源有希望完全取之於海浪。臺灣東部沿海的海浪能源約有 1.25×10^{10}瓦 (註一)，佔全世界海浪能源的千分之五，如果百分之二十用於發電，即得 2.5×10^{6} 瓦的電力，足够臺灣東部使用。以海浪能源可望增加十倍計，即達2.5×10^{7} 瓦的電力，是目前臺灣總電力的四倍，由此可知，臺灣海浪能源非常豐富，使吾人不得不對它加以注意。

* 本文已發表於「科學與技術」，第二卷第二期，第二十八頁，民國 67 年 7 月 6 日

Electronic Conductance and Percolation Theory in an Ultra-thin Bi Film*

SHOU-YIH WANG (王守益), N. T. LIANG (梁乃崇)** and YUEH SHAN

Department of Physics, National Tsing Hua University
Hsinchu, Taiwnn, Republic of China

Abstract

The resistivity of an ultra-thin Bi film was observed and reanalyzed. General percolation theory has been briefly reviewed, emphasizing specially the two-dimensional continuum percolation model. It has been found that electrical conductance is more appropriate than electrical conductivity in describing two-dimensional percolative conduction. The critical exponents for fixing number of nuclei Nn and fixing radius of nuclei γ_n were found 1.15 and 1.19 respectively. These and other results, such as critical area fraction x_c=0.67, were found very interesting and compatible with the 2D continuum model of percolation.

* This paper has been published in Chinese Journal of Physics, Vol. 15, No. 2, 1977.

Annual Report of the Institute of Physics, Academia Sinica, Vol. 8, 1978

Gross Vision of a World Enhances the Perceptibility of Its Component Letters a Model*

CHUN CHIANG (蔣 忻 儒)

Institute Physics, Academia Sinica, Nankang, Taipei, Taiwan. The Republic of China

Abstract

A quantitative model is proposed to explain the order of accuracy for recognizing letters in meaningful words and non-related words. The model is based on the principle that minimum features required for recognition of the whole pattern is equal to or less than the total features required for its components patterns, and the principle that the features extracted in vision are related to the feature density and the field of attention. The condition required for the result of Johnston and McClelland is given.

* This paper has been Published in Vision Research 18, 1599 (1978)

Cybernetic Elucidation of the Nerve Action Potential*

CHUN CHIANG (蔣 忻 儒)

Institute of Physics, Academia Sinica Nankang, Taipei, Taiwan, The Republic of China

Abstract

Using a cybernetic approach, the mechanism of nerve action potential is expressed in a closed loop block diagram. In this diagram, the increasing of Sodium current is governed by thd applied voltage, the Sodium diffusional force, the dipole barrier force in the membrane, and the drag force of the Sodium ions; similarly, the increasing of Potassing current is governed by the applied voltage, the Potassium diffusional force, the dipole barrier force in the membrane and the drag force of the Potassium ions. The difference of Sodium current and Potassium current across the membrane further influences the membrane voltage, thus forms a closed loop. Mathematical equations involved in these processes are dervied and the voltage (action potential) can be solved to be

$$V = a_0 + a_1 e^{-\alpha_1 t} + a_2 e^{-\alpha_2 t} \sin(\omega t + \theta) + a_3 e^{-\alpha_3 t} + a_4 e^{-\alpha_4 t}$$

where $a_0 \ldots a_4$, α_1, α_2, λ_1, λ_2, ω and θ are constant and can be determined by the initial and boundary conditions. With proper value, it can be seen that this equation fits with the experimental data of action potential very well. Particular interesting in this equation is that is predicts the oscillating after potential.

* This paper has been Published in "Current Topics in Cybernetics Fd.: J. Ross

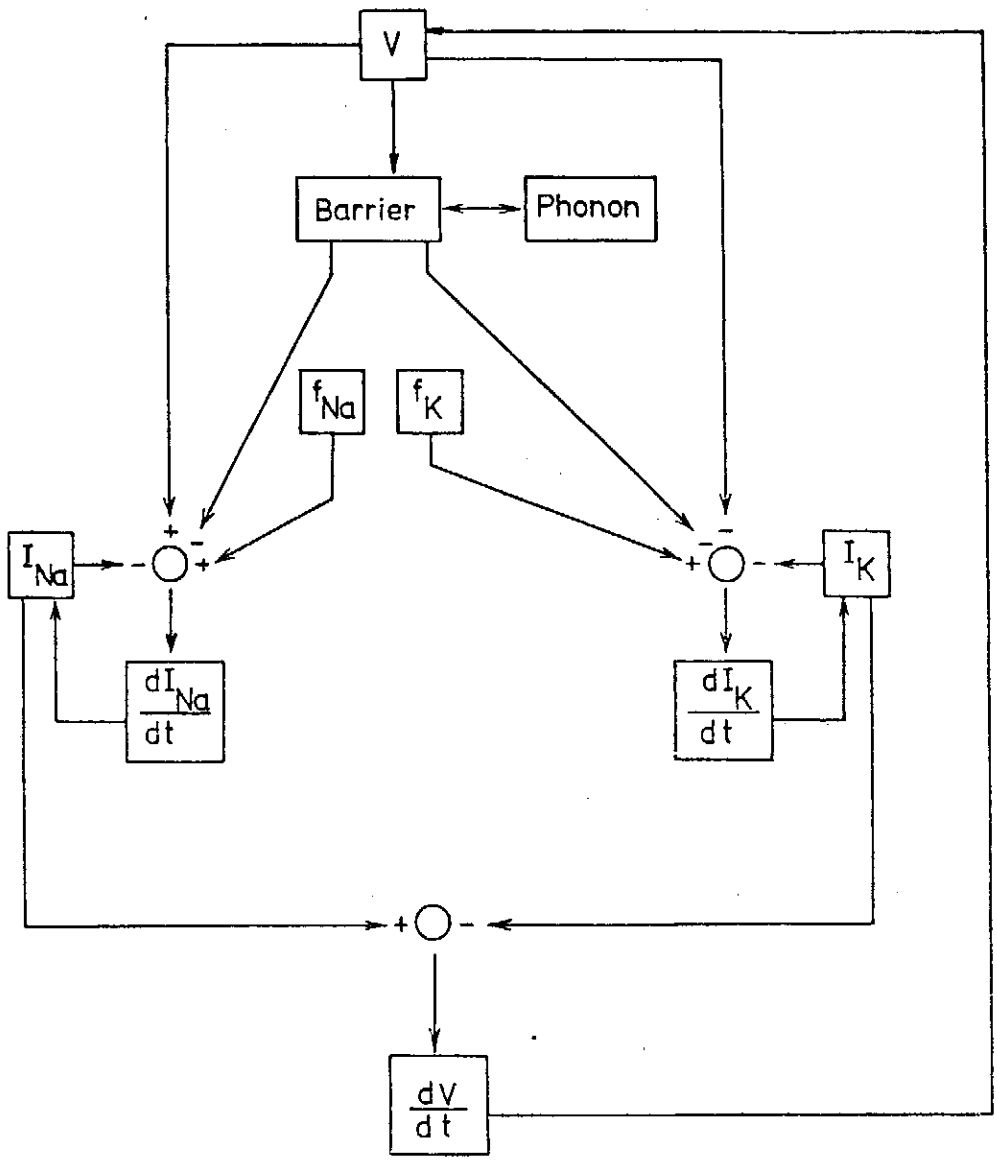

A block diagram showing the mutual dynamic influences of various factors.

Annual Report of the Institute of Physics, Academia Sinica, Vol. 8, 1978

Feedback Loop on LRH Release*

W. C-M WAN, W. K. WANG (王惟工) and N. C. TING

Inst of Zoology and Inst of Physics, Acad. Sin. Taipei and Dept of Biology, Tung Hai Univ. Taichung, R. O. C.

Abstract

Female rats were injected with L-dopa (10^{-4}M) at the day of proestrus through carotid artery. Five, 10, 20, 30 and 60 min following the injection, hypothalamus (Ht) were dissected for LRH measurement by RIA. The content of LRH-Ht falls to 30-50% of saline controls. Ht blocks were incubated with ^{14}C-tyrosine, LRH with or without nalophine (nal) in a specially designed device (1). The rate of $^{14}CO_2$ release were measured. It is stimulated by the present of LRH and inhibited by nal. This indicates the effect of LRH is same as that of morphine. It appears that dopa which converted into dopamine (DA) enhanced the release of LRH. While LRH inhibited the release of DA by a similar mechanism of morphine. A possible feedback loop exists between LRH and Ht catecholamine (Figures+: stimulation; −: inhibition; BK: blockage; OR: opiate receptor; GTH: Gonadotrophin; BBB: blood brain barrier; Dotted line: possible separation of DA and LRH Terminals). (1) Wang and Chiang: Bull Inst Zool, Academia Sinica 16: 131, 1977.

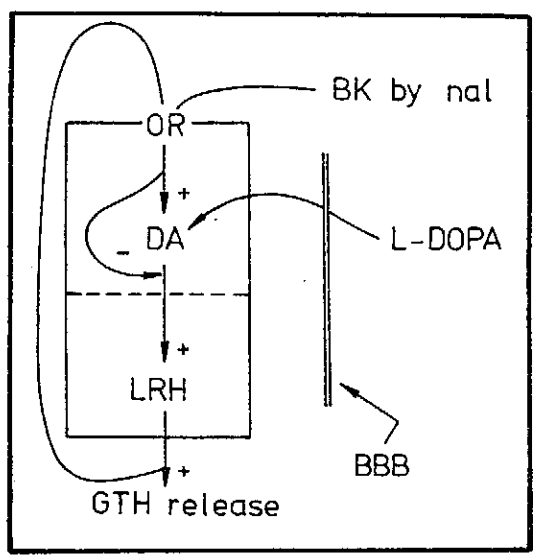

* To be published XITH International Congress of Biochemistry

Annual Report of the Institute of Physics, Academia Sinica, Vol. 8, 1978

Proton Transfer Hypotheses In Visual Excitation

WEI KUNG WANG (王 唯 工)

Institute of Physics, Academia Sinica
Nankang, Taipei, Rep. of China

Abstract

There are several proton transfer hypotheses in recent literature, the original proposal by Kropf[1] has suggested a proton to be picked up by the chromophore during the 11-cis to all-trans isomerization. Shirane[2] and Peters et al[3] has suggested a local proton transfer that happened before the chromophore isomerization. And Wang[4] has suggested a detailed proton transfer process, that involves the sulfhydral group of the apoprotein.

Distinctions between these hypotheses will be discussed.

* This paper has been Presented At International Symposium on Visual Pigment and Purple Membrane.

1. Kropf A. Nature 260, 726, 1976
2. Shirane K. Nature 254, 722- 1975
3. Peters K. et al P. N. A. S. (U. S. A.) 74, 3119, 1977
4. Wang W. K. Abstract 5th IBC 1975 and Chinese Bioscience 10, 42, 1976

密度層變流中的擴散及其在海洋放流之應用*

Dispersion in Stratified Flows and Its Application to Ocean Outfalls

黃榮鑑　傅忠申　王燦汶

摘　　要

本文藉實驗之理論的數值計算，探討線性密度層變水域一垂直二維浮昇射流的擴散特性。浮昇射流之擴散理論用質量、動量、動能量守恒方程，利用斷面積分法，設定速度與密差剖面呈高氏分佈，並引用捲增概念，導出常一微分控制方程組。捲增係數則用動能量守恒推導出，與反局部密度 Froude 數成線性的關係式，而非一通用常數。流場中各物理總量之變化，由此控制方程組與啓始條件解出。

實驗方面，使用鹽水分層填加方法，填製線性密度層變水域，擴散比由實驗中對速度及密度差的剖面分佈之量測定出，介於 1.10～1.40 之間。本文之數值計算取定 1.30。比較實驗測定之縱向軸中心速度及軸中心密度差分佈與數值之計算結果，以印證理論之分析。

* 本文已發表於土木水利季刊第五卷第三期，中華民國六十七年十一月

Annual Report of the Institute of Physics, Academia Sinica, Vol. 8, 1978

The Application of Kuo's Parameterization of Cumulus Convection in Mei-Yu Weather System*

WEN-JEY LIANG (梁文傑) and CHYI-JANG SHIAU (蕭錫璋)

Institute of Physics, Acamemia Sinica
Nankang, Taipei, Taiwan
Republic of Cnina

Abstract

Kuo's (1965 and 1974) two parameterization schemes of cumulus convection are applied to the numerical weather prediction of Mei-Yu system in East-Asia Area. The applicability of schemes is investigated utilizing the four-layer baroclinic quasi-geostrophic model. The forecast include the height, the vorticity, the vertical velocity, the mixing ratio, the temperature, the cloud coverage, the latent heat released and the precipitation. The results show that both schemes are applicable in Mei-Yu system. The advantages and disadvantages of two schemes are discussed and their relationships are investigated theoretically and numerically. The theoretical considerations are based on the moisture conservation equation and the numerical studies are based on the results of the numerical weather forecasts. Both indicate that Kuo's two schemes are essentially similar if the suitable values are asigned to the constants which are assumed to represent the remained to represent the remaining fraction of the total moisture convergence stored in the air to increase the humidity of the environment atmosphere.

* This abstract has been accepted by the 12th Technical Conference on Hurricanes and tropical Meteorology.